PLACE IN RETURN BOX to remove this checkout from your record.
TO AVOID FINES return on or before date due.
MAY BE RECALLED with earlier due date if requested.

DATE DUE	DATE DUE	DATE DUE

6/01 c:/CIRC/DateDue.p65-p.15

FUNDAMENTAL STUDIES AND ANALYTICAL APPLICATIONS OF SELECTIVE FLUORESCENCE QUENCHING

By

John V. Goodpaster

A DISSERTATION

Submitted to
Michigan State University
in partial fulfillment of the requirements
for the degree of

DOCTOR OF PHILOSOPHY

Department of Chemistry

2000

ABSTRACT

FUNDAMENTAL STUDIES AND ANALYTICAL APPLICATIONS OF SELECTIVE FLUORESCENCE QUENCHING

By

John V. Goodpaster

Selective fluorescence quenching is a photophysical process whereby an excited-state fluorophore is deactivated by a quencher molecule but other, structurally similar fluorophores remain unaffected. In this work, this phenomenon is investigated on theoretical, experimental, and applied levels.

Ab initio calculations were used to study the mechanism by which selective quenchers discriminate between alternant and nonalternant polycyclic aromatic hydrocarbons (PAHs). Calculations of the ground- and excited-state properties of four representative PAHs demonstrated that relative to their alternant isomers, nonalternant PAHs possess higher ground-state energies, lower relative excitation energies, and greater changes in their excited-state geometries. Selective quenching of pyrene (an alternant PAH) versus fluoranthene (a nonalternant PAH) by nitromethane was also studied. Although two routes existed for the deactivation of pyrene, only formation of an ion pair and its subsequent recombination to form a ground-state complex was both energetically feasible and allowed within symmetry selection rules. In contrast, fluoranthene had no energetically favorable route to deactivation via an ion pair.

More rapid and accurate methods for determining the efficiency and selectivity of quenchers have also been developed. A sensitive, multiwavelength fluorescence detection system with a capillary flow cell was designed, built and characterized for this purpose. Flow-injection techniques that automated the preparation and mixing of fluorophore and quencher solutions were developed and validated by comparison to traditional methods. Using this apparatus, primary, secondary, and tertiary mono- and diamines were studied as selective quenchers of nonalternant PAHs. Quenching efficiency increased and selectivity decreased with the electron-donating ability of the amine. However, all compounds studied were more selective than previously reported quenchers for nonalternant PAHs. Nitrated explosives were also studied as quenchers of alternant PAHs, and found to be highly efficient quenchers of pyrene. In particular, nitroaromatic species could be identified based on their unique perturbation of the pyrene excited state.

Lastly, the use of selective fluorescence quenching for novel forms of detection in capillary liquid chromatography has been explored. Adding either nitromethane or diisopropylamine to the effluent of a capillary liquid chromatography column followed by laser-induced fluorescence detection enabled the profiling of complex mixtures of alternant and nonalternant PAHs. Conversely, adding pyrene to the column effluent allowed for indirect detection of nitrated explosives. These techniques were applied to the forensic and environmental analysis of petroleum products and explosives. Both qualitative and quantitative information about the composition and potential common origin of various samples was generated.

To God, Family, and Friends,
Whose Love and Support Made This Possible

ACKNOWLEDGMENTS

"If you see a turtle on a fencepost, you know it had some help."

Alex Haley

Perhaps it is not surprising that even as I write the final words of my dissertation I have not completely internalized the meaning and import of completing of my Ph.D. degree in chemistry. However, I am very capable of bringing to mind the many people whose skills, generosity, and support helped make this endeavor a reality.

First and foremost, my thanks go to my advisor Dr. Victoria McGuffin. Her wisdom, expertise, and guidance were crucial in my attaining the level of intellectual development and independence I now enjoy. I will always admire the example she has set of extraordinary dedication to excellence, genuine concern for her students, and continual creativity and curiosity. As I embark on my own scientific career, I see that her vitality, caring, and support during these important years will help me in whatever path I take.

I also appreciate the effort and input of my Ph.D. committee. Dr. James Harrison served not only as a second reader of this dissertation but as an integral part of our efforts to use ab initio calculations to understand complex chemical processes. Dr. Jay Siegel has helped to solidify and direct my enthusiasm for the forensic sciences, and I am very grateful for his willingness to work with me and encourage applications of our work to criminal justice. Dr. Merlin Bruening was a wonderful addition to my committee whose insight, thoughts, and questions helped encourage a fuller understanding of our work.

I would also like to thank those instructors and mentors from high school and college who have played important roles in my life. Most notably I thank my undergraduate advisor Dr. Larry Potts of Gustavus College in St. Peter, MN. His encouragement and example helped to inspire me to pursue graduate studies and I still appreciate the many practical and personal lessons I learned as one of his students. I also send my thanks to John Geroux of St. Thomas Academy in Mendota Heights, MN for always encouraging my curiosity and independence.

A number of students, faculty, and staff within the Department of Chemistry at Michigan State also made important contributions to this project. Joe Tulock and Dr. Gary Blanchard gave invaluable access to their instrumentation and assistance in measuring fluorescence lifetimes. The literature review and laboratory work of Jason Wolf and Geoff Koboldt, respectively, helped to shape the course of this research and directly led to valuable and novel results. Dick Menke of the Machine Shop was a true craftsman in his construction of the inlet optics assembly of our instrument. Kermit Johnson generously lent his expertise for the acquisition and interpretation of NMR results. Paul Reed of Computing Services was continually available to assist with software, hardware, and network questions of all kinds. Lastly, the expert assistance of Scott Sanderson, Dave Cedarstaff, and Ron Haas of Instrument Services was invaluable throughout the assembly and (eventual) repair of virtually every piece of equipment I used.

My thanks also go out to people outside our department, particularly Michael Hasselhuhn of the Melles Griot Laser Group and Christine Ballard of

PE/Applied Biosystems who generously gave of their time and efforts to assist us with our laser and chromatographic systems, respectively. Lee Brun-Conti, Chris Bommarito, Mike Burritt, and Reinhard Pope of the Michigan State Police provided us with valuable samples of explosives, greatly improving the validation as well as the forensic interest of our analytical methods.

I am also very grateful for financial assistance in the form of graduate fellowships from the College of Natural Science at Michigan State, the National Science Foundation, the Division of Analytical Chemistry of the American Chemical Society (sponsored by Eli Lilly), and the American Association of Crime Laboratory Directors. Grants and computational support from the National Science Foundation, the National Partnership for Advanced Computational Infrastructure, the U.S. Department of Energy, Office of Basic Energy Sciences, and the MSU Center for Fundamental Materials Research are also gratefully acknowledged.

On a personal note, I want to express my utmost and sincere thanks to the many people whose love, care, and support helped me to continue and now complete this process. First, I send my thanks to my parents Ken and Harriet and my sisters Beth and Katie. Thank you for always being there for me no matter what the circumstances, showering me with love, concern and advice, and simply being my best, most wonderful friends. Thanks to my uncle Bob and aunt Chris, and my cousins Mike, Dave, Ben, Joe, Rachel, and Maria. To my delight I have felt like an adopted member of your family; your generous spirit and laughter-filled house were joys to be around.

To Peter Krouskop: you have always served as a good example for me and I truly admire the way you have treated me and those around you. I have no doubt that you will make valuable contributions to this world on both personal and professional levels. Thank you to Sam Howerton for his hard work on our collaborative projects and for being an honorable, continually supportive, as well as goofy friend. I will miss ducking flung paper balls and bracing myself for sudden scares (although perhaps not). To Tom Cullen: I have always considered you a role model for what a graduate student should do and be. Thank you also to Mike Sanregret for his wonderful spirit and dedication to doing good in life.

To Judy Ferris, Ron, Brian, Clarence, Dave, Joe, and my other fellows: your contributions to my sanity, growth, and well-being are both profound and immeasurable. Through your support and fellowship I have achieved a greater sense of serenity and spirituality that will be with me always. Also, my special thanks goes to Beth, Eponine, and Katie for their gentle company along this road. Your love was a vastly important and beautiful experience for me. Finally, I send my thanks to all those who I regrettably did not mention here but should have. I can safely say that I am leaving East Lansing and Michigan State older, wiser, and more capable than I came to them, and for that I can only be eternally grateful.

JVG

TABLE OF CONTENTS

LIST OF TABLES

LIST OF FIGURES

CHAPTER 1

INTRODUCTION AND BACKGROUND

As the demand to analyze increasingly complex samples increases, so does the importance of developing novel analytical techniques that possess higher levels of both selectivity and sensitivity. The combination of efficient separation techniques and sensitive detection methods has long been applied in this area. Furthermore, among the spectroscopic detection techniques used in separations, fluorescence is virtually unrivalled in terms of its sensitivity. However, fluorescence does not yield information about the structure or photochemical properties of analyte molecules.

In this dissertation, the phenomenon of selective fluorescence quenching is studied and applied to the analysis of complex mixtures with both environmental and forensic importance. In particular, polycyclic aromatic compounds (PACs) are a group of analytes that benefit greatly from fluorescence detection combined with selective quenching agents. The structure and properties of PACs, as well as the processes and progress in selective fluorescence quenching shall be reviewed here.

I. Polycyclic Aromatic Compounds (PACs)

A. Classification and Structure

Polycyclic aromatic compounds are a diverse group of molecules that are both naturally occurring and anthropogenic, and are found at trace levels in many sample matrixes. Together they form the largest known class of chemical carcinogens and mutagens, with sixteen PACs identified by the U.S. Environmental Protection Agency (EPA) as priority pollutants. Furthermore, PACs exist in many and various isomeric configurations; only some of which are benign while others have potent biological activity.[1,2]

Some useful schemes have been developed to classify these compounds according to their structural and chemical differences. In this discussion, PACs are defined as any compound consisting of two or more fused aromatic rings. One important subclass of the PACs is the polycyclic aromatic hydrocarbons (PAHs), which are composed solely of carbon and hydrogen atoms, as shown in Figure 1-1. Within the PAH subclass are two structural categories: alternant and nonalternant. To distinguish between these categories, it is helpful to label each carbon atom in the aromatic structure alternatively, skipping an atom between labels (see Figure 1-2). Alternant PAHs possess a structure such that no two atoms of the same type (labeled or unlabeled) are adjacent. Examples include naphthalene, anthracene, and other PAHs that consist solely of six-membered rings. Nonalternant PAHs have a structure where such labeling results in two adjacent atoms of the same type. Examples include fluorene and fluoranthene, which contain one five-membered ring together with six-membered rings. The distribution of electrons is more uniform in alternant than in nonalternant PAH, which in turn influences their photophysical and photochemical properties.[1,2]

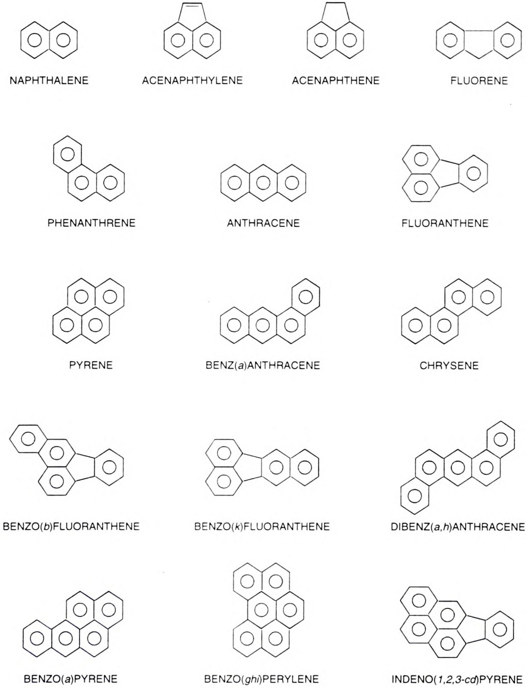

NAPHTHALENE ACENAPHTHYLENE ACENAPHTHENE FLUORENE

PHENANTHRENE ANTHRACENE FLUORANTHENE

PYRENE BENZ(*a*)ANTHRACENE CHRYSENE

BENZO(*b*)FLUORANTHENE BENZO(*k*)FLUORANTHENE DIBENZ(*a,h*)ANTHRACENE

BENZO(*a*)PYRENE BENZO(*ghi*)PERYLENE INDENO(*1,2,3-cd*)PYRENE

Figure 1-1: Structures of various alternant and nonalternant polycyclic aromatic hydrocarbons (PAHs) from the U.S. EPA list of priority pollutants.

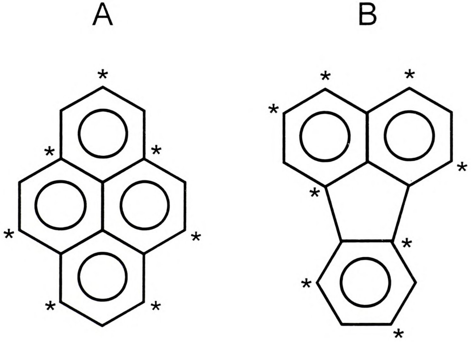

Figure 1-2: Example of an A) alternant and B) nonalternant PAH structure with atom labels.

Many functional groups occur in PACs, which further increases the structural and chemical diversity of the class. Heterocyclic PACs can be formed by substituting oxygen, nitrogen, or sulfur for carbon atoms within the aromatic ring. The terms alternant and nonalternant can also be used to describe these compounds by basing the classification on the structure of the parent PAH. Heterocyclic PACs are commonly found in heavy petroleum products such as crude oil.[1] Alkyl groups often occur in PACs that have been formed during long-term exposure to low or moderate temperatures, such as in geological environments.[3] Hydroxyl, epoxide, carbonyl, carboxyl, and related functional groups are formed by hydrolysis and oxidation of PACs in water and soil, accelerated by ultraviolet (UV) irradiation from the sun.[4] Airborne PACs can react with atmospheric NO_x and SO_x to form the corresponding nitrate and sulfonate derivatives.[4] Finally, other functional groups such as cyano, amine, or halide groups may be present in synthetic PACs, but are not usually found in naturally occurring materials.[5,6]

In general, most PACs are solid materials with limited volatility and water solubility at ambient temperature. Both of these properties decrease with increasing number of aromatic rings, however the presence of polar functional groups generally serves to decrease volatility and increase water solubility.[1,2,4]

B. *Origin and Formation*

The origin of PACs can be either natural or anthropogenic, the latter being the predominant source of environmentally hazardous compounds. In general, any process that exposes organic matter to heat will produce PACs.[3] The

natural processes that generate PACs include forest fires, volcanic activity, and degradation of organic matter, although the latter remains a subject of debate.[1,3] Of these natural processes, prairie and forest fires introduce the most PACs into the environment. Anthropogenic sources include combustion of tobacco or wood, coke production, carbon black production, petroleum fuel production and processing, as well as the consumption of fuels in furnaces and automobiles.[1] The burning of coal mining refuse and coke production are the most significant human-based sources of PACs.[1]

The mechanism of PAC formation begins with pyrolysis of the organic matter, wherein reactive free-radical intermediates are formed. This is followed by pyrosynthesis, wherein the radicals condense to form stable aromatic products.[3] The structure of the resulting PAC is dependent upon the reaction conditions. For example, highly alkylated PACs are less stable and form at lower temperatures over longer time scales (e.g., during geological degradation). In contrast, PACs that are devoid of side chains form rapidly at high temperatures (e.g., during combustion).[3] The high temperature conditions must be sustained over a long time period in order to form the most stable isomers. The PAC isomers that are most stable contain alternant, clustered arrangements of aromatic rings (e.g., pyrene in Figure 1-1), followed by angular arrangements (e.g., phenanthrene) and linear arrangements (e.g., anthracene). Finally, nonalternant PACs tend to form at lower temperatures and the number of non-aromatic rings increases with reaction time.[3] For all PACs, the number of structural and positional isomers increases markedly with the number of rings.

C. Sampling and Analysis

Because of their many and diverse sources, PACs are nearly ubiquitous and are found at trace levels in air, water, and soil samples. As a result, a variety of different methods have been developed for sampling as well as for selective extraction of the PACs from the sample matrix. In atmospheric samples, where PACs are often transported on airborne particulates because of their low volatility, some form of filtering or precipitation is required prior to analysis.[1,7] In water samples, where PACs tend to adsorb on suspended particles because of their low solubility, liquid and solid-phase extraction methods are commonly used.[1,7] Finally, for PACs in soil and other solid samples, Soxhlet extraction or supercritical fluid extraction have proven to be effective methods.[1,7]

After sampling and selective extraction, additional methods are often required to reduce the sample complexity such that the desired individual PAC or classes of PACs can be analyzed. Immunological methods are among the most specific methods for PACs, but are not broadly applicable.[2] In contrast, chromatographic separation methods such as gas, supercritical fluid, and liquid chromatography are widely used to resolve complex mixtures of PACs.[1,2,8,9] Microcolumn or capillary column chromatographic methods have proven to be especially successful because of their high separation efficiency.[10,11] After separation, spectroscopic techniques are often used to identify and to quantitate the individual PAC in the sample. These methods include optical spectroscopic techniques, such as absorption in the infrared, visible, or ultraviolet regions, or

emission of fluorescence/phosphorescence, as well as Raman and other light-scattering techniques.[2] In addition, a wide variety of non-optical techniques, such as mass spectrometry, nuclear magnetic resonance spectroscopy, multiphoton ionization spectroscopy, photothermal spectroscopy, and many others are used.[2]

Because of their inherent sensitivity and selectivity, luminescence techniques such as fluorescence and phosphorescence spectroscopy are among the most popular methods for PAC analysis.[12-23] For example, laser-induced fluorescence has attained detection limits for PAHs at the sub-part-per-trillion level.[24]

II. Fluorescence Quenching

Fluorescence quenching may be simply defined as any process that decreases the observed fluorescence power from a sample. Although quenching is generally thought to be detrimental, it can be used to analytical advantage if invoked in a carefully designed and controlled manner. In this approach, the fluorophore is intentionally deactivated through collision with a quencher that selectively promotes nonradiative deactivation, usually by external conversion but also by enhanced intersystem crossing and phosphorescence pathways.[25,26] This approach can provide valuable photophysical and photochemical information about individual PACs. It can also be used to simplify fluorescence spectra of complex mixtures of PACs by selective removal of interfering components. Not all quenching processes are analytically useful, however, as they may be nonselective or may not provide any characteristic information about the fluorophore or sample.

A. Trivial Quenching Mechanisms

One trivial cause for a decrease in fluorescence power is absorption o either the excitation from the source (primary filtering) or the emission from t fluorophore (secondary filtering).[27] Because the excitation wavelength is alw shorter than the emission wavelength, often in the UV region, primary filterin the fluorophore, quencher, solvent, or other concomitant species is generally more prevalent and problematic than secondary filtering. However, seconda filtering can be important for samples that contain complex mixtures of PACs the emission from smaller molecules may be of an appropriate wavelength fo absorption by those with a greater number of aromatic rings.[27] In addition, th special case of secondary filtering wherein the fluorophore itself reabsorbs th emitted photons, termed *self-absorption*, is also commonly observed at high concentration.[25-27] This source of trivial quenching can be reduced or comple eliminated if the pathlength is sufficiently small.

Other phenomena that are manifested as an apparent decrease in fluorescence power include reflective and refractive losses due to changes ir refractive index of the sample, which become particularly significant at high concentration of PACs. In addition, light scattering may occur if the sample i turbid or contains suspended particulates. Such effects should be minimizec insofar as possible by sample pretreatment in order to prevent their interferer with analytically important quenching phenomena.

B. Dynamic or Excited-State Quenching Mechanisms

The dynamic quenching process is illustrated in the energy-level diagram in Figure 1-3. In this process, an excited-state fluorophore ($^1F_1$) collides and forms a transient complex with a ground-state quencher (Q). Because the complex must be formed during the excited-state lifetime, this form of quenching is diffusion controlled and, hence, is dependent on the concentration of the fluorophore and quencher. The excited-state complex dissociates either upon radiative or nonradiative deactivation, leaving both the fluorophore and quencher in the ground state.[25-27]

If the quencher is a ground-state fluorophore molecule, this process is *self-quenching* and the complex is known as an excited-state dimer or *excimer.*[25-27] PACs are particularly prone to excimer formation at high concentration due to their low solubility in most solvents as well as their planar structure, which facilitates face-to-face interaction. The excimers formed by PACs are often fluorescent or phosphorescent complexes, however the spectral properties differ significantly from those of the monomer. For example, the monomer of pyrene exhibits several sharp emission bands between 370 and 400 nm, whereas the excimer has very broad and featureless emission between 450 and 600 nm.[28,29] Thus, self-quenching can be distinguished if the excitation spectrum remains unchanged but the emission spectrum develops new features at longer wavelength (lower energy) as the concentration of the fluorophore increases.

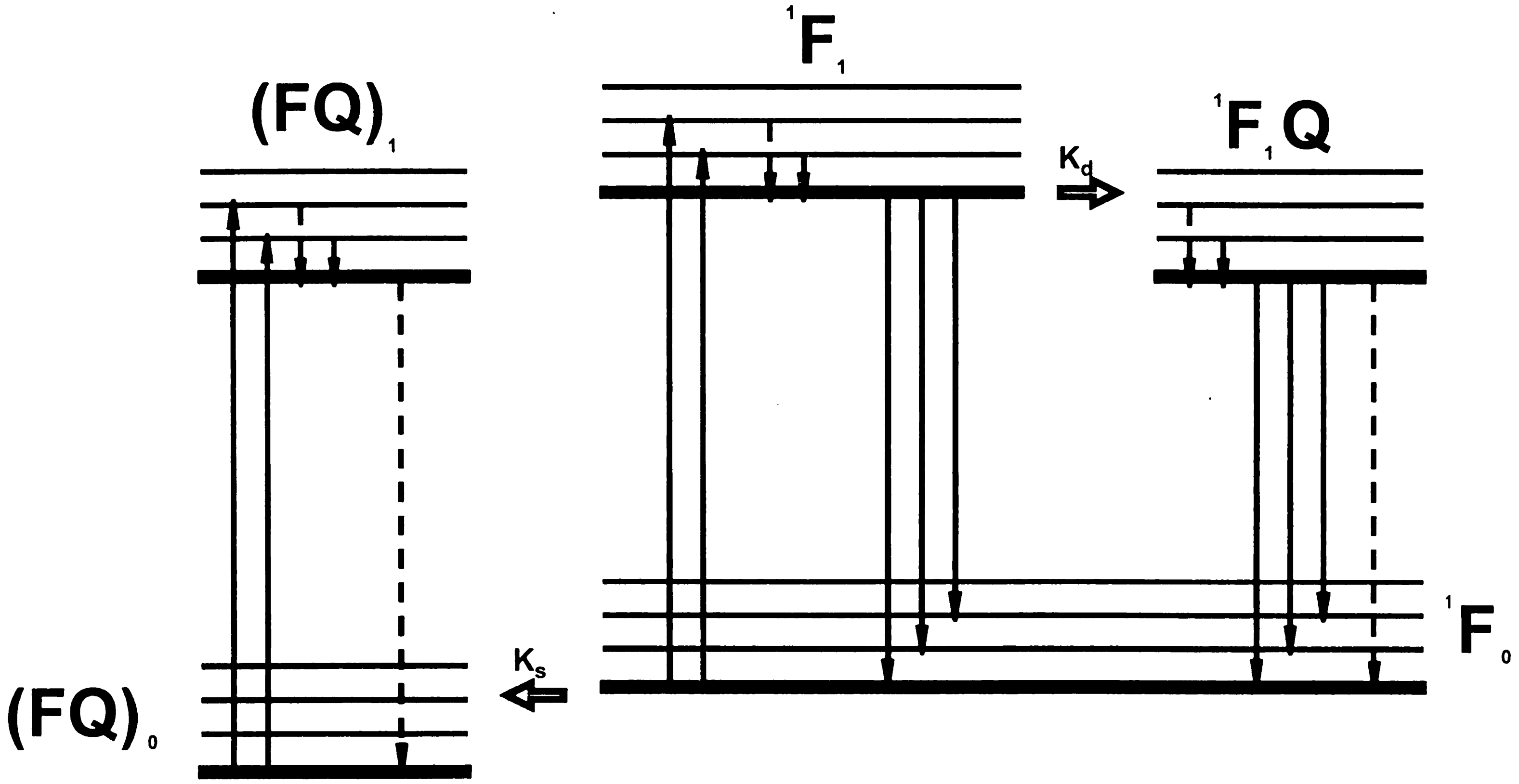

Figure 1-3: Energy-level diagram showing dynamic (K_d) and static (K_s) fluorescence quenching of fluorophore F by quencher Q.

If the quencher is a ground-state species other than the fluorophore, then the excited-state complex is known as an *exciplex*. These complexes often involve substantial charge transfer between the fluorophore and quencher and, thus, can facilitate energy transfer to the quencher. As the exciplex dissociates, both fluorophore and quencher return to the ground state *via* nonradiative pathways so that the excess energy is dissipated through vibrational relaxation and external conversion. This type of dynamic quenching, which is the most useful for analytical purposes, is described by the Stern–Volmer equation[25,26]

$$\frac{\Phi_f^{\circ}}{\Phi_f} = 1 + k_d \tau_f^{\circ} C_q = 1 + K_d C_q \qquad (1\text{-}1)$$

where Φ_f° and Φ_f are the quantum efficiency of the fluorophore in the absence and presence of quencher, respectively, k_d is the bimolecular rate constant for dynamic quenching, τ_f° is the fluorescence lifetime of the fluorophore, C_q is the molar concentration of the quencher, and K_d is the Stern–Volmer constant. For many quenchers, the efficiency of energy transfer is sufficiently high to enable the rate constants to approach the diffusion-controlled limit.

A more useful form of the Stern–Volmer equation can be written if the source power, efficiency of optical irradiation and collection, and fluorophore absorbance remain constant. In this case, the fluorescence power is directly proportional to the quantum efficiency and equation (1-1) becomes

$$\frac{P_f^{\circ}}{P_f} = 1 + K_d C_q \qquad (1\text{-}2)$$

A graph of the ratio of fluorescence power in the absence (P_f°) and presence (P_f) of quencher as a function of the quencher concentration is known as a Stern–Volmer plot. This graph will be linear with a slope equal to the Stern–Volmer constant (K_d) and an intercept of unity.[25,26]

However, if the quencher has a significant absorbance at either the excitation or emission wavelengths, a positive deviation from linearity will be observed due to primary or secondary filtering. The effects of such absorbance can be corrected through a modified form of the Stern–Volmer equation[30]

$$\left(\frac{P_f^{\circ}}{P_f}\right)\left\{\frac{1-\exp\left(-2.3\varepsilon_{Q,1}bC_q\right)}{2.3\varepsilon_{Q,1}bC_q}\right\}\left\{\frac{1-\exp\left(-2.3\varepsilon_{Q,2}bC_q\right)}{2.3\varepsilon_{Q,2}C_q}\right\}=1+K_dC_q \qquad (1\text{-}3)$$

where $\varepsilon_{Q,1}$ and $\varepsilon_{Q,2}$ are the molar absorptivity of the quencher at the excitation and emission wavelengths, respectively, and all other variables are as defined previously.

The presence of dynamic quenching by a species other than the fluorophore can be confirmed by a number of observations. First, the excitation spectrum of the fluorophore will remain unchanged as the quencher concentration is increased. In contrast, the emission spectrum will show a progressive loss in intensity but no substantial change in wavelength. There may be an emission band at longer wavelength, progressively increasing in intensity with quencher concentration, if the exciplex is sufficiently stable to exhibit fluorescence or phosphorescence.[27] Secondly, the dynamic quenching process is dependent upon diffusion of the fluorophore and quencher during the excited-state lifetime. Thus, the Stern–Volmer constant will increase with increasing temperature (T) or with decreasing solvent viscosity (η), and the rate constant will show a linear dependence on T / η.[26] Finally, dynamic quenching is a nonradiative process that will decrease the observed fluorescence lifetime. As the lifetime is proportional to the quantum efficiency, the Stern–Volmer equation can be written as[25,26]

$$\frac{\tau_f^{\circ}}{\tau_f} = 1 + k_d \tau_f^{\circ} C_q = 1 + K_d C_q \tag{1-4}$$

If fluorescence lifetimes are measured in the absence (τ_f°) and presence (τ_f) of quencher, then k_d or K_d can be calculated directly by means of equation (1-4). In contrast to equation (1-2), this approach is completely valid and accurate in the presence of other forms of trivial and static quenching (see below).

C. *Static or Ground-State Quenching Mechanisms*

The static quenching process is also illustrated in the energy-level diagram in Figure 1-3. In this process, a complex is formed between the ground-state fluorophore (${}^1F_0$) and the ground-state quencher (Q). This ground-state complex $(FQ)_0$ is stable and may undergo various photophysical processes, including absorption, fluorescence, and phosphorescence. However, the spectral properties of the complex will necessarily differ from those of the uncomplexed fluorophore.

For static quenching, a linear relationship is observed between the quantum efficiency ratio and the quencher concentration[25,26]

$$\frac{\Phi_f^{\circ}}{\Phi_f} = 1 + K_s C_q \tag{1-5}$$

where K_s is the equilibrium formation constant of the fluorophore-quencher complex, and all other variables are as defined previously. If the spectroscopic and photochemical variables discussed above remain constant, then fluorescence power is directly proportional to quantum efficiency (as above) and equation (1-5) becomes

$$\frac{P_f^\circ}{P_f} = 1 + K_s C_q \qquad (1\text{-}6)$$

Hence, a graph of P_f^0/P_f *versus* C_q for static quenching will be linear with a slope of K_s and an intercept of unity. If trivial quenching due to absorbance effects is important, corrections can be made by using a modified form of equation (1-3).

The most clear and unambiguous demonstration of the presence of static quenching is by examination of the absorbance and fluorescence spectra. The absorbance of the fluorophore will decrease with increasing concentration of the quencher, while a new absorbance band for the complex will appear at a different wavelength and will increase simultaneously. The fluorescence excitation and emission spectra of the fluorophore will both decrease in intensity with increasing quencher concentration and, if the complex is fluorescent, new spectral features will appear. Static quenching may also be readily distinguished by its dependence on viscosity and temperature. Because static quenching is an equilibrium process, rather than a kinetic process like dynamic quenching, it is not controlled by diffusion and is not dependent on solvent viscosity.[26] In addition, K_s will decrease with increasing temperature because of the reduced stability of the ground-state complex, in direct contrast to K_d for dynamic quenching.[26] Finally, because static quenching typically results in non-fluorescent complexes, the original unquenched lifetime of the fluorophore will not change upon addition of quencher.

Some quenchers may act through a combination of static and dynamic mechanisms. This behavior is revealed by a positive deviation from linearity in the Stern–Volmer plot, which remains after correction for absorbance effects according to equation (1-3). For these quenchers, a modified form of the Stern–Volmer equation is necessary to include both static and dynamic processes[25,26]

$$\frac{P_f^{\circ}}{P_f} = \left(1 + K_d C_q\right)\left(1 + K_s C_q\right) \qquad (1\text{-}7)$$

The graph of P_f^0/P_f *versus* C_q must be fit by nonlinear regression methods in order to determine values for the two quenching constants. The fluorescence lifetimes can then be used, together with equation (1-4), to identify which of these constants should be assigned to the dynamic quenching process.

D. Solvent Effects

Before discussing the behavior of specific quenching agents, it is important to consider the effect of the solvent on fluorescence and fluorescence quenching processes. Immediately after excitation and the rapid nonradiative processes that may follow, the fluorophore is in the initial or Franck–Condon excited state.[26] At this point, the solvent molecules that were positioned around the ground-state fluorophore must reorient to accommodate the new electron distribution and dipole moment of the excited-state fluorophore. As solvent reorganization is usually faster than radiative emission, fluorescence and phosphorescence will occur from the "solvent relaxed" or equilibrium excited state whose energy is lower than that of the initial excited state.[26] Thus, the physical and chemical properties of the solvent play an important role in determining the stability of the excited-state fluorophore as well as its spectral properties.[26,31] The solvent effects may be divided into two classes: general solvent effects that uniformly govern the behavior of all fluorophores and solvents, and specific effects that occur for a given fluorophore–solvent pair. The specific solvent effects arise from hydrogen bonding or other strong intermolecular forces, which may overpower or conceal the general solvent effects that are described below.[26,31]

The viscosity of the solvent is known to affect inversely the rate of molecular diffusion or migration. Hence, an increase in viscosity will prolong the time required for solvent relaxation in comparison with the fluorescence lifetime of the initial excited state. This will favor radiative emission from the initial rather than the equilibrium excited state, which will be manifested as a shorter wavelength and shorter lifetime.[26]

Other physical properties of the solvent will influence the stability of the excited-state fluorophore. The excited states of most PACs are more polar and have a larger dipole moment than their ground states. To the extent that the solvent is able to interact with this dipole by induction and orientation forces, it can stabilize and decrease the energy of the excited-state fluorophore. Dipole induction forces are governed by the molecular polarizability of the solvent, which is related to its bulk refractive index, whereas dipole orientation forces are governed by the molecular dipole moment of the solvent, which is related to its bulk dielectric constant. Thus, a decrease in the refractive index or an increase in the dielectric constant of the solvent will cause a shift of the fluorescence emission to longer wavelength.[26] Because the dielectric constant varies over a much wider range than refractive index, its effect on the emission wavelength is usually more apparent.

These same solvent properties can also have a profound effect on the rate and mechanism of fluorescence quenching. In the case of dynamic quenching, the viscosity of the solvent will influence the rate of diffusion of the quencher to the excited-state fluorophore. Specifically, an increase in solvent viscosity will decrease the diffusion-controlled limit for bimolecular collisions. The resultant effect will be to decrease the rate constant for dynamic quenching (k_d) as well as the Stern–Volmer constant (K_d).

The dielectric constant of the solvent will also have an effect on the quenching mechanism. In many cases, static and dynamic quenching involves the formation of a complex between the fluorophore and quencher with significant charge-transfer character. A solvent with high dielectric constant such as acetonitrile will tend to encourage such charge-transfer processes by stabilization of the ion pair. In some cases, the ion pair may be sufficiently stable in polar environments to be observed and spectroscopically characterized.[31] The formation of ion pairs in solvents of low dielectric constant is unlikely, however, and neutral complexes will be favored instead.

Finally, it is important to note that the solvent serves as the intrinsic collisional quencher of all fluorophores. Only those quenchers that can compete effectively with the more abundant solvent molecules will show any discernible quenching behavior. Hence, all quenching rates and mechanisms must be evaluated within the context of the selected solvent.

III. Analytical Applications of Fluorescence Quenching

A. Selective Intersystem Crossing by Halogens and Silver Ions

Numerous efficient quenchers of PAC fluorescence have been reported including oxygen,[32,33] inorganic salts,[34,35] halogenated compounds,[36-38] amines,[39-42] nitriles,[43-45] and nitrated aromatic compounds.[46] However, only a few quenchers have been explored in terms of their selectivity and use in analytical techniques. For example, one of the earliest applications of fluorescence quenching was the use of iodomethane and iodoethane to increase the phosphorescence yield of selected PACs.[47-52] Iodomethane was found to selectively quench the fluorescence of naphthalene, anthracene, fluoranthene, naphthacene, chrysene, and benzo(*a*)pyrene. However, the fluorescence of perylene, 3-methylperylene, dibenzo(*a,f*)perylene, and dibenzo(*b,def*)chrysene was not significantly affected. Iodoethane preferentially quenched the fluorescence of benzo(*a*)fluorene, benzo(*b*)fluorene, benz(*a*)anthracene, naphthacene, benzo(*a*)pyrene, and dibenz(*a,c*)anthracene. However, this quencher did not affect the fluorescence of naphthalene, acenaphthylene, anthracene, phenanthrene, and triphenylene.

Halogenated quenchers such as these promote intersystem crossing through the heavy atom effect and, hence, enhance phosphorescence at the expense of fluorescence. Their selectivity is based, in part, on fluorescence lifetime as the longer-lived fluorophores are more available for deactivating collisions with the quencher. In addition, the relative energy of the singlet and triplet excited states of the fluorophore will also influence its ability to undergo intersystem crossing on a time scale that is competitive with fluorescence.[1,2]

Another quencher that has been used to enhance intersystem crossing is silver nitrate, which tends to selectively quench the fluorescence of nitrogen-substituted heterocyclic PACs relative to their parent PAH.[53] It has been conjectured that the unoccupied 5s orbital of Ag^+ serves as an electron acceptor from either the nonbonded electron pair or the aromatic ring of the heterocyclic PAC.[1]

B. Selective Quenching by Nitromethane

Nitromethane, an electron-accepting quencher that acts through the dynamic mechanism, has received a great deal of attention because of its high selectivity. As first noted by Sawicki and coworkers,[54] nitromethane quenches the fluorescence of PAHs with an alternant structure but not those with a nonalternant structure. The Stern–Volmer constants for the alternant PAH are typically one to two orders-of-magnitude greater than those of the nonalternant PAH. For example, Figures 1-4 and 1-5 illustrate the quenching behavior of

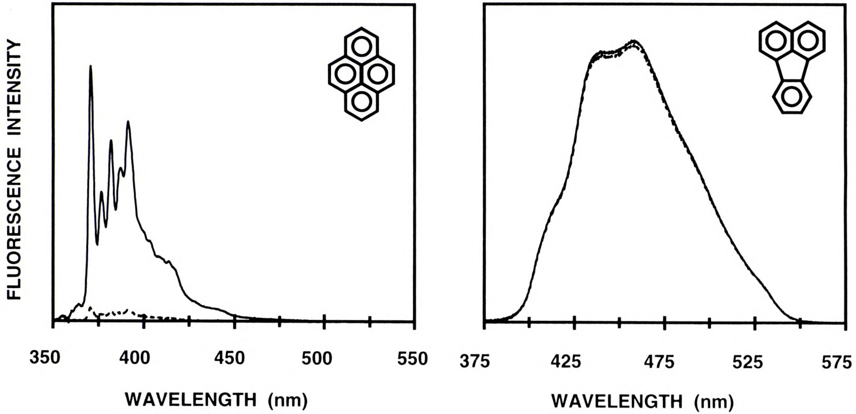

Figure 1-4: Effect of the dynamic quencher nitromethane on the fluorescence spectra of pyrene and fluoranthene. (—) 10^{-5} M fluorophore in methanol, (- -) after addition of 10^{-3} M nitromethane.

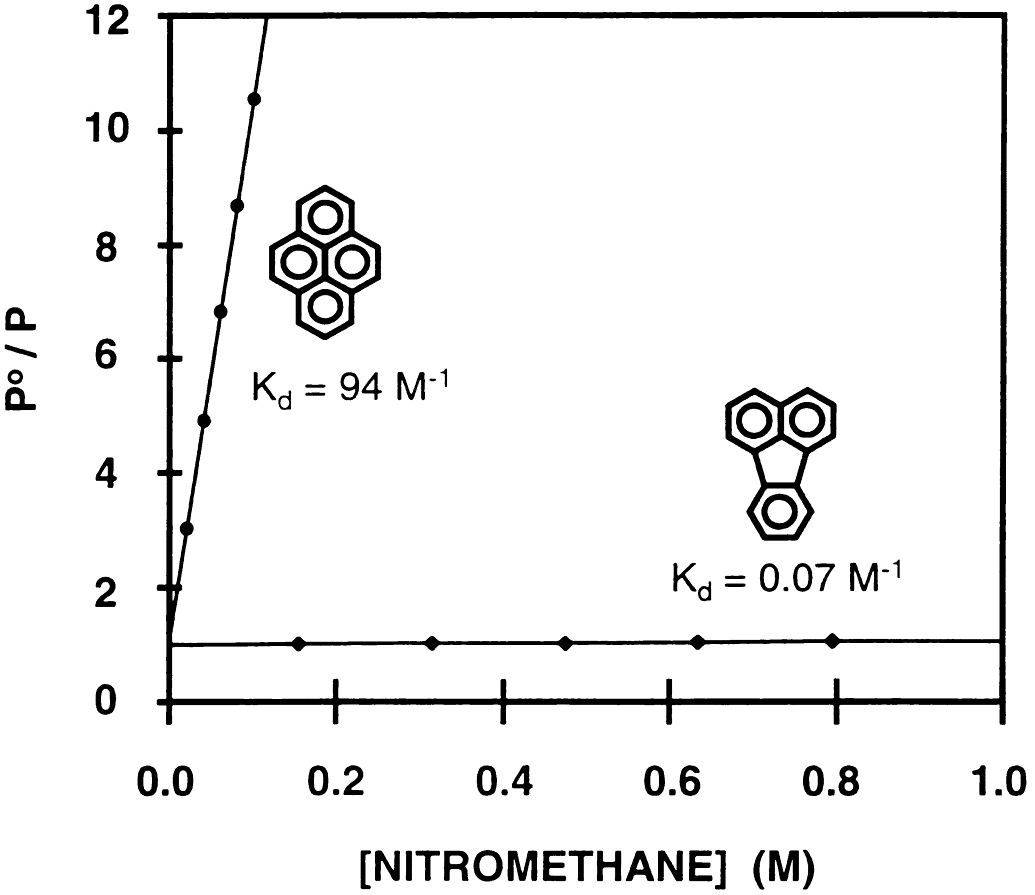

Figure 1-5: Stern–Volmer plots for the fluorescence quenching of pyrene and fluoranthene by nitromethane in methanol.

nitromethane with the alternant and nonalternant PAHs pyrene and fluoranthene.

The selectivity of nitromethane appears to be sustained when substituents such as alkyl groups are present on the aromatic ring.[55,56] In addition, many heterocyclic PACs examined by Tucker *et al.*[57] were significantly quenched by nitromethane, whereas all of the nonalternant compounds examined were not quenched. The protonated form of both alternant and nonalternant heterocyclic PACs were completely immune to quenching, presumably because the electron pair of nitrogen was no longer available to serve as an electron donor to the nitromethane quencher.[57]

Although systematic investigations have shown the selective quenching behavior of nitromethane to be quite extensive, there are some noteworthy exceptions. These exceptions are of two types: nonalternant PACs that are quenched by nitromethane, and alternant PACs that are not quenched. Among the first type of exceptions are acenaphthylene, aceanthrylene, acephenanthrylene, and related compounds. Although these compounds contain a five-membered ring, this ring has a fixed double bond that results in a conjugated system with numerous stable resonance structures. Thus, these compounds behave as alternant PACs and are significantly quenched by nitromethane.[58,59] Other nonalternant PACs that are significantly quenched contain an extended system of alternant aromatic rings, such as benzo(*k*)fluoranthene, naphtho(*2,3b*)fluoranthene, and indeno(*1,2,3-cd*) pyrene.[30,60] Finally, significant quenching can occur when electron-donating substituents are present on the nonalternant PACs, as exemplified by 3-hydroxy- and 3-methoxybenzo(*k*)fluoranthene.[56]

Among the second type of exceptions are alternant PACs that contain electron-withdrawing substituents. These substituents can reduce the electron-donating ability of the aromatic system to such an extent that PACs such as 1-pyrenecarboxaldehyde, 1,3-pyrenedicarboxaldehyde, 3,6-dicyanobenzo(*e*)pyrene, and 1-acetylcoronene are not quenched by nitromethane.[56] Other alternant PACs that are not strongly quenched by nitromethane include dibenzo(*hi,wx*)heptacene and dibenz(*a,h*)anthracene. However, despite the apparently lengthy list of exceptions, quenching by nitromethane is both selective and sufficiently general to find many applications in analytical chemistry (see below).

Some insight to the quenching mechanism of nitromethane has been gained from molecular orbital theory.[61,62] In the Hückel approximation, the highest occupied molecular orbital (HOMO) and the lowest unoccupied molecular orbital (LUMO) of alternant PAHs are symmetrically disposed whereas those of nonalternant PAHs are asymmetrically disposed about a reference energy. As a consequence, the HOMO and LUMO of alternant PAHs are typically 0.3-0.5 eV greater than those of nonalternant PAHs and, hence, the alternant compounds serve as better electron donors. It is postulated that the LUMO of an electron-accepting quencher such as nitromethane must be lower in energy than that of the fluorophores it quenches in order to receive an electron from the LUMO of the excited-state PAH.[61] The rate with which this electron transfer occurs is dependent upon the difference in the LUMO energy of the fluorophore and quencher and, hence, is more favorable for alternant PAHs with nitromethane. Although molecular orbital theory provides some qualitative understanding of the quenching mechanism, it has not been successful in quantitative prediction of the magnitude of the rate constants or Stern–Volmer constants.[30,63] Correlations of the Stern–Volmer constant with other empirical measures of electron-donating ability such as electrochemical reduction potential have been somewhat successful but, to date, there is no completely general model that can predict the effectiveness or selectivity of nitromethane quenching.[30]

C. Selective Quenching by 1,2,4-Trimethoxybenzene

1,2,4-trimethoxybenzene is an electron-donating quencher that selectively quenches the fluorescence of PACs with a nonalternant structure but not those with an alternant structure.[30,61] Although it shows promise for the classification of PACs, trimethoxybenzene has not been as well explored because its selectivity is not as pronounced as nitromethane. The Stern–Volmer constants with trimethoxybenzene are typically three- to six-fold greater for nonalternant than for alternant PACs. As with nitromethane, there are some exceptions to the selectivity of trimethoxybenzene.[57,60]

The quenching mechanism of trimethoxybenzene has also been explained by using molecular orbital theory.[61] It is presumed that the LUMO for trimethoxybenzene is higher in energy than that of the excited-state fluorophores, so that the quencher cannot act as an electron acceptor. Thus, the most likely mechanism is by electron donation from the HOMO of trimethoxybenzene to the partially occupied HOMO of the excited-state fluorophore. Because the orbitals of nonalternant PAHs are lower in energy than those of the alternant PAHs (see above), the nonalternant compounds serve as better electron acceptors. The rate of electron transfer is dependent upon the difference in the HOMO energy of the fluorophore and quencher and, hence, is more favorable for nonalternant PAHs with trimethoxybenzene. In addition to the molecular orbital model, empirical correlations of the Stern–Volmer constant with electrochemical reduction potential and ionization potential have proven to be fairly successful.[30]

D. Selective Determination of PACs in Complex Samples

The use of chromatographic separation methods in combination with fluorescence detection has been a valuable approach for the qualitative and quantitative analysis of complex mixtures of PACs. An additional level of selectivity can be gained, however, through the supplemental use of fluorescence quenching methods.

Sawicki and coworkers[54] first demonstrated the application of selective fluorescence quenching in combination with thin-layer chromatography (TLC). In this work, the PACs in airborne particulate samples were separated by TLC and then detected by means of fluorescence with excitation by a broadband ultraviolet lamp. By applying nitromethane as a spray or fuming agent to the TLC plate, the nonalternant PACs could be readily identified without interference from the alternant PACs. It is noteworthy that several new components in the sample became detectable after treatment with nitromethane, although no explanation was provided. The original chromatogram was regained by simply allowing the nitromethane to evaporate. It was also shown that nitropropane could be used as an additive to the TLC mobile phase, which quenched the fluorescence of alternant PACs. As when nitromethane was used as a spray reagent, these compounds became detectable after the mobile phase was allowed to evaporate. A similar approach has been used for the analysis of PACs with nitro substituents by Jager.[64] Although these compounds have no native fluorescence, they can be easily reduced to the amine form and then classified according to their fluorescence quenching behavior. Jager also demonstrated the use of aniline as a selective quencher, which permits the detection of carbazoles and other nitrogen-containing heterocyclic compounds in complex mixtures of PACs separated by TLC.[64]

The use of selective fluorescence quenching in combination with liquid chromatography (LC) was first demonstrated by Blumer and Zander.[65] In this approach, 5% nitromethane was added to the LC mobile phase so that the alternant PACs were selectively quenched as they passed through the on-line fluorescence detector. This greatly simplified the chromatograms of complex mixtures of PACs and allowed the rapid identification and quantitation of their components. In later studies, Konash and coworkers[66] used this analytical methodology to characterize the PACs in several of the National Institute of Standards and Technology Standard Reference Materials. The extent and selectivity of fluorescence quenching was determined from changes in the chromatographic peak height with 0.5-1.0% nitromethane in the mobile phase. Although this approach was useful, absorbance by nitromethane at the excitation wavelength caused a significant amount of trivial quenching that obscured the true behavior of the quencher.

This problem was eliminated by mathematical correction using a modified form of the Stern–Volmer relationship in equation (1-3) and by reduction of the pathlength of the fluorescence detector flow cell. This approach was used by McGuffin and coworkers[30,67] to determine conditional Stern–Volmer constants for the alternant and nonalternant compounds in the U.S. EPA list of priority pollutants. These constants were considered to be conditional as they were determined from the ratio of chromatographic peak heights in the absence and presence of quencher, determined at fixed excitation and emission wavelengths rather than the optimal wavelengths for each PACs. The conditional Stern–Volmer constants were shown to be valuable for qualitative identification of the PACs in a complex coal-derived fluid.[67] In addition, the high-resolution chromatograms obtained in the presence of various quenchers such as nitromethane and 1,2,4-trimethoxybenzene were able to provide a characteristic profile or fingerprint of the complex sample.[30]

IV. Conclusions

Although fluorescence quenching is a widely recognized phenomenon, its careful and deliberate application for analytical purposes has been relatively limited. Only a few quenching agents have been characterized in sufficient detail to permit routine and reliable analysis of unknown samples. Substantially more research is necessary to explore promising new quenching agents and to elucidate their mechanisms of quenching. Nevertheless, fluorescence quenching offers the opportunity for highly selective and sensitive determination of PACs in complex sample matrices. This method can provide class-selective profiles that characterize a sample and can simplify qualitative and quantitative analysis by reducing the number of interfering components. Thus, fluorescence quenching appears to be a powerful supplement to traditional fluorescence spectroscopy for forensic and environmental analysis.

V. References

---

1. M.L. Lee, M.V. Novotny, and K.D. Bartle, *Analytical Chemistry of Polycyclic Aromatic Compounds*, Academic Press, New York (1981).
2. T. Vo-Dinh, *Chemical Analysis of Polycyclic Aromatic Compounds*, John Wiley and Sons, New York (1989).
3. M. Blumer, *Sci. Am.* **234**, 35 (1976).
4. A. Bjorseth, *Handbook of Polycyclic Aromatic Hydrocarbons*, Marcel Dekker, New York (1983).
5. N. Selvarajan, S. Vaidyanathan, V. Ramachandra Rao, and V. Ramakrishnan, *Ind. J. Chem.* **20B**, 784 (1981).
6. B.F. Plummer, L.K. Steffen, T.L. Braley, W.G. Reese, K. Zych, G. Van Dyke, and B. Tulley, *J. Am. Chem. Soc.* **115**, 11542 (1993).
7. J. Jacob, *Quality Assurance for Environmental Analysis*, Elsevier, Amsterdam, Chapter 23 (1995).
8. R.M. Gadzala and B. Buszewski, *Polish Journal of Environmental Studies* **4**, 5 (1995).

9. J. Cvačka, J. Barek, A.G. Fogg, J.C. Moreira, and J. Zima, *Analyst* **123**, 9R (1998).
10. V.L. McGuffin and M. Novotny, *J. Chromatogr.* **255**, 381 (1983).
11. J.C. Gluckman, A. Hirose, V.L. McGuffin, and M. Novotny, *Chromatographia* **17**, 303 (1983).
12. M.U. Kumke, H.G. Lohmannsroben, and T. Roch, *J. Fluoresc.* **5**, 139 (1995).
13. J.R. Kershaw and J.C. Fetzer, *Polycyclic Aromat. Compd.* **7**, 253 (1995).
14. T. Vo-Dinh, G.W. Suter, A.J. Kallir, and U.P. Wild, *J. Phys. Chem.* **89**, 3026 (1985).
15. F. Ariese, C. Gooijer, and N.H. Velthorst, *Environmental Analysis: Techniques, Applications and Quality Assurance*, D. Barcelo, Ed., Elsevier, Amsterdam, Chapter 13 (1993).
16. E.L. Inman, Jr., A. Jurgensen, and J.D. Winefordner, *Analyst* **107**, 538 (1982).
17. I.S. Kozin, C. Gooijer, and N.H. Velthorst, *Anal. Chim. Acta* **333**, 193 (1996).
18. G.S. Douglas, S.H. Lieberman, W.C. McGinnis, D. Knowles, and C. Peven, *Proceedings of the International Symposium on Field Screening Methods for Hazardous Wastes and Toxic Chemicals,* Air & Waste Management Association, Pittsburgh, pg. 837 (1995).
19. Th. Roch, H.-G. Loehmannsroebe, and Th. Meyer, *Proc. SPIE-Int. Soc. Opt. Eng.* **2504**, 453 (1995).
20. C.L. Stevenson and T. Vo-Dinh, *Anal. Chim. Acta* **303**, 247 (1995).
21. M.P. Fogarty and I.M. Warner, *Appl. Spectrosc.* **36**, 460 (1982).
22. L.B. McGown, S.L. Hemmingson, J.M. Shaver, and L. Geng, *Appl. Spectrosc.* **49**, 60 (1995).
23. J.M. Shaver and L.B. McGown, *Appl. Spectrosc.* **49**, 813 (1995).
24. J.H. Richardson and M.E. Ando, *Anal. Chem.* **49**, 955 (1977).
25. R. Badley, *Fluorescence Spectroscopy*, Plenum Press, New York (1983).
26. J. Lakowicz, *Principles of Fluorescence Spectroscopy*, Plenum Press, New York (1983).
27. J.D. Ingle, Jr. and S.R. Crouch, *Spectrochemical Analysis*, Prentice Hall, Englewood Cliffs (1988).
28. J.M.G. Martinho, *J. Phys. Chem.* **93**, 6687 (1989).
29. R. Andriessen, M. Ameloot, N. Boens, and F.C. De Schryver, *J. Phys. Chem.* **96**, 314 (1992).
30. F.K. Ogasawara, Y. Wang, and V.L. McGuffin, *Appl. Spectrosc.* **49**, 1 (1995).
31. E.L. Wehry, *Modern Fluorescence Spectroscopy*, Vol. 2, Plenum Press, New York, pp. 319-438 (1976).
32. K. Kikuchi, C. Sato, M. Watabe, H. Ikeda, Y. Takahashi, and T. Miyashi, *J. Am. Chem. Soc.* **115**, 5180 (1993).

33. W. Xu, R. Schmidt, J.N. Demas, B.A. DeGraff, E.K. Karikari, and B.L. Farmer, *Anal. Chem.* **67**, 3172 (1995).
34. P.K. Behera, T. Mukherjee, and A.K. Mishra, *Indian J. Chem., Sect. A: Inorg., Bio-inorg., Phys., Theor. Anal. Chem.* **34A**, 419 (1995).
35. M. Mac, *J. Lumin.* **65**, 143 (1995).
36. V. Avila, C.A. Chesta, J.J. Cosa, and C.M. Previtali, *J. Chem. Soc. Faraday Trans.* **90**, 69 (1994).
37. P.K. Behera, T. Mukherjee, and A.K. Mishra, *J. Lumin.* **65**, 131 (1995).
38. P.K. Behera, T. Mukherjee, and A.K. Mishra, *J. Lumin.* **65**, 137 (1995).
39. R.S. Davidson and T.D. Whelan, *J. Chem. Soc. Perkin Trans. II* **3**, 241 (1983).
40. M. Vasilescu, *Rev. Roum. Chim.* **34**, 1819 (1989).
41. J. Mai, J. Cheng, and T. Ho, *J. Photochem. Photobiol. A:Chem.* **66**, 53 (1992).
42. S. Oh and Y. Shirota, *J. Photochem. Photobiol. A:Chem.* **92**, 79 (1995).
43. R.M. Bowman, T.R. Chamberlain, C. Huang, and J.J. McCullough, *J. Am. Chem. Soc.* **96**, 692 (1974).
44. J.E. Baggott and M.J. Pilling, *J. Chem. Soc. Faraday Trans. 1* **79**, 221 (1983).
45. E.B. Abuin and E.A. Lissi, *J. Photochem. Photobio. A:Chem.* **71**, 263 (1993).
46. M. Ayad, *Z. Phys. Chem. (Munich)* **187**, 123 (1994).
47. M. Zander, *Fresenius Z. Anal. Chem.* **226**, 251 (1967).
48. M. Zander, *Erdoel. Kohle, Erdgas, Petrochem.* **22**, 81 (1969).
49. M. Zander, *Fresenius Z. Anal. Chem.* **263**, 19 (1973).
50. M. Zander, *Fresenius Z. Anal. Chem.* **229**, 352 (1967).
51. L.V.S. Hood and J.D. Winefordner, *Anal. Chem.* **38**, 1922 (1968).
52. M. Zander, *Int. J. Environ. Anal. Chem.* **3**, 29 (1973).
53. M. Zander, *Z. Naturforsch.* **33A**, 998 (1978).
54. E. Sawicki, T.W. Stanley, and W.C. Elbert, *Talanta* **11**, 1433 (1964).
55. S.A. Tucker, J.M. Griffin, W.E. Acree, Jr, J.C. Fetzer, M. Zander, O. Reiser, A. De Meijere, and I. Murata, *Polycyclic Aromat. Compd.* **4**, 141 (1994).
56. S.A. Tucker, J.M. Griffin, W.E. Acree, Jr., M.J. Tanga, J.E. Bupp, T.K. Tochimoto, J. Lugtenburg, K. Van Haeringer, J. Cornelisse, P.C. Cheng, and L.T. Scott, *Polycyclic Aromat. Compd.* **4**, 161 (1994).
57. S.A. Tucker, W.E. Acree, Jr., and C. Upton, *Polycyclic Aromat. Compd.* **3**, 221 (1993).
58. S.A. Tucker, H.C. Bates, V.L. Amszi, W.E. Acree, Jr., H. Lee, P. Di Raddo, R.G. Harvey, J.C. Fetzer, and G. Dyker, *Anal. Chim. Acta* **278**, 269 (1993).
59. S.A. Tucker, J.M. Griffin, W.E. Acree, Jr., P.J. Mulder, J. Lugtenburg, and J. Cornelisse, *Analyst* **119**, 2129 (1994).

60. S.A. Tucker, H.C. Bates, W.E. Acree, Jr., and J.C. Fetzer, *Appl. Spectrosc.* **47**, 1775 (1993).
61. U. Breymann, H. Dreeskamp, E. Koch, and M. Zander, *Chem. Phys. Lett.* **59**, 68 (1978).
62. K. Yates, *Hückel Molecular Orbital Theory*, Academic Press, New York, NY (1978).
63. R.A. Hites and W.J. Simonsick, *Calculated Molecular Properties of Polycyclic Aromatic Hydrocarbons*, Elsevier, Amsterdam (1987).
64. J. Jager, *J. Chromatogr.* **152**, 575 (1978).
65. B. Blumer and M. Zander, *Fresenius Z. Anal. Chem.* **296**, 409 (1979).
66. P.L. Konash, S.A. Wise, and W.E. May, *J. Liq. Chromatogr.* **4**, 1339 (1981).
67. S.H. Chen, C.E. Evans, and V.L. McGuffin, *Anal. Chim. Acta* **246**, 65 (1991).

CHAPTER 2

CALCULATED GROUND- AND EXCITED-STATE PROPERTIES OF POLYCYCLIC AROMATIC HYDROCARBONS

I. Introduction

As discussed previously, polycyclic aromatic hydrocarbons (PAHs) are found in numerous natural and man-made materials. In addition, the two main structural classes of alternant and nonalternant isomers demonstrate systematic differences. The contrasting characteristics of alternant and nonalternant PAHs is likely based upon their differing electron distributions. Hence, a study of the electronic structure of both alternant and nonalternant PAHs is a valuable first step towards understanding PAHs as well as the phenomenon of selective fluorescence quenching.

To date, calculations of the ground state properties of PAHs have focused on predicting their geometries, charge distributions, ionization energies, heats of formation, and vibrational frequencies. Conjugated hydrocarbons were first treated with a self-consistent field (SCF) method by Chung and Dewar.[1] Later, other workers combined molecular mechanics and molecular orbital methods to predict the geometries and heats of formation for numerous PAHs.[2,3] Semi-empirical molecular orbital calculations have also been used to compute PAH properties.[4] More recently, Schulman *et al.* used a Hartree–Fock (HF) method with a 6-31G* basis set to compute the geometries and heats of formation of some alternant PAHs.[5,6] The geometries of nonalternant isomers have also been calculated with both semi-empirical and ab initio methods.[7] The carcinogenic activity of such isomers was estimated by computing the properties of their reactive intermediates using semi-empirical methods.[8] Finally, semi-empirical, ab initio, and density functional methods have been used to calculate the infrared spectra of various neutral and ionized PAHs.[9,10]

The excited state properties of PAHs have also been studied computationally. Initial work utilized the Pariser–Parr–Pople (PPP) approximation to calculate the transition energies and intensities of alternant PAHs.[11-13] More recently, semi-empirical configuration interaction (CI) methods have been used to calculate the electronic spectra of alternant and nonalternant isomers[14-16] as well as their ions and derivatives.[17,18] Furthermore, the energies of numerous PAH excited states as well as the energy gap between their highest occupied molecular orbital (HOMO) and lowest unoccupied molecular orbital (LUMO) have been predicted. The magnitude of the HOMO-LUMO energy gap was then correlated with observed photoinduced toxicity.[19] Semi-empirical methods were also used by Chen and McGuffin to calculate the charge distribution of pyrene in its ground and lower excited states.[20] Both ab initio and semi-empirical methods have been used to predict the absorption and emission spectra for some smaller PAHs and their radical cations.[21,22] Lastly, Gittins *et al.* used ab initio calculations to predict the geometry and vibrational frequencies of benzo(*a*)pyrene in its ground and excited states.[23]

Despite these advancements, ab initio calculations of large PAHs using a large basis set have been limited. Furthermore, alternant PAHs have received more attention than their nonalternant isomers, and there are few calculations involving excited states. In this work, two pairs of alternant and nonalternant PAH isomers have been selected: pyrene, fluoranthene, benzo(*a*)pyrene, and benzo(*b*)fluoranthene. This set of molecules will be used to augment what is known about the properties of large PAHs in both their ground and excited states. Novel calculations reported here include the ground state geometry of benzo(*b*)fluoranthene, the excited state geometries of pyrene and benzo(*b*)fluoranthene, the ground and excited state frequencies of fluoranthene and benzo(*b*)fluoranthene, and the change in electron density for all four molecules upon excitation. Furthermore, our calculations are internally consistent, allowing direct comparison of alternant and nonalternant isomers in their ground and excited states.

II. Methods

Ground and excited state calculations have been completed using the Gaussian 94[24] and Spartan[25] programs on R10000 Silicon Graphics workstations. The molecular structures, together with a bond designation scheme and axes definitions, are contained in Figure 2-1. The PAHs were assumed to be planar with the following symmetries: pyrene (D_{2h}), fluoranthene (C_{2v}), benzo(*a*)pyrene (C_s), and benzo(*b*)fluoranthene (C_s). The optimized ground state geometries of the four molecules were determined at the HF/6-31G* level (see Appendix A for Cartesian coordinates). In order to establish that true minima had been located on the potential energy surfaces (PES), normal mode analyses of the optimized geometries were completed with a 6-31G* basis set. Finally, the electron density surfaces of the ground states were generated.

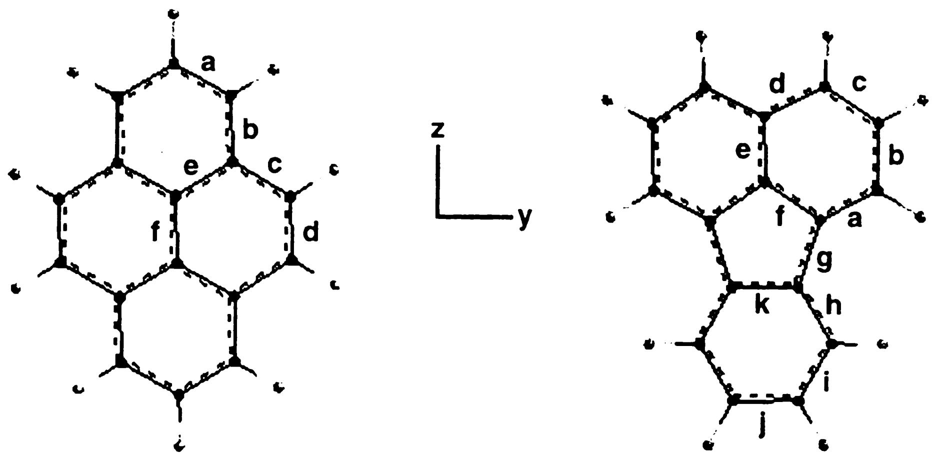

PYRENE

FLUORANTHENE

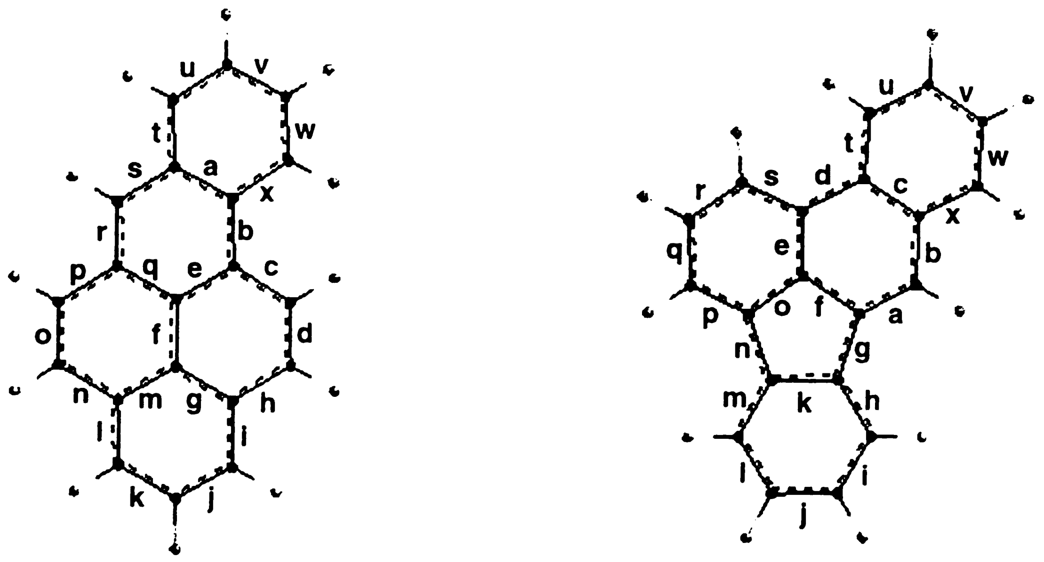

BENZO(*a*)PYRENE

BENZO(*b*)FLUORANTHENE

Figure 2-1: Optimized HF/6-31G* ground-state geometries of the four PAHs with bond and axis designations.

For the excited state calculations, the Franck–Condon excitation energies for the five lowest lying singlet excited states were determined using the configuration interaction with single excitations (CIS) method at the optimum HF/6-31G* geometry. Selected excited state geometries were then optimized using a 6-31G* basis set, assuming the same symmetries as above (see Appendix A for Cartesian coordinates). Adiabatic transitions were calculated from the energy difference between the minima on the ground and excited state PES. The electron density surfaces of the excited states were also generated, and the changes in those densities from the ground state were visualized. Finally, due to computational limitations the frequencies of the excited states could only be determined using a 3-21G basis set.

III. Results and Discussion

A. *Ground-State Calculations*

1. Energies and Optimized Geometries

The optimized geometries of the four molecules together with their total energies are contained in Table 2-1. Our results show that the nonalternant isomers possess slightly higher calculated SCF energies than the alternant isomers. There is a difference of 0.6 eV between pyrene and fluoranthene and a difference of 0.3 eV between benzo(*a*)pyrene and benzo(*b*)fluoranthene. These differences include the contribution from zero-point vibrational energy for each of the molecules (which was very similar between isomers). Overall these results

Table 2-1: Calculated (HF/6-31G*) versus Experimental Ground-State C–C Bond Lengths

Molecule	pyrene		fluoranthene		benzo(*a*)pyrene		benzo(*b*)fluoranthene	
Symmetry	D_{2h}		C_{2v}		C_s		C_s	
State	^1A_g		$^1A_1$		$^1A'$		$^1A'$	
Energy (au)	-611.7680		-611.7456		-764.4158		-764.4034	
Geometry[a]	Calc.	Expt.[28]	Calc.	Expt.[29]	Calc.	Expt.[30]	Calc.	Expt.
a	1.384	1.395	1.360	1.361	1.410	1.410	1.342	N.A.
b	1.391	1.406	1.424	1.433	1.439	1.436	1.449	N.A.
c	1.446	1.438	1.366	1.383	1.438	1.423	1.413	N.A.
d	1.339	1.367	1.423	1.415	1.345	1.352	1.459	N.A.
e	1.412	1.425	1.384	1.413	1.395	1.393	1.378	N.A.
f	1.433	1.430	1.413	1.415	1.434	1.419	1.433	N.A.
g			1.481	1.498	1.405	1.417	1.479	N.A.
h			1.379	1.390	1.432	1.441	1.380	N.A.
i			1.391	1.413	1.403	1.412	1.390	N.A.
j			1.385	1.375	1.372	1.375	1.386	N.A.
k			1.411	1.408	1.395	1.378	1.408	N.A.
l					1.380	1.402	1.390	N.A.
m					1.418	1.415	1.381	N.A.
n					1.453	1.433	1.481	N.A.
o					1.333	1.342	1.403	N.A.
p					1.453	1.446	1.368	N.A.
q					1.435	1.444	1.409	N.A.
r					1.361	1.361	1.374	N.A.
s					1.416	1.418	1.412	N.A.
t					1.421	1.425	1.406	N.A.
u					1.357	1.374	1.370	N.A.
v					1.413	1.397	1.400	N.A.
w					1.359	1.364	1.368	N.A.
x					1.422	1.418	1.407	N.A.

[a] bond designations as shown in Figure 2-1, bond lengths in angstroms

are consistent with a greater amount of ring strain[26] and/or disrupted aromaticity[27] which is found in nonalternant molecules.

The calculated geometries for pyrene, fluoranthene, and benzo(*a*)pyrene (Table 2-1) agree well with published neutron diffraction results.[28-30] No experimental ground state geometry could be found for benzo(*b*)fluoranthene, hence our results for this molecule await experimental verification. All calculated bond lengths for the PAHs fall within ±3 pm (0.03 Å) of experiment with a root mean square (rms) deviation of ±1 pm (0.01 Å). While most of the calculated values underestimate the experimental bond lengths, there are examples of the opposite. Such overestimations are uncommon, although prior calculations for pyrene,[6] fluoranthene,[7] and benzo(*a*)pyrene[23] agree with the calculated values reported here. The calculated SCF bond lengths for pyrene differ slightly from experiment but their relative size (c>f>e>b>a>d) is preserved. Furthermore, the calculated values tend to exaggerate differences between the bonds. Benzo(*a*)pyrene tends to have longer bond lengths in the region of the additional aromatic ring (i.e., bonds a and s), with the remainder of the molecule being similar to pyrene (i.e., bonds j and k). The bond lengths for fluoranthene are consistent with its formal structure of a benzene and naphthalene molecule joined by a long aliphatic bond. Similarly, benzo(*b*)fluoranthene resembles the joining of a benzene and phenanthrene unit.

The calculated bond angles also agree well with experiment with all deviations within ±0.3° for pyrene, ±1.5° for benzo(*a*)pyrene, and ±2.3° for fluoranthene. Finally, experimental results for the PAHs have shown that they deviate slightly from planarity in the solid state. These deviations are most likely due to thermal and/or packing forces and, hence, our assumption of planarity should not introduce significant error in calculating gas phase properties.

2. Vibrational Frequencies

Ground state vibrational frequencies of the molecules are compared with experimental spectra[31] in Figures 2-2 to 2-5 (see Appendix B for numerical frequencies). Based on the point groups and orientation of the PAHs, their normal modes can be assigned as follows. Pyrene in-plane vibrations have b_{1u} or b_{2u} symmetry, while out-of-plane vibrations have b_{3u} symmetry. Fluoranthene has in-plane vibrations with a_1 or b_2 symmetry and out-of-plane vibrations with a_2 or b_1 symmetry. Finally, both benzo(*a*)pyrene and benzo(*b*)fluoranthene have in-plane vibrations with a' symmetry and out-of-plane vibrations with a" symmetry. All calculated frequencies are scaled by a canonical factor of 0.89 to correct for electronic correlation and anharmonicity.[32] Assignment of the calculated frequencies to experimental data[31] is based on the adjusted frequency of the normal modes, their symmetry as discussed above, and their relative intensity.

In order to quantify the extent of agreement between the calculated and experimental frequencies, the rms deviations of the predicted vibrational modes from experimental values have been calculated. These results are as follows: ±16 cm^{-1} for pyrene (11 points), ±17 cm^{-1} for benzo(*a*)pyrene (11 points), ±22 cm^{-1} for fluoranthene (7 points), and ±27 cm^{-1} for benzo(*b*)fluoranthene (8 points). Experimental frequencies were obtained in the gas phase at 563 K and 1 atm[31]

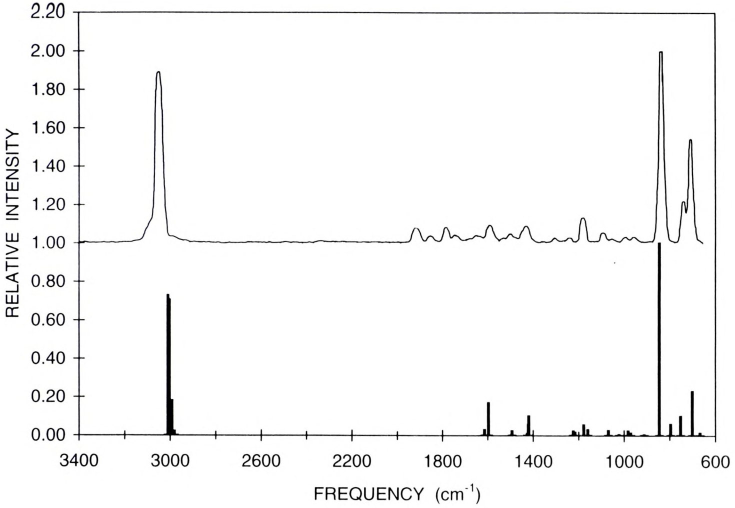

Figure 2-2: Experimental versus calculated (HF/6-31G*) ground state IR frequencies for pyrene. Experimental data adapted from Semmler *et al.*[31]

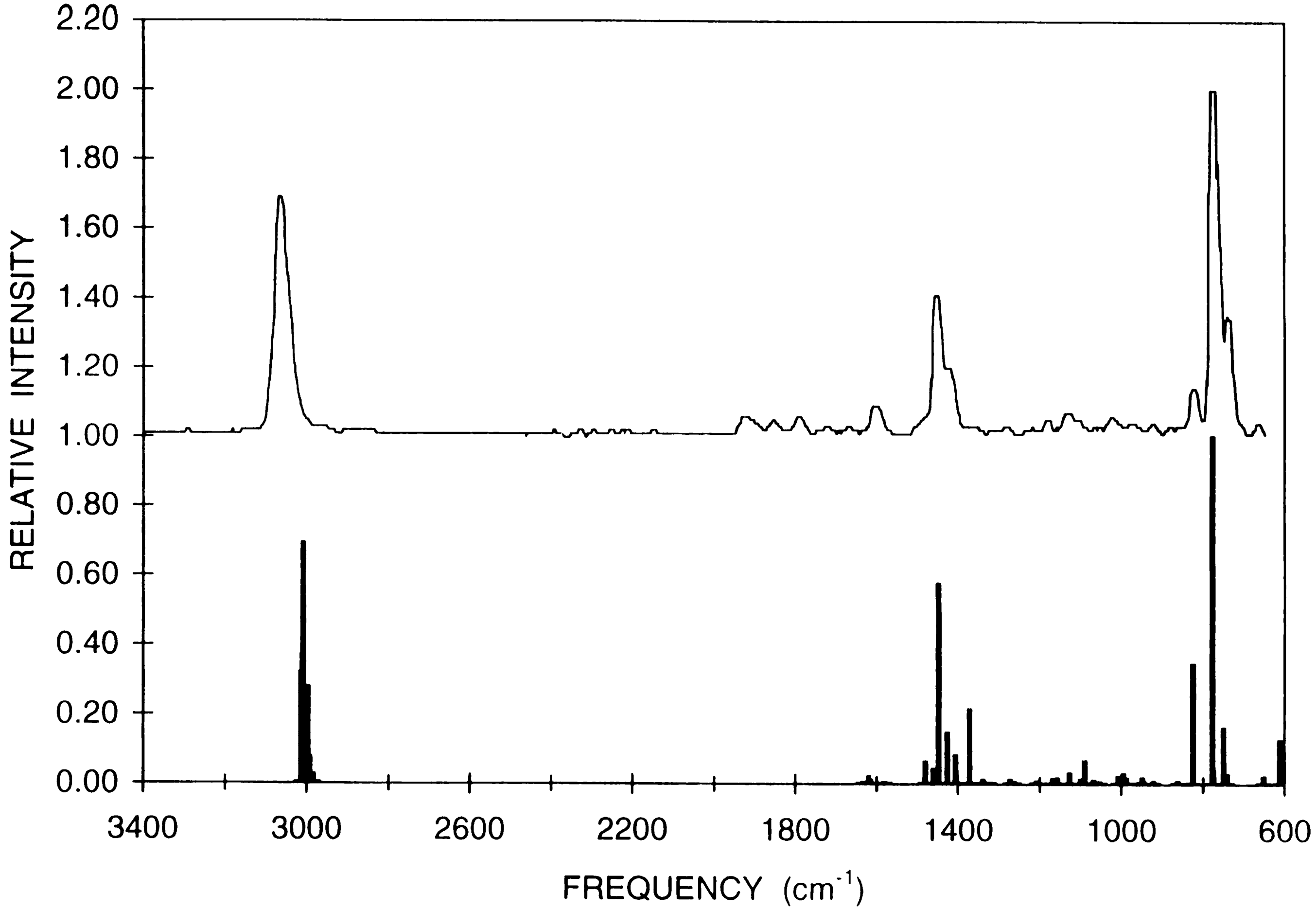

Figure 2-3: Experimental versus calculated (HF/6-31G*) ground state IR frequencies for fluoranthene. Experimental data adapted from Semmler *et al.*[31]

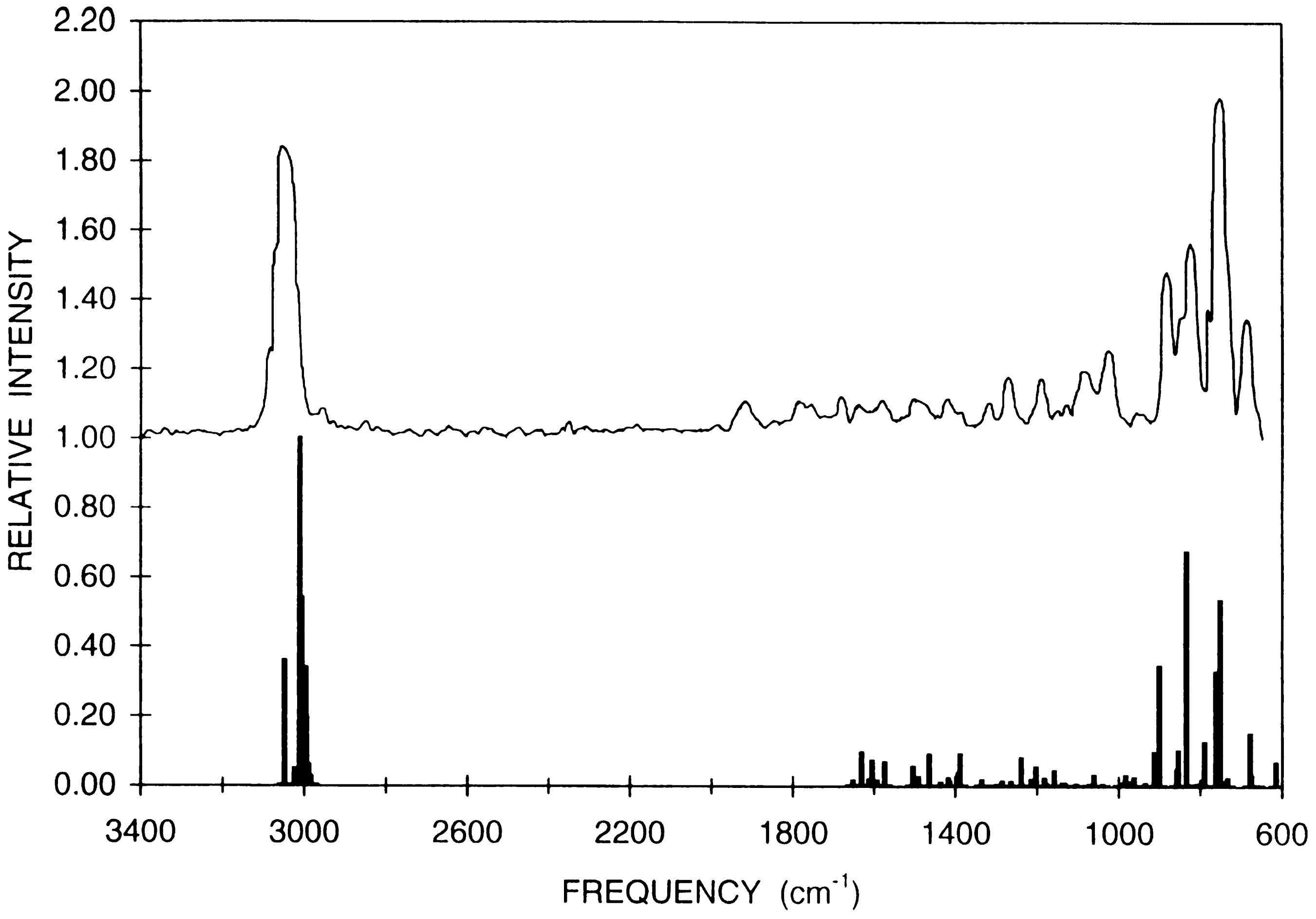

Figure 2-4: Experimental versus calculated (HF/6-31G*) ground state IR frequencies for benzo(*a*)pyrene. Experimental data adapted from Semmler *et al.*[31]

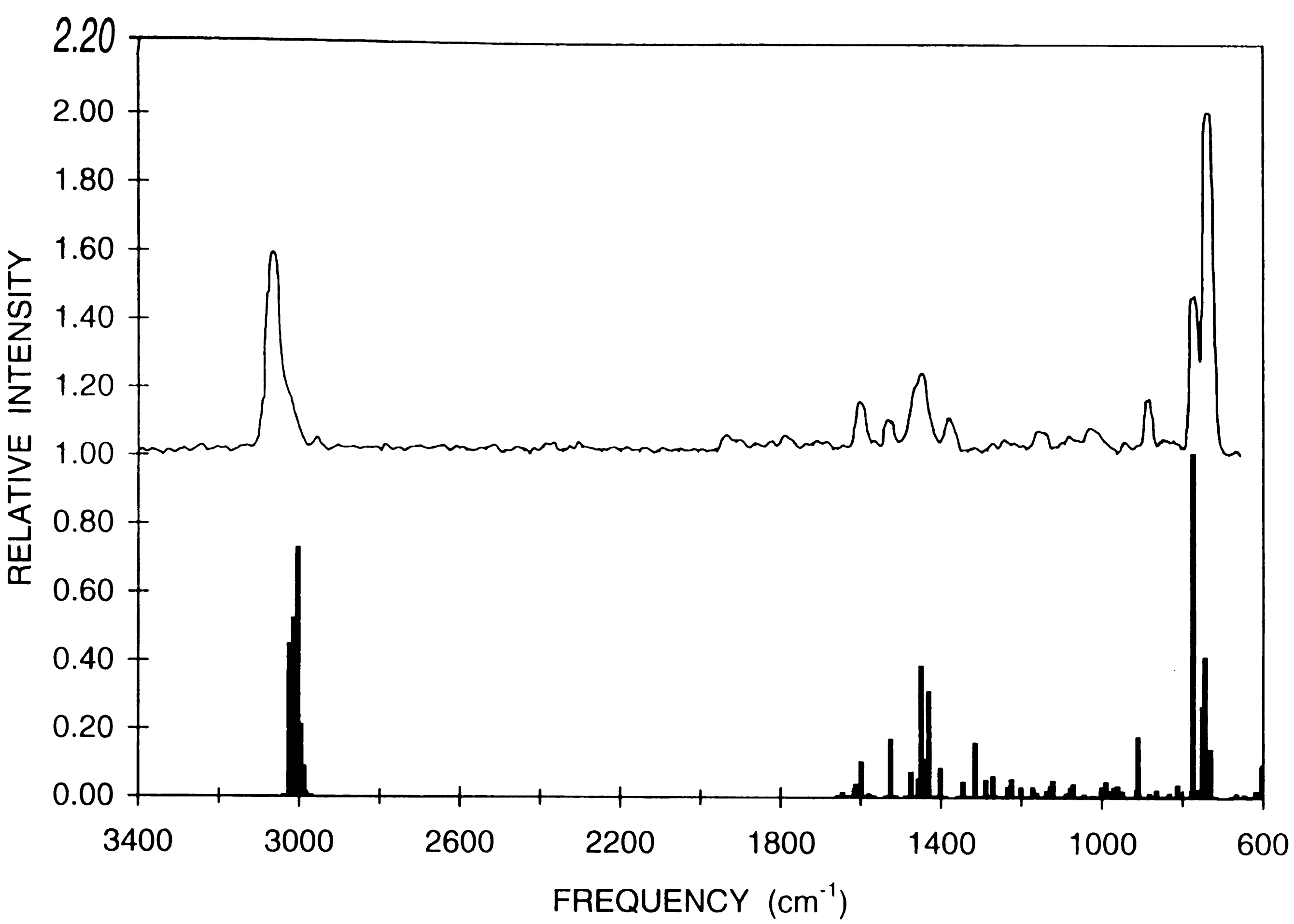

Figure 2-5: Experimental versus calculated (HF/6-31G*) ground state IR frequencies for benzo(*b*)fluoranthene. Experimental data adapted from Semmler *et al.*[31]

for all four PAHs with the exception of the three lowest frequency bands of pyrene, which were in the gas phase at 623 K and 1 atm.[33] For all four PAHs, deviations from experiment are the most severe when predicting the frequency of the aromatic C–H stretch. This band is found in the region 3050-3070 cm^{-1} experimentally, but was predicted to be 40-60 cm^{-1} lower in frequency. It is known from experiment that this band is sensitive to changes in both phase[33] and temperature.[11,34] While calculated frequencies correspond to gas phase molecules, they do not account for any temperature effects.

The deviation of the calculated IR intensities from experiment has been calculated using an algorithm suggested by Crawford and Morrison.[35] In this algorithm, the calculated peak intensities (P_n(calc)) and experimental peak intensities (P_n(exp)) are normalized so that their sum is unity according to the equation:

$$\sum P_n = 1 \tag{2-1}$$

Then the normalized peak intensities are compared to calculate the similarity index (SI) according to the equation:

$$SI = \left[1 - \sum \left| \frac{P_n(\text{calc}) - P_n(\text{exp})}{2} \right| \right] \times 100\% \tag{2-2}$$

A similarity index of 100% indicates complete similarity whereas 0% indicates complete dissimilarity. The results for the four PAHs are as follows: 87.0% for pyrene (8 points), 70.3% for benzo(*a*)pyrene (11 points), 86.6% for fluoranthene (7 points), and 69.8% for benzo(*b*)fluoranthene (8 points). This demonstrates the level of agreement obtainable when using ab initio methods to predict IR intensities. However, because of the lower agreement for benzo(*a*)pyrene and benzo(*b*)fluoranthene, the most prominent bands in the spectra are not correctly identified. Theory predicts a lower intensity for the C–H bend of benzo(*a*)pyrene at 757 cm^{-1} relative to its C–H stretch as well as a lower intensity for the C–H bend of benzo(*b*)fluoranthene at 741 cm^{-1} relative to its C–H bend at 774 cm^{-1}.

Lastly, it should be noted that our frequency assignments differ from those reported for benzo(*a*)pyrene.[23] Based on the assignments for the other PAHs,[31] we suggest that the experimental bands in the benzo(*a*)pyrene spectrum at 757, 822, and 879 cm^{-1} are more likely out-of-plane C–H bending modes (a" symmetry) than in-plane modes (a' symmetry) as previously published.[23] Our calculations predict three intense modes of a" symmetry at 752, 835, and 901 cm^{-1} which are assigned to the above experimental bands. In addition, the intensity of the calculated band at 3011 cm^{-1} implies that it, rather than the weaker calculated band at 3049 cm^{-1}, should be assigned to the most intense C–H stretching mode seen in the experimental results. Overall, these differing assignments improve the correspondence between calculation and experiment.

B. *Excited-State Calculations*

1. Excitation Energies

The calculated excitation energies for the five lowest lying singlet excited states of each PAH are contained in Table 2-2. There are some difficulties in

Table 2-2: Calculated (CIS/6-31G*) versus Experimental Excited-State Energies

	Theory					Experiment			
Molecule	State	Polarization	Energy[a]	Energy[b]	f[c]	Solvent	Energy[b]	f[c] or (log ε)[d]	Ref.
pyrene	$^1B_{2u}$	y	4.88	4.67	0.0002	vapor	3.41	0.002[e]	38
	$^1B_{1u}$	z	4.73	4.51	0.33	vapor	3.85	0.33[e]	38
	$^1B_{3g}$		5.81		0	CH	4.12		40
	$^1B_{3g}$		6.33		0	CH	4.29		40
	$^1B_{2u}$	y	6.60		1.06	vapor	4.68	0.35[e]	38
fluoranthene	$^1B_2$	y	4.64	4.03	0.01	3-MP	3.07	0.01	42
	$^1A_1$	z	4.88		0.39	3-MP	3.44	0.17	42
	$^1B_2$	y	5.41		0.06	3-MP	3.84	0.05	42
	$^1A_1$	z	5.85		0.14	3-MP	4.30	0.55	42
	$^1B_2$	y	6.60		0.11	3-MP	4.70	~0.14	42
benzo(*a*)pyrene	$^1A'$		4.68	4.43	0.002	HP	3.06	(3.32)[d]	44
	$^1A'$		4.33	4.04	0.43	HP	3.22	(4.47)[d]	44
	$^1A'$		5.67		0.06				
	$^1A'$		5.85		0.25	HP	4.18	(4.80)[d]	44
	$^1A'$		5.91		0.001				
benzo(*b*)fluoranthene	$^1A'$		4.75	4.18	0.08	CH	3.10	0.004	46
	$^1A'$		4.82		0.33	CH	3.36	0.50	46
	$^1A'$		5.12		0.07	CH	3.63	0.50	46
	$^1A'$		5.67		0.01	CH	4.12	0.30	46
	$^1A'$		6.03		0.71	CH	4.46	0.30	46

CH = cyclohexane at room temperature, 3-MP = 3-methylpentane at 77 K, HP = n-heptane at room temperature

[a] vertical transition (eV)

[b] adiabatic transition (eV)

[c] calculated and/or experimental oscillator strength

[d] logarithm of the experimental molar absorptivity (L mol^{-1} cm^{-1})

[e] in n-heptane at room temperature (Ref. 41)

comparing these results to experiment that deserve comment. First, the lack of diffuse functions in the basis set as well as no consideration of differential electron correlation contribute to an inherent overestimation of excitation energies by the CIS method. Second, the CIS method predicts gas-phase vertical excitation energies, and adiabatic energies can only be calculated when the energy of an optimized excited state structure is also computed. The published experimental values for these compounds are exclusively adiabatic transitions, which are intrinsically lower in energy than vertical transitions. Lastly, in some cases, the experimental data were acquired in the liquid or solid phase. This reduces the observed transition energies relative to the gas phase and, hence, reduces agreement with our calculations. Despite these limitations, the relative excitation energies and oscillator strengths for excited states can be reliably reproduced. What follows is a comparison of our calculated excitation energies for the four PAHs to experimental transition energies.

The excited states of pyrene have been well characterized and there is general agreement on their ordering and characteristics. The ground state of pyrene (S_0) has symmetry ^1A_g, while the lowest excited state singlets (S_1 and S_2) have symmetry $^1B_{2u}$ and $^1B_{1u}$, respectively,[20,36] and are accessible via one-photon excitation. The $S_1 \leftarrow S_0$ transition is very weak and is polarized along the short (y) axis of the molecule, while the $S_2 \leftarrow S_0$ transition is much stronger and is polarized along the long (z) axis. In addition, the energy separation of these states is quite small (2700 cm^{-1} in the solution phase[37] or 3500 cm^{-1} in the gas phase[38]). The CIS calculations (see Table 2-2) correctly predict the existence of these two states, their polarizations, as well as their disproportionate oscillator strengths (0.0002 and 0.33, respectively), but invert their order. Such an inversion has been seen previously in a PPP calculation of the S_5 and S_6 states of pyrene.[13] Given the proximity of these states and the known limitations of the CIS method to estimate excitation energies, this result is not surprising. Subsequent calculations citing our results have confirmed this inversion and demonstrated that the multireference effect is crucial in predicting the correct order of the two lowest-lying singlet excited states.[39]

The S_3 and S_4 states of pyrene are two-photon active with symmetry $^1B_{3g}$. These states have been studied using semi-empirical methods[11,12] as well as measured in a two-photon fluorescence excitation experiment of pyrene in cyclohexane.[40] In this experimental work, the authors tentatively identified another two-photon active band of ^1A_g symmetry between the S_3 and S_4 states; however this band has not been predicted by previous calculations or by our results. Finally, the S_5 state of pyrene has $^1B_{2u}$ symmetry and is one-photon active, polarized along the short axis of the molecule. While its relative excitation energy is in agreement with experimental gas phase results,[38] its predicted oscillator strength is significantly larger than that measured in n-heptane.[41]

In general, the calculated excitation energies for fluoranthene show better agreement with experiment than the results for pyrene. The ground state (S_0) has symmetry $^1A_1$ and the one-photon active S_1 through S_5 states alternate between $^1B_2$ and $^1A_1$ symmetry. The $^1B_2$ excited states are polarized along the short (y) axis of the molecule, while the $^1A_1$ excited states are polarized along the long (z) axis. Although the calculated excitation energies are higher than experiment, their relative values are correct. There are no published gas phase excitation energies for this molecule, hence we have compared our calculated values to experimental results acquired in 3-methylpentane at 77 K. These solid state experimental energies are further lowered from those in the solution phase by 250-500 cm^{-1}.[42] These discrepancies notwithstanding, there is good agreement between the calculated and measured oscillator strengths. For example, the CIS model correctly predicts the forbidden nature of the first singlet. In addition, CIS calculations correctly predict lower excitation energies for fluoranthene relative to pyrene as well as a larger difference between the vertical and adiabatic excitation energies for the S_1 state. Discrepancies from experiment include the lower calculated oscillator strength for S_4. Interestingly, this error has also been seen in previous semi-empirical PPP results.[43] Lastly, the polarization of S_5 is calculated to be along the short (y) axis of the molecule, in contrast to experimental work where it was tentatively assigned along the long (z) axis.[42] However, this weak band occurs amidst stronger transitions in the fluoranthene absorbance spectrum, and its characterization must be considered incomplete.

Benzo(*a*)pyrene is similar to pyrene in that the S_1 and S_2 states are closely spaced. Furthermore, the $S_1 \leftarrow S_0$ transition is forbidden while the $S_2 \leftarrow S_0$ transition is allowed.[44,45] The calculations correctly predict these singlets, however there appears to be an inversion of the forbidden and allowed states based on their calculated oscillator strengths (see Table 2-2). Since the symmetry of the states is identical, their assignment is difficult. Furthermore, our calculations predict the spacing between these states to be larger than has been found in solution[44] or in the gas phase.[45] Overall agreement is somewhat improved by comparing to gas phase results (experimental values of 3.13 eV and 3.4 eV for S_1 and S_2, respectively).[45] Of the remaining calculated singlets, only the S_4 state is assigned to an observed transition in benzo(*a*)pyrene. This assignment is based on the relative energy of the S_4 state as well as its higher calculated oscillator strength versus the surrounding singlets. Given the forbidden nature of the calculated S_3 state, it would be difficult to discern experimentally. Note that similar oversights have occurred with the S_1 and S_3 states of fluoranthene[15] as well as the S_1 state of benzo(*b*)fluoranthene.[16]

The results for benzo(*b*)fluoranthene agree fairly well with experiment. The forbidden nature of the S_1 state is correctly predicted, although the S_1-S_2 spacing is smaller than has been found experimentally.[46] In addition, while the relative energies of the remaining singlets are correctly predicted, the calculated intensities of S_3 and S_4 are much lower than solution phase experimental data. In contrast to the trend observed for fluoranthene and pyrene, the excitation energies for benzo(*b*)fluoranthene are higher than for its isomer benzo(*a*)pyrene, which is in agreement with experiment.[46] However, there continues to be a larger difference between the vertical and adiabatic values for benzo(*b*)fluoranthene versus benzo(*a*)pyrene, reflecting a greater degree of relaxation in the excited state for the nonalternant PAHs.

2. Optimized Geometries

Despite the inherent overestimation of the excitation energies, it has been shown that the geometries and frequencies of excited states can be reliably simulated by using the CIS method.[23] Geometries for selected low lying singlets optimized using the CIS method are contained in Table 2-3. Given the close spacing of the first two excited singlets of pyrene and benzo(*a*)pyrene, both states are reported. The changes in the bond lengths from the ground state are also included in the table. All molecules have been constrained to planar geometries with the same symmetry as the ground state. Overall, the calculated bond lengths agree with semi-empirical calculations for fluoranthene within ±5 pm (0.05 Å)[16] and CIS/3-21G results for benzo(*a*)pyrene within ±0.5 pm (0.005 Å).[23]

For the $^1B_{1u}$ state of pyrene, the largest changes in bond lengths upon excitation occur in the central region of the molecule with a contraction along its short (y) axis and a lengthening along its long (z) axis. Bonds c and f contract by 3-4 pm, while bonds b and d lengthen by approximately the same amount. For the $^1B_{2u}$ state of pyrene, the changes in geometry yield a contraction along its long (z) axis and a lengthening along the short (y) axis. Bonds c and f contract by 3 and 6 pm, respectively, while bonds d and e lengthen by 2-3 pm.

The changes in the $^1B_2$ state of fluoranthene are even more pronounced and result in a contraction along the long (z) axis of the molecule, centered around the five-membered ring. The two bonds labeled g, which connect the benzene and naphthalene moieties of fluoranthene, show the largest change by

Table 2-3: Calculated (CIS/6-31G*) Excited-State C–C Bond Lengths

Molecule	pyrene		pyrene		fluoranthene		benzo(*a*)pyrene		benzo(*a*)pyrene		benzo(*b*)fluoranthene	
Symmetry	D_{2h}		D_{2h}		C_{2v}		C_s		C_s		C_s	
State	$^1B_{2u}$		$^1B_{1u}$		$^1B_2$		$^1A'$		$^1A'$		$^1A'$	
Energy (au)	-611.5962		-611.6023		-611.5973		-764.2528		-764.2672		-764.2496	
Geometry[a]	Calc.	Change[b]	Calc.	Change[b]	Calc.	Change[b]	Calc.	Change[b]	Calc.	Change[b]	Calc.	Change[b]
a	1.395	0.011	1.385	-0.025	1.403	0.043	1.457	0.047	1.431	1.431	1.383	0.041
b	1.398	0.006	1.419	-0.020	1.386	-0.038	1.416	-0.023	1.464	1.464	1.416	-0.034
c	1.420	-0.026	1.409	-0.029	1.397	0.032	1.423	-0.014	1.409	1.409	1.427	0.014
d	1.363	0.024	1.376	0.032	1.408	-0.015	1.363	0.018	1.365	1.365	1.453	-0.006
e	1.447	0.035	1.430	0.035	1.409	0.025	1.449	0.055	1.426	1.426	1.399	0.020
f	1.377	-0.055	1.402	-0.032	1.434	0.022	1.389	-0.045	1.408	1.408	1.431	-0.002
g					1.404	-0.077	1.442	0.037	1.426	1.426	1.415	-0.063
h					1.418	0.039	1.416	-0.016	1.421	1.421	1.413	0.032
i					1.355	-0.036	1.398	-0.004	1.394	1.394	1.359	-0.031
j					1.441	0.056	1.386	0.014	1.401	1.401	1.441	0.055
k					1.473	0.062	1.396	0.001	1.369	1.369	1.472	0.064
l							1.393	0.013	1.421	1.421	1.354	-0.035
m							1.436	0.018	1.429	1.429	1.421	0.040
n							1.427	-0.026	1.408	1.408	1.398	-0.083
o							1.354	0.021	1.371	1.371	1.442	0.038
p							1.424	-0.029	1.413	1.413	1.410	0.042
q							1.439	0.003	1.432	1.432	1.372	-0.038
r							1.392	0.031	1.400	1.400	1.413	0.039
s							1.397	-0.019	1.405	1.405	1.395	-0.018
t							1.412	-0.008	1.410	1.410	1.412	0.006
u							1.367	0.010	1.378	1.378	1.363	-0.007
v							1.415	0.002	1.389	1.389	1.413	0.013
w							1.366	0.007	1.392	1.392	1.358	-0.010
x							1.420	-0.002	1.389	1.389	1.426	0.018

[a] bond designations as shown in Figure 2-1, bond lengths in angstroms

[b] difference between excited state (CIS/6-31G*) and ground state (HF/6-31G*) optimized geometries

contracting almost 8 pm. In contrast, bond k, which is also in the five-membered ring, lengthens by 6 pm.

Benzo(*a*)pyrene, while also an alternant PAH, shows larger changes in bond length than pyrene. For the S_1 ($^1A'$) state, most changes occur in alternating bonds around the perimeter of the molecule. This includes the shortening of bonds c, f, k, n, p, and x and the lengthening of bonds a, d, e, j, l, o, r, and w. In contrast, the changes in bond lengths for the S_2 ($^1A'$) state are more pronounced and clustered around the center of the molecule at bonds a, e, f, and g.

Finally, in benzo(*b*)fluoranthene, as in fluoranthene, there is a large change in geometry about the five-membered ring. For example, bonds g and n contract by 6 and 8 pm, respectively, while bond k lengthens by 6 pm. Also like fluoranthene, benzo(*b*)fluoranthene demonstrates an overall contraction along the long (z) axis of the molecule through bonds b, i, l, and q.

It has been observed that there is a large energy loss for absorbed photons that are subsequently emitted by fluorescence of nonalternant PAHs.[47] This large Stokes shift, as well as the lack of vibrational structure in their emission spectra, has been associated with large changes in their geometry upon reaching the excited state.[47] In fact, a non-planar excited state for fluoranthene has been proposed.[47] This possibility has been explored previously using semi-empirical calculations.[16] These calculations suggested that the bond length changes for fluoranthene are large but the excited state remains planar.[16] That observation has been confirmed in this work by optimizing the geometry for fluoranthene with C_1 symmetry at the CIS/3-21G level. The deviation from planarity as measured by dihedral angles was less than ±0.02° and the bond lengths of the optimized structure were within ±0.1 pm (0.001 Å) of a constrained planar structure. Hence, it is likely that large in-plane rather than out-of-plane bond length changes are sufficient to give rise to some of the unusual excited state properties of nonalternant PAHs.

3. Changes in Electron Density

When a molecule is promoted from the ground to excited state, the spatial distribution of electrons may undergo a significant change. These changes in electron density for the four molecules of interest are visualized in Figure 2-6. This figure represents the subtraction of the ground state electron density from the excited state density, where positive differences (+0.002 electrons/bohr^3) are white and negative differences (-0.002 electrons/bohr^3) are black.

For the excited states of pyrene ($^1B_{2u}$ in Figure 2-6A and $^1B_{1u}$ in Figure 2-6B), the regions of electron density increase or decrease correspond well to bonds that shorten or lengthen, respectively, upon optimization in the excited state (Table 2-3). Even the relative magnitude of the change correlates with the size of the isosurface generated. In addition, the areas of electron density decrease tend to cluster along the axis of polarization (the transition moment axis) for each state. This behavior explains the overall lengthening of the molecule along its transition moment axis as described above. Finally, the transition appears to relocate electrons almost exclusively from within the π

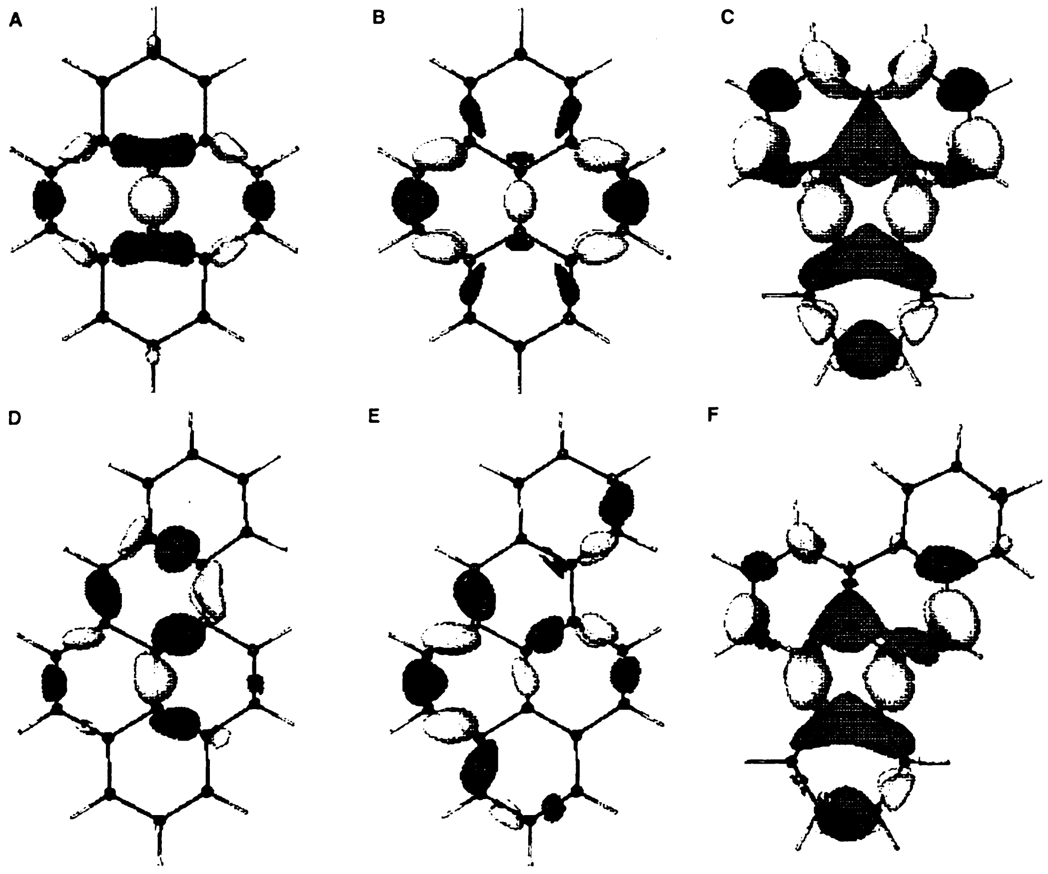

Figure 2-6: Visualizations of electron density differences after subtracting the ground state electron density (HF/6-31G*) from the excited state density (CIS/6-31G*). Positive differences (+0.002 electrons/bohr^3) are white and negative differences (-0.002 electrons/bohr^3) are black. Molecules shown are A) pyrene (${}^1B_{2u}$), B) pyrene (${}^1B_{1u}$), C) fluoranthene (${}^1B_2$), D) benzo(*a*)pyrene (${}^1A'$), E) benzo(*a*)pyrene (${}^1A'$), and F) benzo(*b*)fluoranthene (${}^1A'$).

system, although the use of a smaller isovalue of ± 0.001 electrons/bohr^3 is able to discern some changes in the electron density of σ bonds.

For fluoranthene (Figure 2-6C), the redistribution is more complex. Around the perimeter of the molecule is an alternating pattern of electron density increase and decrease which shows good agreement with excited-state optimization results, including the large change in electron density around the central five-membered ring. This $^1B_2$ state is polarized along the short (y) axis and, while the trend is not as clear as with pyrene, the majority of bonds that undergo a decrease in electron density and a lengthening upon excitation are oriented along this axis (i.e., bonds a, c, f, k, and j). Finally, in contrast to pyrene, it is readily apparent that electrons are redistributing between both the π and σ bonds within the molecule.

Benzo(*a*)pyrene shows results similar to those of pyrene with an alternating pattern of electron density increase and decrease around the molecule, all localized within the π system. The S_1 state (Figure 2-6D) also shows differences from the S_2 state (Figure 2-6E). Although the pattern of density changes are similar, they are concentrated in the central portion of the molecule in the S_1 state but spread more evenly throughout the molecule in the S_2 state. Furthermore, there are qualitative similarities between the states of benzo(*a*)pyrene and pyrene. For example, both the $^1B_{2u}$ state of pyrene and the S_1 state of benzo(*a*)pyrene have more localized changes in electron density and a larger contraction of bond f. In contrast, the $^1B_{1u}$ state of pyrene and the S_2 state of benzo(*a*)pyrene both possess a more uniform distribution of density

changes, with a smaller contraction of the central bond (f). These similarities tend to support the potential inversion of the S_1 and S_2 states of benzo(*a*)pyrene, as was seen with the $^1B_{2u}$ and $^1B_{1u}$ states of pyrene.

Finally, benzo(*b*)fluoranthene (Figure 2-6F) shows behavior very similar to that of fluoranthene, with a complex redistribution of electron density largely centered about the five-membered ring. In addition, exchange of density between π and σ bonds is apparent.

4. Vibrational Frequencies

As mentioned above, the excited state vibrations of the alternant and nonalternant PAHs have been calculated at the CIS/3-21G level. The effects of a smaller basis on the calculation of ground state frequencies has been explored by Langhoff,[10] who found that increasing the size of the basis set tends to decrease the calculated frequencies and intensities only slightly. In analogous calculations for this work, increasing the basis set from 3-21G to 6-31G* for the ground state of pyrene tends to decrease those frequencies below 1400 cm^{-1} but increase those above 1400 cm^{-1}. In all cases the change in frequency is less than 10% and there is no clear trend for changes in intensities. This suggests that the use of a smaller basis for excited state frequencies should not introduce significant error.

The CIS/3-21G results for the $^1B_{2u}$ and $^1B_{1u}$ states of pyrene are reported in Tables 2-4 and 2-5 and compared with experimental results using supersonic jet expansions.[36,48,49] In the fluorescence excitation experiments, only vibrational

Table 2-4: Calculated (CIS/3-21G) versus Experimental Excited-State Vibrations for Pyrene ($^1B_{2u}$)

Symmetry	Theory (cm^{-1})	Experiment[36,48] (cm^{-1})	Symmetry	Theory (cm^{-1})	Experiment[36,48] (cm^{-1})
b_{3u}	89		a_g	1017	1022
a_u	149		b_{1u}	1046	
b_{3u}	194		b_{3g}	1095	1110
b_{1g}	224		b_{2u}	1098	
b_{2g}	237		a_g	1135	1144
b_{2u}	348		b_{2u}	1146	
a_u	378		b_{3g}	1162	1155
a_g	396	393	b_{2u}	1188	
b_{3u}	448		b_{1u}	1227	
b_{3g}	450	443	a_g	1237	1250
b_{2g}	478		b_{3g}	1242	1245
b_{1u}	482		b_{2u}	1284	
b_{3g}	495	494	a_g	1288	1330
b_{1g}	498		b_{1u}	1340	
b_{2g}	508		b_{3g}	1380	1356
b_{2u}	529		a_g	1392	1424
a_g	545	572	b_{3g}	1409	1396
a_u	659		b_{2u}	1429	
b_{1u}	669		b_{1u}	1433	
b_{3u}	683		b_{3g}	1467	1466
b_{3g}	729	730	b_{2u}	1470	
b_{3u}	740		a_g	1502	1486
b_{2g}	746		b_{2u}	1525	
a_g	778	780	b_{1u}	1536	
b_{1u}	782		b_{3g}	1545	1573
b_{1g}	806		a_g	1621	1629
b_{2g}	829		b_{1u}	2978	
b_{3u}	845		b_{3g}	2978	
a_u	900		a_g	2985	
b_{2u}	912		b_{1u}	2987	
b_{1g}	916		b_{2u}	2990	
b_{1u}	951		b_{3g}	2992	
b_{2g}	967		a_g	2998	
b_{3u}	975		b_{2u}	2998	
a_u	1004		b_{1u}	3014	
b_{2g}	1008		a_g	3015	

Table 2-5: Calculated (CIS/3-21G) versus Experimental Excited-State Vibrations for Pyrene ($^1B_{1u}$)

Symmetry	Theory (cm^{-1})	Experiment[49] (cm^{-1})	Symmetry	Theory (cm^{-1})	Experiment[49] (cm^{-1})
b_{3u}	98		b_{2g}	1016	
a_u	142		b_{2u}	1028	
b_{3u}	200		a_g	1034	
b_{1g}	213		b_{1u}	1066	
b_{2g}	256		a_g	1119	
b_{2u}	338		b_{3g}	1123	1125
a_u	380		b_{2u}	1133	
a_g	399	412	b_{2u}	1142	
b_{3g}	437		b_{3g}	1163	
b_{2g}	473		b_{2u}	1182	
b_{3u}	479		a_g	1189	
b_{3g}	485		b_{1u}	1226	
b_{1u}	494		b_{3g}	1255	1232
b_{1g}	517		a_g	1264	
b_{2u}	526		b_{2u}	1318	
b_{2g}	550		a_g	1336	
a_g	558	600	b_{1u}	1375	
b_{1u}	663		b_{3g}	1411	1412
a_u	664		b_{2u}	1418	
b_{3u}	695		b_{1u}	1448	
b_{3g}	702		b_{3g}	1457	
b_{2g}	745		a_g	1465	
b_{3u}	753		b_{1u}	1484	
a_g	798		b_{3g}	1484	
b_{1u}	799		b_{2u}	1497	
b_{1g}	809		a_g	1502	
b_{2g}	863		b_{1u}	2980	
b_{3u}	869		b_{3g}	2981	
a_u	885		a_g	2983	
b_{1g}	906		b_{1u}	2985	
b_{2u}	919		b_{2u}	2991	
b_{1u}	955		b_{3g}	2992	
b_{3g}	979		b_{2u}	3000	
b_{2g}	988		a_g	3000	
a_u	995		b_{1u}	3008	
b_{3u}	1012		a_g	3009	

modes of a_g or b_{3g} symmetry are observed. For both excited states, modes with a_g symmetry arise from Franck–Condon overlap with the ground state, while b_{3g} modes tend to arise from vibronic coupling of the excited states.[48] Overall, the agreement of the calculated frequencies of the $^1B_{2u}$ state of pyrene with supersonic expansion results[36,48,49] is satisfactory with an rms deviation of ±17 cm^{-1} (20 points), which is larger than that of the ground state but still quite good. In this case, assignment of vibrational modes above 1700 cm^{-1} is difficult due to the presence of many combination and overtone bands from lower energy modes, as well as the overlapping transitions from the $^1B_{1u}$ state which complicate the experimental spectra.[48]

Vibrations of the $^1B_{1u}$ state of pyrene have also been observed experimentally.[36,49] Although no experimental symmetry designations have been reported, some tentative assignments are made in Table 2-5. The rms deviation from experiment is larger than the $^1B_{2u}$ state at ±22 cm^{-1} (5 points), but this is to be expected given the difficulty of resolving these bands experimentally.

The excited state vibrations for benzo(*a*)pyrene are contained in Table 2-6. Both the number and range of frequencies are larger than for pyrene. Gittins *et al.* compared the calculated frequencies for the S_1 state of benzo(*a*)pyrene to those obtained for the experimental S_1 state and found good agreement with an rms deviation of only ±5 cm^{-1} (32 points).[23] However, based on our calculated oscillator strengths of the first two states of benzo(*a*)pyrene and their similar excitation character when compared to the $^1B_{2u}$ and $^1B_{1u}$ states of pyrene (Figure

Table 2-6: Calculated (CIS/3-21G) versus Experimental Excited-State Vibrations for Benzo(*a*)pyrene (^{1}A')

Symmetry	Theory (cm^{-1})	Experiment[23] (cm^{-1})	Symmetry	Theory (cm^{-1})	Experiment[23] (cm^{-1})
a"	54	54	a"	1017	
a"	75	76	a"	1019	
a"	137	141	a'	1040	1020
a"	177	175	a'	1087	
a"	199	198	a'	1093	1111
a'	208	204	a'	1129	1129
a"	267		a'	1144	
a"	276		a'	1157	
a'	326	321	a'	1172	1166
a'	370	372	a'	1180	1182
a"	379		a'	1201	1191
a"	435		a'	1216	1215
a'	450	450	a'	1236	1239
a'	474	472	a'	1260	1249
a"	481		a'	1269	1253
a"	493		a'	1278	
a'	499	515	a'	1307	
a'	508	521	a'	1332	
a"	511		a'	1339	
a"	522		a'	1365	
a'	556	551	a'	1375	
a'	590	591	a'	1412	
a'	628	625	a'	1430	
a"	660		a'	1437	
a"	676		a'	1448	
a'	676	686	a'	1463	
a"	733		a'	1485	
a'	746	748	a'	1506	
a"	753		a'	1531	
a"	756		a'	1534	
a'	780	792	a'	1537	1549
a"	811		a'	1571	
a'	818	827	a'	1618	
a"	827		a'	2977	
a"	845		a'	2980	
a"	860		a'	2983	
a'	873		a'	2983	
a"	912		a'	2986	
a"	925		a'	2991	
a'	935		a'	2994	
a'	978	960	a'	2999	
a"	986		a'	3011	
a"	991		a'	3012	
a'	999	998	a'	3020	
a"	1005		a'	3042	

2-6), we suspect that an inversion of states has occurred in the calculations for this molecule. Hence, the experimental frequencies should be compared to those calculated for the higher singlet state. This comparison results in slightly poorer agreement, with an rms deviation of ±9 cm^{-1} (32 points).

Lastly, the calculated frequencies for both excited state fluoranthene and benzo(*b*)fluoranthene are included in Tables 2-7 and 2-8. The increase in the number and range of frequencies with the size of the PAH is also seen in these nonalternant compounds. However, no experimental results for the excited-state frequencies of the nonalternant PAHs could be found for comparison.

IV. Conclusions

Ground state geometries are reliably predicted by ab initio methods and agree well with experimental crystallographic results. In addition, the total energies of the PAHs reflect the greater stability of the alternant isomers. The calculations reliably predict the ground state IR spectra in good agreement with gas phase experimental results, with the greatest discrepancies occurring when predicting the frequency of the CH stretching vibration.

The prediction of either vertical or adiabatic excitation energies is not as accurate, given the inherent overestimation of the CIS method. However, the relative excitation energies and intensities are more reliably calculated. Interestingly, it appears that in the case of the alternant isomers the CIS method with a 6-31G* basis set has inverted the two lowest-lying singlet states. Despite these limitations, the changes in the electron density of the molecules agree well with calculated excited state geometries, and reveal a lengthening of the

Table 2-7: Calculated (CIS/3-21G) Excited-State Vibrations for Fluoranthene ($^1B_2$)

Symmetry	Theory (cm^{-1})	Symmetry	Theory (cm^{-1})
b_1	92	a_1	1030
a_2	115	a_2	1039
b_1	179	a_1	1056
b_2	199	b_2	1056
a_2	218	b_2	1063
b_1	276	b_2	1124
a_1	343	a_1	1164
a_2	379	b_2	1180
b_2	407	a_1	1188
b_1	436	b_2	1210
a_1	476	a_1	1249
b_1	500	b_2	1273
a_2	514	a_1	1293
a_1	539	a_1	1299
b_2	557	b_2	1306
b_1	576	a_1	1344
b_2	606	b_2	1364
a_2	617	b_2	1426
a_1	638	a_1	1427
b_2	732	a_1	1443
a_2	733	a_1	1448
b_1	764	b_2	1468
b_1	768	a_1	1504
a_1	768	a_1	1520
a_2	786	b_2	1521
a_1	834	b_2	1557
b_1	844	b_2	2981
a_2	865	a_1	2982
a_2	880	b_2	2992
b_1	903	a_1	2998
a_1	919	b_2	2999
b_2	953	a_1	3001
b_2	973	b_2	3010
a_2	1013	b_2	3013
b_1	1013	a_1	3013
b_1	1017	a_1	3019

Table 2-8: Calculated (CIS/3-21G) Excited-State Vibrations for Benzo(*b*)fluoranthene (${}^1A'$)

Symmetry	Theory (cm^{-1})	Symmetry	Theory (cm^{-1})
a''	60	a''	1019
a''	94	a''	1037
a''	108	a'	1039
a''	143	a''	1040
a'	157	a'	1060
a''	230	a'	1079
a''	251	a'	1115
a'	260	a'	1119
a''	298	a'	1159
a'	313	a'	1173
a'	374	a'	1182
a''	395	a'	1188
a''	422	a'	1214
a'	451	a'	1245
a''	469	a'	1256
a''	504	a'	1259
a''	528	a'	1277
a'	537	a'	1303
a'	554	a'	1304
a''	581	a'	1341
a'	587	a'	1358
a''	598	a'	1383
a'	604	a'	1414
a'	644	a'	1431
a'	661	a'	1438
a''	745	a'	1449
a'	746	a'	1463
a''	753	a'	1481
a''	758	a'	1506
a'	763	a'	1520
a''	773	a'	1532
a''	782	a'	1552
a''	836	a'	1587
a''	845	a'	2979
a'	857	a'	2988
a'	858	a'	2991
a''	877	a'	2992
a''	900	a'	2998
a''	911	a'	2999
a'	919	a'	3002
a'	926	a'	3009
a'	986	a'	3011
a''	1005	a'	3014
a''	1011	a'	3020
a'	1017	a'	3023

molecules along their axis of polarization. In addition, the nonalternant isomers dramatically contract along the long aliphatic bonds within their five-membered rings upon excitation. Finally, the excited state frequencies for the alternant isomers compare well to gas phase fluorescence excitation results. Overall, the ab initio methods presented here have provided a deeper insight into the ground- and excited-state properties of four important PAHs, as well as expanding what is known about alternant and nonalternant isomers.

V. References

---

1. A.H. Chung and M.S. Dewar, *J. Chem. Phys.* **42**, 756 (1965).
2. J. Kao and N.L. Allinger, *J. Am. Chem. Soc.* **99**, 975 (1977).
3. J. Kao, *J. Am. Chem. Soc.* **109**, 3817 (1987).
4. R.A. Hites and W.J. Simonsick, *Calculated Molecular Properies of Polycyclic Aromatic Hydrocarbons*, Elsevier, Amsterdam (1987).
5. J.M. Schulman, R.C. Peck, and R.L. Disch, *J. Am. Chem. Soc.* **111**, 5675 (1989).
6. R.C. Peck, J.M. Schulman, and R.L. Disch, *J. Phys. Chem.* **94**, 6637 (1990).
7. B.F. Plummer, L.K. Steffen, and W.C. Herndon, *Struct. Chem.* **279**, 4 (1993).
8. J.R. Rabinowitz and S.B. Little, *Int. J. Quantum Chem.* **52**, 681 (1994).
9. M. Vala, J. Szczepanski, F. Pauzat, O. Parisel, D. Talbi, and Y. Ellinger, *J. Phys. Chem.* **98**, 9187 (1994).
10. S.R. Langhoff, *J. Phys. Chem.* **100**, 2819 (1996).
11. K. Nishimoto and L.S. Forster, *Theoret. Chim. Acta (Berl.)* **3**, 407 (1965).
12. K. Nishimoto, *Theoret. Chim. Acta (Berl.)* **7**, 207 (1967).
13. R. Pucci, M. Baldo, A. Martin-Rodero, G. Piccitto, and P. Tomasello, *Int. J. Quantum Chem.* **26**, 783 (1984).
14. N.K. Das Gupta and F.W. Birss, *Bull. Chem. Soc. Jpn.* **51**, 1211 (1978).
15. A. Das Gupta, S. Chatterjee, and N.K. Das Gupta, *Bull. Chem. Soc. Jpn.* **52**, 3070 (1979).
16. J. Suhnel, U. Kempka, and K. Gustav, *Journal F. Prakt. Chemie* **322**, 649 (1980).
17. P. Du, F. Salama, and G.H. Loew, *Chem. Phys.* **173**, 421 (1993).
18. F. Negri and Z. Zgierski, *J. Chem. Phys.* **100**, 1387 (1994).

19. O.G. Mekenyan, G.T. Ankley, G.D. Veith and D.J. Call, *SAR and QSAR in Environmental Research* **2**, 237 (1994).
20. S.H. Chen and V.L. McGuffin, *Appl. Spectrosc.* **48**, 596 (1994).
21. C. Niederalt, S. Grimme, and S.D. Peyerimhoff, *Chem. Phys. Lett.* **245**, 455 (1995).
22. F. Negri and M.Z. Zgierski, *J. Chem. Phys.* **104**, 3486 (1996).
23. C.M. Gittins, E.A. Rohlfing, and C.M. Rohlfing, *J. Chem. Phys.* **105**, 7323 (1996).
24. M. J. Frisch, G. W. Trucks, H. B. Schlegel, P. M. W. Gill, B. G. Johnson, M. A. Robb, J. R. Cheeseman, T. Keith, G. A. Petersson, J. A. Montgomery, K. Raghavachari, M. A. Al-Laham, V. G. Zakrzewski, J. V. Ortiz, J. B. Foresman, J. Cioslowski, B. B. Stefanov, A. Nanayakkara, M. Challacombe, C. Y. Peng, P. Y. Ayala, W. Chen, M. W. Wong, J. L. Andres, E. S. Replogle, R. Gomperts, R. L. Martin, D. J. Fox, J. S. Binkley, D. J. Defrees, J. Baker, J. P. Stewart, M. Head-Gordon, C. Gonzalez, and J. A. Pople, *Gaussian 94,* Revision D.3, Gaussian, Inc., Pittsburgh (1995).
25. *Spartan,* Version 3.1, Wavefunction, Inc. (1994).
26. M. Blumer, *Sci. Am.* **234**, 35 (1976).
27. K. Yates, *Huckel Molecular Orbital Theory,* Academic Press, New York (1978).
28. A.C. Hazell, F.K. Larson, and M.S. Lehmann, *Acta Cryst.* **B28**, 2977 (1972).
29. A.C. Hazell, D.W. Jones, and J.M. Sowden, *Acta Cryst.* **B33**, 1516 (1977).
30. J. Iball, S.N. Scrimgeour, and D.W. Young, *Acta Cryst.* **B32**, 328 (1976).
31. J. Semmler, P.W. Yang, and G.E. Crawford, *Vib. Spectrosc.* **2**, 189 (1991).
32. W.J. Hehre, L. Radom, P.R. Schleyer, and J.A. Pople, *Ab Initio Molecular Orbital Theory*, John Wiley and Sons, New York (1986).
33. K. Zhang, B. Guo, P. Colarusso, and P.F. Bernath, *Science* **274**, 582 (1996).
34. C. Pouchert, *The Aldrich Library of FTIR Spectra Volume 3: Vapor Phase*, 1st ed., Aldrich Chemical Company, Milwaukee (1989).
35. L.R. Crawford and J.D. Morrison, *Anal. Chem.* **40**, 1464 (1968).
36. N. Ohta, H. Baba, and G. Marconi, *Chem. Phys. Lett.* **133**, 222 (1987).
37. G. Marconi and P.R. Salvi, *Chem. Phys. Lett.* **123**, 254 (1986).
38. R.S. Becker, I.S. Singh, and E.A. Jackson, *J. Chem. Phys.* **38**, 2144 (1963).
39. Y. Bito, N. Shida, and T. Toru, *Chem. Phys. Lett.* **328**, 310 (2000).
40. P.R. Salvi, P. Foggi, and E. Castellucci, *Chem. Phys. Lett.* **98**, 206 (1983).
41. J. Tanaka, *Bull. Chem. Soc. Jpn.* **38**, 86 (1964).
42. J. Kolc, E.W. Thulstrup, and J. Michl, *J. Am. Chem. Soc.* **96**, 7188 (1974).
43. J. Michl, *J. Mol. Spectrosc.* **30**, 66 (1969).

---

44. J. Malkin, *Photophysical and Photochemical Properties of Aromatic Compounds*, CRC Press, Ann Arbor, pg. 92 (1992).
45. G.D. Greenblatt, E. Nissani, E. Zaroura, and Y. Haas, *J. Phys. Chem.* **91**, 570 (1987).
46. M.A. Souto, D. Otteson, and J. Michl, *J. Am. Chem. Soc.* **100**, 6892 (1978).
47. I.B. Berlman, *J. Phys. Chem.* **74**, 3085 (1970).
48. N.A. Borisevich, L.B. Vodovatov, G.G. D'yachenko, V.A. Petukhov, and M.A. Semyonov, *J. Appl. Spectrosc.* **62**, 482 (1995).
49. E.A. Mangle and M.R. Topp, *J. Phys. Chem.* **90**, 802 (1986).

CHAPTER 3

POTENTIAL MECHANISMS OF SELECTIVE FLUORESCENCE QUENCHING REACTIONS

I. Introduction

Lack of progress in developing current and novel selective quenching agents is due in part to incomplete understanding of the mechanism for fluorescence quenching. The current theory for selective quenching of alternant and nonalternant PAHs presumes an electron-transfer mechanism, where the fluorophore serves as an electron donor or acceptor in a charge-transfer complex with the quencher.[1] In this mechanism, the fluorophore and quencher form an "encounter complex" in solution, followed by partial or full electron transfer. This is followed by a rapid back electron transfer, which returns both quencher and fluorophore to their ground-state electronic configurations. In the Hückel approximation, the highest occupied molecular orbital (HOMO) and lowest unoccupied molecular orbital (LUMO) of alternant PAHs have higher one-electron energies than their nonalternant isomers.[2] In this mechanism, the LUMO of an electron-accepting quencher such as nitromethane is assumed to lay at a lower energy than the LUMO of the alternant PAH that is serving as the electron donor.[3] Therefore, an excited-state alternant PAH should undergo electron transfer with nitromethane more readily than an excited-state nonalternant isomer.

Although this model for the selectivity of fluorescence quenching seems intuitively reasonable, it has not been confirmed experimentally. For example, ionization energies and reduction potentials of PAHs (which would presumably reflect electron donating or accepting ability) have not been good empirical predictors of quenching efficiency.[4,5] In addition, this model considers only the electronic properties of the fluorophores and not the quenchers to be important to the quenching mechanism. This model cannot quantitatively predict quenching efficiencies, nor does it predict the numerous PAHs that possess an alternant or nonalternant structure but do not adhere to typical selective quenching behavior. Furthermore, previous ab initio calculations have shown that while pyrene and fluoranthene adhere to the HOMO/LUMO trend discussed above, benzo(*a*)pyrene and benzo(*b*)fluoranthene do not.[6] Finally, the calculated LUMO energy of nitromethane is found to be higher than the LUMO energy of any of the above PAHs (in the gas phase).

The use of ab initio quantum mechanics to study this phenomenon is attractive as such methods may provide an in-depth view and increased understanding of the photophysical processes that underlie fluorescence quenching. To date, ab initio calculations have been used to predict geometries,[7-10] heats of formation,[11-14] vibrational frequencies,[15-17] charge distributions, and ionization energies[18] of ground-state PAHs. For excited states, the Pariser–Parr–Pople (PPP) approximation has been applied to the calculation of PAH electronic spectra.[19-21] Other semiempirical methods have also been used on excited-state PAHs[22-25] as well as their ions and derivatives.[26-29] More recently, time-dependent density functional theory has been applied to the calculation of PAH excitation energies.[30] Finally, other excited-state properties such as charge distributions[31] and vibrational frequencies[32] have also been calculated.

Previous calculations by Goodpaster et al. have established clear differences in the ground- and excited-state properties of alternant and nonalternant PAHs.[6] In this work, good agreement was observed between the computed ground-state geometries and experimental data from neutron diffraction. In addition, ground- and excited-state vibrations were accurately predicted. Interestingly, the ground-state geometries of nonalternant isomers contain five-membered rings with bonds that are not conjugated with the aromatic π system. Upon reaching an excited state, the aliphatic C–C bonds tend to contract more than the aromatic C–C bonds in other parts of the molecule, explaining the lack of vibrational fine structure in the emission spectra of these molecules.[6,33] Furthermore, the excited states of nonalternant PAHs are generally at lower energy relative to the ground state when compared to their alternant isomers.

Published calculations involving complexes between PAHs and other chemical species have not been as well developed as those for individual PAH molecules. For example, there is significant interest in studying both ground- and excited-state charge transfer reactions using computational techniques.[34-37] In addition, semiempirical calculations have been used to study the ground- and excited-state structures of some PAH charge-transfer complexes.[38-40] However, the majority of the work in this area has not involved large PAH molecules or the transient excited-state complexes that are characteristic of selective quenching reactions.

The development of a quantitative model for selective fluorescence quenching would allow the computational evaluation of novel quenchers and help to direct experimental efforts. Towards that end, this study has examined energy and electron transfer in various fluorophore–quencher and fluorophore–solvent complexes involving the PAHs pyrene and fluoranthene, the quencher nitromethane, and the solvent acetonitrile.

II. Methods

Ground- and excited-state calculations have been completed using the Gaussian 98[41] program on a SGI Origin 2400 server with 32 300 MHz R12000 processors and a CRAY T90. All ground-state calculations used the Hartee–Fock (HF) method while excited states were treated using configuration interaction with single excitations (CIS). The geometries of all molecules were optimized individually at the HF/6-31G* level while constrained to the following point groups: pyrene (D_{2h}), fluoranthene (C_{2v}), nitromethane (C_s), and acetonitrile (C_{3v}).

Partial optimizations were completed where the relative separation distance and orientation of the molecules were varied while their respective molecular geometries were held constant. In initial studies of the pyrene–nitromethane system, ten archetypal orientations were chosen where a plane of symmetry was preserved (for an overall C_s point group). Two

orientations (one attractive and one repulsive) were then chosen for use with all molecular complexes and a custom basis set. In these calculations, a 6-31G basis set was used for the atoms of the fluorophore molecule while a 6-31+G basis set was used for the atoms of the quencher or solvent molecule in order to more adequately simulate the diffuse electron density characteristic of an anion. In all calculations, the energies and properties of the ground state and ten lowest singlet and triplet excited states were determined as a function of intermolecular separation distance.

III. Results and Discussion

A. Effect of Molecular Orientation

Ten representative configurations of pyrene and nitromethane are shown in Figure 3-1. In an initial study, the intermolecular separation distance for each configuration was optimized at the HF/STO-3G and HF/3-21G levels and the energy of the molecular complex relative to that of the separated molecules was computed (see Table 3-1). These energies demonstrate that the relative orientation of the dipole moment of nitromethane with respect to the electrostatic potential of pyrene dominates the energy of their interaction. Nitromethane is a highly polar molecule, with a calculated dipole moment that is oriented towards its nitro functionality along the C–N bond axis (4.2 D at the HF/3-21G level). Those configurations where this dipole moment is oriented towards the positive electrostatic potential of the hydrogen atoms on pyrene (e.g., A, B, and C) are

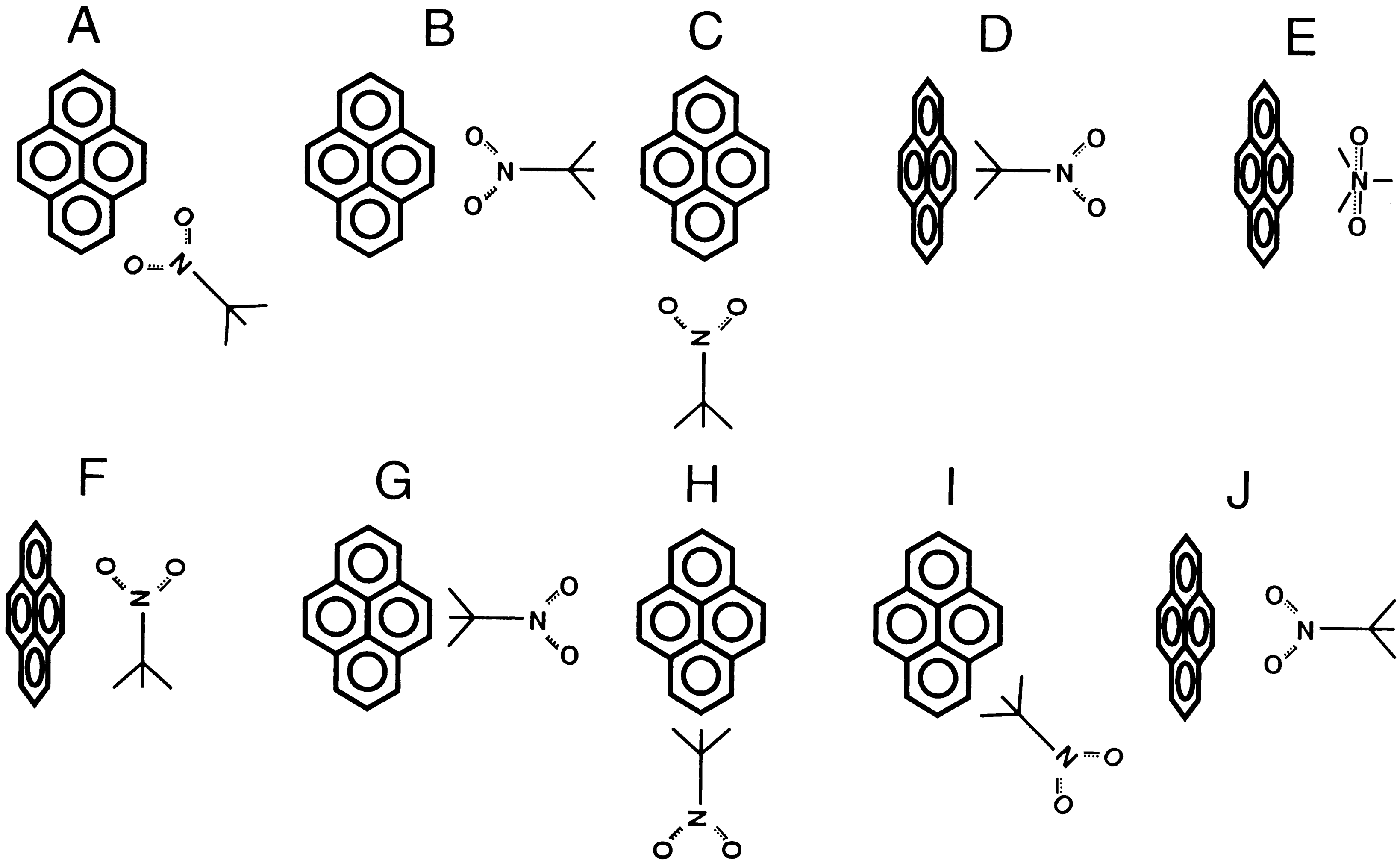

Figure 3-1: Representative orientations of the pyrene–nitromethane molecular complex. All complexes were constrained to C_s symmetry.

Table 3-1: Energies of Interaction (E_a) Between Pyrene and Nitromethane

Orientation[1]	**E_a (eV)**[2]	**E_a (eV)**[3]
A	-0.0373	-0.2623
B	-0.0372	-0.2669
C	-0.0263	-0.2475
D	-0.0205	-0.1412
E	-0.0136	-0.0977
F	-0.0114	-0.0816
G	0.0025	0.0158
H	0.0026	0.0126
I	0.0026	0.0007
J	0.0028	0.0006

[1] See Figure 3-1

[2] HF/STO-3G

[3] HF/3-21G

the most stable. The configuration where the dipole moment is oriented towards the negative electrostatic potential of the aromatic carbon atoms (e.g., J) is the least stable. In configurations such as this, the optimized intermolecular separation distance is large and the energy of the molecular complex is slightly higher than that of the separated molecules.

Optimizing all intermolecular variables resulted in various final configurations, all of which were similar to orientations A, B, C, or D (regardless of starting position). Furthermore, for each of these optimized molecular complexes it was found that the energy of interaction of an excited-state pyrene molecule with a ground-state nitromethane molecule was similar to the energy of interaction of the ground-state molecules. In general, the final location of the optimized molecules differed depending on their initial locations. This suggests that while there is a substantial driving force for the association of the nitro-group of nitromethane with the hydrogens of pyrene, there are multiple local minima on the potential energy surface of the pyrene–nitromethane system. Accordingly, it was decided that two representative orientations, one attractive (B) and one repulsive (J), would be used in further studies. This approach is appropriate given that excited-state quenching interactions are thought to be transient and collisional in nature, allowing many possible orientations of the two molecules as they diffuse together in solution.

B. Effect of Basis Set

The effect of basis set on the relative energies of the first six singlet excited-states of pyrene–nitromethane and fluoranthene–nitromethane are shown in Figures 3-2 and 3-3, respectively. Both sets of molecules were held in configuration B at an intermolecular separation distance of 2.0 Å. In Figure 3-2, two singlet excited states of pyrene ($^1P_1 + {}^1N_0$ and $^1P_2 + {}^1N_0$), two singlet excited states of nitromethane ($^1P_0 + {}^1N_1$ and $^1P_0 + {}^1N_2$), and an additional singlet excited state of pyrene ($^1P_3 + {}^1N_0$) are shown. In addition, a singlet ion-pair state ($^2P^+ + {}^2N^-$) was seen which was of particular interest as its interactions with neutral excited states has previously been implicated in the mechanism for fluorescence quenching. The analogous states for fluoranthene–nitromethane are shown in Figure 3-3.

Overall, and as expected, there is a large decrease in the excitation energies of both complexes as the basis set is expanded, particularly from the CIS/3-21G to CIS/6-31G levels. More importantly, however, the relative energies of the excited states change. In particular, the energy of the lowest ion-pair state of pyrene–nitromethane decreases dramatically with respect to the adjacent singlet excited state ($^1P_3 + {}^1N_0$). In fact, this decrease was sufficient at the CIS/6-31G level to make the ion pair less energetic than $^1P_3 + {}^1N_0$ at the separation distance studied. Notably, this behavior was not seen with fluoranthene–nitromethane. Adding diffuse (+) functions to the atoms of nitromethane lowered the energy of this ion pair further and resulted in a new ion-pair state being seen for both the pyrene and fluoranthene systems.

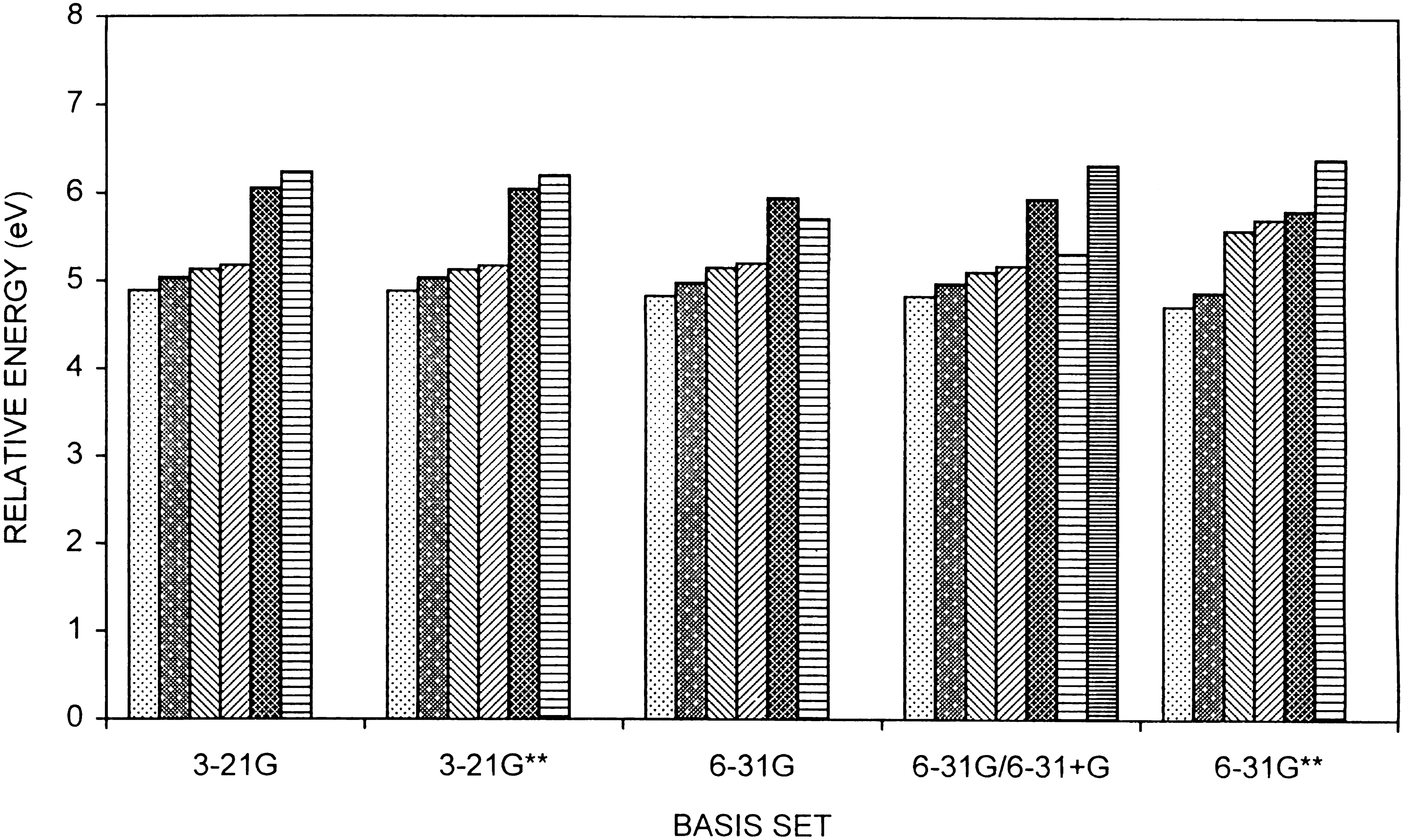

Figure 3-2: Effect of basis set on the relative energies of the excited states of a pyrene–nitromethane complex (configuration B, 2.0 Å intermolecular separation). States: ░ S_1 ($^1P_1$ + $^1N_0$), ▒ S_2 ($^1P_2$ + $^1N_0$), ▧ S_3 ($^1P_0$ + $^1N_1$), ▨ S_4 ($^1P_0$ + $^1N_2$), ▩ S_5 ($^1P_3$ + $^1N_0$), ▤ S_6 ($^2P^+$ + $^2N^-$), ▤ S_7 ($^2P^+$ + $^2N^-$).

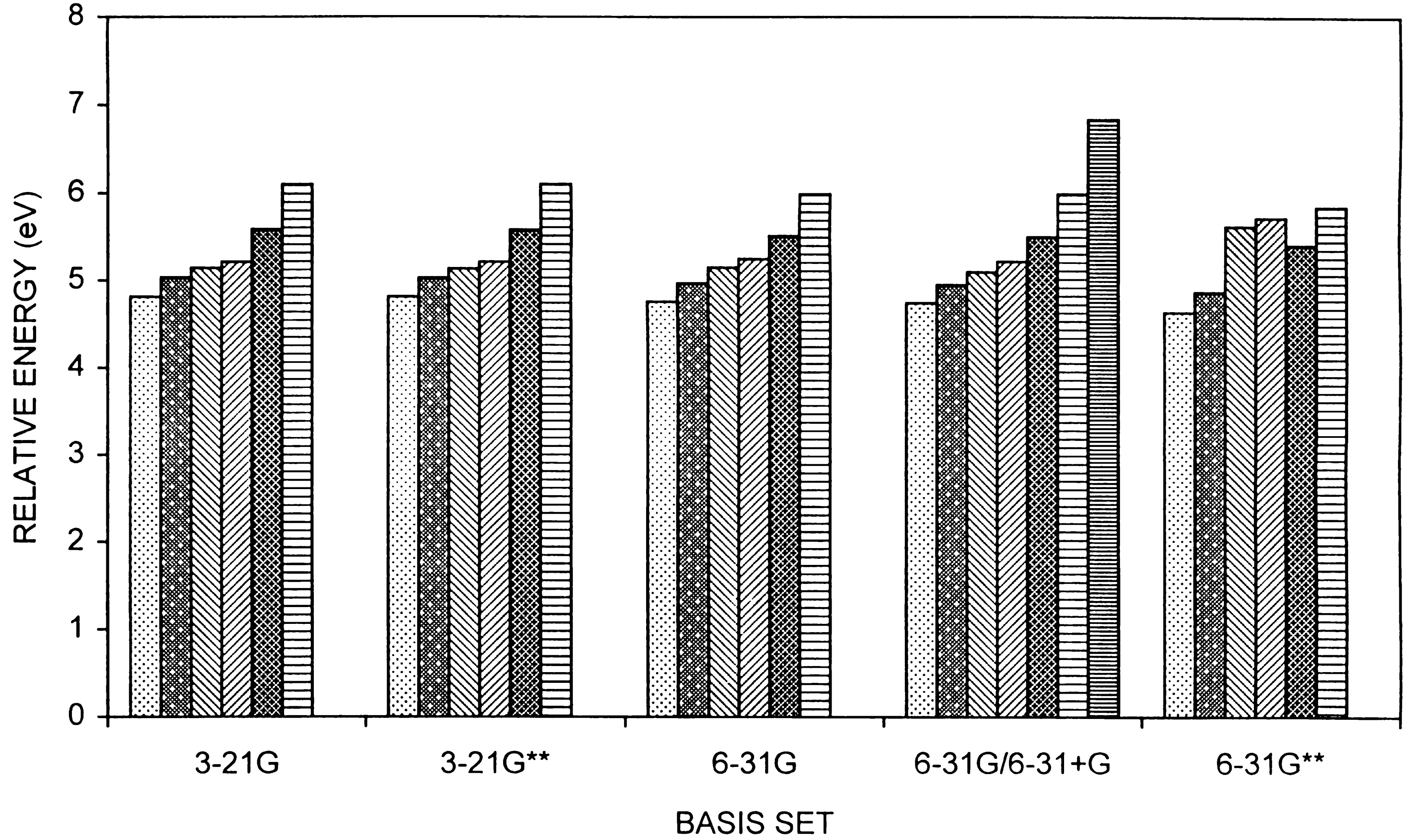

Figure 3-3: Effect of basis set on the relative energies of the excited states of a fluoranthene–nitromethane complex (configuration B, 2.0 Å intermolecular separation). States: ░ S_1 ($^1F_1$ + $^1N_0$), ▦ S_2 ($^1F_2$ + $^1N_0$), ▧ S_3 ($^1F_0$ + $^1N_1$), ▨ S_4 ($^1F_0$ + $^1N_2$), ▩ S_5 ($^1F_3$ + $^1N_0$), ▤ S_6 ($^2F^+$ + $^2N^-$), ▤ S_7 ($^2F^+$ + $^2N^-$).

Therefore, a mixed 6-31G/6-31+G basis set was applied in the remaining studies in order to represent the anionic character of the quencher in the ion pair more accurately.

C. Singlet-State Potential Energy Surfaces

1. PAH–Nitromethane Complexes

As previously mentioned, two orientations (B and J) were chosen to generate singlet-state potential energy surfaces using a 6-31G/6-31+G basis set. The energies of the PAHs with either nitromethane or acetonitrile were calculated as functions of intermolecular separation distance and the results are discussed in the following section.

Figures 3-4 and 3-5 show the interaction of pyrene (P) and nitromethane (N) in orientations B and J, respectively. In both cases, a number of curves that represent the energies of various excited states are displayed. At large separation distances, these states are (in increasing order of energy): excited-state pyrene with ground-state nitromethane (${}^1P_1 + {}^1N_0$, ${}^1P_2 + {}^1N_0$, ${}^1P_3 + {}^1N_0$, and ${}^1P_4 + {}^1N_0$; ${}^1A'$ symmetry), ground-state pyrene with excited-state nitromethane (${}^1P_0 + {}^1N_1$ and ${}^1P_0 + {}^1N_2$; ${}^1A''$ symmetry), and two ion pairs consisting of a pyrene cation with a nitromethane anion (${}^2P^{\cdot} + {}^2N^{-}$; ${}^1A'$ symmetry).

In the context of a fluorescence quenching experiment, the pyrene excited states are populated via absorption of photons with appropriate wavelengths. Furthermore, when pyrene and nitromethane diffuse together in solution, their intermolecular separation distance is reduced. Figures 3-4 and 3-5 illustrate how

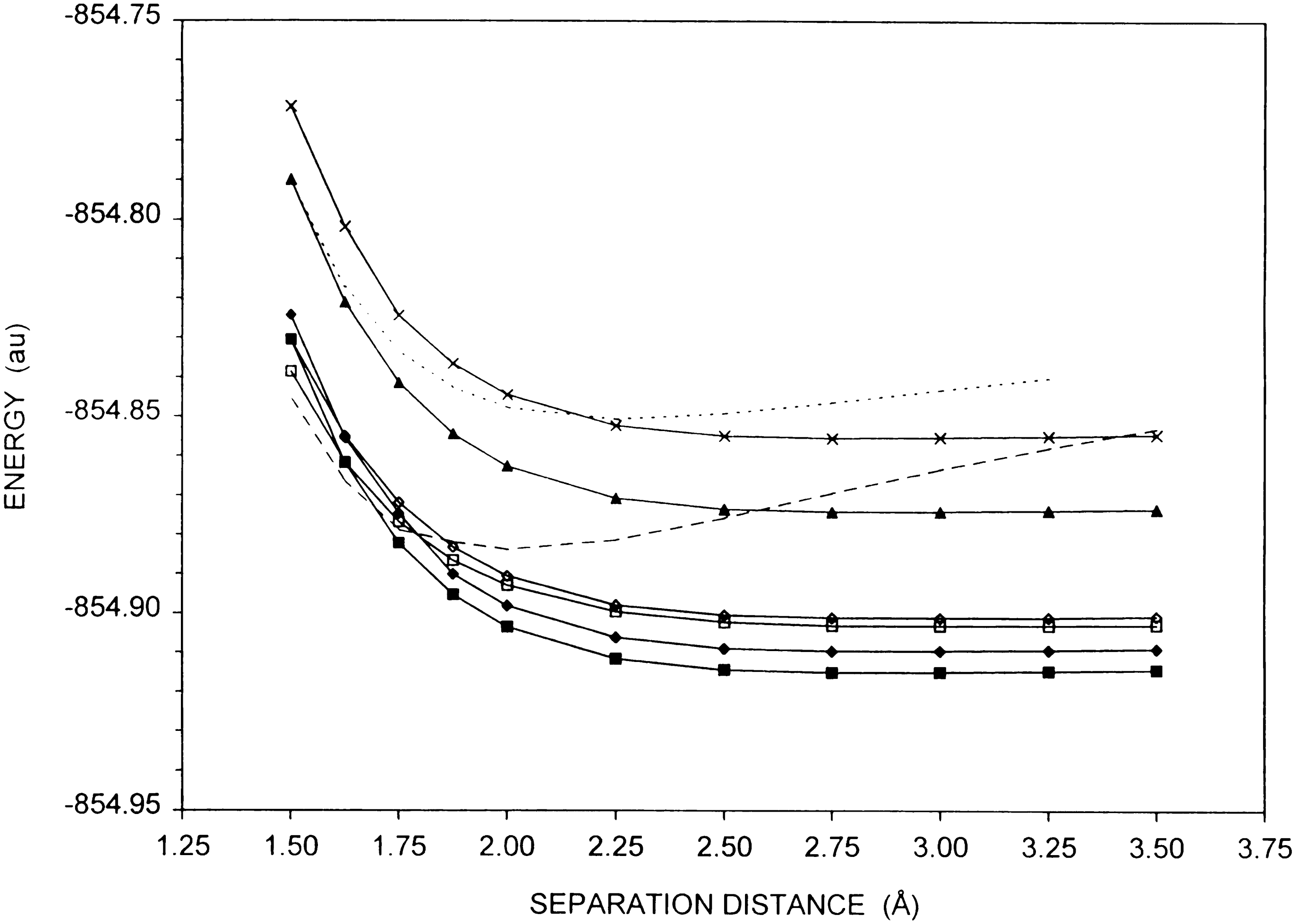

Figure 3-4: Interaction of pyrene (P) with nitromethane (N) in configuration B. States: ■ S_1 ($^1P_1$ + $^1N_0$), ◆ S_2 ($^1P_2$ + $^1N_0$), □ S_3 ($^1P_0$ + $^1N_1$), ◇ S_4 ($^1P_0$ + $^1N_2$), ▲ S_5 ($^1P_3$ + $^1N_0$), X S_6 ($^1P_4$ + $^1N_0$), --- S_7 ($^2P^+$ + $^2N^-$), - - - S_8 ($^2P^+$ + $^2N^-$).

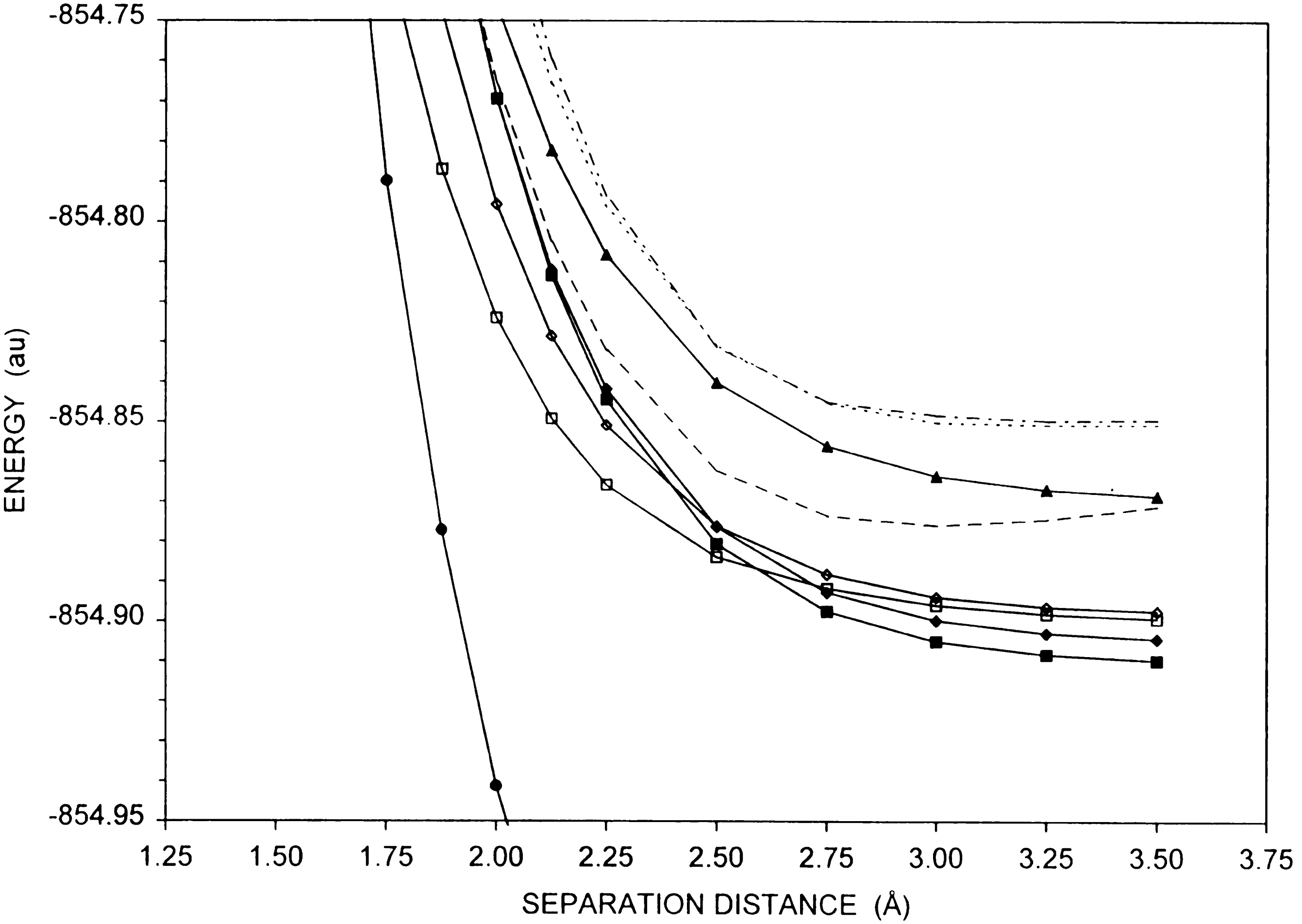

Figure 3-5: Interaction of pyrene (P) with nitromethane (N) in configuration J. States: ● S_0 ($^1P_0$ + $^1N_0$), ■ S_1 ($^1P_1$ + $^1N_0$), ◆ S_2 ($^1P_2$ + $^1N_0$), □ S_3 ($^1P_0$ + $^1N_1$), ◇ S_4 ($^1P_0$ + $^1N_2$), --- S_5 ($^2P^+$ + $^2N^-$), ▲ S_6 ($^1P_3$ + $^1N_0$), - - - S_7 ($^2P^+$ + $^2N^-$), - - - S_8 ($^2P^+$ + $^2N^-$).

the energies for the various excited states change with separation distance and, in some cases, the curves for these states cross. These crossing points represent separation distances where an excited-state pyrene complex may change from one state to another and eventually reach the ground state without emission of a photon.

In particular, $^1P_1 + {}^1N_0$ and $^1P_2 + {}^1N_0$ become isoenergetic with $^1P_0 + {}^1N_1$, $^1P_0 + {}^1N_2$, and $^2P^+ + {}^2N^-$. When the molecules are brought together in an attractive orientation (Figure 3-4), these crossing points occur at a distance of 1.625 – 1.875 Å. In the repulsive configuration (Figure 3-5) these crossing points occur at farther distances of 2.25 – 2.75 Å, and the ion pair does not intersect either $^1P_1 + {}^1N_0$ or $^1P_2 + {}^1N_0$ until a short intermolecular distance (and very high energy) is reached. Lastly, the intersections of the $^1P_1 + {}^1N_0$ and $^1P_2 + {}^1N_0$ surfaces with those of $^1P_0 + {}^1N_1$ and $^1P_0 + {}^1N_2$ occur at relatively the same energy in both configurations. This implies that the energy barrier for transitions between excited-state pyrene and excited-state nitromethane is largely independent of molecular orientation.

Assessing the likelihood of an excited-state pyrene complex undergoing a transition to either an excited-state nitromethane complex or an ion pair must be based on both energetic and symmetry considerations. By optimizing the intermolecular separation of the attractive configuration (B), the energies for adiabatic transitions between the minima of various potential energy surfaces can be calculated. Those results are contained in Table 3-2 for the pyrene–nitromethane complex. For example, the energy barrier for a transition

Table 3-2: Adiabatic Transition Energies for Pyrene (Orientation B, 6-31G/6-31+G)

Intial State	Sym.	R_i (Å)	E_i (au)	Final State	Sym.	R_f (Å)	E_f (au)	ΔE (eV)	Sym. Allowed?	f
$^1P_0 + {}^1N_0$	$^1A'$	2.838	-855.093	$^1P_1 + {}^1N_0$	$^1A'$	2.816	-854.915	4.838	Y	0.392
$^1P_0 + {}^1N_0$	$^1A'$	2.838	-855.093	$^1P_2 + {}^1N_0$	$^1A'$	2.828	-854.910	4.984	Y	0.001
$^1P_1 + {}^1N_0$	$^1A'$	2.816	-854.915	$^1P_2 + {}^1N_0$	$^1A'$	2.828	-854.910	0.146	Y	?
$^1P_1 + {}^1N_0$	$^1A'$	2.816	-854.915	$^1P_0 + {}^1N_1$	$^1A''$	2.944	-854.903	0.333	N	?
$^1P_1 + {}^1N_0$	$^1A'$	2.816	-854.915	$^1P_0 + {}^1N_2$	$^1A''$	2.865	-854.902	0.365	N	?
$^1P_1 + {}^1N_0$	$^1A'$	2.816	-854.915	$^2P^+ + {}^2N$	$^1A'$	2.027	-854.884	0.849	Y	?
$^1P_2 + {}^1N_0$	$^1A'$	2.828	-854.910	$^2P^+ + {}^2N$	$^1A'$	2.027	-854.884	0.703	Y	?
$^1P_0 + {}^1N_1$	$^1A''$	2.944	-854.903	$^1P_0 + {}^1N_0$	$^1A'$	2.838	-855.093	-5.171	N	0.000
$^1P_0 + {}^1N_2$	$^1A''$	2.865	-854.902	$^1P_0 + {}^1N_0$	$^1A'$	2.838	-855.093	-5.203	N	0.000
$^2P^+ + {}^2N^-$	$^1A'$	2.027	-854.884	$^1P_0 + {}^1N_0$	$^1A'$	2.838	-855.093	-5.688	Y	0.028
$^1P_0 + {}^1A_0$	$^1A'$	3.039	-743.427	$^1P_1 + {}^1A_0$	$^1A'$	3.017	-743.249	4.839	Y	0.408
$^1P_0 + {}^1A_0$	$^1A'$	3.039	-743.427	$^1P_2 + {}^1A_0$	$^1A'$	3.025	-743.244	4.983	Y	0.001
$^1P_1 + {}^1A_0$	$^1A'$	3.017	-743.249	$^1P_2 + {}^1A_0$	$^1A'$	3.025	-743.244	0.144	Y	?
$^1P_1 + {}^1A_0$	$^1A'$	3.017	-743.249	$^2P^+ + {}^2A^-$	$^1A''$	2.411	-743.195	1.456	N	?
$^1P_2 + {}^1A_0$	$^1A'$	3.025	-743.244	$^2P^+ + {}^2A^-$	$^1A''$	2.411	-743.195	1.312	N	?
$^2P^+ + {}^2A^-$	$^1A''$	2.411	-743.195	$^1P_0 + {}^1A_0$	$^1A'$	3.039	-743.427	-6.295	N	0.003

between ${}^1P_1 + {}^1N_0$ and ${}^1P_2 + {}^1N_0$ is 0.15 eV. The relatively small barrier between these two states as well as their disproportionate oscillator strengths (0.392 and 0.001) is consistent with what is known about the lowest-lying excited states of pyrene. Experimental measurements have shown that these states are accessible via one-photon excitation, although one state is allowed while the other is forbidden.[42-44] Although CIS calculations correctly predict the existence of these two states, it has been found that their order is inverted.[6] Subsequent calculations have confirmed this inversion and demonstrated that the multireference effect is crucial in predicting the correct order of the two lowest-lying singlet excited states.[45] Importantly, it is has been shown experimentally that excitation to the allowed singlet state can result in population of the forbidden singlet state through vibrational coupling.[6,46] Therefore, either pyrene singlet state is available for deactivation by nitromethane.

Other transitions involving the lowest-lying excited states of pyrene involve either excited-state nitromethane or an ion pair. The barrier for transitions to a ${}^1P_0 + {}^1N_1$ or ${}^1P_0 + {}^1N_2$ surface are 0.33 – 0.36 eV, while the barrier for formation of ${}^2P^+ + {}^2N^-$ is 0.70 – 0.85 eV. Despite the larger barrier for formation of an ion pair, symmetry selection rules dictate that two states must have equivalent symmetries for $\nu_0 - \nu_0$ transitions between excited states to be allowed.[47] Hence, while ${}^1P_0 + {}^1N_1$, ${}^1P_0 + {}^1N_2$, and ${}^2P^+ + {}^2N^-$ are potential partners for energy transfer with ${}^1P_1 + {}^1N_0$ and/or ${}^1P_2 + {}^1N_0$, only the route involving the ion pair is allowed by selection rules. Similarly, given that the symmetry of the ground-state complex is ${}^1A'$, the only allowed transition to the ground state (other than fluorescence from the ${}^1P_1 + {}^1N_0$ or ${}^1P_2 + {}^1N_0$ state) is via the ion pair. Furthermore, this state had a charge separation ranging from ±0.99 to ±0.85, which decreases as the separation distance decreases. The high charge separation of this ionic state implies that if it is an intermediate in a fluorescence quenching reaction, full electron transfer occurs between the fluorophore and quencher rather than the formation of a charge-transfer complex.

Various similarities and differences can be seen in the behavior of the fluoranthene–nitromethane complex. Figures 3-6 and 3-7 show the interaction of fluoranthene (F) and nitromethane (N) in orientations B and J, respectively. As with pyrene, the lowest energy states represented are (in increasing order of energy): excited-state fluoranthene with ground-state nitromethane (${}^1F_1 + {}^1N_0$, ${}^1F_2 + {}^1N_0$, ${}^1F_3 + {}^1N_0$, and ${}^1F_4 + {}^1N_0$; ${}^1A'$ symmetry), ground-state fluoranthene with excited-state nitromethane (${}^1F_0 + {}^1N_1$ and ${}^1F_0 + {}^1N_2$; ${}^1A''$ symmetry), and two ion pairs consisting of a fluoranthene cation with a nitromethane anion (${}^2F^+ + {}^2N^-$; ${}^1A'$ symmetry). While various crossing points are seen in these potential energy surfaces, only the ${}^1F_2 + {}^1N_0$ and ${}^1F_0 + {}^1N_1$ states are involved. In addition, although an ion pair is shown to form between fluoranthene and nitromethane, it is energetically inaccessible from either the ${}^1F_1 + {}^1N_0$ or ${}^1F_2 + {}^1N_0$ surface. A final unique characteristic of this system is that the second ion-pair state of fluoranthene–nitromethane exhibits an “avoided crossing” with the ${}^1F_4 + {}^1N_0$ state. In this case, the two states exchange identities but have a discontinuity at the point of their intersection. This phenomenon is most likely to occur when the two

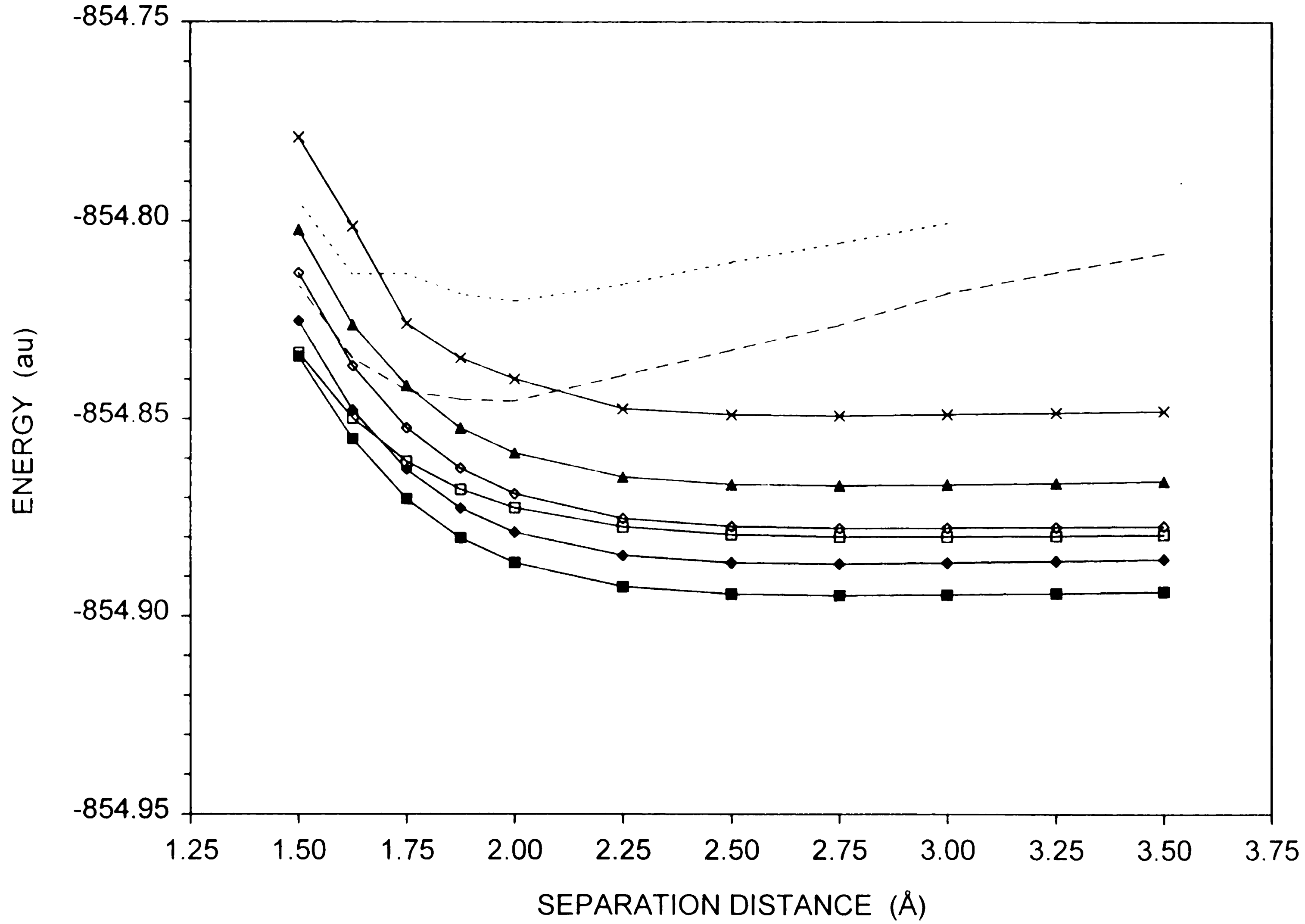

Figure 3-6: Interaction of fluoranthene (F) with nitromethane (N) in configuration B. States: ■ S_1 ($^1F_1$ + $^1N_0$), ◆ S_2 ($^1F_2$ + $^1N_0$), □ S_3 ($^1F_0$ + $^1N_1$), ◇ S_4 ($^1F_0$ + $^1N_2$), ▲ S_5 ($^1F_3$ + $^1N_0$), X S_6 ($^1F_4$ + $^1N_0$), --- S_7 ($^2F^+$ + $^2N^-$), - - - S_8 ($^2F^+$ + $^2N^-$).

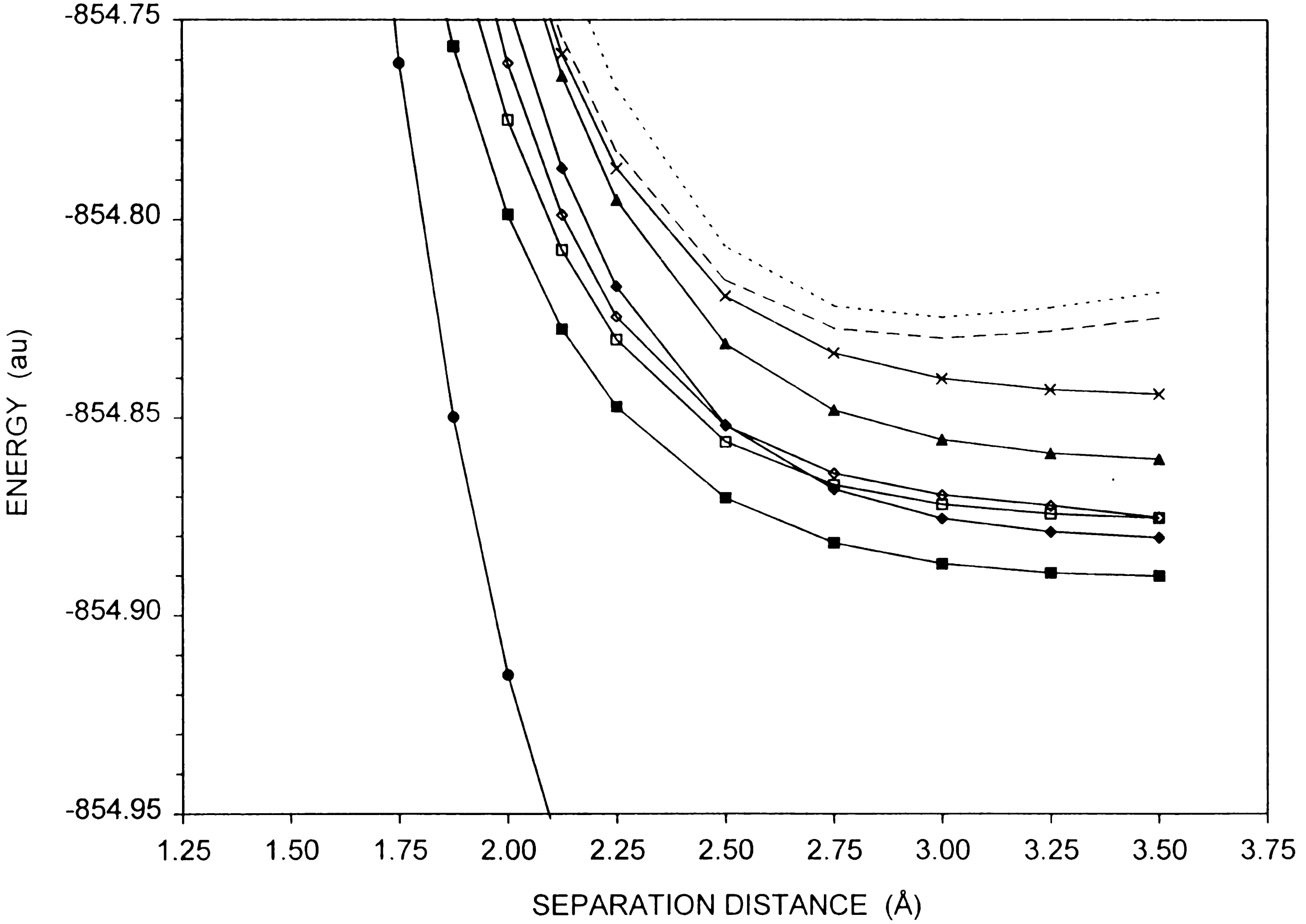

Figure 3-7: Interaction of fluoranthene (F) with nitromethane (N) in configuration J. States: ● S_0 ($^1F_0$ + $^1N_0$), ■ S_1 ($^1F_1$ + $^1N_0$),◆ S_2 ($^1F_2$ + $^1N_0$), □ S_3 ($^1F_0$ + $^1N_1$), ◇ S_4 ($^1F_0$ + $^1N_2$), ▲ S_5 ($^1F_3$ + $^1N_0$), X S_6 ($^1F_4$ + $^1N_0$), ––– S_7 ($^2F^+$ + $^2N^-$), - - - S_8 ($^2F^+$ + $^2N^-$).

states have electronic wave functions that strongly mix and the force of their approach (*dE/dR*) is high.[48,49]

Adiabatic transition energies for fluoranthene–nitromethane complexes (Table 3-3) show some similar trends as pyrene–nitromethane complexes. However, major differences include larger barriers for transitions from the $^1F_1$ + $^1N_0$ or $^1F_2$ + $^1N_0$ surfaces to other excited states, particularly to the ion-pair state (ΔE = 1.1 – 1.3 eV). In addition, the transition from the ion pair thus formed to the ground state exhibits a smaller oscillator strength for fluoranthene than for pyrene (f = 0.01 versus f = 0.03). Lastly, symmetry considerations are the same for this complex as for the pyrene–nitromethane complex in that transitions to the $^1F_0$ + $^1N_1$ or $^1F_0$ + $^1N_2$ states are forbidden.

2. PAH–Acetonitrile Complexes

The importance of elucidating the origin of nitromethane's selectivity is matched by the importance by contrasting that behavior with solvent molecules. Solvents such as methanol or acetonitrile are far more abundant than quencher molecules in solution-phase studies and ultimately limit the unquenched energy and lifetime of an excited-state fluorophore. Towards that end, Figure 3-8 shows the interaction of pyrene (P) and acetonitrile (A) in orientation B. In this case, only states corresponding to excited-state pyrene with ground-state acetonitrile ($^1P_1$ + $^1A_0$ and $^1P_2$ + $^1A_0$; $^1A'$ symmetry) and a pyrene cation with an acetonitrile anion ($^2P^+$ + $^2A^-$, $^1A''$ symmetry) are seen. Importantly, no excited-state acetonitrile states are located within a reasonable amount of energy of the $^1P_1$ + $^1A_0$ and $^1P_2$ + $^1A_0$ surfaces, precluding direct energy transfer between pyrene and

Table 3-3: Adiabatic Transition Energies for Fluoranthene (Orientation B, 6-31G/6-31+G)

Intial State	Sym.	R_i (Å)	E_i (au)	Final State	Sym.	R_f (Å)	E_f (au)	ΔE (eV)	Sym. Allowed?	f
$^1F_0 + {}^1N_0$	$^1A'$	2.759	-855.070	$^1F_1 + {}^1N_0$	$^1A'$	2.737	-854.895	4.759	Y	0.012
$^1F_0 + {}^1N_0$	$^1A'$	2.759	-855.070	$^1F_2 + {}^1N_0$	$^1A'$	2.709	-854.887	4.978	Y	0.425
$^1F_1 + {}^1N_0$	$^1A'$	2.737	-854.895	$^1F_2 + {}^1N_0$	$^1A'$	2.709	-854.887	0.219	Y	?
$^1F_1 + {}^1N_0$	$^1A'$	2.737	-854.895	$^1F_0 + {}^1N_1$	$^1A''$	2.861	-854.880	0.404	N	?
$^1F_1 + {}^1N_0$	$^1A'$	2.737	-854.895	$^1F_0 + {}^1N_2$	$^1A''$	2.825	-854.878	0.464	N	?
$^1F_1 + {}^1N_0$	$^1A'$	2.737	-854.895	$^2F^+ + {}^2N$	$^1A'$	1.966	-854.845	1.344	Y	?
$^1F_2 + {}^1N_0$	$^1A'$	2.709	-854.887	$^2F^+ + {}^2N$	$^1A'$	1.966	-854.845	1.126	Y	?
$^1F_0 + {}^1N_1$	$^1A''$	2.861	-854.880	$^1F_0 + {}^1N_0$	$^1A'$	2.759	-855.070	-5.163	N	0.000
$^1F_0 + {}^1N_2$	$^1A''$	2.825	-854.878	$^1F_0 + {}^1N_0$	$^1A'$	2.759	-855.070	-5.223	N	0.000
$^2F^+ + {}^2N^-$	$^1A'$	1.966	-854.845	$^1F_0 + {}^1N_0$	$^1A'$	2.759	-855.070	-6.103	Y	0.011
$^1F_0 + {}^1A_0$	$^1A'$	2.930	-743.404	$^1F_1 + {}^1A_0$	$^1A'$	2.914	-743.229	4.760	Y	0.013
$^1F_0 + {}^1A_0$	$^1A'$	2.930	-743.404	$^1F_2 + {}^1A_0$	$^1A'$	2.886	-743.221	4.979	Y	0.442
$^1F_1 + {}^1A_0$	$^1A'$	2.914	-743.229	$^1F_2 + {}^1A_0$	$^1A'$	2.886	-743.221	0.219	Y	?
$^1F_1 + {}^1A_0$	$^1A'$	2.914	-743.229	$^2F^+ + {}^2A^-$	$^1A''$	2.275	-743.153	2.074	N	?
$^1F_2 + {}^1A_0$	$^1A'$	2.886	-743.221	$^2F^+ + {}^2A^-$	$^1A''$	2.275	-743.153	1.855	N	?
$^2F^+ + {}^2A^-$	$^1A''$	2.275	-743.153	$^1F_0 + {}^1A_0$	$^1A'$	2.930	-743.404	-6.834	N	0.000

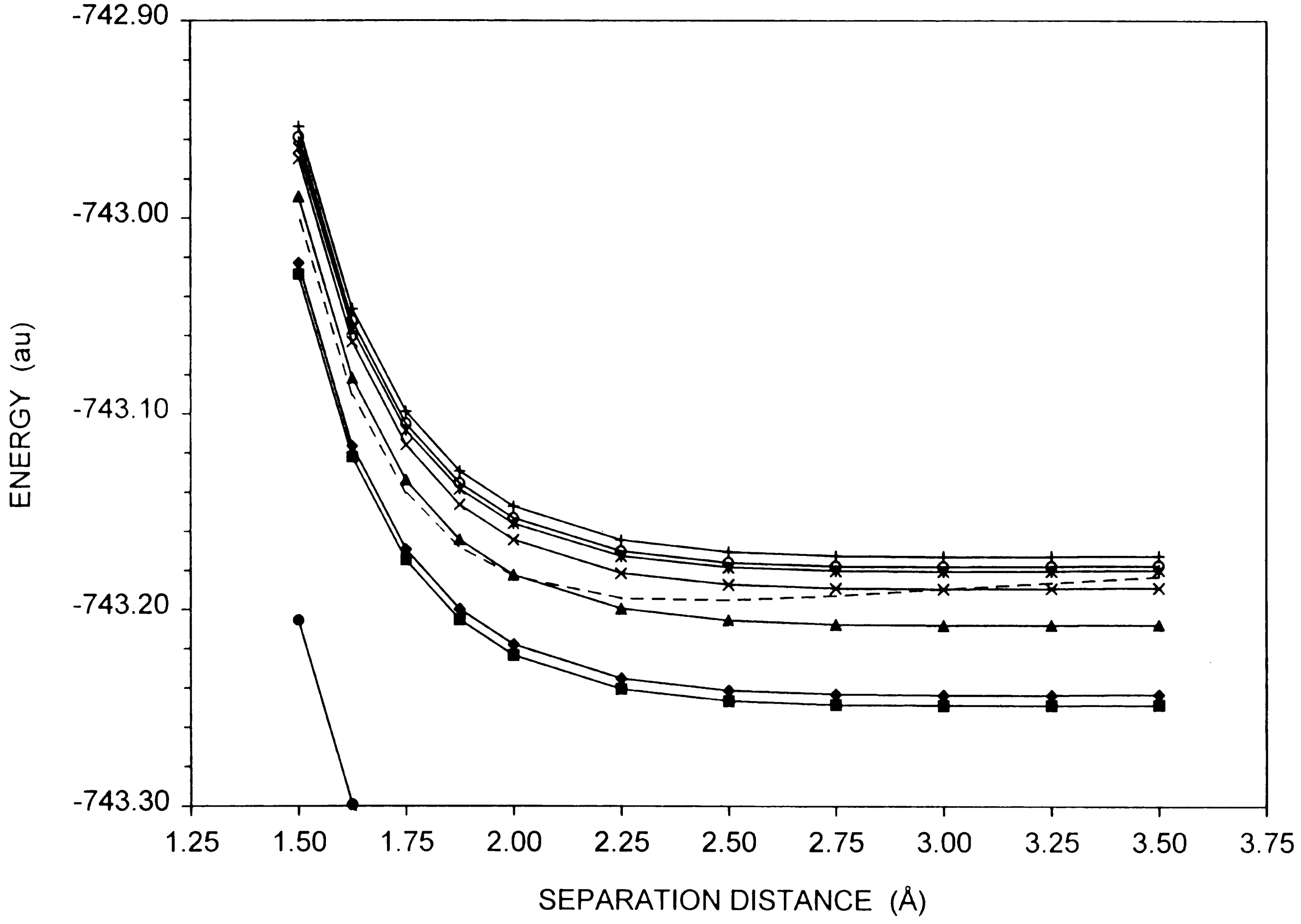

Figure 3-8: Interaction of pyrene (P) with acetonitrile (A) in configuration B. States: ● S_0 ($^1P_0$ + $^1A_0$), ■ S_1 ($^1P_1$ + $^1A_0$), ◆ S_2 ($^1P_2$ + $^1A_0$), ▲ S_3 ($^1P_3$ + $^1A_0$), X S_4 ($^1P_4$ + $^1A_0$), --- S_5 ($^2P^+$ + $^2A^-$), ⋇ S_6 ($^1P_5$ + $^1A_0$), ○ S_7 ($^1P_6$ + $^1A_0$), + S_8 ($^1P_7$ + $^1A_0$).

acetonitrile. Secondly, while ion pairs are shown to form between pyrene and acetonitrile, the transition energies from excited-state pyrene to a pyrene–acetonitrile ion pair (see Table 3-2) are unfavorable (1.3 – 1.4 eV). Furthermore, symmetry dictates that energy transfer from the $^1P_1$ + $^1A_0$ and $^1P_2$ + $^1A_0$ surfaces to the $^2P^+$ + $^2A^-$ surface is forbidden. Similarly, the transition from $^2P^+$ + $^2A^-$ to the ground state is forbidden.

The interaction of pyrene with acetonitrile in a repulsive configuration (orientation J) is shown in Figure 3-9. These potential energy surfaces are noticeably similar to those for the attractive configuration (orientation B) as shown in Figure 3-8. This demonstrates that the smaller dipole moment of acetonitrile relative to nitromethane reduces the influence of molecular orientation on the energy of the complex. Of further note is an avoided crossing between the $^1P_2$ + $^1A_0$ and $^1P_3$ + $^1A_0$ surfaces. As this is a transition between excited states of pyrene, it represents perturbation of the fluorescence emission through internal conversion rather than deactivation or quenching of the pyrene molecule.

Finally, Figures 3-10 and 3-11 show the interaction of fluoranthene (F) and acetonitrile (A) in orientations B and J, respectively. The calculated surfaces demonstrate the same trends as with pyrene in that there are very few crossing points and no opportunities for energy transfer to either excited-state acetonitrile states or fluoranthene–acetonitrile ion pairs. Also, as shown in Table 3-3, there is a larger barrier for formation of a fluoranthene–acetonitrile ion pair (1.8 – 2.1 eV). As with the pyrene–acetonitrile complex, energy transfer from the $^1F_1$ + $^1A_0$

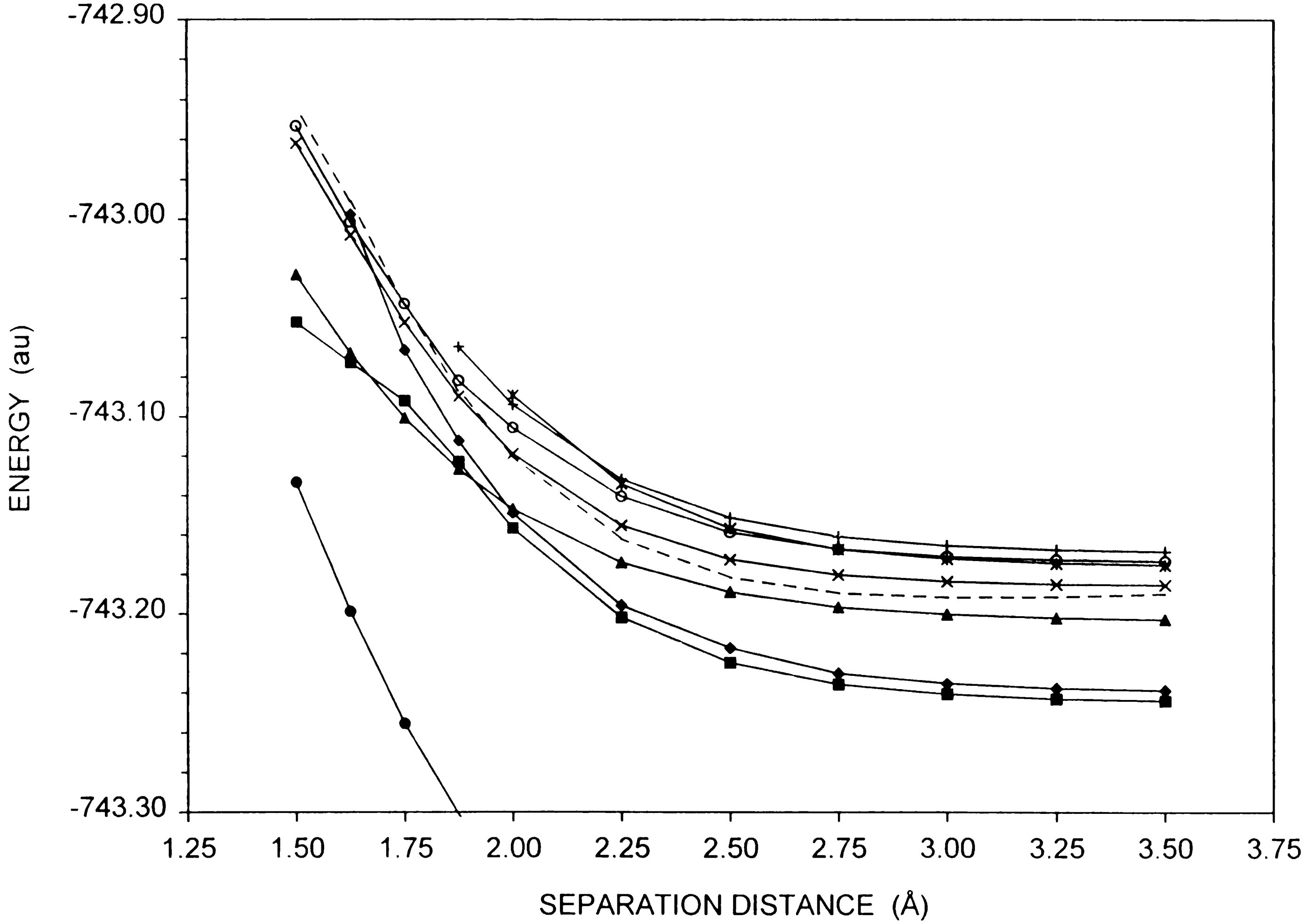

Figure 3-9: Interaction of pyrene (P) with acetonitrile (A) in configuration J. States: ● S_0 ($^1P_0$ + $^1A_0$), ■ S_1 ($^1P_1$ + $^1A_0$), ◆ S_2 ($^1P_2$ + $^1A_0$), ▲ S_3 ($^1P_3$ + $^1A_0$), --- S_4 ($^2P^+$ + $^2A^-$), X S_5 ($^1P_4$ + $^1A_0$), ⋇ S_6 ($^1P_5$ + $^1A_0$), ○ S_7 ($^1P_6$ + $^1A_0$), + S_8 ($^1P_7$ + $^1A_0$).

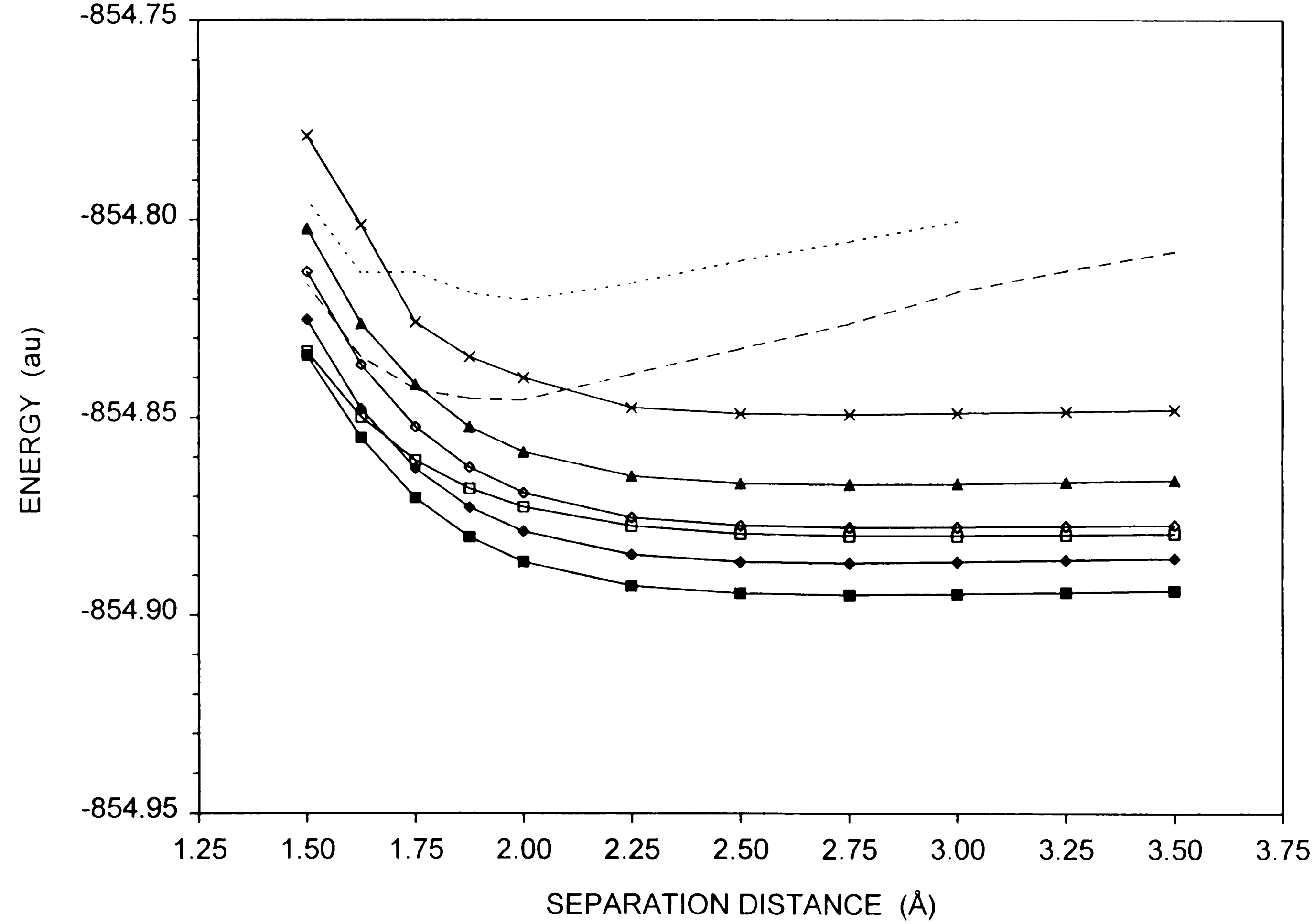

Figure 3-10: Interaction of fluoranthene (F) with acetonitrile (A) in configuration B. States: ● S_0 ($^1F_0$ + $^1A_0$), ■ S_1 ($^1F_1$ + $^1A_0$), ◆ S_2 ($^1F_2$ + $^1A_0$), ▲ S_3 ($^1F_3$ + $^1A_0$), X S_4 ($^1F_4$ + $^1A_0$), ✱ S_5 ($^1F_5$ + $^1A_0$), ○ S_6 ($^1F_6$ + $^1A_0$), --- S_7 ($^2F^+$ + $^2A^-$), - - - S_8 ($^2F^+$ + $^2A^-$).

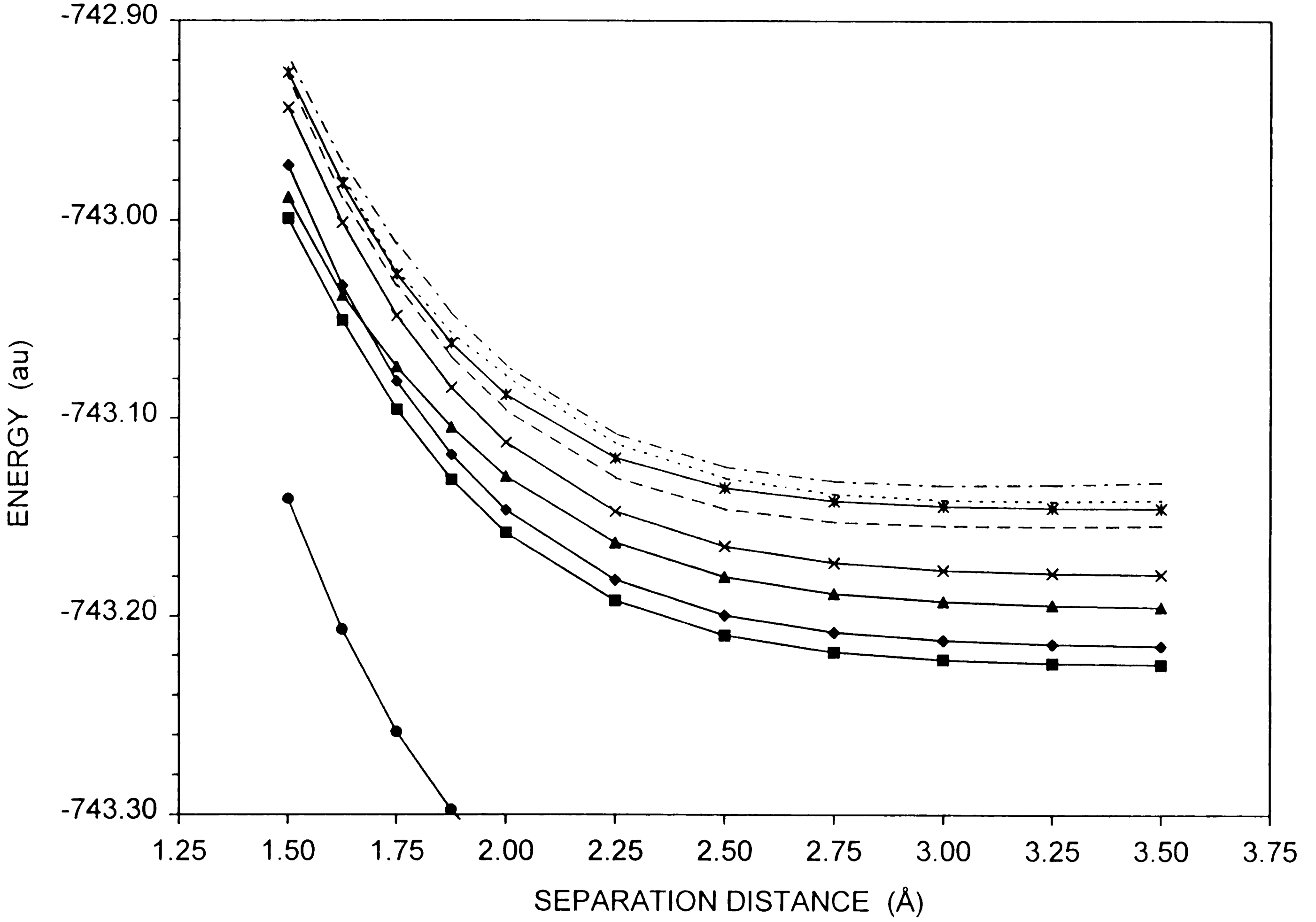

Figure 3-11: Interaction of fluoranthene (F) with acetonitrile (A) in configuration J. States: ● S_0 ($^1F_0 + {}^1A_0$), ■ S_1 ($^1F_1 + {}^1A_0$), ◆ S_2 ($^1F_2 + {}^1A_0$), ▲ S_3 ($^1F_3 + {}^1A_0$), X S_4 ($^1F_4 + {}^1A_0$), --- S_5 ($^2F^+ + {}^2A^-$), ✱ S_6 ($^1F_5 + {}^1A_0$), - - - S_7 ($^1F_6 + {}^1A_0$), - - - S_8 ($^2F^+ + {}^2A^-$).

and $^1F_2 + {}^1A_0$ surfaces to the $^2F^+ + {}^2A^-$ surface is forbidden by symmetry selection rules. Similarly, the transition from $^2F^+ + {}^2A^-$ to the ground state is forbidden.

D. Triplet-State Potential Energy Surfaces

Currently, the mechanisms for selective fluorescence quenching discussed above have considered only interactions between singlet states of the fluorophore and quencher. However, it is also important to consider deactivation of a singlet-state fluorophore by internal conversion to a triplet state. This process is especially prevalent in the presence of atoms with a high atomic number (the heavy atom effect), where electron spin and orbital motions are efficiently coupled.[50,51] The consequence of this spin-orbit coupling is mixing of electronic states with different multiplicity, which facilitates intersystem crossing of the fluorophore from the singlet to triplet state. In fact, one of the earliest applications of fluorescence quenching was the use of iodomethane and iodoethane to increase the phosphorescence yield of selected PAHs.[52 53]

In order to investigate the possible role of triplet states in the selective deactivation of PAHs by nitromethane, calculations at the 3-21G level were completed with pyrene–nitromethane and fluoranthene–nitromethane in configuration B. Various excited-state triplets were comparable in energy to the low-lying singlets of pyrene–nitromethane, including triplet states of pyrene ($^3P + {}^1N_0$) and triplet states of nitromethane ($^1P_0 + {}^3N$). In addition, at close separation distances (1.5 Å), a triplet ion-pair state ($^2P^+ + {}^2N^-$) was also seen where the unpaired electrons of the ions had the same, rather than opposite, spin.

Energetically, these triplet states of pyrene and the triplet ion-pair state were accessible from the singlet states of pyrene, which would be expected to be populated by absorption of photons ($^1P_1 + {}^1N_0$ or $^1P_2 + {}^1N_0$). In both cases, intersystem crossing to the neutral or ionic triplet states could lead to the quenching of fluorescence by promotion of phosphorescence or deactivation of the longer-lived triplet states by subsequent collisions with ground-state quencher molecules.

Excited-state triplets of fluoranthene–nitromethane were also comparable in energy to the low-lying singlets of this complex, including triplet states of fluoranthene ($^3F + {}^1N_0$) and triplet states of nitromethane ($^1F_0 + {}^3N$). However, unlike pyrene–nitromethane, no triplet ion-pair state was seen. These results suggest that, as with the singlet excited states, selective deactivation of excited-state PAHs via a triplet-state intermediate involves electron transfer. However, these transitions are forbidden by symmetry selection rules for both pyrene and fluoranthene and neither the fluorophore nor quencher has heavy atoms to promote intersystem crossing. Therefore, the likelihood of this deactivation route is low.

E. Visualization of Ion-Pair Formation

As a final illustration of the quenching phenomenon and its potential quantum chemical mechanism, changes in the electron density of pyrene–nitromethane excited states are visualized in configuration B (see Figure 3-12). In this diagram, three singlet excited states are portrayed at various

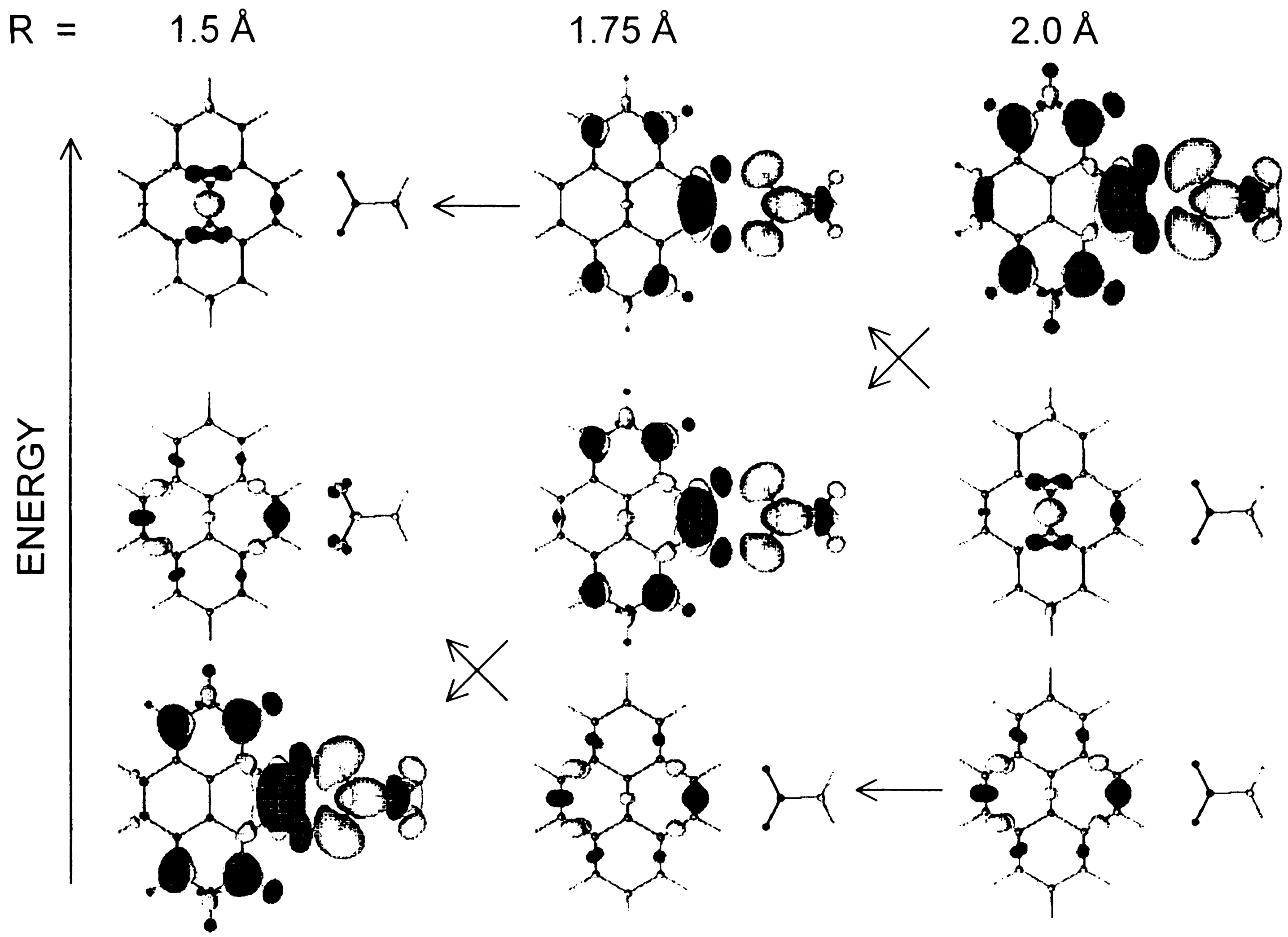

Figure 3-12: Mixing of states between the first two excited-state singlets of pyrene ($^1P_1 + {}^1N_0$ and $^1P_2 + {}^1N_0$) and a pyrene–nitromethane ion pair ($^2P^+ + {}^2N^-$) as a function of intermolecular separation.

separation distances with their relative energies reflected in their placement on the vertical axis. Areas of electron density increase are shaded in white, whereas areas of electron density decrease are shaded in black. At large separation distances, the two lowest-lying excited states can be identified as singlet states of pyrene ($^1P_1 + {}^1N_0$ or $^1P_2 + {}^1N_0$, respectively). Changes in electron density are localized on the pyrene molecule and reflect their excitation character.[6] In contrast, the third excited state can be identified as a pyrene–nitromethane ion pair ($^2P^+ + {}^2N^-$). There is a large decrease in charge on the pyrene molecule and a similarly large increase in charge on the nitromethane molecule. As the intermolecular separation distance is reduced, the relative energies of these states change. When the molecules are at a separation distance of 1.75 Å, there is strong mixing of the excitation character of the ion-pair state with the $^1P_2 + {}^1N_0$ state. This implies that in the quenching mechanism, ionization of this singlet state of pyrene may initiate the deactivation process.

IV. Conclusions

The use of ab initio techniques to elucidate the photophysical mechanism of selective fluorescence quenching is a powerful and novel approach for studying a long observed but little understood phenomenon. First, the importance of accurately simulating the diffuse electron density of the neutral and anionic states of the quencher has been demonstrated. Specifically, the relative energy of the ionic states was much reduced upon addition of diffuse functions to the atoms of the quencher molecule. As electron transfer appears to be the basis for the selective deactivation of alternant fluorophores such as pyrene, inclusion of diffuse basis functions on the atoms of the fluorophore as well as the quencher would serve to more accurately account for these interactions.

Using standard configurations of pyrene, fluoranthene, nitromethane and acetonitrile, the nature of their molecular complexes has been detailed. In particular, the magnitude and orientation of the dipole moment of either nitromethane or acetonitrile with respect to the electron density of the PAH is critical in determining energies of interaction or repulsion. In the case of nitromethane, the formation of planar complexes such as A, B, and C in Figure 3-1 appears to be highly favored and may indicate the preferred orientation of quencher molecules within the solvent cage of the excited-state fluorophore.

Studies of the interaction of the fluorophores with nitromethane as a function of distance have shown that energy transfer between excited-state PAHs and nitromethane has two possible mechanisms: direct energy transfer to an excited-state nitromethane quencher, or formation of a fluorophore–quencher ion pair. Both are energetically feasible for the alternant isomer pyrene, but only energy transfer to nitromethane is indicated as energetically possible for the nonalternant isomer fluoranthene. Furthermore, symmetry selection rules dictate that formation of the ion pair is allowed, while direct energy transfer to nitromethane is forbidden. Similar studies with acetonitrile clearly showed that ionization of the fluorophores is neither energetically favorable nor allowed by symmetry selection rules. These results indicate that the only viable alternative

route to the ground state for an excited state pyrene molecule is through the formation of an ion pair with nitromethane. This is in agreement with experimental results, which show that nitromethane selectively deactivates alternant PAHs such as pyrene whereas acetonitrile demonstrates no such ability.[4,5,54] However, given that the calculations described here are analogous to gas-phase interactions, quantitative prediction of solution-phase behavior is not reliable. It is expected that the inclusion of a model for the solvation of the excited-state complexes would enable accurate predictions of solution-phase experimental data and promising novel quenchers.

V. References

---

1. D. Rehm and A. Weller, *Israel J. Chem.* **8**, 259 (1970).
2. K. Yates, *Hückel Molecular Orbital Theory*, Academic Press, New York (1978).
3. U. Breymann, H. Dreeskamp, E. Koch, and M. Zander, *Chem. Phys. Lett.* **59**, 68 (1978).
4. S.H. Chen, C.E. Evans, and V.L. McGuffin, *Anal. Chim. Acta* **246**, 65 (1991).
5. F.K. Ogasawara, Y. Wang, and V.L. McGuffin, *Appl. Spectrosc.* **49**, 1 (1995).
6. J.V. Goodpaster, J.F. Harrison, and V.L. McGuffin, *J. Phys. Chem. A* **102**, 3372 (1998).
7. A.H. Chung and D.S. Dewar, *J. Chem. Phys.* **42**, 756 (1965).
8. R.A. Hites and W.J. Simonsick, *Calculated Molecular Properties of Polycyclic Aromatic Hydrocarbons,* Elsevier, Amsterdam (1987).
9. B.F. Plummer, L.K. Steffen, and W.C. Herndon, *Struct. Chem.* **4**, 279 (1993).
10. J.R. Rabinowitz and S.B. Little, *Int. J. Quantum Chem.* **52**, 681 (1994).
11. J. Kao and N.L. Allinger, *J. Am. Chem. Soc.* **99**, 975 (1977).
12. J. Kao, *J. Am. Chem. Soc.* **109**, 3817 (1987).
13. J.M. Schulman, R.C. Peck, and R.L. Disch, *J. Am. Chem. Soc.* **111**, 5675 (1989).

14. R.C. Peck, J.M. Schulman, and R.L. Disch, *J. Phys. Chem.* **94**, 6637 (1990).
15. F. Pauzat, D. Talbi, M.D. Miller, D.J. DeFrees, and Y. Ellinger, *J. Phys. Chem.* **96**, 7882 (1992).
16. M. Vala, J. Szczepanski, F. Pauzat, O. Parisel, D. Talbi, and Y. Ellinger, *J. Phys. Chem.* **98**, 9187 (1994).
17. S.R. Langhoff, *J. Phys. Chem.* **100**, 2819 (1996).
18. V.G. Zakrzewski, O. Dolgounitcheva, and J.V. Ortiz, *J. Chem. Phys.* **105**, 8748 (1996).
19. K. Nishimoto and L.S. Forster, *Theoret. Chim. Acta (Berl.)* **3**, 407 (1965).
20. K. Nishimoto, *Theoret. Chim. Acta (Berl.)* **7**, 207 (1967).
21. R. Pucci, M. Baldo, A. Martin-Rodero, G. Piccitto, and P. Tomasello, *Int. J. Quantum Chem.* **26**, 783 (1984).
22. N.K. Das Gupta and F.W. Birss, *Bull. Chem. Soc. Jpn.* **51**, 1211 (1978).
23. A. Das Gupta, S. Chatterjee, and N.K. Das Gupta, *Bull. Chem. Soc. Jpn.* **52**, 3070 (1979).
24. J. Sühnel, U. Kempka, and K. Gustav, *Journal F. Prakt. Chemie* **322**, 649 (1980).
25. O.G. Mekenyan, G.T. Ankley, G.D. Veith, and D.J. Call, *SAR and QSAR in Environmental Research* **2**, 237 (1994).
26. P. Du, F. Salama, and G.H. Loew, *Chem. Phys.* **173**, 421 (1993).
27. F. Negri and Z. Zgierski, *J. Chem. Phys.* **100**, 1387 (1994).
28. C. Niederalt, S. Grimme, and S.D. Peyerimhoff, *Chem. Phys. Lett.* **245**, 455 (1995).
29. F. Negri and M.Z. Zgierski, *J. Chem. Phys.* **104**, 3486 (1996).
30. S. Hirata, T.J. Lee, and M. Head-Gordon, *J. Chem. Phys.* **111**, 8904 (1999).
31. S.H. Chen and V.L. McGuffin, *Appl. Spectrosc.* **48**, 596 (1994).
32. C.M. Gittins, E.A. Rohlfing, and C.M. Rohlfing, *J. Chem. Phys.* **105**, 7323 (1996).
33. I.B. Berlman, *J. Phys. Chem.* **74**, 3085 (1970).
34. S. Reiling, M. Basnard, and P.A. Bopp, *J. Phys. Chem. A* **101**, 4409 (1997).
35. N.H. Martin, N.W. Allen III, C.A. Cottle, and C.K. Marschke, Jr., *J. Photochem. Photobio. A.: Chem.* **103**, 33 (1997).
36. R.J. Cave and M.D. Newton, *J. Chem. Phys.* **106**, 9213 (1997).
37. J.T. Su and A.H. Zewail, *J. Phys. Chem. A* **102**, 4082 (1998).
38. G.L. Heard and R.J. Boyd, *J. Phys. Chem. A* **101**, 5374 (1997).
39. T. Ohta, H. Kuroda, and T.L. Kunii, *Theoret. Chim. Acta (Berl.)* **19**, 167 (1970).
40. A. Tramer, V. Brenner, P. Millie, and F. Piuzzi, *J. Phys. Chem. A* **102**, 2798 (1998).
41. M.J. Frisch, G.W. Trucks, H.B. Schlegel, G.E. Scuseria, M.A. Robb, J.R. Cheeseman, V.G. Zakrzewski, J.A. Montgomery, Jr., R.E. Stratmann, J.C.

Burant, S. Dapprich, J.M. Millam, A.D. Daniels, K.N. Kudin, M.C. Strain, O. Farkas, J. Tomasi, V. Barone, M. Cossi, R. Cammi, B. Mennucci, C. Pomelli, C. Adamo, S. Clifford, J. Ochterski, G.A. Petersson, P.Y. Ayala, Q. Cui, K. Morokuma, D.K. Malick, A.D. Rabuck, K. Raghavachari, J.B. Foresman, J. Cioslowski, J.V. Ortiz, A.G. Baboul, B.B. Stefanov, G. Liu, A. Liashenko, P. Piskorz, I. Komaromi, R. Gomperts, R.L. Martin, D.J. Fox, T. Keith, M.A. Al-Laham, C.Y. Peng, A. Nanayakkara, C. Gonzalez, M. Challacombe, P.M.W. Gill, B. Johnson, W. Chen, M.W. Wong, J.L. Andres, C. Gonzalez, M. Head-Gordon, E.S. Replogle, J.A. Pople, *Gaussian 98,* Revision A.7, Gaussian, Inc., Pittsburgh (1998).

42. N. Ohta, H. Baba, and G. Marconi, *Chem. Phys. Lett.* **133**, 222 (1987).
43. G. Marconi and P.R. Salvi, *Chem. Phys. Lett.* **123**, 254 (1986).
44. R.S. Becker, I.S. Singh, and E.A. Jackson, *J. Chem. Phys.* **38**, 2144 (1963).
45. Y. Bito, N. Shida, and T. Toru, *Chem. Phys. Lett.* **328**, 310 (2000).
46. N.A. Borisevich, L.B. Vodovatov, G.G. D'yachenko, V.A. Petukhov, and M.A. Semyonov, *J. Appl. Spectrosc.* **62**, 482 (1995).
47. A. Gilbert and J. Baggott, *Essentials of Molecular Photochemistry*, CRC Press, Boston, pg. 128 (1991).
48. L.D. Landau and E.M. Lifshitz, *Quantum Mechanics: Non-Relativistic Theory (2nd ed.)*, J.B. Sykes and J.S. Bell, trans., Pergamon Press, New York, pp. 322-331 (1965).
49. J.I. Steinfeld, J.S. Francisco, and W.L. Hase, *Chemical Kinetics and Dynamics*, Prentice Hall, Englewood Cliffs, pp. 237-245 (1989).
50. R. Badley, *Fluorescence Spectroscopy*, Plenum Press, New York (1983).
51. J. Lakowicz, *Principles of Fluorescence Spectroscopy*, Plenum Press, New York (1983).
52. M.L. Lee, M.V. Novotny, and K.D. Bartle, *Analytical Chemistry of Polycyclic Aromatic Compounds,* Academic Press, New York (1981).
53. T. Vo-Dinh, *Chemical Analysis of Polycyclic Aromatic Compounds*, John Wiley and Sons, New York (1989).
54. J.V. Goodpaster and V.L. McGuffin, *Appl. Spectrosc.* **53**, 1000 (1999).

CHAPTER 4

IMPROVING THE DETERMINATION OF STERN–VOLMER QUENCHING CONSTANTS

I. Introduction

To date, the development of quenching as a tool for chemical analysis has been relatively limited. This is partly due to the methods for determining Stern–Volmer constants, which remain both time and labor intensive. In a typical study, a series of solutions with constant fluorophore concentration and varying quencher concentration is prepared and the attenuation of the fluorescence power (or lifetime) at a single wavelength is measured. While this technique is effective, it is also slow, tedious, and prone to experimental error. Hence, such an approach is not well-suited for the evaluation of large numbers of fluorophores and quenchers.

Recently, some novel approaches to quenching experiments have been proposed. For example, Desilets and coworkers used a gradient pump from a liquid chromatograph to linearly increase the concentration of quencher in a flowing stream of a fluorophore, measuring the decrease in fluorescence power at a single wavelength.[1] This method required little solution preparation, allowed for greater precision in solution concentrations, acquired a large number of fluorescence power ratios in each quenching experiment, and increased the overall speed of the quenching measurements. However, this method was limited to the analysis of one fluorophore–quencher pair at a single wavelength, and only acquired one fluorescence power ratio at each quencher concentration. Moreover, it was reliant on the precision of the linear gradient program to calculate the quencher concentration and did not make corrections for absorbance effects.

A different approach was taken by Chen and coworkers, who measured quenching constants using a laser for excitation in a capillary flow cell.[2] The short path length of the capillary minimized absorption by the quencher at both the excitation and emission wavelengths. However, this system required pre-mixed solutions of the fluorophore and quencher and was also limited to a single wavelength. A final approach for determining the quenching constants of a number of fluorophores involved separating a complex mixture using capillary liquid chromatography with laser-induced fluorescence detection.[2,3] The observed peak heights both with and without quencher dissolved in the mobile phase were used to calculate conditional quenching constants at the detected wavelength. While this approach obviated the need for purifying the fluorophores as well as allowed for the analysis of complex samples, it required the use of lengthy chromatographic separations. Furthermore, it was limited to a single wavelength for all fluorophores, and only one fluorescence power ratio was used to calculate each quenching constant.[2,3]

In the present study, novel instrumentation for evaluating Stern–Volmer constants has been developed which combines the advances of previous studies while overcoming many of their limitations. In this system, solution preparation is automated through the use of flow injection techniques. This allows the measurement of quenching constants for many fluorophores in a single experiment with precise control over the quencher concentration. Moreover, a large number of replicate measurements can be made at each quencher concentration, leading to greater accuracy and precision. A capillary flow cell is used to eliminate absorbance effects and a charge-coupled device (CCD) detector allows for the calculation of Stern–Volmer constants based on either single wavelengths or integrated emission spectra. The performance of this system is evaluated and the accuracy and precision are compared with traditional methods for the determination of Stern–Volmer constants.

II. Methods

A. Reagents

Quinine sulfate (Baker) is used as received. Stock solutions of quinine sulfate are prepared in 0.05 M H_2SO_4 in deionized distilled water (Corning Glass Works, Model MP-3A). Pyrene (MCB), fluoranthene (Aldrich), benzo(*a*)pyrene (Aldrich) and benzo(*b*)fluoranthene (Aldrich) are purified by vacuum sublimation. Reagent-grade nitromethane (EM Science) and triethylamine (Spectrum) are used as received. Stock solutions of the polycyclic aromatic hydrocarbons and quenchers are prepared in high purity, spectroscopic-grade methanol (Baxter Healthcare, Burdick and Jackson Division).

B. Flow Injection System

In order to allow for the rapid evaluation of quenching constants, a flow injection apparatus that combines solutions of fluorophores and quenchers has been developed (Figure 4-1). The apparatus consists of a dual syringe pump (Brownlee Labs, Model G) that is programmed to deliver a step gradient of the quencher in a suitable solvent at a flow rate of 35 μL/min. A second syringe pump (Applied Biosystems, Model 140) delivers the solvent at 35 μL/min to an injector with a 75 μL loop (Valco Instruments, Model EC6W), which is used to introduce discrete zones of the fluorophore. The solutions of the quencher and fluorophore are combined with a mixing tee (Upchurch Scientific, Model P-727) in fused-silica capillary tubing (200 μm i.d., 375 μm o.d., Polymicro Technologies). After mixing, the fluorophore–quencher solution is directed to a fluorescence detector (see below) followed by a UV–visible absorbance detector (Jasco, Model UVIDEC-100-V).

C. Fluorescence System

A ray tracing program (Stellar Software, BEAM4 Optical Ray Tracer) has been used to aid in the design and optimization of the spectroscopic system. In this system, a helium–cadmium laser (Melles Griot, Model 3074-40M, 325 nm, 40 mW) is utilized as the excitation source and all optics are enclosed within an aluminum housing to minimize light leaks and other sources of stray light. The flow cell is constructed of fused-silica capillary tubing (75 – 200 μm i.d., 375 μm o.d., Polymicro Technologies). Fluorescence emission is collected and

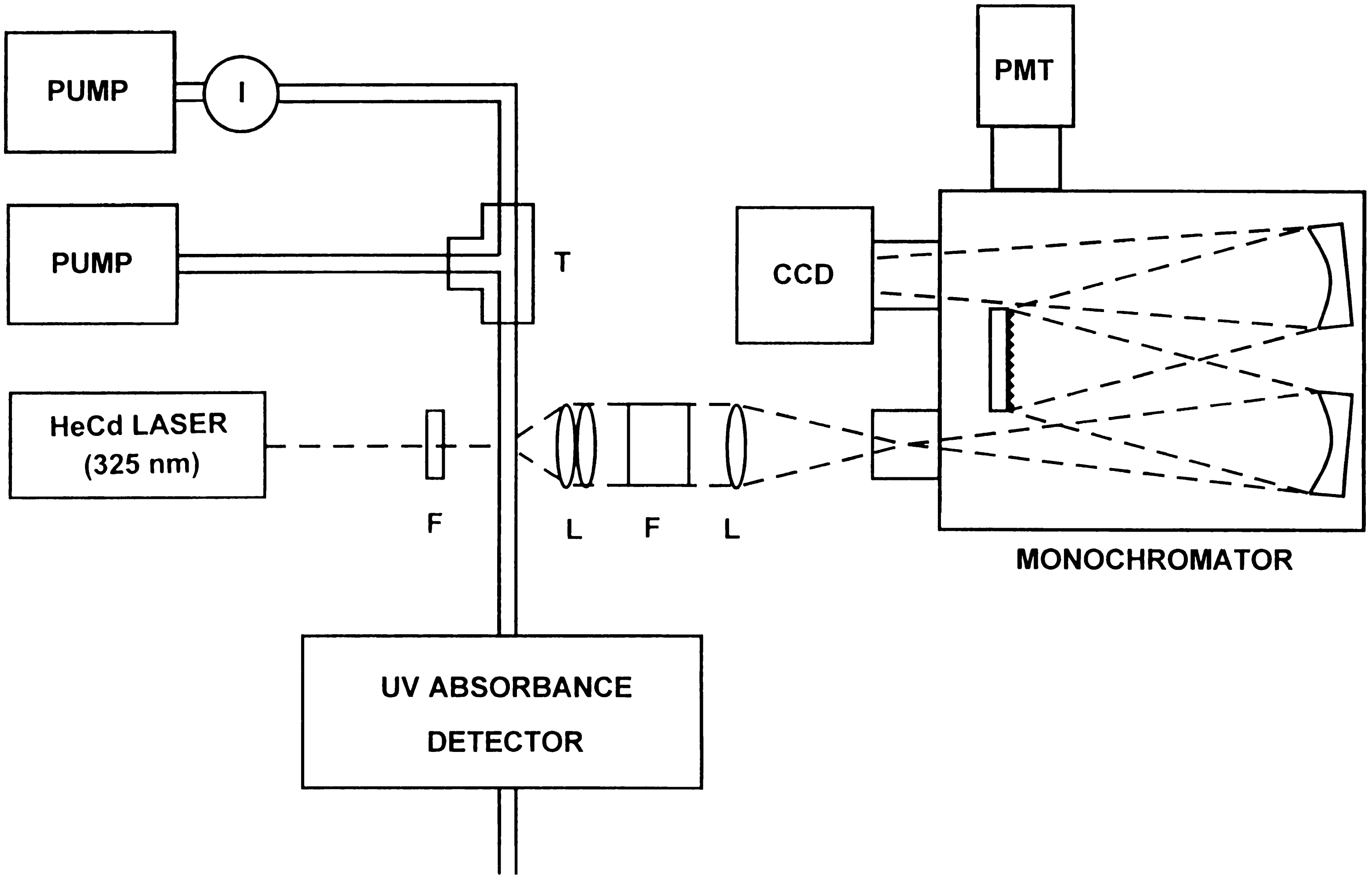

Figure 4-1: Schematic diagram of the instrumentation for fluorescence quenching studies. I = injection valve, T = mixing tee, F = filter, L = lens, CCD = charge-coupled device, PMT = photomultiplier tube.

collimated by using either two F/2 fused-silica lenses (Melles Griot, Model 01 LQP 001/066) or a single F/1 concave mirror (Oriel, Model 44351). Scattered light originating from the laser is attenuated by passing the collimated emission through either a long-pass glass filter (Andover Corporation, Model ANDV4922) or a liquid filter consisting of an aqueous solution of 2 M KNO_3 contained in a 1-cm cylindrical fused-silica cell (Perfector Scientific). The filtered emission is refocused with an F/6 fused-silica lens (Melles Griot, Model 01 LQP 013/066) onto the entrance slit of a 0.34 m Czerny–Turner monochromator (Instruments SA, Model 340E, 300 groove/mm grating), which is equipped with a photomultiplier tube (PMT) (Hamamatsu, Model R-106) and a charge-coupled device (CCD) detector (Instruments SA, Model (A)TECCD-2000x800-7). The CCD detector is thermoelectrically cooled and is maintained at a temperature of –40 °C. Instrument control and data acquisition are provided by commercially available electronic interfaces (Instruments SA, Model DS1010 and Model CCD 2000) and the associated software (Instruments SA, Spectramax for Windows, Version 2.76).

For purposes of validation and performance evaluation, the system described above is compared with a commercially available scanning fluorimeter (Hitachi, Model F-4500) with a 1-cm cuvette cell. This fluorimeter contains a 150 W xenon lamp, excitation and emission monochromators (900 groove/mm grating, 2.5 nm bandpass), and a PMT detector, which is operated at 700 V.

D. Calculations

For the characterization studies, the fluorescence spectra of quinine sulfate are integrated from 370 – 540 nm and the integrated power is plotted *versus* the variable of interest. For calculations of the signal-to-noise (S/N) ratio, the signal is defined as the height of the quinine sulfate emission spectrum at its wavelength of maximum intensity (450 nm). The noise is calculated by first smoothing the spectrum using a Savitsky–Golay routine[4] with a second-order polynomial and 213/n points, where n is the number of pixels that are horizontally binned on the CCD chip. The smoothed spectrum is then subtracted from the original spectrum and the standard deviation of the remaining noise from 445 – 455 nm is calculated. The logarithm of the calculated S/N ratio is then plotted *versus* the logarithm of the signal.

Stern–Volmer plots are prepared by calculating the fluorescence power at a single wavelength or an integrated range of wavelengths as a function of the quencher concentration. The wavelength range for each fluorophore is as follows: pyrene (350 – 500 nm), fluoranthene (380 – 560 nm), benzo(*a*)pyrene (370 – 510 nm), and benzo(*b*)fluoranthene (373 – 560 nm). The ratio of the fluorescence power in the absence and presence of quencher is then graphed as a function of the quencher concentration. The slope of this graph is determined by linear regression in order to obtain the Stern–Volmer constant.

III. Results and Discussion

A. Fluorescence System Characterization

Ray tracing simulations have been used to evaluate the performance of various configurations of the optical components. These studies have identified a number of factors as important to our optical design. For example, simulations demonstrate that a properly oriented plano-convex lens yields higher throughput than a biconvex lens. Moreover, two F/2 objective lenses in series provide sharper focus than a single F/1 collimating lens. Finally, a concave condenser mirror decreases spherical and chromatic aberrations as well as increases the overall throughput relative to the lens systems.

These simulation results provided the impetus for experimental studies of the optical components and how they affect the system performance. Figures 4-2A and 4-2B show the contrasting performance of four different configurations of the collection optics using a 3.0×10^{-7} M solution of quinine sulfate as a means of comparison. These data indicate that using a concave mirror as the condensing objective with a glass filter to remove laser scatter results in the poorest performance. Although overall throughput is high, as predicted by the ray tracing simulations, the resulting S/N ratio is lower than that for the other optical configurations. In addition, the longest attainable integration time is lower than for the other configurations. This integration time is ultimately limited by the dark charge from the CCD as well as by background from laser scatter and other

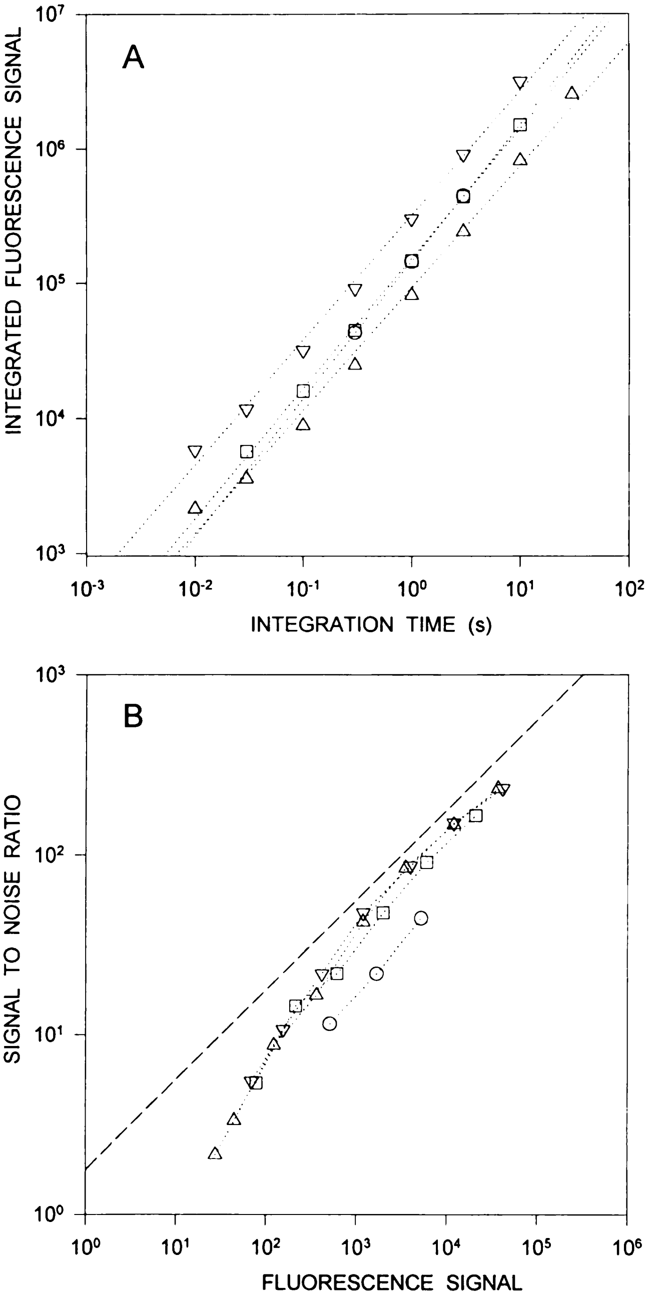

Figure 4-2: Effect of optical configuration on the signal (A) and S/N ratio (B) of a 3.0 x 10^{-7} M solution of quinine sulfate at various integration times. Data correspond to the following optical configurations: concave mirror, glass filter, and capillary cell (○), two plano-convex lenses, glass filter, and capillary cell (□), two plano-convex lenses, liquid filter, and capillary cell (△), and two plano-convex lenses, liquid filter, and capillary cell contained in refractive-index matching fluid (▽). The dashed line in (B) represents optimum theoretical performance under shot-noise limited conditions (slope = 0.5).

stray light, which is highest for this optical configuration. Using two plano-convex lenses as the condensing objective with a glass filter yields similar throughput but higher S/N ratio. Performance is further enhanced by replacing the glass filter with a liquid filter composed of aqueous 2 M KNO_3. When using this filter, the S/N ratio is higher than other optical configurations for any given signal level and the longest attainable integration time is increased as a result of the lower background. However, because of the smaller aperture of the liquid filter, longer integration times are necessary to achieve the same signal levels as the glass filter. Finally, it has been reported[5] that scattered laser light can be effectively reduced by immersing the fused-silica capillary cell in a refractive-index matching fluid, such as carbon tetrachloride. In the present study, however, there is no significant improvement in S/N ratio because of the larger fluorescence background originating from the cell and fluid.

Using the best optical configuration determined from these studies, additional methods of S/N enhancement have been explored such as varying the laser power, entrance slit width, electronic binning of the CCD pixels, and integration time. In the first study, the power of the helium–cadmium laser has been varied from 0.40 – 35 mW (Figure 4-3). The fluorescence of a standard solution of quinine sulfate increases linearly with laser power, where the square of the correlation coefficient (r^2) is 0.999 and the number of measurements (n) is 11. A logarithmic graph of the S/N ratio *versus* signal is linear ($r^2 = 0.982$, n = 11) with a slope (m) of 0.54 ± 0.02. Next, the entrance slit width of the

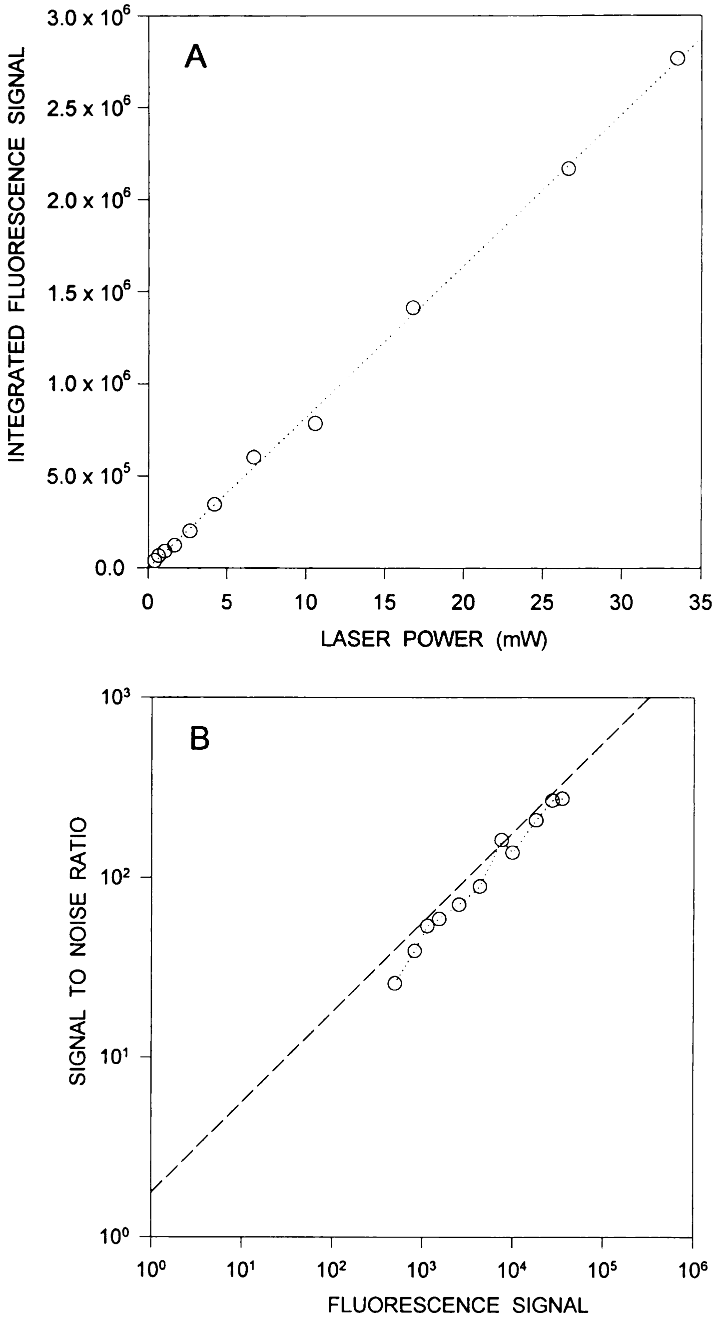

Figure 4-3: Effect of laser power on the signal (A) and S/N (B) of a 2.2 x 10^{-3} M solution of quinine sulfate. Other experimental conditions as described in Figure 4-2.

monochromator has been varied from 100 – 1000 μm, corresponding to a spectral bandpass of 1 – 10 nm (Figure 4-4). The fluorescence of quinine sulfate increases linearly with slit width ($r^2 = 0.997$, $n = 6$) and the logarithmic graph of the S/N ratio *versus* signal is also linear ($m = 0.42 \pm 0.05$, $r^2 = 0.937$, $n = 6$). Next, the CCD pixels have been horizontally binned in groups ranging from 1 – 10, corresponding to a spectral bandpass of 0.15 – 1.5 nm (Figure 4-5). The fluorescence of quinine sulfate increases linearly with the extent of binning ($r^2 = 1.000$, $n = 6$) and the logarithmic graph of the S/N ratio *versus* signal is also linear ($m = 0.60 \pm 0.07$, $r^2 = 0.948$, $n = 6$). Finally, the integration time has been varied from 0.01 – 30 s (Figure 4-6). The fluorescence of quinine sulfate increases linearly with integration time ($r^2 = 1.000$, $n = 6$) and the logarithmic graph of the S/N ratio *versus* signal is also linear ($m = 0.59 \pm 0.03$, $r^2 = 0.988$, $n = 6$). For each of these variables, the slope of the logarithmic graphs indicates that the noise is proportional to the square root of the fluorescence signal. This behavior is characteristic of the quantized nature of fluorescence emission, and implies that the spectroscopic system is quantum or shot noise limited.[6-8] Although any of these variables can be used to enhance the S/N ratio in a similar manner, they may have other detrimental effects on the system performance. For example, an increase in these variables will increase the background, thereby decreasing the available dynamic range of the analog-to-digital (A/D) converter and the resulting linear range of the fluorescence measurements and Stern–Volmer plots. Furthermore, an increase in either slit width or the extent of binning will decrease the spectral resolution and an increase in laser power may

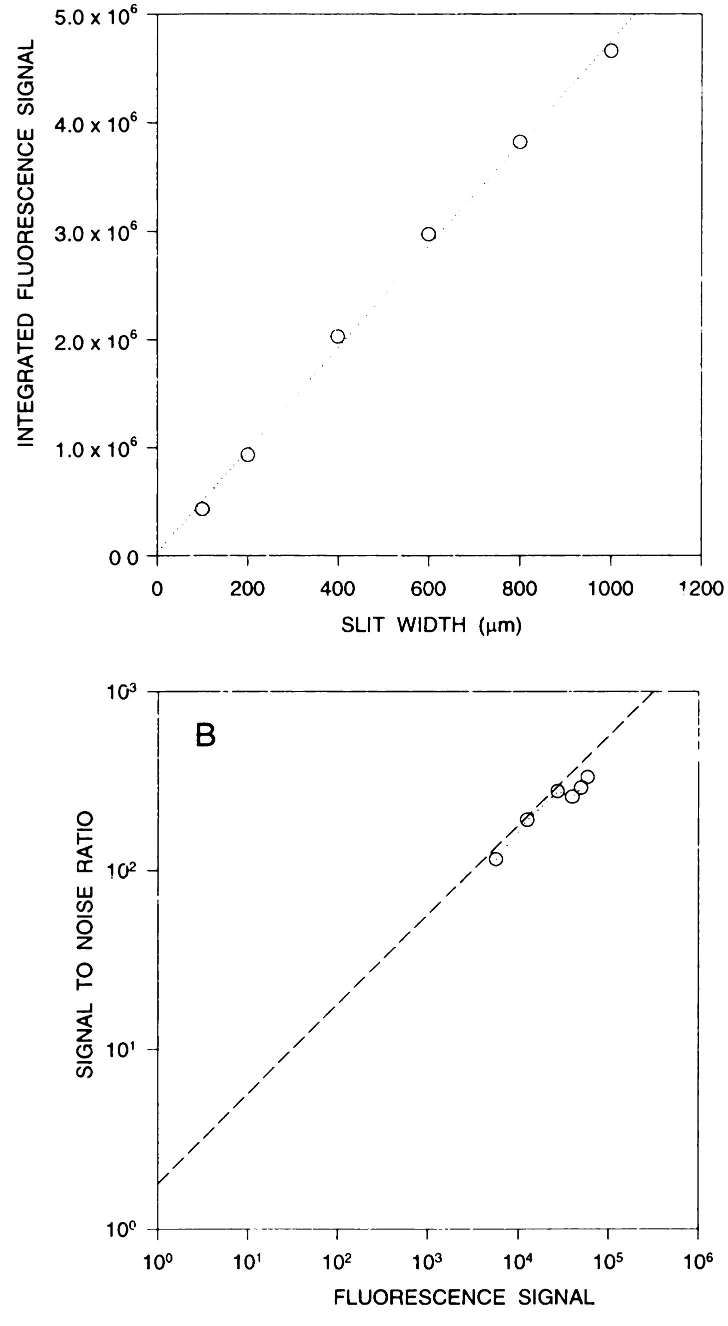

Figure 4-4: Effect of slit width on the signal (A) and S/N (B) of a 3.0 x 10^{-7} M solution of quinine sulfate. Reciprocal linear dispersion: 100 μm/nm. Other experimental conditions as described in Figure 4-2.

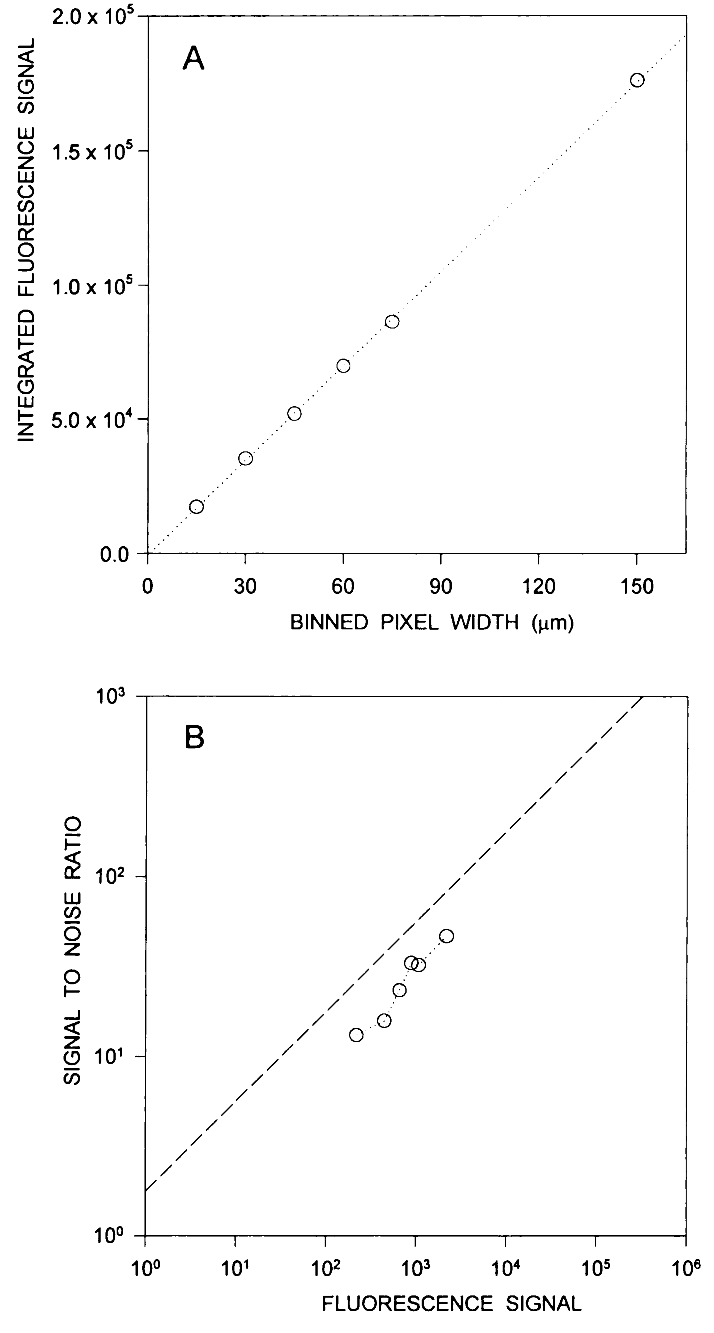

Figure 4-5: Effect of horizontal binning on the signal (A) and S/N (B) of a 2.2 x 10^{-5} M solution of quinine sulfate. Reciprocal linear dispersion: 100 μm/nm. Other experimental conditions as described in Figure 4-2.

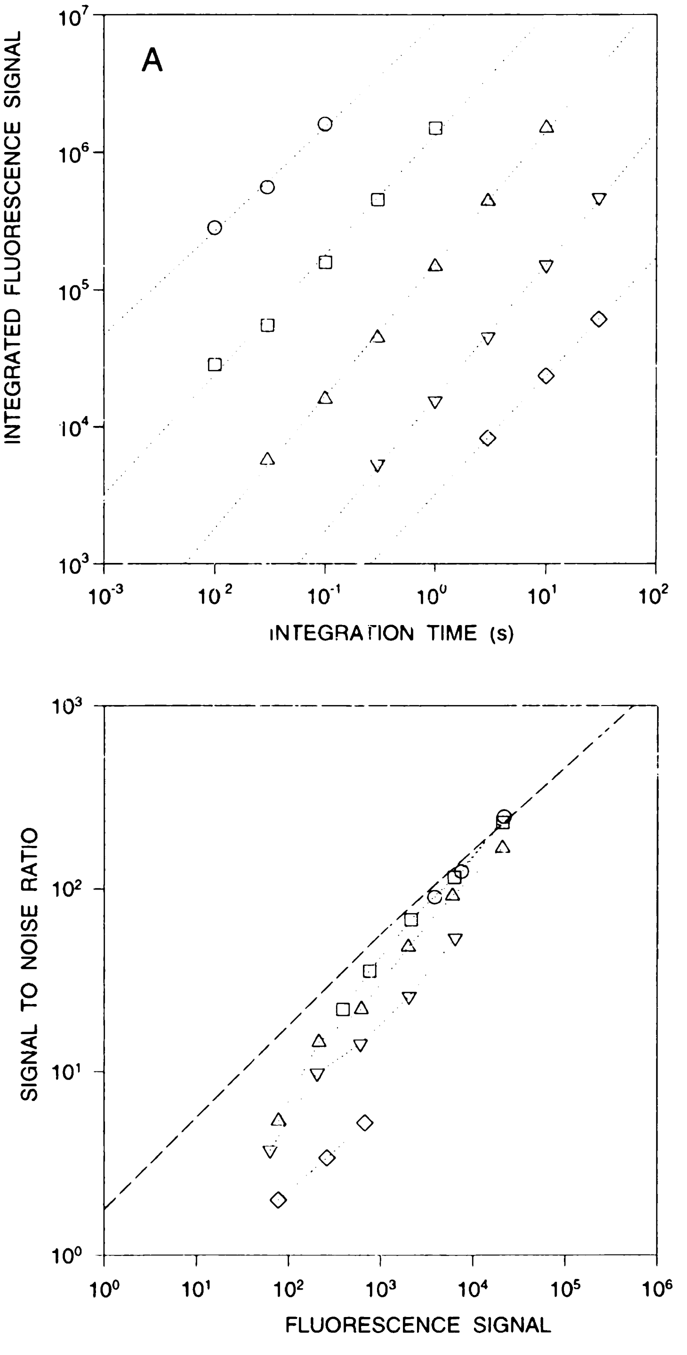

Figure 4-6: Effect of integration time on the signal (A) and S/N (B) of 3.0 x 10^{-9} M (◇), 3.0 x 10^{-8} M (▽), 3.0 x 10^{-7} M (△), 3.0 x 10^{-6} M (□), and 3.0 x 10^{-5} M (○) solutions of quinine sulfate. Other experimental conditions as described in Figure 4-2.

cause photochemical reaction or degradation.[9] The most simple and least detrimental approach to increase the S/N ratio is by means of the integration time, although problems can arise at long integration times (*see below*).

The performance of the fluorescence spectrometer has been characterized by means of the calibration curves for quinine sulfate shown in Figure 4-7A. Overall, the linearity of the calibration curves is quite good (r^2 = 0.994 – 1.000, n = 3 – 6). Deviations from linearity near the limit of detection arise from blank noise in the signal, which contributes a larger proportion of the integrated fluorescence power at low concentrations of quinine sulfate. With an integration time of 10 s, the detection limit for quinine sulfate is 3.0×10^{-9} M (2.3 ppb) at a S/N ratio of 3.4 (n = 3).[6] At high concentrations, there is no curvature or other evidence of absorbance effects because of the short path length of the capillary flow cell. Hence, the limit of linearity is determined solely by the shortest integration time of the CCD detector (0.01 s). At this integration time, the highest concentration that does not exceed the dynamic range of the A/D converter (2^{16}) is 3.0×10^{-4} M (230 ppm). Thus, the linear range of the calibration curves for quinine sulfate is 1.0×10^5.

The effect of quinine sulfate concentration on the S/N ratio is shown in Figure 4-7B. This logarithmic graph shows two distinct regions of behavior. The first occurs at signal levels above 10^3 counts, where the slopes range from m = 0.50 – 0.80 (r^2 = 0.993 – 1.000, n = 2 – 3) and generally increase with integration time. This slope implies that the noise is proportional to the square root of the signal and that the system is exhibiting shot-noise limited behavior, as described

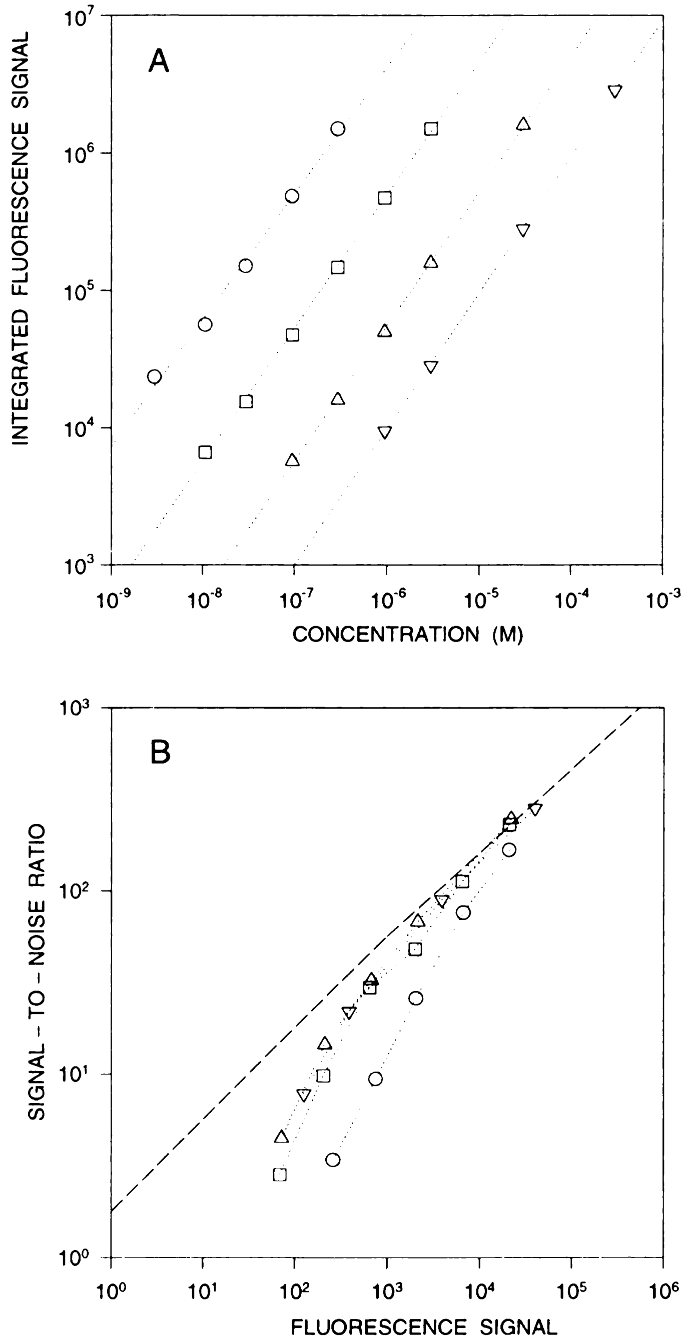

Figure 4-7: Effect of quinine sulfate concentration on the signal (A) and S/N ratio (B) using integration times of 0.01 s (▽), 0.1 s (△), 1 s (□), and 10 s (○). Other experimental conditions as described in Figure 4-2.

above. At lower signal levels, however, the S/N ratio becomes linearly dependent on the signal, with slopes ranging from m = 0.88 – 1.05 (r^2 = 0.981 – 1.000, n = 2 – 3). This implies that the noise is independent of the signal and that the system is exhibiting blank-noise limited behavior. Additional studies have indicated that this noise is predominantly due to dark and read noise of the CCD, with a smaller component due to fluctuations in the background arising from laser scatter and other stray light. The dark current is largely independent of integration time up to 1 s (e.g. 1303 ± 14 counts), but increases significantly thereafter. Thus, the region with blank-noise limited behavior appears at higher signal levels with increasing integration time in Figure 4-7B.

Overall, these studies have indicated that optimum performance of the system can be achieved by first reducing the background to its fundamental limit. This limit is determined by the dark and read noise of the CCD.[10] Once this has been achieved, the integration time can then be adjusted to control the signal level and maximize the S/N ratio. Ideally, the signal level should be near the upper limit of the dynamic range of the A/D converter so that the subsequent fluorescence quenching measurements will have the largest possible linear range.

B. Quenching Studies

The ability of the fluorescence system to measure quenching constants accurately has been assessed by using two well-known and well-characterized quenchers: nitromethane and triethylamine. Both of these compounds are known to be effective quenchers of alternant and nonalternant polycyclic aromatic hydrocarbons (PAHs), respectively.[11,12]

Two representative pairs of PAHs have been selected for this study: pyrene and fluoranthene, as well as benzo(*a*)pyrene and benzo(*b*)fluoranthene. These isomeric PAHs have the same molecular formula, the same number of aromatic rings, a similar length-to-breadth ratio, and differ only in their alternant/nonalternant ring structure. Figures 4-8A and 4-8B show the Stern–Volmer plots for these representative PAHs with triethylamine and nitromethane, respectively, as quenchers. These plots are constructed from fluorescence power ratios derived from the integrated emission spectra, as described previously. Both quenchers are demonstrating the expected selectivity for PAH isomers, with nitromethane being a more effective quencher of the alternant PAHs and triethylamine being a more effective quencher of the nonalternant PAHs. The linearity of the Stern–Volmer plots is best for those fluorophore–quencher systems with large quenching constants, where the correlation coefficients range from $r^2 = 0.998 - 1.000$. Determination of smaller quenching constants is necessarily more difficult as the smaller differences in the fluorescence power ratio are more sensitive to random errors in concentration and instrumental response.[3] As a result, these quenching constants have lower correlation coefficients of $r^2 = 0.889 - 0.995$. The y-intercepts for all plots fall within the range of 0.98 – 1.09, as expected from the Stern–Volmer equation. Finally, there is no evidence of curvature in the plots, which would be indicative of either absorbance effects or static quenching.

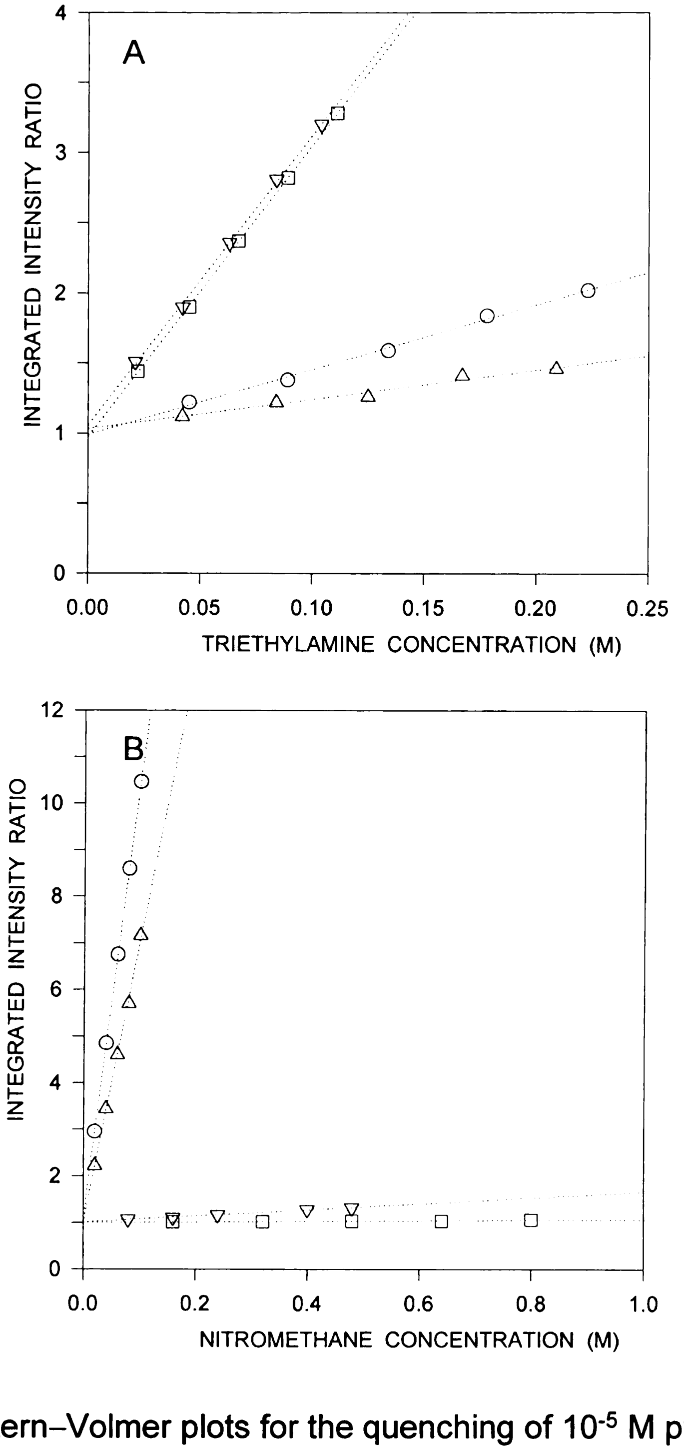

Figure 4-8: Stern–Volmer plots for the quenching of 10^{-5} M pyrene (○), fluoranthene (□), benzo(*a*)pyrene (△), and benzo(*b*)fluoranthene (▽) by triethylamine (A) and nitromethane (B) in methanol.

Table 4-1 compares the quenching constants for the PAHs with triethylamine determined from Figure 4-8A with those obtained by using a commercially available scanning fluorimeter with a 1-cm cuvette cell. The agreement is quite good and, in general, the Stern–Volmer constants determined by using the two systems are statistically indistinguishable. The small discrepancies may arise from differences in the spectral bandpass, which is 1 nm for the present system and 2.5 nm for the conventional fluorimeter. The linearity of the Stern–Volmer plots for the present system is at least comparable to and, in some cases, superior to that for the conventional fluorimeter with absorbance corrections. Table 4-2 compares the quenching constants for the PAHs with nitromethane determined from Figure 4-8B with previously published results.[2,3] Again, the agreement is reasonably good in spite of significant differences in instrumentation and experimental methods. Thus, the performance of the present system has been validated by comparison to traditional methods using premixed solutions for the determination of Stern–Volmer quenching constants.

C. Flow Injection Approach

A powerful modification of this system is to use flow injection techniques[13] to automate the measurement of quenching constants, as shown in Figure 4-1. This approach facilitates the rapid determination of quenching constants with minimal solution preparation, requiring only one solution of the fluorophore and one of the quencher. A dual-piston syringe pump is used to deliver the quencher

Table 4-1: Stern–Volmer Constants for Polycyclic Aromatic Hydrocarbons with Triethylamine in Methanol[a]

PAH	Classification	K_d (M^{-1})[b]	$s(K_d)$ (M^{-1})	R^2	K_d (M^{-1})[c]	$s(K_d)$ (M^{-1})	R^2
pyrene	alternant	4.4	0.3	0.986	4.6	0.2	0.996
benzo(*a*)pyrene	alternant	1.8	0.2	0.967	2.1	0.2	0.974
fluoranthene	non-alternant	23.0	0.6	0.998	20.7	0.1	1.000
benzo(*b*)fluoranthene	non-alternant	21.7	0.3	0.999	20.6	0.4	0.999

[a] K_d = Stern–Volmer constant; $s(K_d)$ = standard deviation of Stern–Volmer constant; R^2 = square of correlation coefficient

[b] Use of a 1 cm cuvette cell; this work

[c] Use of a 75 μm capillary flow cell; this work

Table 4-2: Stern–Volmer Constants for Polycyclic Aromatic Hydrocarbons with Nitromethane in Methanol[a]

Fluorophore	**Classification**	**K_d (M^{-1})[b]**	**K_d (M^{-1})[c]**	**R^{2c}**	**K_d (M^{-1})[d]**	**$s(K_d)$ (M^{-1})[d]**	**R^{2d}**
pyrene	alternant	125	100	0.999	94	0.3	1.000
benzo(*a*)pyrene	alternant	-	67	0.998	61	1.6	0.998
fluoranthene	non-alternant	0.15	1	0.954	0.07	0.01	0.900
benzo(*b*)fluoranthene	non-alternant	-	2	0.994	0.64	0.02	0.997

[a] K_d = Stern–Volmer constant; $s(K_d)$ = standard deviation of Stern–Volmer constant; R^2 = square of correlation coefficient

[b] Use of a 1 cm cuvette cell, absorbance corrected (Ref. 2)

[c] Use of a 1 cm cuvette cell, absorbance corrected (Ref. 3)

[d] Use of a 75 μm capillary flow cell; this work

solution in a step gradient, which offers several advantages over the linear gradient used in previous work.[1] Each step is programmed for a specified duration, which allows for replicate injections of a single fluorophore or injections of several fluorophores. The concentration of the quencher is accurately known and does not vary over the width of the fluorophore zone. The fluorophore zones are injected in sufficiently large volume that they form flat-topped peaks. In this way, the concentration at the zone center is the same as that in the prepared solution and is not dependent on the broadening processes in the flow injection system. Hence, the resulting precision of the quenching constants is independent of fluctuations in flow rate, injection volume, etc. Moreover, the flat-topped profile enables the integration time of the CCD detector to be varied as necessary to achieve the optimal S/N ratio and linear range. Finally, the method of merging zones is used in order to ensure adequate mixing of the fluorophore and quencher solutions.[13]

An example of the data resulting from this flow injection approach is illustrated in Figure 4-9 for pyrene quenched by nitromethane. The lower trace from the UV-visible absorbance detector at 254 nm shows the step gradient of the quencher ranging in concentration from 0 to 0.05 M in increments of 0.01 M, together with triplicate injections of the fluorophore at each step. This absorbance trace provides independent verification of the fluorophore and quencher concentrations and their precisions as well as evidence for or against static complexation. The middle trace shows the fluorescence of pyrene with

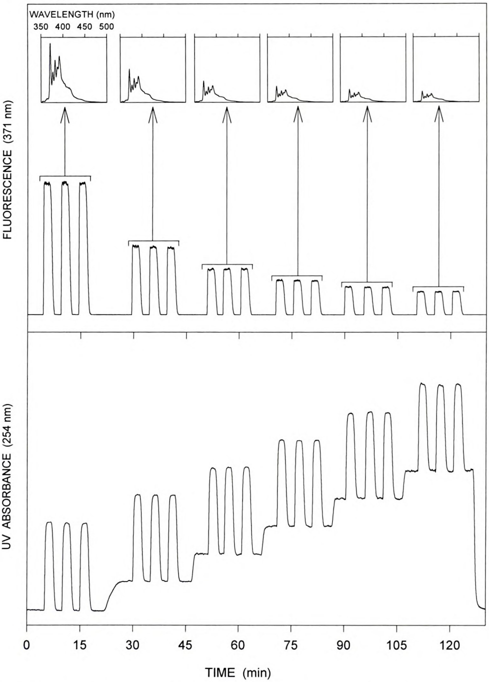

Figure 4-9: Experimental data obtained by using the flow injection approach to determine Stern–Volmer constants. Fluorophore: 75 μL injections of 10^{-5} M pyrene in methanol, 35 μL/min. Quencher: 0 - 0.05 M nitromethane in increments of 0.01 M per 20 min step, 35 μL/min. Lower trace shows UV absorbance at 254 nm. Middle trace shows fluorescence detected by PMT at 371 nm, 1 nm bandpass. Upper traces show fluorescence spectra detected by CCD detector at 350 - 500 nm, 1 nm bandpass, 0.2 s integration time.

excitation at 325 nm and emission detected by the PMT detector at 371 nm. The decrease in fluorescence power with increasing nitromethane concentration is evident, and provides the information necessary for the determination of the Stern–Volmer quenching constant and its precision at a single wavelength. Finally, the upper traces show the fluorescence spectra of pyrene obtained with the CCD detector, which are used to determine the quenching constant and its precision at a single wavelength (371 nm) or over an integrated range of wavelengths (350 – 500 nm).

Table 4-3 summarizes the quenching constants determined from this flow injection experiment as well as a comparison to the static system with premixed solutions, as described above. These results confirm that quenching constants determined by flow injection are statistically equivalent to those determined by static measurements, both of which show a high degree of linearity (r^2 = 0.999 – 1.000). In addition, the quenching constants obtained with the PMT detector are comparable in magnitude but higher in precision than those obtained with the CCD detector at the same wavelength. By increasing the number of measurements (n) at each quencher concentration from 5 to 50, the magnitude of the resulting quenching constants remains relatively constant and the precision is improved. However, the PMT detector shows a more significant improvement in precision than the CCD detector, which is limited by dark and read noise. Finally, the quenching constants calculated at a single wavelength of 371 nm tend to be larger in magnitude than those calculated over an integrated wavelength range of 350 – 500 nm. This observation suggests that

Table 4-3: Comparison of Experimental Methods for the Determination of Stern–Volmer Constants for Pyrene in Methanol[a]

Method	Pathlength (μm)	Detector	Wavelength (nm)	K_d (M^{-1})	s(K_d) (M^{-1})	b	R^2	n
static	75	CCD	371	103.0	0.99	1.02	1.000	5
static	75	CCD	350 - 500	93.8	0.33	1.09	1.000	5
flow injection	200	PMT	371	96.1	0.35	0.99	1.000	5
flow injection	200	PMT	371	95.5	0.13	1.00	1.000	50
flow injection	200	CCD	371	96	1.4	0.89	0.999	5
flow injection	200	CCD	350 - 500	91	1.7	0.92	0.999	5
flow injection	200	CCD	371	97	1.1	0.90	1.000	50
flow injection	200	CCD	350 - 500	92	1.3	0.93	0.999	50

[a] K_d = Stern–Volmer constant; s(K_d) = standard deviation of Stern–Volmer constant; b = y-intercept; R^2 = square of correlation coefficient; n = number of measurements at each quencher concentration

this vibronic transition of pyrene interacts differently with nitromethane when compared to the integrated emission spectrum. This is consistent with previous measurements of the quenching of pyrene by nitromethane at a series of single wavelengths.[3] In cases such as this, the integrated spectra can provide more reproducible and reliable quenching constants. This approach is also beneficial for fluorophores with emission spectra that are highly structured or that vary with the concentration of the quencher or solvent.[2,3]

IV. Conclusions

Although selective fluorescence quenching is a promising technique, only a few fluorophore–quencher systems have been characterized in sufficient depth and detail to permit their use for routine analysis. The further development and application of this technique will require more rapid and accurate methods for the determination of Stern–Volmer constants. The system developed in the present work automates the preparation and mixing of fluorophore and quencher solutions by means of capillary flow injection methods. The small diameter of the capillary allows the fluorescence measurements to be made without interference from primary and secondary absorbance effects. The fluorescence spectrometer is equipped with a charge-coupled device that has a detection limit of 3.0×10^{-9} M (2.3 ppb) and a linear range of 10^{5} with integration times of 0.01 – 10 s. This spectrometer has a 300 nm spectral range with 1 nm resolution, which allows the Stern–Volmer constants to be calculated at single wavelengths or over integrated wavelength ranges. This system was validated by determination of the quenching constants for selected alternant and nonalternant PAHs as fluorophores with nitromethane and triethylamine as quenchers. These quenching constants compare favorably with those determined by traditional methods in terms of both accuracy and precision.

V. References

1. D.J. Desilets, P.T. Kissinger, and F.E. Lytle, *Anal. Chem.* **59**, 1244 (1987).
2. S.H. Chen, C.E. Evans, and V.L. McGuffin, *Anal. Chim. Acta* **246**, 65 (1991).
3. F.K. Ogasawara, Y. Wang, and V.L. McGuffin, *Appl. Spectrosc.* **49**, 1 (1995).
4. A. Savitsky and M.J.E. Golay, *Anal. Chem.* **36**, 1627 (1964).
5. X. Lu and E.S. Yeung, *Appl. Spectrosc.* **49**, 605 (1995).
6. J.J. Cetorelli, W.J. McCarthy, and J.D. Winefordner, *J. Chem. Educ.* **45**, 98 (1968).
7. C.Th.J. Alkemade, W. Snelleman, G.D. Boutilier, B.D. Pollard, J.D. Winefordner, T.L. Chester, and N. Omenetto, *Spectrochim. Acta* **33B**, 383 (1978).
8. G.D. Boutilier, B.D. Pollard, J.D. Winefordner, T.L. Chester, and N. Omenetto, *Spectrochim. Acta* **33B**, 401 (1978).
9. Y.P. Sun, B. Ma, G.E. Lawson, C.E. Bunker, and H.W. Rollins, *Anal. Chim. Acta* **319**, 379 (1996).
10. J.V. Sweedler, *Crit. Rev. Anal. Chem.* **24**, 59 (1993).
11. E. Sawicki, T.W. Stanley, and W.C. Elbert, *Talanta* **11**, 1433 (1964).
12. M.P. Fogarty and I.M. Warner, *Appl. Spectrosc.* **36**, 460 (1982).
13. J. Ruzicka and E.H. Hansen, *Flow Injection Analysis*, John Wiley and Sons, New York (1988).

CHAPTER 5

ALIPHATIC AMINES AS NOVEL SELECTIVE QUENCHERS OF NONALTERNANT POLYCYCLIC AROMATIC HYDROCARBONS

I. Introduction

To date, no highly selective quencher of nonalternant polycyclic aromatic hydrocarbons (PAHs) has been discovered that is equivalent to nitromethane for the alternant PAHs. Selective quenchers of nonalternant PAHs are likely to act as electron donors in the excited-state complex. Thus, the most promising functional groups to explore in novel selective quenchers are nitrile, amine, carbonyl, thionyl, etc. Furthermore, aromatic molecules tend to be more effective but less selective quenchers than the corresponding aliphatic molecules.[1] In view of these observations, we have initiated a systematic search for promising quenchers of nonalternant PAHs. In preliminary studies, we examined a series of aliphatic mono- and di-nitriles including acetonitrile, propionitrile, acrylonitrile, and succinonitrile. None of these quenchers had measurable quenching constants or exhibited useful selectivity for nonalternant PAHs.[2] In the present study, we have investigated a series of aliphatic mono- and di-amines. The quenching efficiency and selectivity of primary, secondary, and tertiary amines are reported for representative alternant and nonalternant PAHs in methanol and acetonitrile solvents. These amines are compared to previously known selective quenchers as well as an empirical model of excited-state electron-transfer reactions.

II. Methods

A. Reagents

Pyrene, fluoranthene, benzo(*a*)pyrene and benzo(*b*)fluoranthene (Aldrich) were purified by vacuum sublimation. Reagent-grade hexylamine, diisopropylamine, triethylamine, 1,6-diaminohexane, and 1,4-diazabicyclo(2.2.2)octane (Aldrich) were used as received. Stock solutions of the polycyclic aromatic hydrocarbons and quenchers were prepared in high purity, spectroscopic-grade acetonitrile and methanol (Baxter Healthcare, Burdick and Jackson Division).

Note that the quenchers studied here are intended for use in conventional spectroscopy and/or chromatography. As it is typically not possible to scrupulously remove oxygen in these cases, quenching efficiency and selectivity data should be acquired under analogous conditions. Therefore, no effort was made to remove dissolved oxygen from these solutions.

B. Determination of Quenching Constants

Steady-state fluorescence power measurements were made by using a laser-induced fluorescence spectrometer, which has been described in detail in Chapter 4 (see Figure 4-1).[3] The solutions containing the fluorophore and quencher were introduced using a gas displacement pump into a flow cell constructed of fused-silica capillary tubing (75 μm i.d., 360 μm o.d., Polymicro Technologies). The capillary had been treated with chlorotrimethylsilane (Aldrich) to prevent adsorption of the amines onto active silanol sites. A

helium–cadmium laser (Melles Griot, Model 3074-40M, 325 nm, 40 mW) was utilized as the excitation source. Fluorescence emission was collimated, filtered, and then focused onto the entrance slit of a 0.34 m Czerny–Turner monochromator (Instruments SA, Model 340E, 300 groove/mm grating). The monochromator was equipped with a charge-coupled device detector (Instruments SA, Model (A)TECCD-2000x800-7), which was thermoelectrically cooled to a temperature of –40 °C. Instrument control and data acquisition were provided by a commercially available electronic interface (Instruments SA, Model CCD 2000) and the associated software (Instruments SA, Spectramax for Windows, Version 2.76).

Stern–Volmer plots were prepared by calculating the fluorescence power over an integrated range of wavelengths for each PAH: pyrene (350 – 500 nm), fluoranthene (380 – 560 nm), benzo(*a*)pyrene (370 – 510 nm), and benzo(*b*)fluoranthene (373 – 560 nm). The ratio of the fluorescence power in the absence and presence of quencher was then graphed as a function of the quencher concentration (see equation 1-1). The slope of this graph was determined by linear regression in order to obtain the Stern–Volmer constant, with typical correlation coefficients (R^2) from 0.992 to 1.000.

C. Determination of Fluorescence Lifetimes

Fluorescence lifetimes were measured by using a time-correlated single photon counting spectrometer, which has been described in detail elsewhere.[4] In this system, the second harmonic of a continuous-wave mode-locked Nd:YAG laser (Quantronix, Model 416) was used to excite a cavity-dumped, synchronously pumped dye laser (Coherent, Model 702-2, 325 nm, 1 mW). Fluorescence emission was collected and focused on a subtractive double monochromator of Czerny–Turner design (American Holographic, Model DB10-S) with a 10 nm bandpass. The emission was detected with a cooled two-stage microchannel plate photomultiplier (Hamamatsu, Model R2809U-07) operated at 10 °C. Single photon counting was performed with commercially available electronic instrumentation (Tennelec, Models TC454, TC864, TC412A, TC525, and PCA-II) and commercially available software (Oxford Instruments, PCAME, Version 2.45).

Fluorescence lifetimes were determined at individual wavelengths for each PAH: pyrene (390 nm), fluoranthene (460 nm), benzo(*a*)pyrene (410 nm), and benzo(*b*)fluoranthene (450 nm). Five replicate measurements of the fluorescence time decay were acquired by single photon counting. The data were fit by nonlinear regression to a single exponential function, with typical correlation coefficients (R^2) from 0.996 to 0.999. Because the fluorescence lifetimes of the PAHs ranged from 9 to 30 ns, it was not necessary to deconvolute the instrument response function (~35 ps full width at half maximum) from the experimental data. Consistent with the quenching studies detailed above, no effort was made to deaerate the solutions in order to accurately calculate rate constants of quenching in the presence of oxygen.

D. Determination of Singlet Excitation Energies

UV-visible absorbance and fluorescence emission spectra of the PAHs were acquired by using commercially available spectrometers (ATI Unicam, Model UV2 and Hitachi, Model F-4500) with a 2.5 nm bandpass.

For fluorophores whose absorbance and emission spectra are mirror images, the energy of the singlet excited state can be measured by overlaying the normalized absorption and emission spectra and determining the wavelength at which the curves intersect. However, in cases where the lowest singlet excited state (S_1) is forbidden or where the Born–Oppenheimer approximation does not hold, this approach is more difficult. Such was the case with the PAHs used in this study and, hence, special precautions were necessary in the calculation of their excitation energies. For example, pyrene and benzo(*a*)pyrene have been found to possess a lowest singlet excited state that is forbidden by symmetry selection rules.[5,6] Consequently, it was necessary to expand their absorbance spectra greatly in order to normalize the small band associated with the $S_1 \leftarrow S_0$ absorption with respect to the $S_0 \leftarrow S_1$ emission band. In both cases, these bands were nearly coincident and their intersection was close to the absorption and emission maxima. In contrast, fluoranthene and benzo(*b*)fluoranthene have been found to undergo a large geometry change upon reaching their excited states and, therefore, experience a loss of vibrational fine structure in their emission spectra.[6] In these cases, the $S_1 \leftarrow S_0$ absorption bands were normalized with respect to the maximum of the broad $S_0 \leftarrow S_1$

emission band and the intersection was used as the best estimate of the excitation energy.

III. Results and Discussion

A. Quenching Studies

Aliphatic amines are dynamic quenchers that serve as electron donors through the nonbonding electron pair of nitrogen. Despite what is known about amines as quenchers, only one published report has suggested any selectivity for PAH isomers.[7] Two representative pairs of PAHs were selected for these studies: pyrene and fluoranthene, as well as benzo(*a*)pyrene and benzo(*b*)fluoranthene. These isomeric PAHs have the same molecular formula, the same number of aromatic rings, a similar length-to-breadth ratio, and differ only in their alternant/nonalternant ring structure. The fluorescence lifetimes of these PAHs are summarized in Tables 5-1 and 5-2.

The first quenching studies for the PAHs with aliphatic amines were performed in the solvent methanol. A series of isomeric monoamines consisting of hexylamine, diisopropylamine, and triethylamine was examined. In general, quenching was negligible for the primary amine and increased systematically for the secondary and tertiary amines (Table 5-1). The alkyl groups serve to increase the electron-donating ability as well as the basicity of the nitrogen, thereby increasing the quenching constants.[8] The effect of the number of amine groups was examined with the isomeric diamines 1,6-diaminohexane and 1,4-diazabicyclo(2.2.2)octane. The quenching constants for the primary diamine

Table 5-1: Quenching Constants for Polycyclic Aromatic Hydrocarbons (PAHs) with Aliphatic Amines in Methanol[a]

			diisopropylamine				triethylamine				1,4-diazabicyclo[2.2.2]octane			
PAH	τ^o (ns)	Class	K_d (M^{-1})	b	R^2	k_d ($M^{-1}s^{-1}$)	K_d (M^{-1})	b	R^2	k_d ($M^{-1}s^{-1}$)	K_d (M^{-1})	b	R^2	k_d ($M^{-1}s^{-1}$)
pyrene	15.8	A	0.12	1.03	0.733	7.6×10^6	4.6	1.00	0.996	2.9×10^8	20.3	1.06	0.998	1.3×10^9
benzo(*a*)pyrene	11.8	A	ND[b]	–	–	ND	2.1	1.03	0.974	1.8×10^8	13.3	0.98	0.999	1.1×10^9
fluoranthene	30.0	NA	0.76	0.99	1.000	2.5×10^7	20.7	0.98	1.000	6.9×10^8	78.3	1.03	1.000	2.6×10^9
benzo(*b*)fluoranthene	26.9	NA	0.96	1.00	0.999	3.6×10^7	20.6	1.06	0.999	7.7×10^8	96.2	0.89	1.000	3.6×10^9
		α^c	6.3			3.3	4.5			2.4	3.9			2.0
		α^d	–			–	9.8			4.3	7.2			3.2

[a] K_d = Stern–Volmer constant; b = intercept of equation (1-1); R^2 = square of correlation coefficient; k_d = bimolecular quenching rate constant

[b] Not detectable, i.e. K_d less than 0.005, k_d less than 5×10^5.

[c] Selectivity for four-ring PAHs, defined as K_d(fluoranthene) / K_d(pyrene) or k_d(fluoranthene) / k_d(pyrene).

[d] Selectivity for five-ring PAHs, defined as K_d(benzo(*b*)fluoranthene) / K_d(benzo(*a*)pyrene or k_d(benzo(*b*)fluoranthene) / k_d(benzo(*a*)pyrene).

Table 5-2: Quenching Constants for Polycyclic Aromatic Hydrocarbons (PAHs) with Aliphatic Amines in Acetonitrile[a]

			diisopropylamine				triethylamine				1,4-diazabicyclo[2.2.2]octane			
PAH	τ° (ns)	Class	K_d (M^{-1})	b	R^2	k_d ($M^{-1}s^{-1}$)	K_d (M^{-1})	b	R^2	k_d ($M^{-1}s^{-1}$)	K_d (M^{-1})	b	R^2	k_d ($M^{-1}s^{-1}$)
pyrene	11.9	A	1.2	1.02	0.997	9.9×10^7	45.5	1.07	1.000	3.8×10^9	234.7	0.98	1.000	2.0×10^{10}
benzo(*a*)pyrene	9.0	A	0.47	1.01	0.992	5.2×10^7	27.8	1.04	0.998	3.1×10^9	171.5	0.99	1.000	1.9×10^{10}
fluoranthene	29.2	NA	17.1	0.99	1.000	5.9×10^8	200.6	0.98	1.000	6.9×10^9	451.3	1.03	1.000	1.5×10^{10}
benzo(*b*)fluoranthene	25.5	NA	21.2	1.02	1.000	8.3×10^8	195.4	0.99	1.000	7.7×10^9	418.8	1.02	1.000	1.6×10^{10}
		α^b	15			5.9	4.4			1.8	1.9			0.8
		α^c	45			16	7.0			2.5	2.4			0.9

[a] K_d = Stern–Volmer constant; b = intercept of equation (1-1); R^2 = square of correlation coefficient; k_d = bimolecular quenching rate constant

[b] Selectivity for four-ring PAHs, defined as K_d(fluoranthene) / K_d(pyrene) or k_d(fluoranthene) / k_d(pyrene).

[c] Selectivity for five-ring PAHS, defined as K_d(benzo(*b*)fluoranthene) / K_d(benzo(*a*)pyrene or k_d(benzo(*b*)fluoranthene) / k_d(benzo(*a*)pyrene).

were still negligibly small but those for the tertiary diamine were approximately five times greater than the corresponding tertiary monoamine (Table 5-1). Each of the amine groups can act independently and, thus, can serve to increase the overall quenching constants.[9]

All of the aliphatic amines were more effective quenchers of the nonalternant PAHs than the alternant isomers (Table 5-1), which is to be expected on the basis of their strong electron-donating ability.[7] The selectivity can be defined by the ratio of the quenching constants for the nonalternant and alternant isomers. The ratio of the Stern–Volmer constants represents the net or effective selectivity, whereas the ratio of the rate constants represents the intrinsic selectivity that has been corrected for the differing fluorescence lifetimes. Since the lifetimes of the nonalternant PAHs are longer than those of the alternant PAHs, the selectivity based on the Stern–Volmer constants is greater than that based on the rate constants. In general, it is apparent that the more efficient quenchers have lower selectivity (Table 5-1). Hence, primary amines are more selective than secondary and tertiary amines, monoamines are more selective than diamines, etc. Nevertheless, all of the aliphatic amines are more selective than the previously reported quencher for nonalternant PAHs, 1,2,4-trimethoxybenzene.[1] It is also noteworthy that the selectivity of the amines is uniformly greater for the five-ring PAH isomers (benzo(*b*)fluoranthene and benzo(*a*)pyrene) than for the four-ring PAH isomers (fluoranthene and pyrene). This trend is the opposite of that observed previously for the electron-accepting quencher nitromethane, where selectivity decreased with increasing ring number.[1,10] This property may be exploited to provide selective detection of the larger PAHs in complex forensic and environmental samples.

The next quenching studies for the PAHs with aliphatic amines were performed in the solvent acetonitrile (Table 5-2). These data exhibit many of the same trends as were observed in methanol, including an increase in the quenching constants with increased electron-donating ability of the amine and with the number of amine groups. The most noteworthy distinction is that the amines are more effective quenchers in acetonitrile than in methanol, with all quenching constants being larger by approximately an order of magnitude. There are a number of solvent properties that may be contributing to this phenomenon. The viscosities of acetonitrile and methanol are 0.358 and 0.581 cP, respectively, at 20 °C.[11] The lower viscosity of acetonitrile can increase the rate of diffusion and the number of collisions between the quencher and the fluorophore during its excited-state lifetime. The dielectric constants of acetonitrile and methanol are 36.6 and 33.0, respectively, at 20 °C.[12] The larger dielectric constant of acetonitrile can enhance electron transfer by stabilizing the resulting ion pair between the fluorophore and quencher. Finally, acetonitrile cannot be involved in hydrogen bonding with the amines as is methanol.[13-17] Consequently, the nonbonding electron pair of nitrogen is more accessible and available for fluorescence quenching in acetonitrile.

The selectivity of the amine quenchers in acetonitrile also shows trends similar to those in methanol. Specifically, selectivity is observed for nonalternant PAHs relative to alternant PAHs, and an increase in selectivity is observed with

increasing ring number of the PAH isomers. It is noteworthy that the selectivity of diisopropylamine, a relatively weak quencher, is greater in acetonitrile than in methanol. In contrast, the selectivity of both triethylamine and 1,4-diazabicyclo(2.2.2)octane is reduced. There are two main factors that contribute to this phenomenon. First, the fluorescence lifetimes of all PAHs decrease in acetonitrile, most likely due to the lower viscosity and increased rate of collisions between the solvent and the excited-state fluorophore. However, the lifetimes of the nonalternant PAHs decrease to a lesser extent than those of the alternant PAHs. This would tend to increase the quenching constants of the nonalternant PAHs relative to their alternant isomers, thereby enhancing the selectivity. Second, the rate constants for all quenchers increase in acetonitrile owing to the nonselective solvent effects described above. For the stronger quenchers, these rate constants rapidly approach the diffusion-controlled limit for bimolecular reactions. As a result, there is relatively less ability to discriminate between the isomeric PAHs and the selectivity decreases.

B. Comparison to Theory

A common and widely studied mechanism for dynamic quenching is that of electron transfer between the fluorophore and quencher. This mechanism is dominant in polar solvents where an electron donor (such as an amine) may transfer an electron from its highest occupied molecular orbital (HOMO) to the lowest unoccupied molecular orbital (LUMO) of the singlet excited-state fluorophore to yield a solvated ion pair. Subsequent back electron transfer from the fluorophore to the quencher yields two neutral species, both of which are in their ground states. The free energy change for an outer-sphere electron-transfer process (ΔG_{et}) has been related to spectroscopic and electrochemical parameters of the fluorophore and quencher by Rehm and Weller:[18]

$$\Delta G_{et} = E_{ox} - E_{red} - E_{0,0} - C \tag{5-1}$$

where E_{ox} and E_{red} are the half-wave oxidation and reduction potentials of the electron donor and acceptor, respectively, $E_{0,0}$ is the energy of the singlet excited-state fluorophore and C is a Coulombic term relating the energy of the separated ions

$$C = \frac{\mathrm{k}e^2}{\varepsilon \mathrm{r}} \tag{5-2}$$

where k is Coulomb's constant, *e* is the elementary charge, ε is the dielectric constant of the solvent, and r is the separation distance of the two ions.[19] Rehm and Weller also demonstrated that ΔG_{et} is empirically related to the rate constant for quenching (k_q):[18]

$$k_q = \frac{2.0 \times 10^{10}\ \mathrm{M}^{-1}\mathrm{s}^{-1}}{\left\{1 + 0.25\left[\exp\left(\frac{\Delta G^{*}_{et}}{RT}\right) + \exp\left(\frac{\Delta G_{et}}{RT}\right)\right]\right\}} \tag{5-3}$$

where the coefficient in the numerator represents the diffusion-limited rate constant (k_0) in acetonitrile, R is the gas constant, T is the absolute temperature, and ΔG^{*}_{et} is the activation energy for the electron-transfer process, which is given by a monotonous function of ΔG_{et}.[18]

Table 5-3 summarizes the relevant electrochemical[20-23] and spectroscopic parameters for the fluorophores and quenchers used in the

Table 5-3: Electrochemical and Spectroscopic Parameters for Polycyclic Aromatic Hydrocarbons and Aliphatic Amines

Molecule	**E_{ox} (V)**	**E_{red} (V)**	**Solvent**	**Ref.**	**$\Delta E_{0,0}$ (eV)[b]**	**Solvent**	**$\Delta E_{0,0}$ (eV)[b]**	**Solvent**
pyrene		-2.09	dimethylformamide	20	3.33	acetonitrile	3.33	methanol
benzo(*a*)pyrene		-2.10	dimethylformamide	20	3.07	acetonitrile	3.08	methanol
fluoranthene		-1.74	dimethylformamide	20	3.16	acetonitrile	3.15	methanol
diisopropylamine	1.41[a]		acetonitrile	21				
triethylamine	1.15		acetonitrile	22				
1,4-diazabicyclo[2.2.2]octane	0.68		acetonitrile	23				

[a] Oxidation potential of dipropylamine has been adjusted by +0.49 V to correspond to a saturated calomel reference electrode.

[b] this work

present study. It should be noted that the oxidation potential for diisopropylamine was not available in the literature, so the value for dipropylamine is used. Furthermore, this value has been adjusted by +0.49 V to correct for the use of a $Ag^+/AgCl$ reference electrode instead of a saturated calomel electrode. This correction factor was calculated from the difference in measured oxidation potentials for triethylamine using the same reference electrodes. A similar problem arose with regard to the reduction potential of benzo(*b*)fluoranthene reported in the literature.[24] Because it was measured in an ethylene glycol solvent system *versus* a mercury pool electrode, it was not possible to correct the value to correspond to the other PAHs.

In general, the electrochemical data show that the amines become better oxidizing agents in the order diisopropylamine < triethylamine < 1,4-diazabicyclo(2.2.2)octane, which is in agreement with the structures and trends discussed above. In addition, the alternant PAHs are more difficult to reduce than fluoranthene, which is consistent with the tendency of nonalternant PAHs to serve as electron acceptors. The spectroscopic data do not show any discernible trends in the singlet excited-state energies for the alternant and nonalternant isomers, and there is little variation in these values from acetonitrile to methanol.

The parameters given in Table 5-3 were used to calculate the rate constants for quenching according to the Rehm–Weller model in equations (5-1) to (5-3). A comparison of the theoretically predicted rate constants with those measured experimentally in acetonitrile and methanol is shown in Figures 5-1

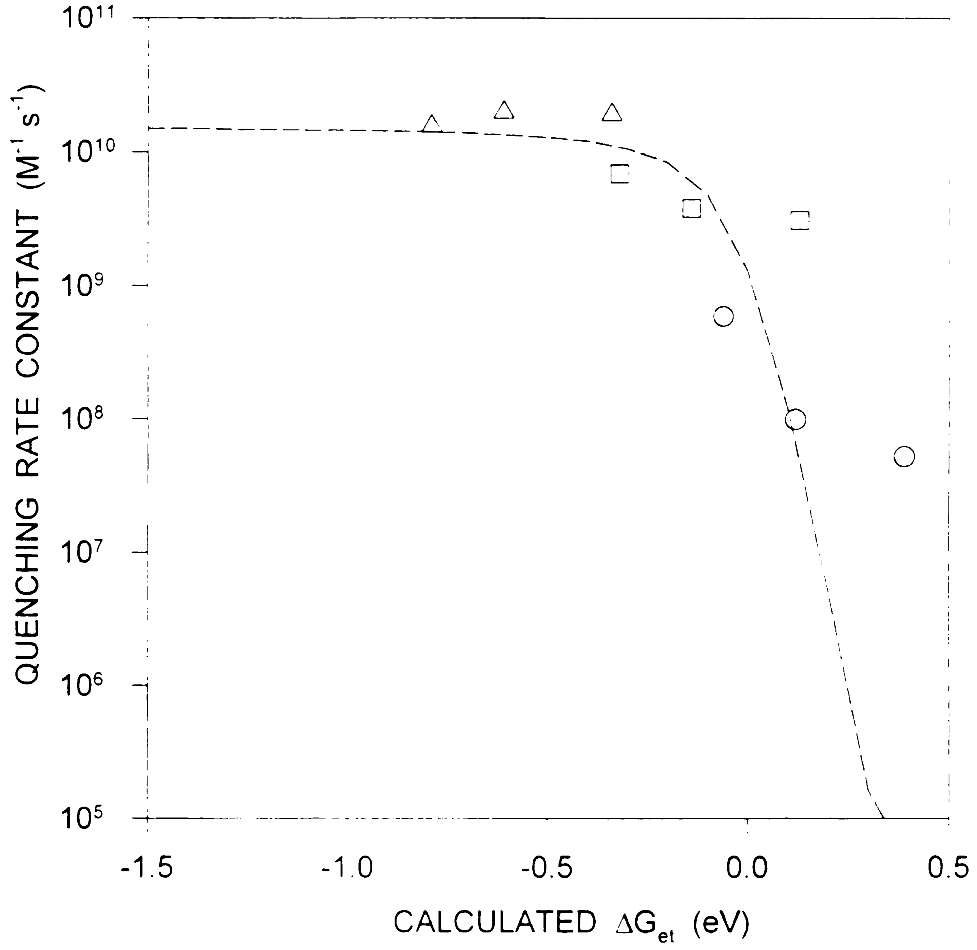

Figure 5-1: Comparison of experimental quenching rate constants for polycyclic aromatic hydrocarbons with diisopropylamine (○), triethylamine (□), and 1,4-diazabicyclo[2.2.2]octane (△) in acetonitrile with Rehm–Weller theory (- - -); see equation (5-3).

and 5-2, respectively. Overall, the experimental values determined in acetonitrile correspond well with Rehm–Weller theory, exhibiting a sharp decrease in the quenching rate constant with increasing values of ΔG_{et}. In contrast, the rate constants determined in methanol are one or two orders of magnitude lower than would be predicted from this theoretical model. Some decrease in the quenching rate constants is expected due to differences in the viscosity and dielectric constant of the solvents. In particular, the diffusion-limited rate constant (k_0) can be estimated by using the Smoluchowski equation:[25]

$$k_q = \left(\frac{4\pi N}{1000}\right)\left(R_f + R_q\right)\left(D_f + D_q\right) \tag{5-4}$$

where N is Avogadro's number, R_f and R_q are the molecular radii of the fluorophore and quencher, respectively, and D_f and D_q are the diffusion coefficients of the fluorophore and quencher, respectively. In turn, the diffusion coefficients are inversely related to the solvent viscosity (η) according to the Stokes–Einstein equation:[26]

$$D_f = \frac{RT}{6\pi R_f \eta N} \tag{5-5}$$

From the viscosities of acetonitrile and methanol cited above, the diffusion-limited rate constant in methanol is expected to be a factor of 0.616 smaller than that in acetonitrile. This decrease of k_0 to 1.2 x 10^{10} M^{-1} s^{-1} is not sufficient to explain the larger decrease shown in Figure 5-2, which is on the order of 5 x 10^{9} M^{-1} s^{-1}. Prior work[13-17] suggests that this decrease is predominantly due to hydrogen bonding between the amine and the alcohol solvent, leading to a

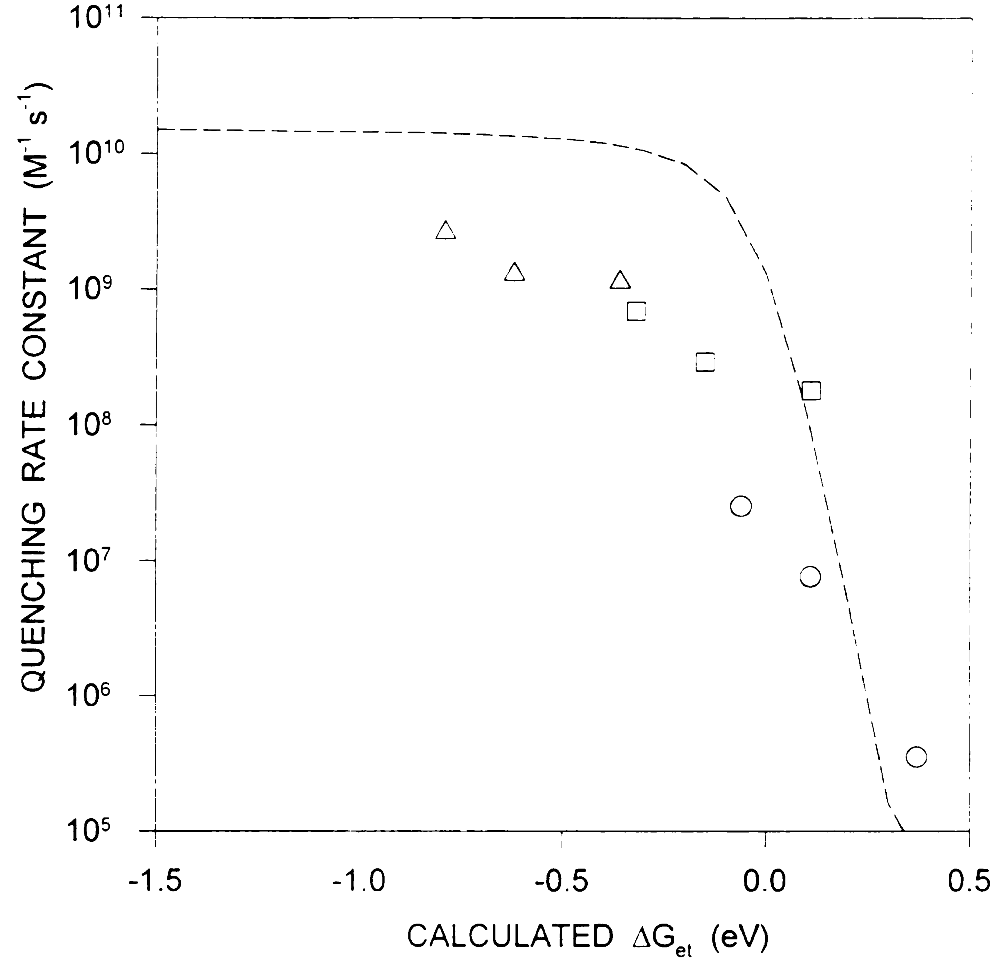

Figure 5-2: Comparison of experimental quenching rate constants for polycyclic aromatic hydrocarbons with diisopropylamine (○), triethylamine (□), and 1,4-diazabicyclo(2.2.2)octane (△) in methanol with Rehm–Weller theory (- - -); see equation (5-3).

decrease in the concentration of the free amine and its adduct with the PAH. As these nonideal quencher–solvent interactions are not implicitly considered in the Rehm–Weller model, its use for the prediction of quenching rate constants is not appropriate under these conditions.

IV. Conclusions

Although selective fluorescence quenching is a promising technique, only a few fluorophore–quencher systems have been characterized in sufficient depth and detail to permit their use for routine analysis. The further development and application of this technique will require systematic measurements of quenching constants to determine the effectiveness and selectivity of potential quenchers. In this study, a series of aliphatic amines have been examined as quenchers of alternant and nonalternant PAHs. It was found that these quenchers exhibit selectivity for nonalternant PAHs that tends to decrease with the electron-donating ability of the amine and with the number of amine groups. Furthermore, the effect of solvent has been shown to be important in these systems. All of the amines were more effective quenchers in acetonitrile than in methanol due to decreased solvent–quencher interactions. Among the quenchers studied, diisopropylamine was found to exhibit very high selectivity in acetonitrile, making it an attractive candidate for use in the analysis of PAH isomers.

V. References

---

1. F.K. Ogasawara, Y. Wang, and V.L. McGuffin, *Appl. Spectrosc.* **49**, 1 (1995).

---

2. G.R. Koboldt, J.V. Goodpaster, and V.L. McGuffin, Unpublished research, Michigan State University, 1997.
3. J.V. Goodpaster and V.L. McGuffin, *Appl. Spectrosc.* **53**, 1000 (1999).
4. L. DeWitt, G.J. Blanchard, E. LeGoff, M.E. Benz, J.H. Liao, and M.G. Kanatzidis, *J. Am. Chem. Soc.* **115**, 12158 (1993).
5. D.S. Karpovich and G.J. Blanchard, *J. Phys. Chem.* **99**, 3951 (1995).
6. J.V. Goodpaster, J.F. Harrison, and V.L. McGuffin, *J. Phys. Chem. A* **102**, 3372 (1998).
7. M.P. Fogarty and I.M. Warner, *Appl. Spectrosc.* **36**, 460 (1982).
8. V.L. McGuffin and J.V. Goodpaster, *Encyclopedia of Environmental Analysis and Remediation*, R.A. Meyers, Ed., John Wiley and Sons, New York (1998).
9. M. Vasilescu, *Rev. Roum. Chim.* **34**, 1819 (1989).
10. S.H. Chen, C.E. Evans, and V.L. McGuffin, *Anal. Chim. Acta* **246**, 65 (1991).
11. G.J. Ganz and R.P.T. Tomkins, *Nonaqueous Electrolytes Handbook,* Academic Press, New York (1972).
12. D.R. Lide, Ed., *CRC Handbook of Chemistry and Physics, 78th ed.,* CRC Press, New York (1997).
13. M. Bellas, D. Bryce-Smith, M.T. Clarke, A. Gilbert, G. Klunkin, C. Manning, S. Krestononish, and S. Wilson, *J. Chem. Soc., Perkin Trans.* **1**, 2752 (1977).
14. F.D. Lewis and T.-I. Ho, *J. Am. Chem. Soc.* **99**, 7991 (1977).
15. J. Gebecki, *Acta Phys. Polon. A* **55**, 411 (1979).
16. S. Oh and Y.J. Shirota, *J. Photochem. Photobiol. A: Chem.* **92**, 79 (1995).
17. M.V. Encinas, E.A. Lissi, A.M. Rufs, M. Altamirano, and J.J. Cosa, *Photochem. Photobiol.* **68**, 447 *(*1998).
18. D. Rehm and A. Weller, *Israel J. Chem.* **8**, 259 (1970).
19. P. Suppan, *J. Chem. Soc., Faraday Trans. 1* **82**, 509 (1986).
20. E.S. Pysh and N.C. Yang, *J. Am. Chem. Soc.* **85**, 2124 (1963).
21. C.K. Mann, *Anal. Chem.* **36**, 2424 (1964).
22. L. Meites and P. Zuman, *CRC Handbook Series in Organic Electrochemistry, Volume I-V,* CRC Press, Boca Raton, (1977-82).
23. T.M. McKinney and D.H. Geske, *J. Am. Chem. Soc.* **87**, 3013 (1965).
24. I. Bergman, *Trans. Faraday Soc.* **50**, 829 (1954).
25. J. Lakowicz, *Principles of Fluorescence Spectroscopy*, Plenum Press, New York (1983).
26. P.W. Atkins, *Physical Chemistry,* W.H. Freeman, San Francisco, pg. 835 (1978).

CHAPTER 6

ANALYSIS OF COMMERCIAL PETROLEUM PRODUCTS USING CAPILLARY LIQUID CHROMATOGRAPHY WITH SELECTIVE FLUORESCENCE QUENCHING DETECTION

I. Introduction

Commercial petroleum products have steadily gained importance in the fields of criminalistics and trace evidence. This is due not only to the severity of the crimes in which this type of evidence is found, but also to the wealth of information available from appropriate chemical analysis of these materials. For example, analysis of petroleum mixtures can provide circumstantial links between motor oil and a particular vehicle, fossil fuels and fires of suspicious origin, crude oil and sites of environmental contamination, or petrolatum jellies and crime scenes involving sexual assault.

In all cases, qualitative and quantitative analysis of polycyclic aromatic hydrocarbons (PAHs) can be used for fingerprinting of petroleum-based samples. The ability to differentiate PAH isomers in petroleum products is important as their distribution can indicate the formation conditions and history of the sample,[1] thereby creating a more unique "fingerprint" for comparison with other samples. To date, various techniques have been utilized to determine PAHs in petroleum products.[2-6] Among these techniques, luminescence is especially beneficial because of its high sensitivity and selectivity for PAHs. Spectra can be obtained by scanning the excitation and emission wavelengths

independently or synchronously,[7] or by acquiring multiwavelength excitation–emission matrices.[8] Both of these latter techniques have been applied to the selective determination of PAHs in petrolatum jellies, lubricants, and motor oils.[6,9-13] Finally, fluorescence lifetime measurements can provide further information for the identification and characterization of PAHs[14] and phase-resolved excitation-emission matrices offered improved discrimination of petrolatum jellies.[15]

However, these techniques are not always sufficiently selective for the analysis of PAHs in complex environmental samples. Furthermore, luminescence spectra in the solution phase exhibit a loss of vibrational fine structure when compared to the gas or solid phase. This loss of structure predominantly arises from collisions of the excited-state PAH with solvent molecules.[16,17] Although alternant PAH isomers often display some structure in their solution-phase emission spectra, nonalternant PAHs that experience large changes in their molecular geometry upon excitation do not.[16-18] Because of their rather featureless spectra, identification of unknown PAHs can be difficult.

In this study, laser-induced fluorescence with selective fluorescence quenching is combined with high-efficiency capillary liquid chromatography for the analysis of petroleum-based samples. This experimental approach provides unparalleled separation efficiency as well as detection sensitivity and specificity for particular PAH isomers. A wide range of information is acquired from a sample that can be used to identify individual PAHs, including chromatographic retention time, fluorescence emission spectra, and Stern–Volmer quenching constants. In addition, the use of selective quenching agents provides many ways to profile the distribution of PAHs in a sample, including chromatograms at individual fluorescence wavelengths, chromatograms at integrated fluorescence wavelengths, chromatograms with fluorescence quenching of alternant PAHs by nitromethane, and chromatograms with fluorescence quenching of nonalternant PAHs by diisopropylamine. Through study of the relative distribution of PAHs, the formation conditions of an unknown petroleum mixture can be deduced and can aid in its classification and identification. Finally, this approach may help determine if a known and unknown petroleum sample share a common source through qualitative and quantitative comparison of their resultant chromatograms.

II. Methods

A. Reagents

A standard mixture (EPA 610, Supelco) of sixteen alternant and nonalternant PAHs ranging in size from 2-6 rings and in concentration from 98-1990 μg/mL was obtained. This mixture was volumetrically diluted with spectroscopic-grade nitromethane (EM Science) to yield a 10% (v/v) solution prior to injection. A reference sample of motor oil (Pennzoil™, 5W30), a sample of the same oil brand after 1,371 miles of highway use, and three commercial formulations of petrolatum jellies (Vaseline™, Meijer™, and Smart Choice™ brands), were also obtained.

Two quenchers were chosen for these studies based upon their previously reported selectivity for alternant and nonalternant PAHs. Nitromethane (EM Science) was volumetrically diluted with high purity, spectroscopic-grade methanol (Baxter Healthcare, Burdick and Jackson Division) to yield a 2% (v/v) solution. Diisopropylamine (Aldrich) was volumetrically diluted with high purity, spectroscopic-grade acetonitrile (Baxter Healthcare, Burdick and Jackson Division) to yield a 50% (v/v) solution. High purity, spectroscopic-grade methanol (Baxter Healthcare, Burdick and Jackson Division) was used as the mobile phase for liquid chromatography.

B. Sample Preparation

For the motor oil samples, 20 mL portions of oil were extracted directly with five 20 mL portions of spectroscopic-grade nitromethane (EM Science) in order to isolate any polycyclic aromatic compounds.[3-5] The nitromethane was then removed by using a rotary evaporator (Büchi/Brinkmann, Rotavapor-R), yielding a brown, oily residue. Extracts were redissolved in 2 mL of nitromethane and analyzed by liquid chromatography.

Weighed portions (~10 g) of the petrolatum jelly samples were first dissolved in 20 mL of spectroscopic-grade hexane (Baxter Healthcare, Burdick and Jackson Division). The hexane solutions were then extracted five times with 20 mL portions of nitromethane. The nitromethane was then evaporated, yielding a yellow residue. This residue was then redissolved in 2 mL of nitromethane before chromatographic analysis.

C. Instrumentation

Each of the samples was analyzed on the system shown in Figure 6-1. A reciprocating piston pump (Beckman Instruments, Model 114M) was used to deliver the methanol mobile phase at a nominal flow rate of 1.0 μL/min. The sample was introduced by means of a valve with a fixed volume of 1.0 μL (Valco Instruments, Model ECI4W1), which was subsequently split 1:23 to provide an injection volume of approximately 43 nL. The sample constituents were then separated on a fused-silica capillary column (Hewlett-Packard, 200 μm i.d., 320 μm o.d., 1.5 m length) that was packed with a 5 μm octadecylsilica stationary phase (Shandon, Hypersil C18, 115,000 theoretical plates), as described previously.[19] The column was immersed within a water bath maintained at 24 °C to minimize the effect of temperature fluctuations on the separation. The column effluent was combined and thoroughly mixed with the quencher solution, which was delivered by a syringe pump (PE/Applied Biosystems, Model 140) at a nominal flow rate of 1.0 μL/min.

The PAHs were then detected by laser-induced fluorescence in a fused-silica capillary flow cell (Polymicro Technologies, 75 μm i.d., 360 μm o.d). A helium–cadmium laser (Melles Griot, Model 3074-40M, 325 nm, 32 mW) was used to irradiate the entire cross section of the flow cell. Fluorescence emission was collected orthogonal to the incident radiation and was collimated and filtered to remove stray light. The resulting emission was then refocused onto the entrance slit of a 0.34 m Czerny–Turner monochromator (Instruments SA, Model 340E, 300 groove/mm grating) and detected by a charge-coupled device

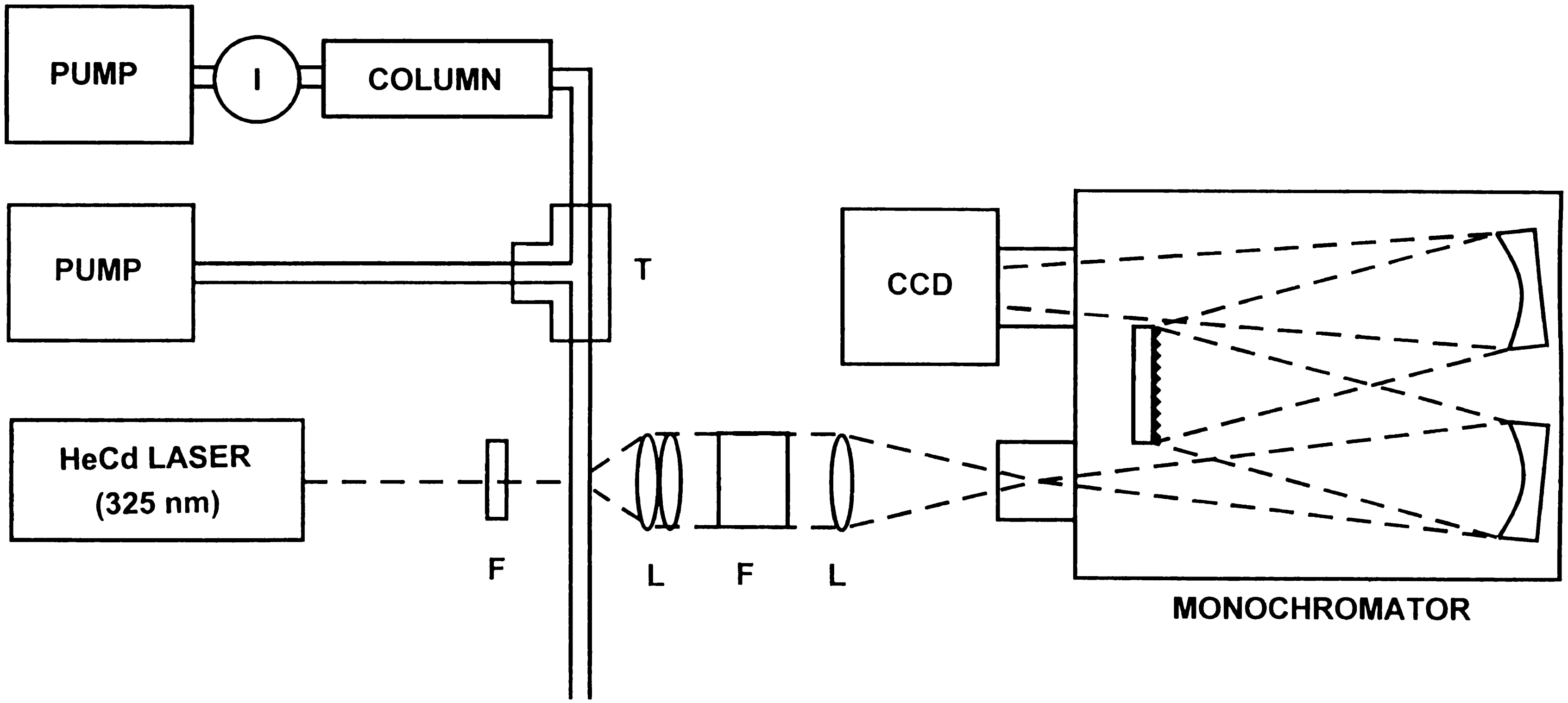

Figure 6-1: Schematic diagram of the experimental system for capillary liquid chromatography with laser-induced fluorescence and fluorescence quenching detection. I = injection valve, T = mixing tee, L = lens, F = filter, CCD = charge-coupled device.

(Instruments SA, Model (A)TECCD-2000x800-7). The CCD detector was thermoelectrically cooled and maintained at a temperature of -40 °C. Instrument control and data acquisition were provided by a commercially available electronic interface (Instruments SA, Model CCD 2000) and the associated software (Instruments SA, Spectramax for Windows, Version 3.1). This detection system has a detection limit of 3 nM (2.3 ppb) of quinine sulfate, a linear range of 10^5, and a spectral range of 300 nm with 1 nm resolution.[20]

D. Data Analysis

As PAHs emit over a wide range of wavelengths, the CCD was integrated over the wavelength range of 350 – 564 nm and the resultant area was displayed as a function of time. The time axes of all chromatograms were normalized with respect to the retention time of the solvent peak in the standard 16 component PAH mixture. For correlation of the petrolatum jelly samples, each time axis was aligned with respect to the solvent peak of the Vaseline™ sample as well as a peak found in all samples such that known PAHs had the same retention times in each chromatogram. The resulting chromatograms were then exported as ASCII files into the statistical analysis software (Jandel, SigmaStat, Version 1.02). The chromatograms were correlated with one another by using the product moment method.[21,22] This method is useful to establish the extent of similarity between two chromatograms, both of which are regarded as independent variables. This parametric method assumes that the association (if any) is linear and that the residuals are normally distributed with constant

variance. The resulting scatter plot shows the relationship between the relative peak heights or concentrations of the PAHs in the two samples. The correlation coefficient (r) of this plot quantifies the degree of similarity, where a coefficient of 1.000 indicates complete correspondence and 0.000 indicates no similarity. The corresponding P-value expresses the statistical reliability of the results, where valid conclusions can be drawn about the probability of the two samples originating from the same source whenever the P-value is less than 0.05 (95% C.L.).

III. Results and Discussion

In the discussion that follows, a standard mixture of PAHs and five petroleum samples are analyzed without and with selective fluorescence quenchers. The retention time, fluorescence emission spectrum, and observed quenching behavior are used to deduce the identity of each component. In addition, comparison of the chromatograms obtained with either nitromethane or diisopropylamine present allows for profiling of the mixtures based on their alternant and nonalternant PAH content. This approach can help establish the relative similarity and dissimilarity of two samples without specific identification of their respective components.

A. Standard PAH Mixture

A chromatogram of the standard mixture of PAHs (EPA 610) with laser-induced fluorescence detection is shown in Figure 6-2A. The identity of each PAH was confirmed by comparison of the retention time and fluorescence

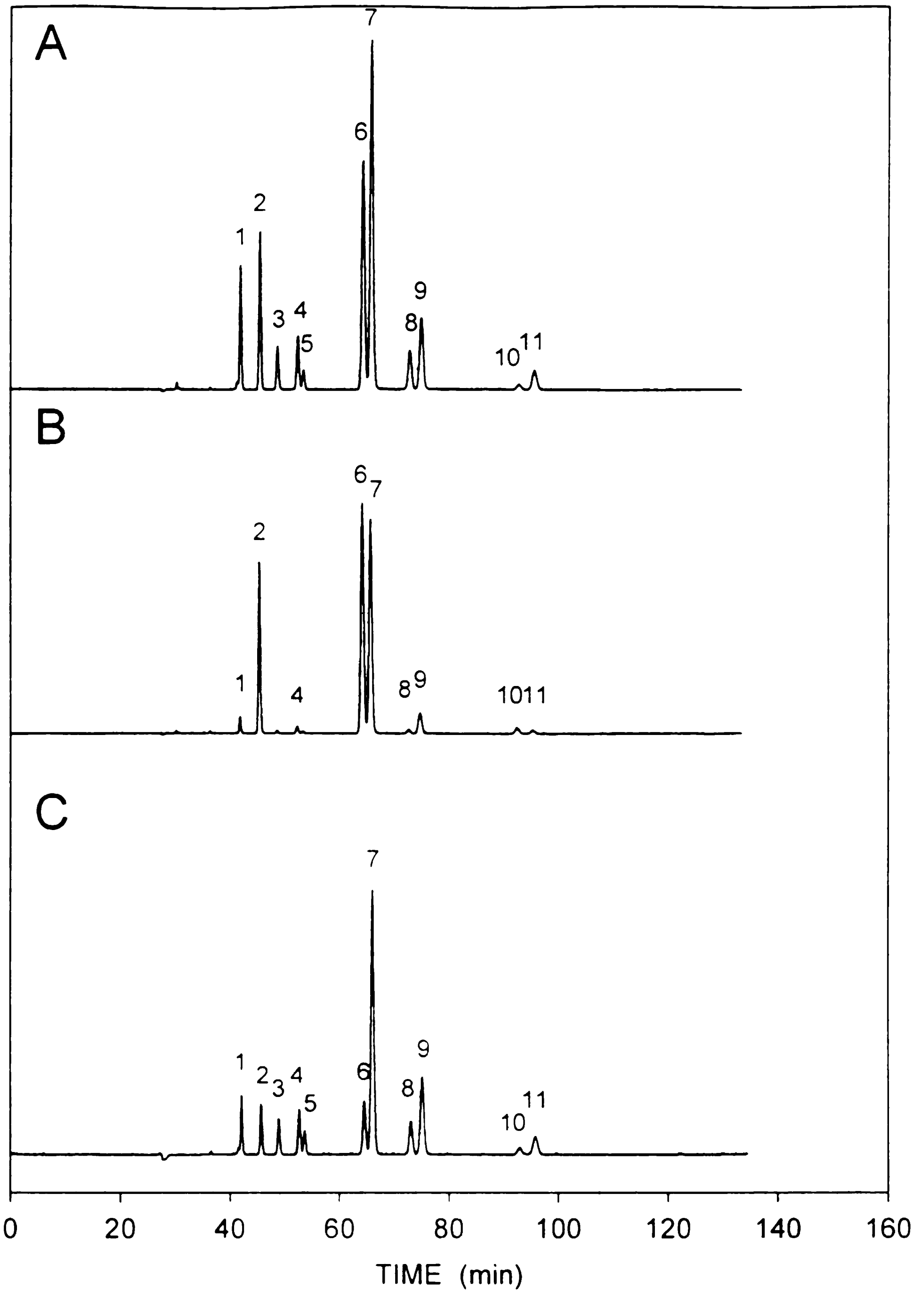

Figure 6-2: Chromatograms of standard polycyclic aromatic hydrocarbons (EPA 610) with post-column addition of (A) 100% methanol, 1.0 μL/min, (B) 2% v/v nitromethane in methanol, 1.0 μL/min, (C) 50% v/v diisopropylamine in acetonitrile, 1.0 μL/min. Column: 1.5 m × 200 μm i.d. fused-silica capillary, packed with 5 μm Shandon Hypersil C18. Mobile phase: methanol, 1.0 μL/min, 24 °C. Laser-induced fluorescence detection: 325 nm excitation, 350 - 564 nm emission. Solutes: (1) anthracene, (2) fluoranthene, (3) pyrene, (4) benz(*a*)anthracene, (5) chrysene, (6) benzo(*b*)fluoranthene, (7) benzo(*k*)fluoranthene, (8) benzo(*a*)pyrene, (9) dibenz(*a,h*)anthracene, (10) indeno(1,2,3-*cd*)pyrene, (11) benzo(*ghi*)perylene.

spectrum with authentic standards.[23,24] Note that of the sixteen known components in this sample, only eleven are fluorescent with excitation at 325 nm. Several of the smaller PAHs, including naphthalene, acenaphthylene, acenaphthene, fluorene, and phenanthrene, are not excited efficiently at this wavelength. The remainder of the PAHs, however, are readily detected in spite of the relatively small mass injected (0.42 – 0.85 ng).

A chromatogram of the standard after addition of nitromethane is shown in Figure 6-2B. It is immediately evident that the nonalternant PAHs (fluoranthene, benzo(*b*)fluoranthene, benzo(*k*)fluoranthene, and indeno(*1,2,3-cd*)pyrene) substantially retain their original fluorescence intensity. In contrast, the alternant PAHs (anthracene, pyrene, benz(*a*)anthracene, chrysene, benzo(*a*)pyrene, and benzo(*ghi*)perylene) are significantly quenched. This observation is consistent with the previously reported Stern–Volmer constants of 0.07 and 0.64 M^{-1} for the representative nonalternant PAHs fluoranthene and benzo(*b*)fluoranthene, and 94 and 61 M^{-1} for the representative alternant PAHs pyrene and benzo(*a*)pyrene.[20] It is also noteworthy in Figure 6-2A that benzo(*k*)fluoranthene appears to be more highly quenched than the other nonalternant PAHs. This is consistent with differences in the electron-donating ability of the aromatic system to the nitromethane quencher.[25,26] In fact, the gas-phase ionization energy[27] of benzo(*k*)fluoranthene (8.167 eV) is substantially less than that of fluoranthene (8.466 eV) and benzo(*b*)fluoranthene (8.410 eV), which suggests that it is a better electron donor. Rather, benzo(*k*)fluoranthene is more

similar to the alternant PAHs benz(*a*)anthracene (8.111 eV) and chrysene (8.261 eV), which is reflected in the quenching behavior.

Chromatograms of the PAH standard after addition of diisopropylamine are shown in Figure 6-2C. In general, the nonalternant PAHs are moderately quenched and the alternant PAHs are unaffected. This observation is consistent with the previously reported Stern–Volmer constants of 17.1 and 21.2 M^{-1} for the representative nonalternant PAHs fluoranthene and benzo(*b*)fluoranthene, and 1.2 and 0.47 M^{-1} for the representative alternant PAHs pyrene and benzo(*a*)pyrene.[28] Benzo(*k*)fluoranthene is an interesting exception to this general trend, as it is relatively unquenched by diisopropylamine. Its behavior, again, is more similar to the alternant PAHs benz(*a*)anthracene and chrysene than to the other nonalternant PAHs fluoranthene and benzo(*b*)fluoranthene.

B. Automotive Engine Oil

Chromatograms for a sample of unused Pennzoil™ motor oil are shown in Figures 6-3A to 6-3C. None of the components in this sample could be identified from the standard mixture, and all of the components exhibited relatively low retention and featureless emission spectra. In addition, the quenching behavior of all components was ambiguous. All PAHs were significantly quenched upon addition of nitromethane (Figure 6-3B), whereas only slight quenching is seen in some of the peaks upon addition of diisopropylamine (Figure 6-3C). This quenching behavior indicates alternant character, which contrasts with the unstructured nature of the emission spectra. Such lack of vibrational structure

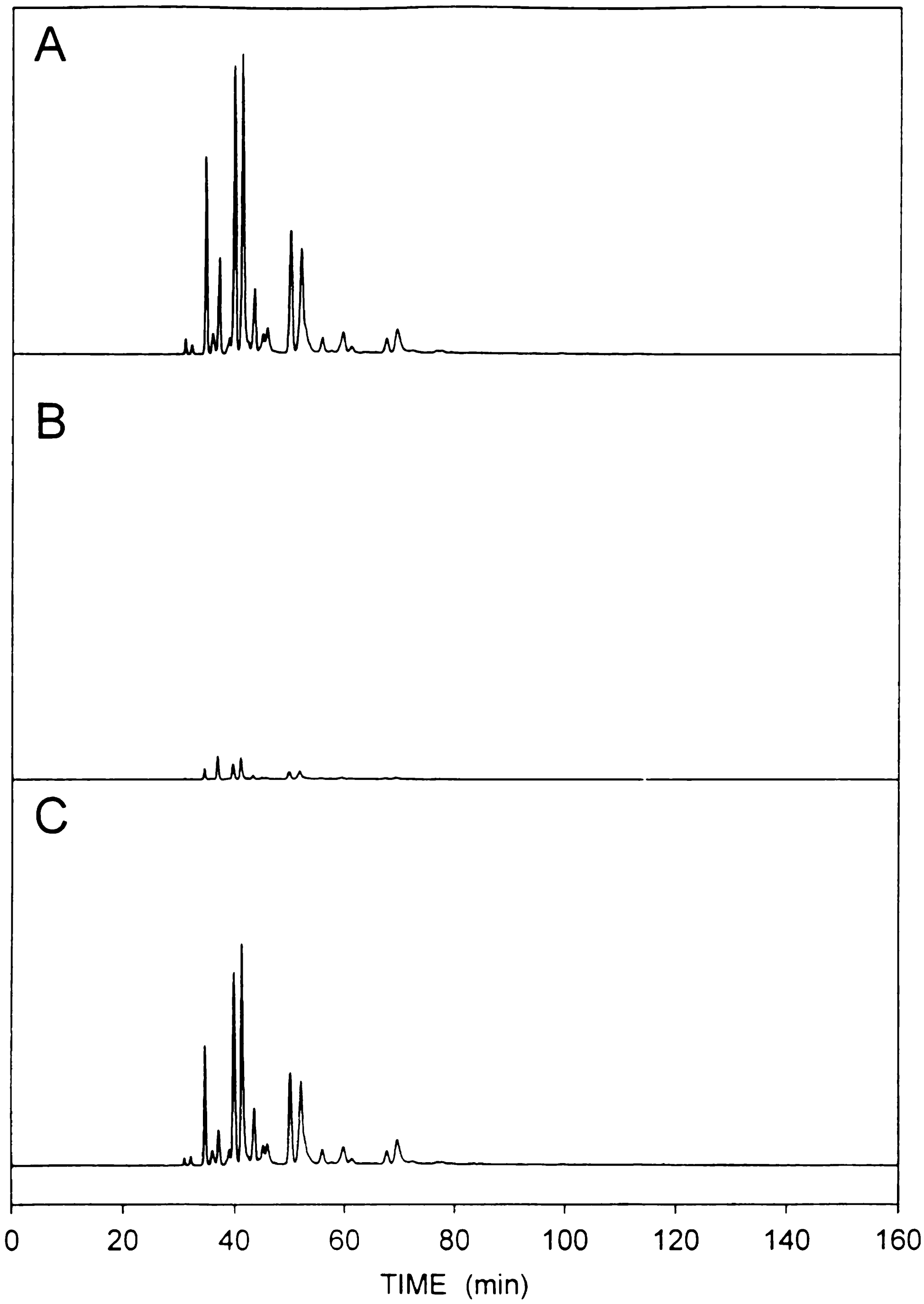

Figure 6-3: Chromatograms of unused Pennzoil motor oil (5W30) with post-column addition of (A) 100% methanol, 1.0 μL/min, (B) 2% v/v nitromethane in methanol, 1.0 μL/min, (C) 50% v/v diisopropylamine in acetonitrile, 1.0 μL/min. Other experimental conditions and solutes as described in Figure 6-2.

tends to indicate nonalternant character, as discussed previously. Taken together, these data indicate two possible explanations. First, as PAHs become more heavily alkylated, they tend to lose vibrational fine structure in their emission spectra even if their parent PAH structure is alternant in nature (e.g., dimethylbenz(*a*)anthracene).[24] Despite this lack of structure, however, these compounds would be expected to behave as alternant PAHs and be quenched by nitromethane. Second, alternant PAHs with nearly circular arrangements of rings (e.g., benzo(*c*)phenanthrene and benzo(*c*)chrysene) also lack vibrational spectral detail due to the inherent flexibility of their non-planar structures but may preserve their alternant quenching behavior.[24] Given the low retention of the compounds in unused motor oil, it is likely that they are small, highly alkylated alternant PAHs, rather than larger benzo- analogs.

This explanation is supported by the dramatic changes that were observed in the motor oil after use in an automobile. The results for an identical sample of oil as discussed above, but after 1,371 miles of use, are shown in Figures 6-4A to 6-4C. A number of the components from the unused motor oil are detected in this sample and are denoted with asterisks. However, the overall chromatogram is decidedly more complex, including numerous components of higher molecular weight. In particular, a number of PAHs from the standard mixture were found at relatively high levels including both alternant (anthracene, pyrene, benz(*a*)anthracene, benzo(*a*)pyrene, benzo(*ghi*)perylene) and nonalternant (fluoranthene, benzo(*k*)fluoranthene) isomers.

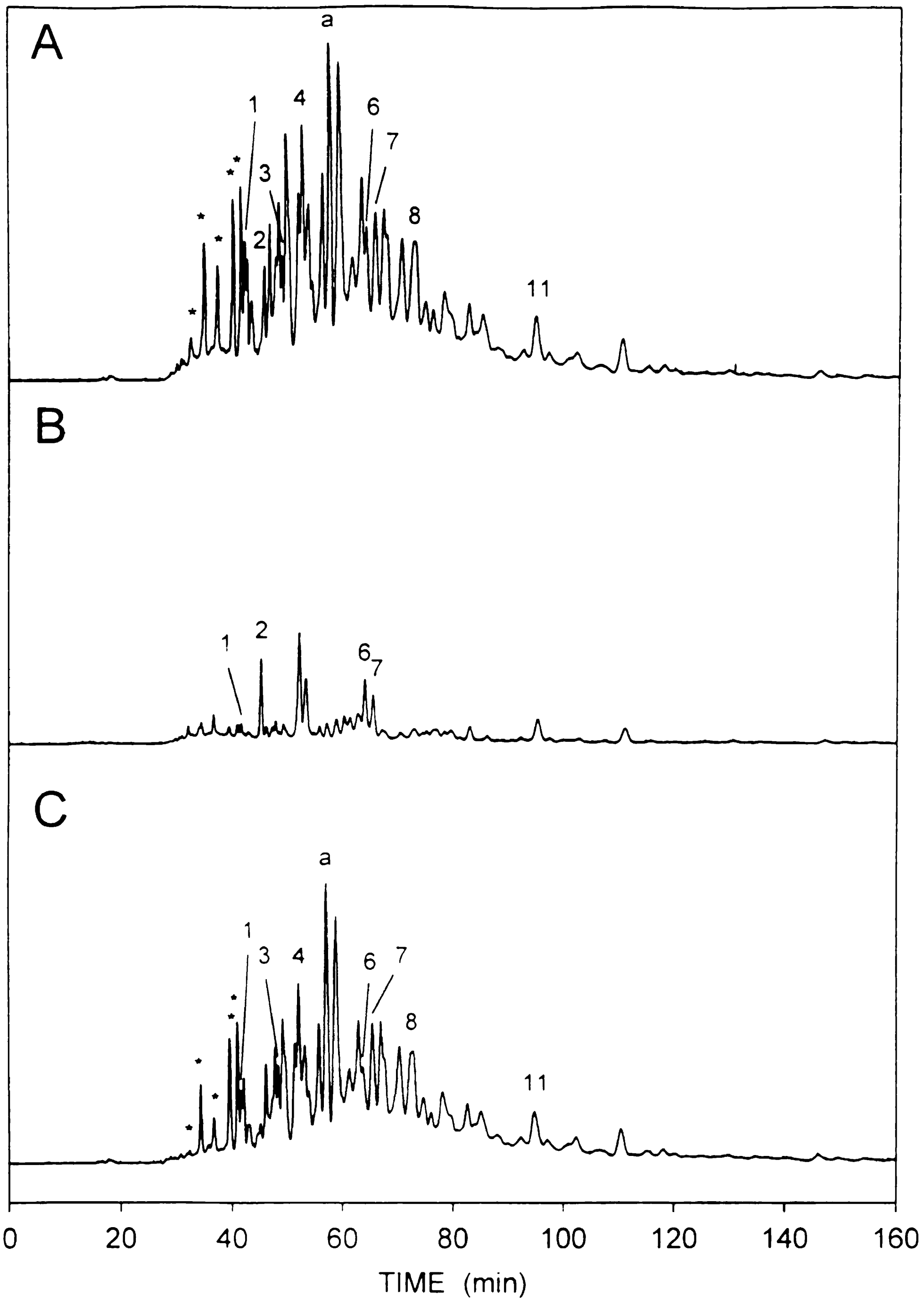

Figure 6-4: Chromatograms of used Pennzoil motor oil (5W30) with post-column addition of (A) 100% methanol, 1.0 μL/min, (B) 2% v/v nitromethane in methanol, 1.0 μL/min, (C) 50% v/v diisopropylamine in acetonitrile, 1.0 μL/min. Solutes: (*) residual peaks from unused oil, (1) anthracene, (2) fluoranthene, (3) pyrene, (4) benz(*a*)anthracene, (a) consistent with methylchrysene and methylbenz(*a*)anthracene isomers, (7) benzo(*k*)fluoranthene, (8) benzo(*a*)pyrene. Other experimental conditions and solutes as described in Figure 6-2.

Although the remaining peaks in the chromatogram cannot be identified from the standard 16 component mixture, in some cases the general structure and class of the compounds can be deduced from their emission spectra and quenching behavior. Specific identifications are not possible due to the large number of positional isomers for any given PAH structure and the lack of vibrational fine structure in their fluorescence spectra. For example, peak (a) has a retention time and spectrum consistent with methylated PAHs with angular arrangements of four rings (i.e., isomers of methylchrysene and/or methylbenz(*a*)anthracene). In addition, this peak is quenched upon addition of nitromethane but is not affected by diisopropylamine (see Figures 6-4B and 6-4C, respectively). This further confirms that the overall structure of this PAH is alternant in character.

There are two likely sources of new PAHs in motor oil after use, the first being reactions of highly alkylated PAHs to form methylated or unsubstituted PAH isomers. In particular, highly alkylated PAHs are less stable and form at lower temperatures over longer time scales (e.g., during formation of crude oil).[1] In contrast, PAHs that are devoid of side chains form rapidly at high temperatures (e.g., during exposure to high engine temperatures).[1] Such high temperature conditions must be sustained over a long time period in order to form the most stable isomers. The PAH isomers that are most stable contain alternant, clustered arrangements of aromatic rings (e.g., pyrene), followed by angular arrangements (e.g., benz(*a*)anthracene) and linear arrangements (e.g., anthracene). Finally, non-alternant PAHs (e.g., fluoranthene) tend to form at

lower temperatures and the number of non-aromatic rings increases with reaction time.[1] Therefore, the wide variety of reactions that are possible at the high and low temperatures typical of automobile engines allows for the formation of a number of PAHs, whose identity and distribution should be reflective of the particular engine, the operating conditions, and motor oil used.

The second possible source of unsubstituted PAHs in used motor oil is normal contamination by fuel from the engine cylinders. Gasoline and diesel fuels are known to contain alternant and nonalternant PAHs that would be expected to be highly soluble in oil.[24] In addition, the distribution and identity of these PAHs may differ by type or even brand of fuel as well as the combustion temperature of the engine. Therefore, the process of driving should impart a number of characteristics on the motor oil that could be used for its unique identification and comparison to a reference sample, regardless of the source of detected PAHs.

C. Petrolatum Jelly

A chromatogram of Vaseline™ brand petrolatum jelly is shown in Figure 6-5A. After comparison of retention times and reference spectra, two PAHs that are present in the standard mixture (fluoranthene and pyrene) have been successfully identified at trace levels in this sample. Fluoranthene appears to be co-eluting with a compound whose emission, while shifted to shorter wavelengths, is similarly unstructured. This would imply that, like fluoranthene, this compound is nonalternant.[18] These conclusions are confirmed by the quenching behavior of these peaks. For example, upon addition of nitromethane

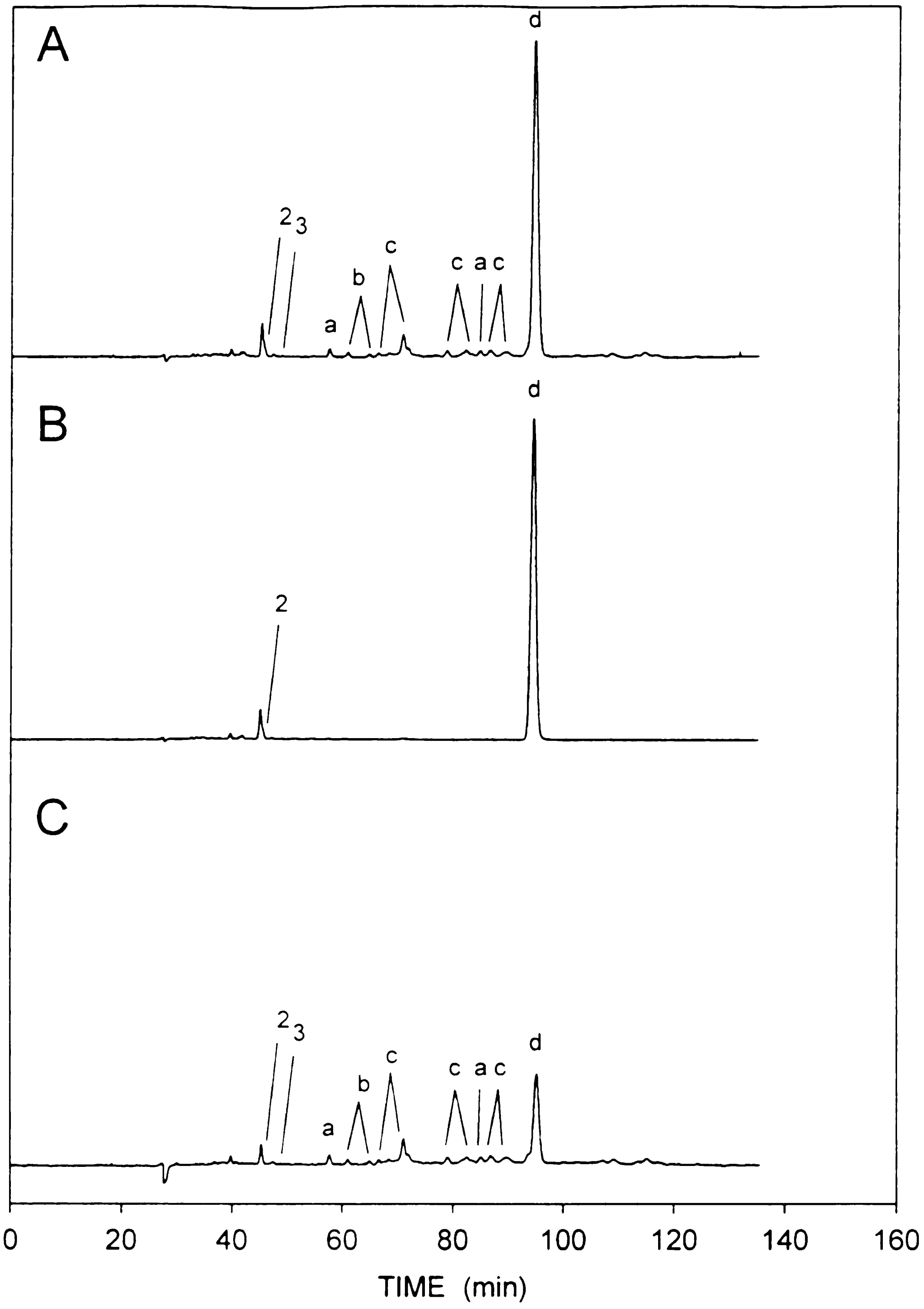

Figure 6-5: Chromatograms of Vaseline brand petrolatum jelly with post-column addition of (A) 100% methanol, 1.0 μL/min, (B) 2% v/v nitromethane in methanol, 1.0 μL/min, (C) 50% v/v diisopropylamine in acetonitrile, 1.0 μL/min. Solutes: (2) fluoranthene, (3) pyrene, (a) consistent with methylchrysene and methylbenz(*a*)anthracene isomers, (b) unknown alternant PAHs, (c) consistent with benzacridine and dibenzacridine isomers, (d) consistent with alkylated fluoranthene or dibenzfluoranthene isomer. Other experimental conditions and solutes as described in Figure 6-2.

(Figure 6-5B), no decrease is observed for the unknown/fluoranthene peak whereas the pyrene peak is completely quenched. The reverse trend is seen in Figure 6-5C, where addition of diisopropylamine causes a significant decrease in the unknown/fluoranthene peak but has little effect on the pyrene peak.

Four main classes of PAHs were identified in the Vaseline™ sample. As discussed previously, class (a) has retention times and spectra consistent with alkylated PAHs with angular arrangements of four rings (i.e., isomers of methylchrysene and/or methylbenz(*a*)anthracene). These PAHs are quenched upon addition of nitromethane but are not affected by diisopropylamine (Figure 6-5B and 6-5C, respectively). This confirms that the overall structure of these PAHs is alternant in character. The second group (b) has structured emission spectra centered at ~360 nm. This group remains as yet unidentified, but shares the same quenching behavior as group (a) and, therefore, can be tentatively identified as alternant. The third group (c) has emission spectra that are differentiable from class (a) and are consistent with heterocyclic PAHs with angular arrangements of four to five rings (i.e., isomers of benzacridine and dibenzacridine). These PAHs also demonstrate alternant character in their quenching behavior. The final class (d) is the major component of this extract, and has a retention time and slightly structured emission spectrum consistent with highly alkylated fluoranthene or benzo(*b*)fluoranthene, or a larger dibenzofluoranthene isomer. Furthermore, like fluoranthene and benzo(*b*)fluoranthene, this component shows no change upon addition of nitromethane and a marked decrease in intensity upon addition of diisopropylamine, which supports the inference of a nonalternant structure.

A number of similarities and differences can be seen in the results for different brands of petrolatum jelly. For example, the chromatograms obtained for a Meijer™ brand product are shown in Figures 6-6A to 6-6C. Major similarities include the presence of fluoranthene and pyrene, as well as a number of PAHs that are assigned to classes (a), (b), and (c) as described above. In addition, the retention times for these latter PAHs correspond to those seen in the Vaseline™ sample, indicating that a number of the same PAHs are present in both samples. Major differences include a larger number of components, the presence of a small amount of anthracene, and the lack of any large, nonalternant PAH such as peak (d) in Figure 6-6A. Indeed, upon addition of nitromethane (Figure 6-6B), the vast majority of peaks for this sample were rendered undetectable, with only the fluoranthene peak clearly remaining. Conversely, only this peak is affected upon addition of diisopropylamine (Figure 6-6C), implying that the remainder of the PAHs present are alternant in structure.

The results for a final brand of petrolatum (Smart Choice™) are shown in Figures 6-7A to 6-7C. This sample also possesses unique characteristics such as the presence of pyrene in the absence of any other standard PAH. Furthermore, no peaks corresponding to class (b) (as described above) could be found. The presence of peaks assigned to classes (a) and (c) again demonstrates that a number of the same alkylated and heterocyclic PAHs appear in these samples, but their relative distribution varies. Finally, quenching

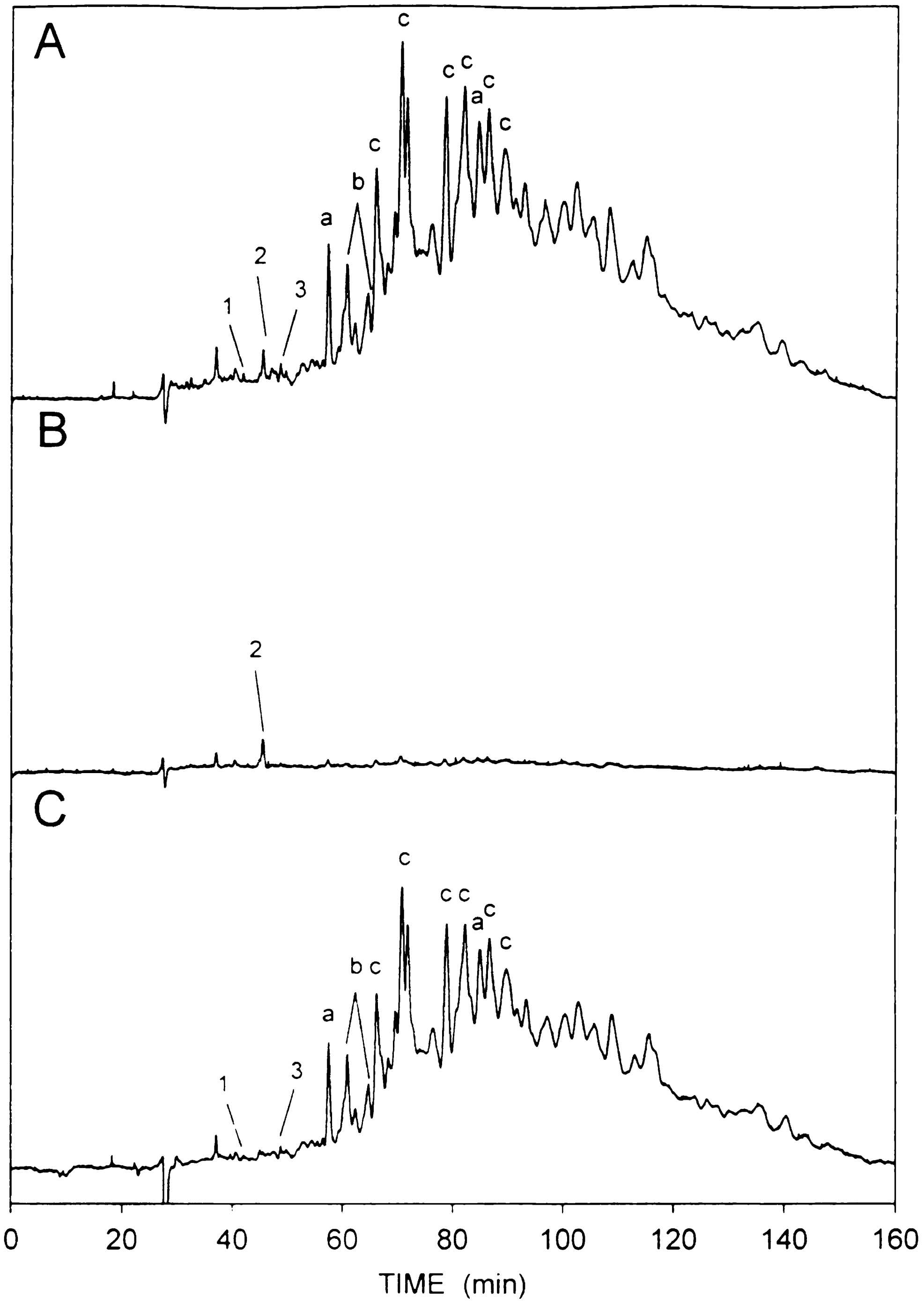

Figure 6-6: Chromatograms of Meijer brand petrolatum jelly with post-column addition of (A) 100% methanol, 1.0 μL/min, (B) 2% v/v nitromethane in methanol, 1.0 μL/min, (C) 50% v/v diisopropylamine in acetonitrile, 1.0 μL/min. Solutes: (1) anthracene, (2) fluoranthene, (3) pyrene, (a) consistent with methylchrysene and methylbenz(*a*)anthracene isomers, (b) unknown alternant PAHs, (c) consistent with benzacridine and dibenzacridine isomers. Other experimental conditions and solutes as described in Figure 6-2.

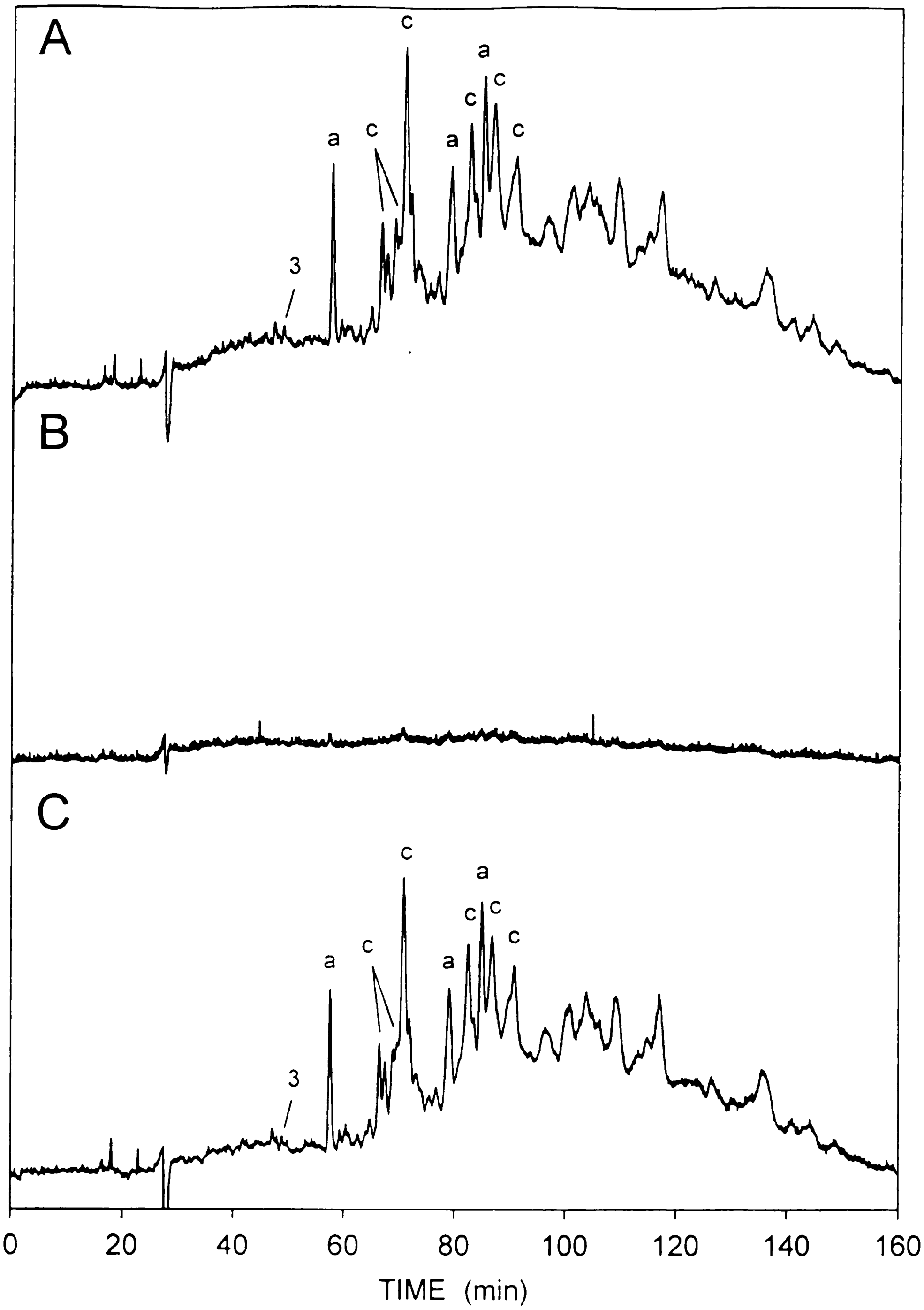

Figure 6-7: Chromatograms of Smart Choice brand petrolatum jelly with post-column addition of (A) 100% methanol, 1.0 μL/min, (B) 2% v/v nitromethane in methanol, 1.0 μL/min, (C) 50% v/v diisopropylamine in acetonitrile, 1.0 μL/min. Solutes: (3) pyrene, (a) consistent with methylchrysene and methylbenz(*a*)anthracene isomers, (c) consistent with benzacridine and dibenzacridine isomers. Other experimental conditions and solutes as described in Figure 6-2.

data in Figures 6-7B and 6-7C demonstrate that this sample contains no detectable levels of nonalternant PAHs.

D. Statistical Correlation Analysis

The results discussed above demonstrate that different brands of petrolatum jellies can be easily discriminated on the basis of the presence or absence of various alternant and nonalternant PAHs. Furthermore, rigorous identification of all components is not necessary for profiling of these mixtures. Successful differentiation can be achieved through qualitative comparisons of the chromatograms obtained without and with selective quenching agents that correspond to different populations of PAH isomers within the sample. Alternatively, correlations of the chromatograms can be obtained through quantitative techniques such as the product moment method.[21,22] When samples are derived from exactly the same origin, the relative peak heights or concentrations of PAHs in each sample are identical and the resulting correlation coefficient (r) would be equal to 1.000. When samples are of similar or related origin, many of the same PAHs may be present but at different concentrations. This results in an intermediate degree of correlation with typical values of r in the range of 0.50 to 0.90. Finally, when samples are of distinctly unrelated origin, the disparate distribution of PAHs will result in little or no correlation with typical values of r less than 0.50. In all cases, valid conclusions can be drawn about the identity or origin of the samples when the P-value for the product moment correlation is less than 0.05, or the 95% confidence limit. For the data discussed below, the largest calculated P-value was 0.03, or the 97% confidence level.

Table 6-1 summarizes the results of the product moment correlation for the three petrolatum jelly samples examined with fluorescence detection alone (see Figures 6-5A, 6-6A, and 6-7A). It is apparent that there is little correlation between the Vaseline™ and the Meijer™ or Smart Choice™ samples, despite the common PAHs found in each sample ($r = 0.159$ and 0.142, respectively). As many of the PAHs in the more complex Meijer™ and Smart Choice™ samples are not found in the Vaseline™ sample, these samples present the unique challenge of profiling with limited information for which this correlation method is well suited. The Meijer™ and Smart Choice™ samples show a rather high degree of correlation ($r = 0.931$), which is consistent with the similar appearance of their chromatograms in Figures 6-6A and 6-7A. In addition, this reflects a similarity in their overall composition, petroleum source, and manufacturing conditions. However, slight variations in their components allow for differentiation of these samples (see below).

PAH profiling using statistical correlation methods becomes even more versatile and powerful when combined with selective fluorescence quenching. Table 6-2 summarizes the results of the product moment correlation for the three samples with fluorescence quenching by nitromethane (see Figures 6-5B, 6-6B, and 6-7B). As the alternant PAHs are selectively quenched, this correlation discriminates on the basis of the distribution of nonalternant PAHs in the samples. When viewed on this basis, the Vaseline™ sample is still distinctly different from the Meijer™ or Smart Choice™ brands. In fact, the degree of correlation decreases, as the many alternant components that exist in common

Table 6-1: Correlation Coefficient (r) of the Product Moment Method for Chromatograms Obtained by Using Laser-Induced Fluorescence Detection

Sample	Vaseline^{TM}	Meijer^{TM}	Smart Choice^{TM}
Vaseline^{TM}	1.000	0.159	0.142
Meijer^{TM}	0.159	1.000	0.931
Smart Choice^{TM}	0.142	0.931	1.000

Table 6-2: Correlation Coefficient (r) of the Product Moment Method for Chromatograms Obtained by Using Laser-Induced Fluorescence Detection with Quenching by Nitromethane

Sample	Vaseline$^{\text{TM}}$	Meijer$^{\text{TM}}$	Smart Choice$^{\text{TM}}$
Vaseline$^{\text{TM}}$	1.000	0.146	0.100
Meijer$^{\text{TM}}$	0.146	1.000	0.895
Smart Choice$^{\text{TM}}$	0.100	0.895	1.000

between the three samples are diminished in these quenched chromatograms. This behavior is also seen for the Meijer™ and Smart Choice™ samples, whose nonalternant content is limited to a small amount of fluoranthene in the Meijer™ sample and no detectable nonalternant PAHs in the Smart Choice™ sample.

Table 6-3 summarizes the results of the product moment correlation with fluorescence quenching by diisopropylamine (see Figures 6-5C, 6-6C, and 6-7C). As the nonalternant PAHs are selectively quenched, this correlation discriminates on the basis of the distribution of alternant PAHs in the samples. In all cases, the correlation between samples based on the alternant PAHs is larger than that for either the nonalternant PAHs (Table 6-2) or the unquenched chromatograms (Table 6-1). These results show that the samples are most similar in their alternant character.

IV. Conclusions

In summary, fluorescence and selective fluorescence quenching appear to provide complementary information for profiling PAHs in complex samples. For example, unquenched fluorescence emission offers broad-based information about the possible identities of unknown PAHs. In contrast, fluorescence quenching by nitromethane allows selective discrimination of the nonalternant PAHs and quenching by diisopropylamine allows selective discrimination of the alternant PAHs. Only when all of these results show a high degree of correlation can it be confidently concluded that two forensic samples are of the same origin. In this study, the effect of normal use on motor oil imparted a characteristic profile that may be used to identify the source of such samples. In addition,

Table 6-3: Correlation Coefficient (r) of the Product Moment Method for Chromatograms Obtained by Using Laser-Induced Fluorescence Detection with Quenching by Diisopropylamine

Sample	Vaseline^{TM}	Meijer^{TM}	Smart Choice^{TM}
Vaseline^{TM}	1.000	0.395	0.374
Meijer^{TM}	0.395	1.000	0.936
Smart Choice^{TM}	0.374	0.936	1.000

comparison of chromatograms without and with selective quenchers successfully distinguished three different brands of petrolatum jelly, largely based upon the distribution of nonalternant PAH isomers. The relative distribution of alternant and nonalternant isomers could also be applied to the analysis of arson evidence. In these cases the formation conditions (and hence alternant/nonalternant ratios and degree of alkylation) for petroleum-based accelerants would differ from materials exposed to the high temperatures of a fire. Finally, given the inherent sensitivity of fluorescence, small amounts of petroleum–based materials could be successfully analyzed using this technique.

V. References

---

1. M. Blumer, *Sci. Am.* **234**, 35 (1976).
2. M.L. Lee, M.V. Novotny, and K.D. Bartle, *Analytical Chemistry of Polycyclic Aromatic Compounds*, Academic Press, New York (1981).
3. D. Hoffman and E.L. Wynder, *Anal. Chem.* **32**, 295 (1960).
4. W. Lijinsky, *Anal. Chem.* **32**, 684 (1960).
5. W. Lijinsky, C.R. Raha, and J. Keeling, *Anal. Chem.* **33**, 810 (1961).
6. R.D. Blackledge and L.R. Cabiness, *J. Forensic Sci.* **28**, 451 (1983).
7. C.L. Stevenson and T. Vo-Dinh, *Anal. Chim. Acta* **303**, 247 (1995).
8. M.P. Fogarty and I.M. Warner, *Appl. Spectrosc.* **36**, 460 (1982).
9. J.B.F. Lloyd, *J. Forensic Sci. Soc.* **11**, 235 (1971).
10. J.B.F. Lloyd, *Analyst* **105**, 97 (1980).
11. J.B.F. Lloyd, I.W. Evett, and J.M. Dubery, *J. Forensic Sci.* **25**, 589 (1980).
12. J.A. Siegel, J. Fisher, C. Gilna, A. Spadafora, and D. Krupp, *J. Forensic Sci.* **30**, 741 (1985).
13. J. Gugel and J.A. Siegel, *J. Forensic Sci.* **33**, 1405 (1988).
14. J.M. Shaver and L.B. McGown, *Appl. Spectrosc.* **49**, 813 (1995).
15. P.M.R. Hertz and L.B. McGown, *Appl. Spectrosc.* **45**, 73 (1991).
16. R. Badley, *Fluorescence Spectroscopy*, Plenum Press, New York (1983).
17. J. Lakowicz, *Principles of Fluorescence Spectroscopy*, Plenum Press, New York (1983).
18. J.V. Goodpaster, J.F. Harrison, and V.L. McGuffin, *J. Phys. Chem. A* **102**, 3372 (1998).

19. J.C. Gluckman, A. Hirose, V.L. McGuffin, and M. Novotny, *Chromatographia* **17**, 303 (1983).
20. J.V. Goodpaster and V.L. McGuffin, *Appl. Spectrosc.* **53**, 1000 (1999).
21. R.M. Thorndike, *Correlational Procedures for Research*, Gardner Press, New York (1978).
22. J.L. Devore, *Probability and Statistics for Engineering and the Sciences, 4th ed.*, Duxbury Press, Pacific Grove (1995).
23. S.A. Wise and L.C. Sander, *J. High Resolut. Chromatogr. Chromatogr. Commun.* **8**, 248 (1985).
24. W. Karcher, R.J. Fordham, J.J. Dubois, P.G.J.M. Glaude, and J.A.M. Ligthart, *Spectral Atlas of Polycyclic Aromatic Compounds, Vol. 1.*, Reidel Publishing Company, Boston (1985).
25. F.K. Ogasawara, Y. Wang, and V.L. McGuffin, *Appl. Spectrosc.* **49**, 1 (1995).
26. S.H. Chen, C.E. Evans, and V.L. McGuffin, *Anal. Chim. Acta* **246**, 65 (1991).
27. R.A. Hites and W.J. Simonsick, *Calculated Molecular Properties of Polycyclic Aromatic Hydrocarbons*, Elsevier, Amsterdam (1987).
28. J.V. Goodpaster and V.L. McGuffin, *Anal. Chem.* **72**, 1072 (2000).

CHAPTER 7

ANALYSIS OF NITRATED EXPLOSIVES USING CAPILLARY LIQUID CHROMATOGRAPHY WITH INDIRECT FLUORESCENCE QUENCHING DETECTION

I. Introduction

Nitroaromatic and nitramine explosives are an important group of compounds in both environmental and forensic science. For example, it has been shown that the soil and ground water of military installations can become contaminated by these compounds and their degradation products at toxic levels.[1-5] In addition, the reliable identification of explosives in post-blast residues is of great importance to criminal investigations.[6-8]

In practice, environmental samples are typically processed by using U.S. Environmental Protection Agency (EPA) Method 8330.[9,10] In this method, samples are extracted with acetonitrile, pre-concentrated, and then analyzed by using reversed-phase liquid chromatography (LC) with UV-visible absorbance detection. However, these techniques for the separation and detection of explosives have limited their qualitative and quantitative analysis. For example, the separation of explosives has remained difficult and commercially available liquid chromatography columns are not capable of resolving all 14 components of the standard test mixture.[9,10] In particular, the isomers 2-amino-4,6-dinitrotoluene (2-am-4,6-DNT) and 4-amino-2,6-dinitrotoluene (4-am-2,6-DNT) co-elute, as do the isomers 2,4-dinitrotoluene (2,4-DNT) and 2,6-dinitrotoluene (2,6-DNT).

Various alternative separation methods have been proposed to achieve higher resolution of explosives mixtures. For example, gas chromatography (GC) has been used to analyze dinitrotoluenes found in nitroglycerine-based explosives[11] and to determine nitrated explosives in ground water.[12] The use of solid-phase microextraction with subsequent GC analysis has also been well explored.[13] While detectors for GC generally offer better detection limits than LC with UV absorbance detection, they also have a limited linear range and accurate calibration has been problematic.[12] Furthermore, care must be taken in selecting the chromatographic conditions and in deactivating the injection port to avoid loss of explosive analytes due to thermal degradation or adsorption.[12]

Supercritical fluid chromatography (SFC) has also been studied as a separation technique for explosives. While achieving some degree of success, SFC did not provide full resolution of the standard explosives mixture nor was detection sensitivity adequate.[14] Mixed-mode reversed phase/anion exchange LC successfully separated some of the standard explosives, although it was not able to resolve the isomers 2,4-DNT and 2,6-DNT.[15] More recently, various techniques that take advantage of the high efficiency of a flat electroosmotic flow profile have yielded the best results. In particular, capillary electrochromatography (CEC)[16,17] and micellar electrokinetic capillary chromatography (MEKC)[18,19] have been reported. Of these, only two reports have demonstrated successful resolution of the standard test mixture.[16,18]

In terms of detection of explosives, UV-visible absorbance provides adequate sensitivity but little selectivity for explosive compounds, especially

when they are found in complex environmental matrices. As a result, other detection methods have been explored, including amperometry[17,19,20] and mass spectrometry.[21] Of particular interest to this study is one report of the detection of explosives using indirect fluorescence detection.[22] This method relies upon the displacement of a fluorophore by an analyte, thereby generating a reduction in signal and detection of the analyte. However, indirect fluorescence is completely non-selective and was problematic when used together with micellar separations.

A different approach to the detection of nitrated explosives is that of selective fluorescence quenching. When adapted as an indirect detection method, quenching relies upon deactivation of a fluorophore by the analyte via a selective quenching mechanism. The efficient quenching of various fluorophores by nitroaromatic compounds has been well demonstrated.[23-28] The mechanism of quenching is generally thought to involve the formation of a charge-transfer complex between the fluorophore and quencher.[29] The strong electron-withdrawing ability of nitrated compounds enables them to form strong charge-transfer complexes with fluorophores such as polycyclic aromatic hydrocarbons (PAHs). This, in turn, contributes to large quenching constants for nitrated quenchers. For example, part-per-million levels of 2,4,6-trinitrotoluene (2,4,6-TNT) quenched the fluorescence of pyrene in cyclohexane through both static and dynamic mechanisms.[23] Similarly, dinitro- and trinitrobenzenes in various solvents were found to quench pyrene significantly.[24] Comparisons of the sensitivity of static versus dynamic quenching have also been made. For ionic

fluorophores and quenchers, static quenching shows much increased sensitivity over dynamic quenching.[25] Finally, some sensors have been developed based on fluorescence quenching technology. Part-per-billion levels of 2,4,6-TNT were successfully detected by using a fluorescent ion-exchange resin.[26] Other examples include an optrode membrane impregnated with the fluorophores fluoranthene and fluorescein for the detection of picric acid as well as silica microspheres stained with fluorescent dyes for the detection of nitroaromatic vapors.[27,28]

In this work, the first successful separation of nitrated explosives and their degradation products using liquid chromatography is described. Through careful optimization of the separation conditions and the use of a highly efficient capillary column, baseline resolution of all 14 components of the standard explosives mixture is achieved. In addition, the phenomenon of selective fluorescence quenching is developed as a novel indirect indirect detection technique for nitrated explosives and their degradation products. A solution of the fluorophore pyrene is added through a post-column mixer and is detected by laser-induced fluorescence. The performance of this method is demonstrated for both standard and commercial explosive samples.

II. Methods

A. Reagents

Reagent-grade nitromethane (EM Science) is used as received. Individual standards of trinitroglycerine (TNG), pentaerythritol tetranitrate

(PETN), hexahydro-1,3,5-trinitro-1,3,5-triazine (RDX), octahydro-1,3,5,7-tetranitro-1,3,5,7-tetrazine (HMX), nitrobenzene (NB), 1,3-dinitrobenzene (1,3-DNB), 1,3,5-trinitrobenzene (1,3,5-TNB), 2-nitrotoluene (2-NT), 3-nitrotoluene (3-NT), 4-nitrotoluene (4-NT), 2,4-dinitrotoluene (2,4-DNT), 2,6-dinitrotoluene (2,6-DNT), 2-amino-4,6-dinitrotoluene (2-am-4,6-DNT), 4-amino-2,6-dinitrotoluene (4-am-2,6-DNT), 2,4,6-trinitrotoluene (2,4,6-TNT), and methyl-2,4,6-trinitrophenylnitramine (tetryl) are obtained in acetonitrile from Radian International LLC. Commercial formulations of ammonium nitrate/nitromethane (Kinepak), RDX (M-112-C4 and Demex 100), and 2,4,6-TNT are obtained from the Michigan State Police Laboratory and Michigan State Police Bomb Squad. Pyrene (MCB) is purified by vacuum sublimation. High purity, spectroscopic-grade acetonitrile (Baxter Healthcare, Burdick and Jackson Division) is used for all solutions and is mixed with distilled deionized water (Corning Glass Works, Model MP-3A) to prepare the mobile phases for liquid chromatography.

B. Chromatographic System

A system has been designed and constructed in order to allow for the separation and detection of analytes based on their quenching of a fluorophore (see Figure 6-1). In this system, a reciprocating piston pump (Beckman Instruments, Model 114M) delivers the mobile phase at a flow rate of ~1 μL/min. Samples are introduced by an injection valve (Valco Instruments, Model EC6W) of 1 μL volume, which is split 50:1 before proceeding to the capillary column. The column is fabricated from fused-silica capillary tubing (Hewlett-Packard, 200

μm i.d., 320 μm o.d., 1.5 m length) that is packed with a 5 μm octadecylsilica material (Shandon, Hypersil C18, 80,000 theoretical plates when using a 32.5% acetonitrile/water mobile phase). The column is maintained at a constant temperature of 28 °C in a water bath. The terminus of the column is connected to a mixing tee constructed from Teflon® tubing and packed with silanized glass wool. A solution of 2 x 10^{-4} M pyrene is delivered to this tee by a syringe pump (PE/Applied Biosystems, Model 140A) at a flow rate of ~2 μL/min. After thorough mixing, the effluent is directed to a fluorescence detector (see below) followed by a UV-visible absorbance detector (Jasco, Model UVIDEC-100-V, 254 nm).

C. Spectroscopic System

Chromatographic detection and steady-state fluorescence power measurements are achieved by using a laser-induced fluorescence spectrometer described in detail elsewhere (see Figure 6-1).[30] In this system, a helium–cadmium laser (Melles Griot, Model 3074-40M, 325 nm, 40 mW) is utilized as the excitation source with a fused-silica capillary flow cell (Polymicro Technologies, 75 μm i.d., 190 μm o.d.). Fluorescence emission is collimated, filtered to remove scattered light originating from the laser, and then refocused onto the entrance slit of a 0.34 m Czerny–Turner monochromator (Instruments SA, Model 340E, 300 groove/mm grating, 2 nm resolution). The monochromator is equipped with a photomultiplier tube (Hamamatsu, Model R-106) as well as a charge-coupled device (CCD) detector (Instruments SA, Model (A)TECCD-

2000x800-7). The CCD detector is thermoelectrically cooled and is maintained at a temperature of –40 °C. Instrument control and data acquisition are provided by a commercially available electronic interface (Instruments SA, Models Datascan 2 and CCD 2000) and associated software (Instruments SA, Spectramax for Windows, Version 3.1).

Stern–Volmer plots are prepared by integrating the fluorescence power of pyrene from 350 – 500 nm. The ratio of the integrated fluorescence power in the absence and presence of quencher is then graphed as a function of the quencher concentration. The slope of this graph is determined by linear regression in order to obtain the Stern–Volmer constant as given by equation (1-1).

III. Results and Discussion

A. Separation Optimization

Separations of the 14 component standard mixture of explosives and their degradation products were conducted using various mobile phases, allowing for precise optimization of separation conditions. The effect of mobile phase composition on the capacity factor of each component is shown in Figure 7-1. Over the range of 30 – 50% acetonitrile/water, the capacity factors are linearly related to mobile phase composition as shown in Table 7-1. The y-intercepts of the regression lines represent the predicted retention in pure water and, therefore, reflect the overall polarity of each solute. The magnitude of these intercepts is not surprising based on the structures of the solutes themselves.

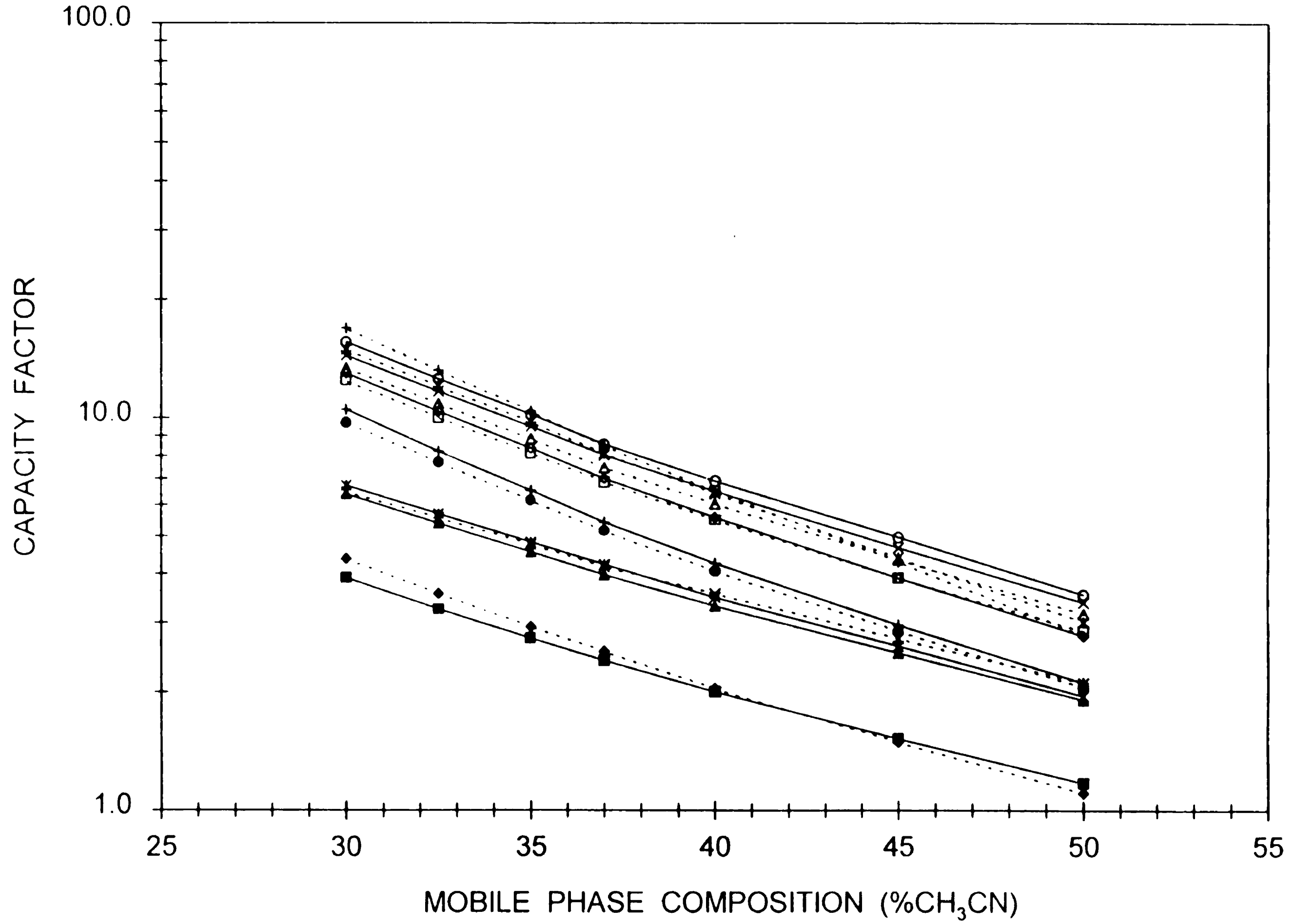

Figure 7-1: Dependence of capacity factor on mobile phase composition. Column: 1.51 m x 200 μm i.d. fused silica capillary, packed with 5 μm Shandon Hypersil C18. Mobile Phase: 30-50% acetonitrile/water, 1.0 μL/min, 30 °C. UV-visible absorbance detection: 254 nm, 0.005 ABFS. Solutes: RDX (■, –), HMX (◆, --), 1,3-DNB (▲, –), 1,3,5-TNB (X, --), NB (✱, –), 2-am-4,6-DNT (●, --), 4-am-2,6-DNT (+, –), 2,4-DNT (□, --), 2,6-DNT (◇, –), 2-NT, (△, --), 4-NT (X, –), 2,4,6-TNT (✱, --), 3-NT (○, –), and tetryl (+, --).

Table 7-1: Linear Regression of Capacity Factor as a Function of Mobile Phase Composition[a]

Explosive	Slope	Intercept	R^{2b}
RDX	-0.0267	1.39	0.995
HMX	-0.0305	1.55	0.995
1,3-DNB	-0.0266	1.60	0.997
1,3,5-TNB	-0.0246	1.54	0.998
NB	-0.0271	1.63	0.999
2-am-4,6-DNT	-0.0345	2.01	0.994
4-am-2,6-DNT	-0.0356	2.08	0.994
2,4-DNT	-0.0326	2.06	0.996
2,6-DNT	-0.0340	2.12	0.996
2-NT	-0.0319	2.07	0.996
4-NT	-0.0320	2.11	0.996
2,4,6-TNT	-0.0349	2.22	0.999
3-NT	-0.0326	2.16	0.996
tetryl	-0.0394	2.40	0.999

[a] see Figure 7-1 for data and chromatographic conditions

[b] R^2, correlation coefficient

For example, the addition of a methyl group tends to decrease water solubility and, therefore, increase the y-intercept (i.e., NB < 2-NT, 1,3-DNB < 2,4-DNT, and 1,3,5-TNB < 2,4,6-TNT). Conversely, the addition of nitro groups tends to increase water solubility and decrease the y-intercept (i.e., NB > 1,3-DNB > 1,3,5-TNB).

The negative slopes of the regression lines imply that all solutes become less retained with increasing concentration of acetonitrile. Some solutes, particularly 2,4,6-TNT and tetryl, experience a larger decrease in retention with increasing concentration of acetonitrile than neighboring solutes. In contrast, 1,3,5-TNB shows a markedly lower sensitivity to acetonitrile. Another interesting trend is that the slopes for the nitrobenzenes increase as the degree of nitration increases (i.e., NB < 1,3-DNB < 1,3,5-TNB). However, the opposite trend occurs for the nitrotoluenes (2-NT > 2,4-DNT > 2,4,6-TNT). Overall, these different slopes reflect the selectivity of the mobile and stationary phases for these components. As will be shown, this selectivity, combined with the high efficiency of the capillary column, allows complete baseline resolution of the 14 component mixture.

From the data summarized in Table 7-1, it is possible to calculate the resolution (R) of various solute pairs using the following equation:[31]

$$R = \left(\frac{\sqrt{N}}{4}\right)\left(\frac{\alpha - 1}{\alpha}\right)\left(\frac{k}{1+k}\right) \tag{7-1}$$

where N is the number of theoretical plates, α is the selectivity of a particular solute pair (where $\alpha = k_1 / k_2$ and $k_1 > k_2$), and k is the average capacity factor of the two solutes.

By graphing the resolution of each solute pair as a function of mobile phase composition, a "window diagram" can be formed (see Figure 7-2).[32,33] In this diagram, mobile phase compositions that produce co-elutions are located where the resolution of a particular solute pair reaches unity and intersects the x axis. In contrast, the mobile phase composition that generates the maximum resolution is located where the resolution of two limiting pairs intersect to create the tallest apex or "window" in the diagram. Despite the complexity of this figure, it can be seen that the optimal resolution is achieved at 32.5% acetonitrile/water. The critical pairs are predicted to be 1,3-DNB/1,3,5-TNB and 1,3,5-TNB/NB, with resolutions of 1.63 and 1.52, respectively, assuming that a column with 80,000 theoretical plates is utilized for the separation.

A more global measure of separation quality that takes into account the resolution of all solutes, rather than just the critical pairs, can be derived from the first term of the chromatographic resolution statistic (CRS1) of Schlabach and Excoffier:[34]

$$CRS1 = \sum_{i=1}^{n-1} \left[\frac{(R_{i,i+1} - R_{opt})^2}{(R_{i,i+1} - R_{min})^2 R_{i,i+1}} \right] \tag{7-2}$$

where n is the number of solutes, $R_{i,i+1}$ is the resolution of adjacent solute pairs, R_{opt} is the desired resolution, and R_{min} is the minimum acceptable resolution.

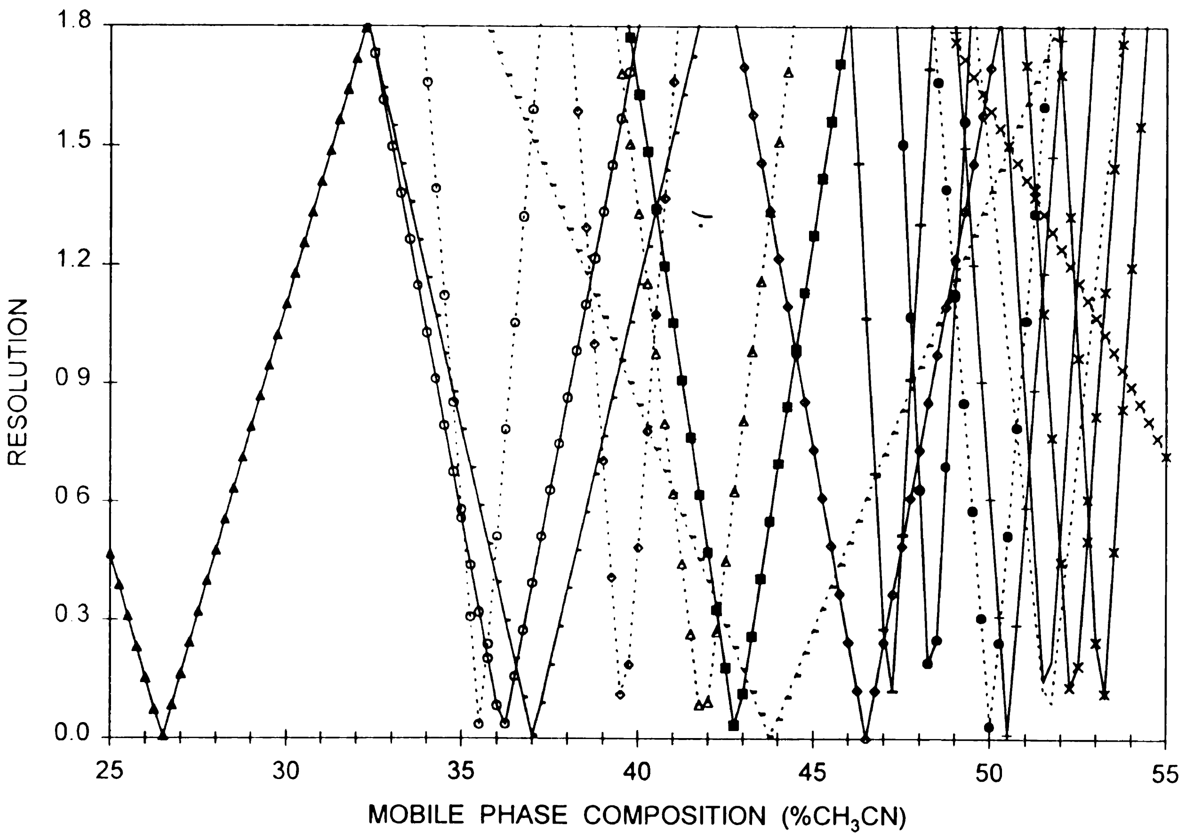

Figure 7-2: Dependence of the resolution according to equation (7-1) on mobile phase composition. Chromatographic conditions as given in Figure 7-1. Solutes: RDX/HMX (■, –), HMX/1,3-DNB (◆, –), 1,3-DNB/1,3,5-TNB (▲, –), 1,3-DNB/2-am-4,6-DNT (X, –), 1,3-DNB/4-am-2,6-DNT (✳, –), 1,3,5-TNB/NB (-, –), 1,3,5-TNB/2-am-4,6-DNT (–, –), 1,3,5-TNB/4-am-2,6-DNT (● –), NB/2-am-4,6-DNT (+, –), NB/4-am-2,6-DNT (–), NB/2,4-DNT (■ --), NB/2,4,6-TNT (◆ --), NB/tetryl (▲, --), 2-am-4,6-DNT/4-am-2,6-DNT (X, --), 4-am-2,6-DNT/2,4-DNT (✳ --), 2,4-DNT/2,6-DNT (-, --), 2,4-DNT/2,4,6-TNT (–, --), 2,4-DNT/tetryl (●, --), 2,6-DNT/2,4,6-TNT (+, --), 2,6-DNT/tetryl (--), 2-NT/4-NT (□, –), 2-NT/2,4,6-TNT (◇, –), 2-NT/3-NT (△, –), 4-NT/2,4,6-TNT (○, –), 4-NT/3-NT (□, --), 4-NT/tetryl (◇, --), 2,4,6-TNT/tetryl (△, --), and 3-NT/tetryl (○, --).

Based on the form of this equation, CRS1 will reach a minimum value of zero as all $R_{i,i+1}$ approach the desired resolution R_{opt}.

The CRS1 for this separation is shown as a function of mobile phase composition in Figure 7-3 with selected values for R_{opt} of 1.5 and R_{min} of 0.0. The minimum in this graph is observed in the range of 31-33% acetonitrile/water, which represents the region where the best possible resolution is achieved for all components in the mixture. Furthermore, because this optimal region is relatively flat, small variations in mobile phase composition will not adversely affect the quality of the separation. Finally, and in agreement with the window diagram in Figure 7-2, the global minimum is located at 32.5% acetonitrile/water.

In contrast, the U.S. EPA method recommends the use of a conventional LC column and a 50% methanol/water mobile phase. Based on the differing solubility parameters for methanol and acetonitrile,[35] this would correspond to a mobile phase composition of approximately 39% acetonitrile/water. Although there is a local optimum located at this mobile phase composition (see Figure 7-3), it does not allow for complete resolution of the mixture. Specifically, the solute pairs 1,3,5-TNB/NB and 4-NT/tetryl are predicted to attain resolutions of only 0.6 when separated on a column with 80,000 theoretical plates.

It is also important to note that a distinct sensitivity to temperature is seen in this separation. As temperature is increased from 30 to 35 °C at the same mobile phase composition, the capacity factors of all solutes decrease by an average of –4.7%. However, some of the solutes change as little as –3.1%

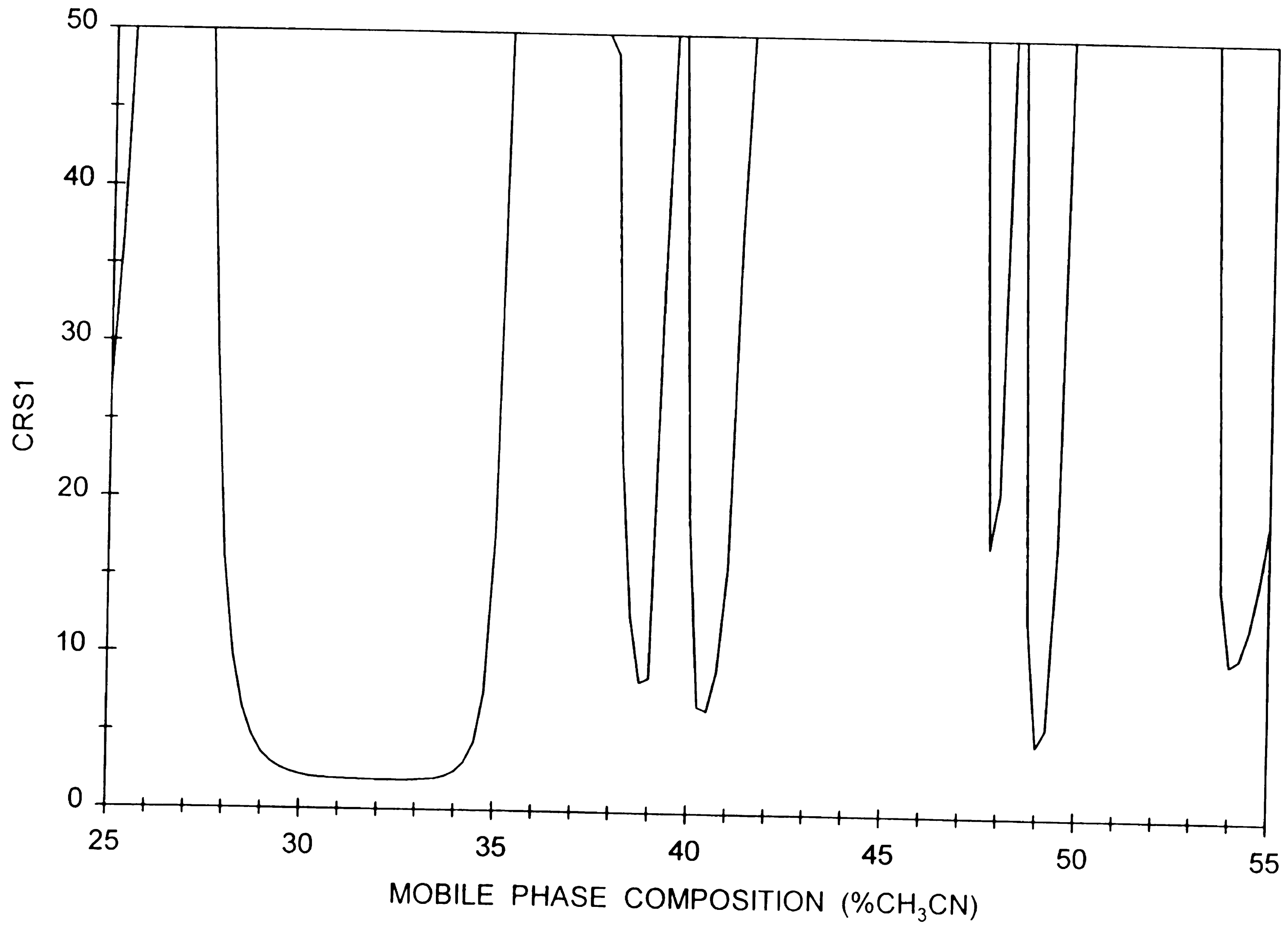

Figure 7-3: Dependence of CRS1 according to equation (7-2) on mobile phase composition. Chromatographic conditions as given in Figure 7-1.

whereas others change as much as –8.2%. Accordingly, this leads to a significant change in resolution for certain solute pairs. Most notably, the resolution of 4-NT/2,4,6-TNT decreases from 1.84 to 0.79 and the resolution of 3-NT/tetryl decreases from 3.13 to 1.37 over this temperature range. As a result, column temperature must be carefully controlled and the optimum was determined to be 28 °C for a mobile phase composition of 32.5% acetonitrile/water.

The ability of the optimal mobile phase composition and temperature to achieve the best overall separation was confirmed experimentally in Figure 7-4 using a standard mixture of explosives. In this figure, baseline resolution of all 14 components is successfully demonstrated for the first time using liquid chromatography. As predicted, the solutes that possess the limiting resolution in the mixture are 1,3-DNB/1,3,5-TNB and 1,3,5-TNB/NB, for which the measured resolutions were 2.1 and 1.6, respectively.

B. Steady-State Fluorescence Quenching Studies

The measured quenching constants for pyrene with some representative nitrated explosives are summarized in Table 7-2. In general, quenching constants tend to increase from aliphatic to nitramine to nitroaromatic structures. The ability of aromatic systems to serve as more efficient quenchers than their aliphatic counterparts has been observed previously.[36] This increased efficiency is likely due to the ease with which aromatic quenchers can serve as electron acceptors in charge-transfer complexes with PAH fluorophores. Efficient coupling of the π electrons on the fluorophore and quencher create a strong

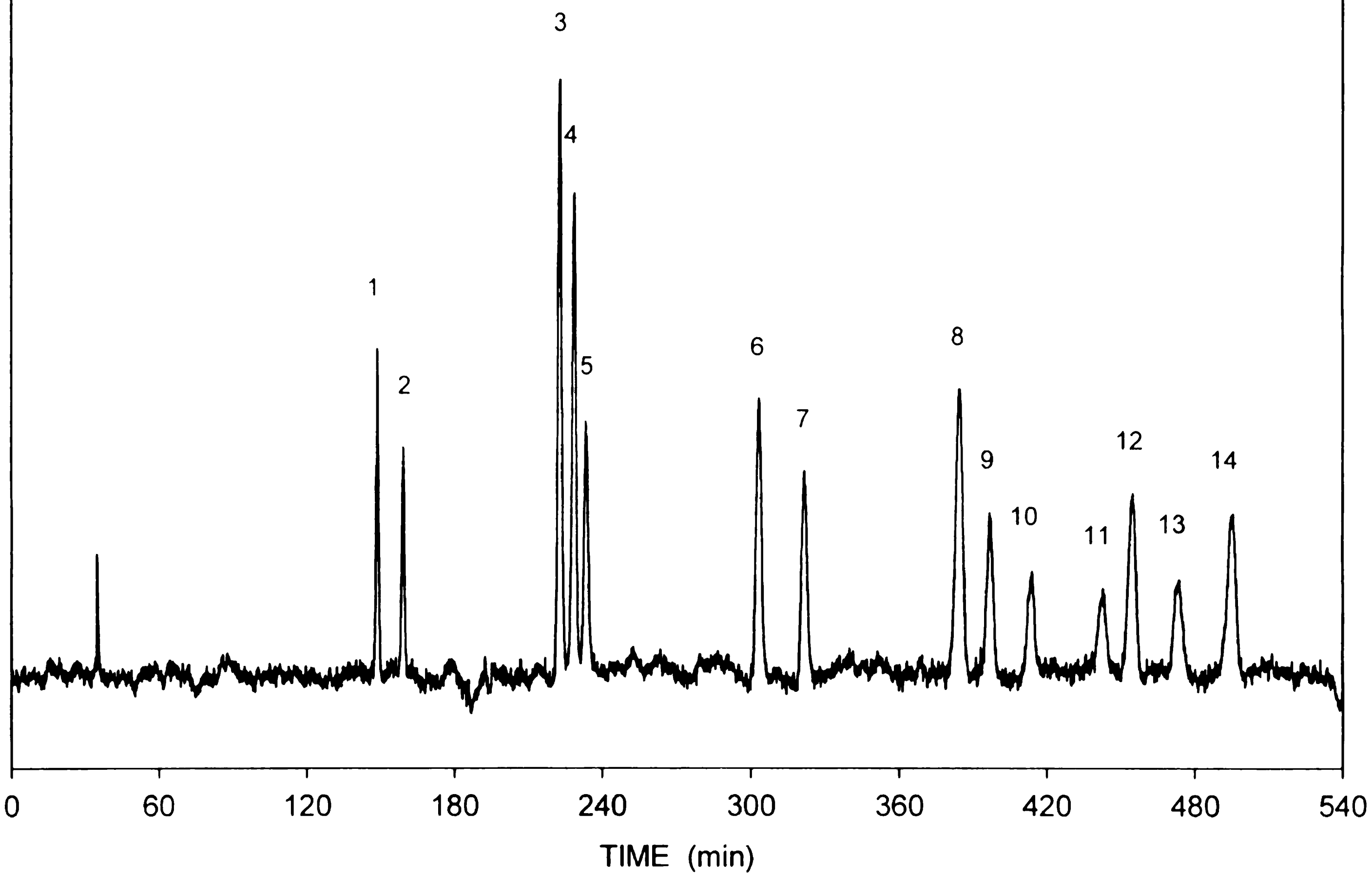

Figure 7-4: Separation of a standard mixture of explosives and degradation products (EPA 8330). Mobile Phase: 32.5% acetonitrile/water, 1.0 μL/min, 28 °C. Other chromatographic conditions as given in Figure 7-1. Solutes: (1) RDX, (2) HMX, (3) 1,3-DNB, (4) 1,3,5-TNB, (5) NB, (6) 2-am-4,6-DNT, (7) 4-am-2,6-DNT, (8) 2,4-DNT, (9) 2,6-DNT, (10) 2-NT, (11) 4-NT, (12) 2,4,6-TNT, (13) 3-NT, (14) tetryl.

Table 7-2: Quenching Constants for Pyrene with Nitrated Explosives in Acetonitrile

Explosive	Abbreviation	Classification	K_d (M^{-1})[a]	b[b]	R^2[c]	k_d (x 10^9 $M^{-1}s^{-1}$)[d]
nitromethane	NM	aliphatic	64	1.00	0.986	5.4
trinitroglycerine	TNG	aliphatic	178	1.00	0.995	15.0
pentaerythritol tetranitrate	PETN	aliphatic	110	0.99	0.957	9.2
cyclotrimethylene trinitramine	RDX	nitramine	196	0.98	0.999	16.5
cyclotetramethylene tetranitramine	HMX	nitramine	105	1.01	0.956	8.8
nitrobenzene	NB	nitroaromatic	332	1.00	0.999	27.9
2-nitrotoluene	2-NT	nitroaromatic	307	1.02	1.000	25.8
2,4-dinitrotoluene	2,4-DNT	nitroaromatic	386	0.99	1.000	32.4
2,4,6-trinitrotoluene	2,4,6-TNT	nitroaromatic	394	0.98	0.999	33.1

[a] K_d, Stern–Volmer quenching constant from Equation (1-1)

[b] b, intercept from Equation (1-1)

[c] R^2, correlation coefficient from Equation (1-1)

[d] k_d, bimolecular quenching rate constant from Equation (1-1)

thermodynamic driving force for the formation of such an exciplex, with subsequent deactivation of the fluorophore.[29,37]

Furthermore, quenching constants tend to increase with the number of nitro groups on the quencher molecule. This can be clearly seen with 2-NT, 2,4-DNT, and 2,4,6-TNT, where the nitro groups are linked directly to an aromatic ring and can effectively increase the overall electron affinity of the molecule. However, some quenchers with more nitro groups are actually less efficient than similar molecules with fewer nitro groups (e.g., TNG < PETN, RDX < HMX). This reflects the fact that dynamic or excited-state quenching is a diffusion-controlled process. Therefore, the diffusion coefficient of the quencher as well as its electronic properties determine its overall efficiency. It is clear from these data that the electron-withdrawing ability imparted by an additional nitro functionality is not sufficient to overcome the reduced diffusion coefficient of the larger quencher molecule.

Another interesting phenomenon discovered in these studies is that the quenching constants of some quenchers exhibit a wavelength dependence. Figures 7-5 and 7-6 show the results obtained when an unquenched spectrum of pyrene is divided by a spectrum quenched by RDX and NB, respectively. For the RDX quencher, the divided result is flat, featureless, and centered about a ratio of P°/P that is appropriate for the concentration used. However, the result for NB has definite structure which mirrors that of an unquenched pyrene spectrum, although the peaks are shifted to shorter wavelengths by

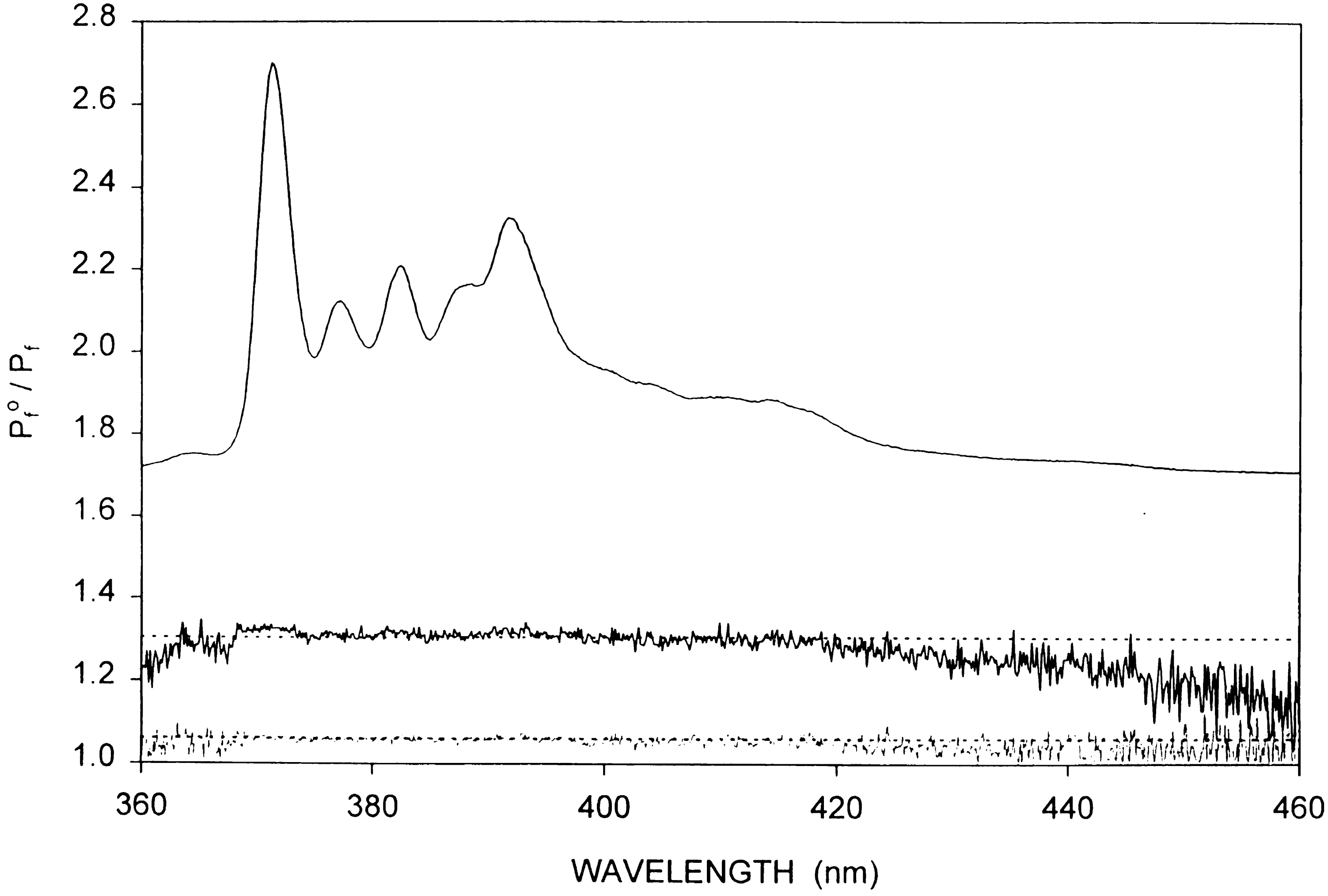

Figure 7-5: Effect of RDX on the emission spectrum of pyrene. The lower trace shows the division of an unquenched pyrene spectrum (P^o_f) by a quenched spectrum (P_f) with 0.31 mM RDX. The middle trace shows division by a quenched spectrum with 1.6 mM RDX. The upper trace is an unquenched spectrum of pyrene. Dashed lines indicate the value of P^o_f / P_f appropriate for the quencher concentration according to Table 7-2.

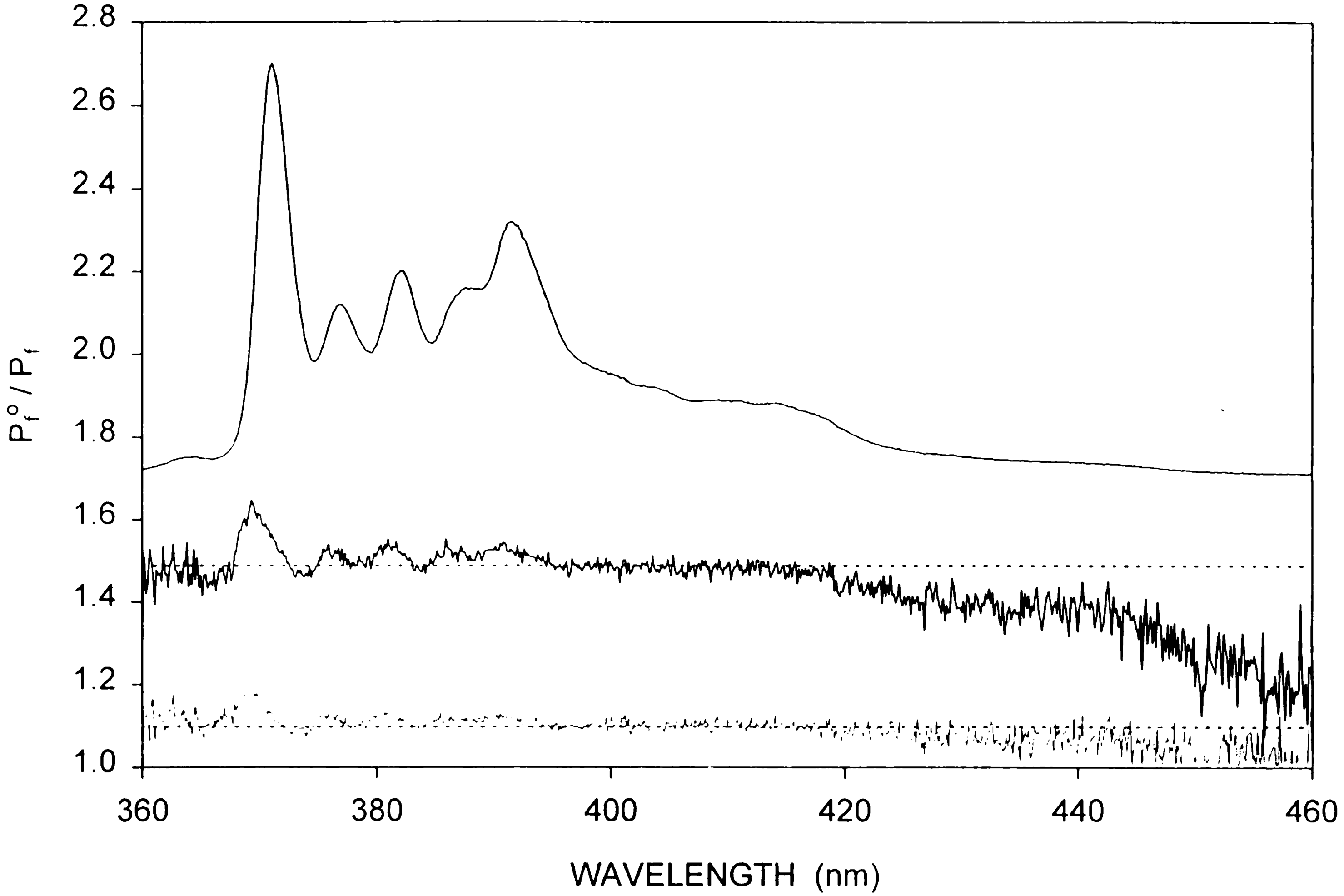

Figure 7-6: Effect of nitrobenzene on the emission spectrum of pyrene. The lower trace shows the division of an unquenched pyrene spectrum (P^o_f) by a quenched spectrum (P_f) with 0.30 mM NB. The middle trace shows division by a quenched spectrum with 1.5 mM NB. The upper trace is an unquenched spectrum of pyrene. Dashed lines indicate the value of P^o_f / P_f appropriate for the quencher concentration according to Table 7-2.

approximately 1.4 nm. Importantly, this wavelength-dependent quenching behavior is seen only with nitroaromatic quenchers. Furthermore, the residual structure tends to decrease with the degree of substitution of the explosive (e.g., NB > 2-NT > 2,4-DNT > 2,4,6-TNT).

Various explanations for this phenomenon have been considered. One possibility is the formation of ground-state complexes between pyrene and the nitroaromatic quenchers. This static complexation could result in a shift of the pyrene emission and, hence, a residual structure in the P°/P ratio. However, the high linearity of the Stern–Volmer plots (see Table 7-2) is a strong indication that only one quenching mechanism (i.e., dynamic) is present for these systems. No evidence has been found in the literature for the formation of ground-state complexes between PAHs and nitrated compounds in polar solvents such as acetonitrile. In addition, those quenchers with additional nitro groups (e.g., 2,4,6-TNT) would be expected to have higher electron affinity, an increased amount of static complexation and, hence, more pronounced residual structure. In fact, the reverse trend is experimentally observed. All of these arguments suggest that ground-state complexation is not the origin of the residual structure in the P°/P ratio.

A second possible explanation is that the UV-visible absorbance of the nitroaromatics perturbs the observed emission of pyrene through secondary filtering, which becomes apparent when the spectra are divided. The UV-visible absorbance spectra of RDX, NB, and 2,4,6-TNT indicate that the nitroaromatic quenchers do indeed absorb in the region where pyrene emits. However, their

absorbance tends to increase with the number of nitro groups, which does not correlate with the observation that the residual structure seen in the P°/P ratio decreases with additional nitro groups on the quencher. Moreover, numerical simulation of the effect of secondary filtering on fluorescence emission suggests that the shape of the divided fluorescence spectra would be identical to that of the absorption spectrum of the quencher rather than the emission spectrum of pyrene. Hence, secondary filtering cannot be responsible for this effect.

Another spectral effect that can be considered is a shift in the emission spectrum of pyrene as a consequence of dynamic quenching. After excitation of the fluorophore to an initial or Franck–Condon excited state, the surrounding solvent molecules rearrange to produce a more stable, solvated excited state. If the fluorophore is strongly quenched, it may exhibit a shift towards shorter wavelengths as the population that successfully emits is artificially perturbed towards those molecules with shorter lifetimes, less solvent relaxation, and higher energies.[38] If this were the case, however, any efficient quencher such as RDX or HMX would be expected to produce this effect. In addition, the residual structure in the P°/P ratio would be expected to increase with the Stern–Volmer quenching constant. Neither prediction is true in these experiments. Furthermore, numerical simulation suggests that a shift of the emission spectrum towards shorter wavelengths would result in a P°/P ratio that is shifted to longer wavelengths with respect to the original fluorescence spectrum. As this is clearly not the case, it seems unlikely that incomplete relaxation of the Franck–Condon excited state is responsible for the residual structure in the P°/P ratio.

A final explanation, which appears to be the most likely, is the occurrence of specific interactions between excited-state pyrene and the nitroaromatic quenchers. This conjecture is supported by various experimental observations. First, pyrene itself serves as a probe of solvent polarity through small changes in the fluorescence power of the individual vibronic bands.[39,40] Specifically, the ratio of the first and third band (I/III ratio) is known to decrease in nonpolar solvents. In these experiments, the I/III ratio of pyrene decreases systematically by –0.07 with the addition of 0 to 1.77 mM nitrobenzene, whereas that with RDX and other nonaromatic quenchers remains relatively constant (± 0.02). However, nitropropane (a molecule with similar polarity to nitrobenzene but no aromatic character) produces a similar change in the I/III ratio, but no residual structure in the P°/P ratio. Therefore, the ability of nitroaromatic molecules to affect the local environment of pyrene is not the sole factor that determines the residual structure.

Upon closer examination of the pyrene spectra, a small but measurable change is observed in the wavelength of the five vibronic bands upon addition of the nitroaromatic quenchers. Specifically, the bands of the pyrene emission spectrum consistently shift towards longer wavelengths in the presence of nitrobenzene, which is not observed with RDX or nitropropane. Numerical simulation of the effect of shifting the emission spectrum of pyrene to longer wavelengths by one CCD pixel (~0.15 nm) produces residual structure that is very similar to the experimental results shown in Figure 7-6. When taken together, these observations imply that nitroaromatic compounds not only affect the local environment of pyrene but also partially stabilize its excited state, thereby shifting its emission to longer wavelengths.

The greatest impact of this phenomenon is that pyrene responds selectively to nitroaromatic species. This photophysical effect should enable the selective identification of nitroaromatic quenchers in the presence of other types of nitroaliphatic or nitramine explosives. Given that quenching techniques typically do not enable the identification of the species responsible for the reduction in emission intensity, this phenomenon has clear potential for the analysis of explosives.

C. Indirect Fluorescence Quenching Detection

The most common method of detection in liquid chromatography is UV-visible absorbance, which has been established by the U.S. EPA for use with nitrated explosives. However, the pathlength of a typical flow cell for capillary liquid chromatography is on the order of 100 μm, which greatly limits the sensitivity of UV-visible absorbance. The use of laser-induced fluorescence greatly improves sensitivity due to the high intensity of the excitation source and intrinsically low background. However, not all molecules are naturally fluorescent and this restricts the use of fluorescence to highly conjugated or chemically labeled analytes. It is within this context that fluorescence quenching can provide contrasting selectivity to traditional UV-visible absorbance and fluorescence by generating negative signals based on the deactivation of a fluorophore by a non-fluorescent analyte.

Before the performance of indirect fluorescence quenching is demonstrated, some discussion of the theoretical aspects of this detection scheme is warranted. By rearrangement of the Stern–Volmer relation in equation (1-1), the fluorescence power in the presence of a quencher (P_f) is given by:

$$P_f = \frac{P_f^\circ}{\left(1 + K_d C_q\right)} \tag{7-3}$$

where all variables are as defined previously. The indirect fluorescence quenching signal (S_{FQ}) can be defined as the difference between the unquenched (background) fluorescence power and the quenched fluorescence power:

$$S_{FQ} = P_f^\circ - P_f \tag{7-4}$$

By substitution of equation (7-3) into equation (7-4):

$$S_{FQ} = P_f^\circ\left(1 - \frac{1}{\left(1 + K_d C_q\right)}\right) \tag{7-5}$$

If S_{FQ} is small, it can be assumed that the noise of the quenched signal (N_{FQ}) is equal to that of the unquenched fluorescence background (N_f°) (i.e., $N_{FQ} \rightarrow N_f^\circ$ as $S_{FQ} \rightarrow 0$). Therefore, the signal-to-noise expression for the indirect fluorescence quenching signal is:

$$\frac{S_{FQ}}{N_{FQ}} = \left(\frac{P_f^\circ}{N_f^\circ}\right)\left[1 - \frac{1}{\left(1 + K_d C_q\right)}\right] \tag{7-6}$$

The form of equation (7-6) suggests that the signal-to-noise ratio for the indirect quenching signal is linearly dependent on and ultimately limited by the signal-to-noise ratio of the fluorescence background.

In our system, the fluorescence background is generated by mixing a pyrene solution with the effluent of a capillary liquid chromatography column. Therefore, one prerequisite for a high signal-to-noise ratio is thorough mixing of the liquid streams in order to minimize local fluctuations in the concentration of pyrene. As a result, a low volume mixer is used to create high linear velocities. In addition, a small amount of glass wool helps to disperse the flow streams and enhance mixing. A second important method of improving the signal-to-noise ratio of the indirect signal is to maximize the sensitivity and throughput of the spectroscopic system.[30] Therefore, the concentration of pyrene, the spectral bandpass of the monochromator, and the integration time of the CCD detector are all chosen to be relatively large. In this way, performance is achieved that is at the upper boundary of the shot-noise limited regime.[30]

The linear range of this technique is limited by S_{FQ} which, in turn, depends upon P_f° according to equation (7-6). Therefore, as in traditional indirect fluorescence methods,[41] the maximum linear range for indirect quenching signals is achieved at large values of P_f°. Within the shot-noise limited regime, an increase in P_f° results in an increase in the signal-to-noise ratio of the fluorescence background (P_f° / N_f°). Thus, the sensitivity of indirect quenching as expressed by the signal-to-noise ratio (S_{FQ} / N_{FQ}) scales linearly with the background signal, in contrast to traditional indirect fluorimetry.[41] Hence, when

using this indirect technique, there is no need to compromise between sensitivity and linear range.

The result of this optimization of the indirect fluorescence quenching detector is illustrated in Figure 7-7, which shows the separation of a standard mixture of explosives and their degradation products. The concentration is 3.0 mg/mL, which corresponds to an injected mass of 60 ng per analyte. Taking into account the dilution due to the liquid chromatography column and the mixing tee, the actual concentration of the analytes at the detector ranges from 5.5 to 14 μg/mL. Under the conditions of this separation, it is evident that fluorescence quenching offers greater sensitivity than UV-visible absorbance. Indeed, the average signal-to-noise ratio for the chromatogram with indirect fluorescence quenching detection is 310, whereas that with UV-visible absorbance is 7.3. Based on these data, equation (7-6) can be used to predict the concentration of explosives that would yield an average signal-to-noise ratio of 3 to estimate the detection limit of the fluorescence quenching detector. For this system, that concentration would be 71 ng/mL after dilution by the column and mixing tee, corresponding to an injected mass of 0.44 ng. Furthermore, as each detector relies upon a different photophysical phenomenon to give rise to the signal, the selectivity of the fluorescence quenching detector provides a useful contrast with that of the UV-visible absorbance instrument. In particular, the nitroaromatic explosives tend to have very large quenching constants and, as such, are preferentially detected by using this indirect method.

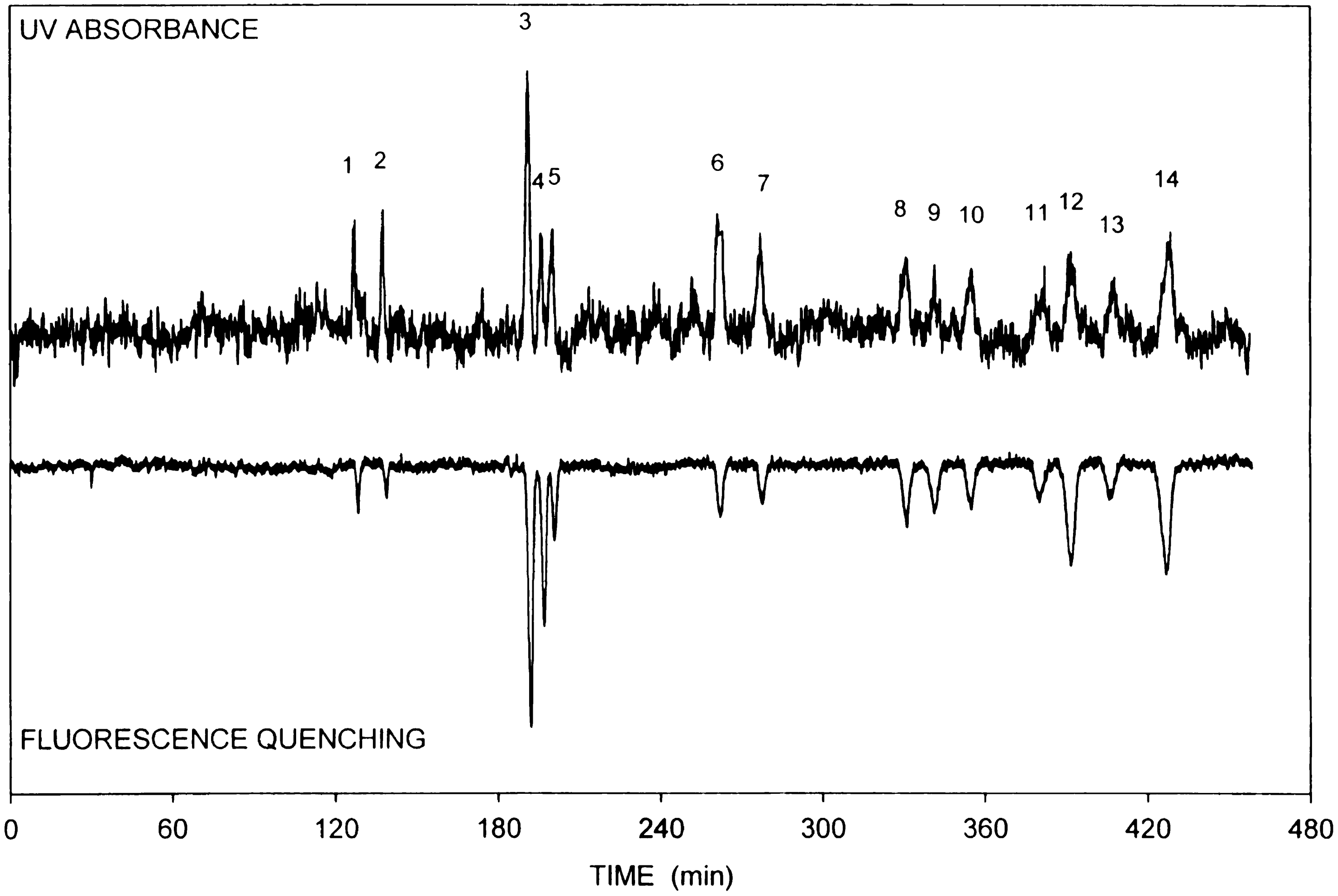

Figure 7-7: Comparison of sensitivity and selectivity of UV-visible absorbance and fluorescence quenching detectors using a 3.0 mg/mL solution of explosives and their degradation products (EPA 8330). Mobile phase: 32.5% acetonitrile/water with 100% acetonitrile added post-column, 3.8 μL/min, 28 °C (upper trace); 32.5% acetonitrile/water with 2 x 10^{-4} M pyrene in acetonitrile added post-column, 3.8 μL/min, 28 °C (lower trace). Indirect fluorescence quenching detection: 325 nm λ_{ex}, 374 nm λ_{em}, 100 μA full scale. Other chromatographic conditions as given in Figure 7-4.

D. Analysis of Nitrated Explosives

The application of this methodology to the analysis of commercially available explosives is shown in Figures 7-8 to 7-11. The chromatograms obtained from acetonitrile extracts of explosives such as these can be used to identify which energetic compounds are present or to draw conclusions as to the origin of the sample. For example, it is known that the military-grade explosive C4 (M112) and the commercial explosive Demex 100 both use RDX as their primary energetic compound. However, it is interesting to note that a small but detectable level of HMX was seen in the C4 sample (Figure 7-8), distinguishing it from the other RDX based explosive (Figure 7-9). Currently, the only U.S.-based producer of RDX is the Holsten Army Ammunition Plant in Kingsport, TN. Their synthesis for RDX is known to introduce several percent of HMX into the final product. However, as HMX is also a powerful high explosive no effort is made to remove it.[42] Therefore, the presence of HMX in the C4 sample confirms that it is domestically produced and intended for military use. In contrast, the Demex sample (which lacks HMX) is not of U.S. origin.

In contrast to most high explosives that use large, heavily nitrated molecules as their energetic compounds, Kinepak is a binary mixture of ammonium nitrate and nitromethane. While the signals are weak, both nitrate and nitromethane generate clear indirect fluorescence quenching signals before and after the solvent peak, respectively (Figure 7-10). It is also worthy of note that UV-visible absorbance is unable to detect either compound present in this explosive. Hence, the indirect quenching detection method not only

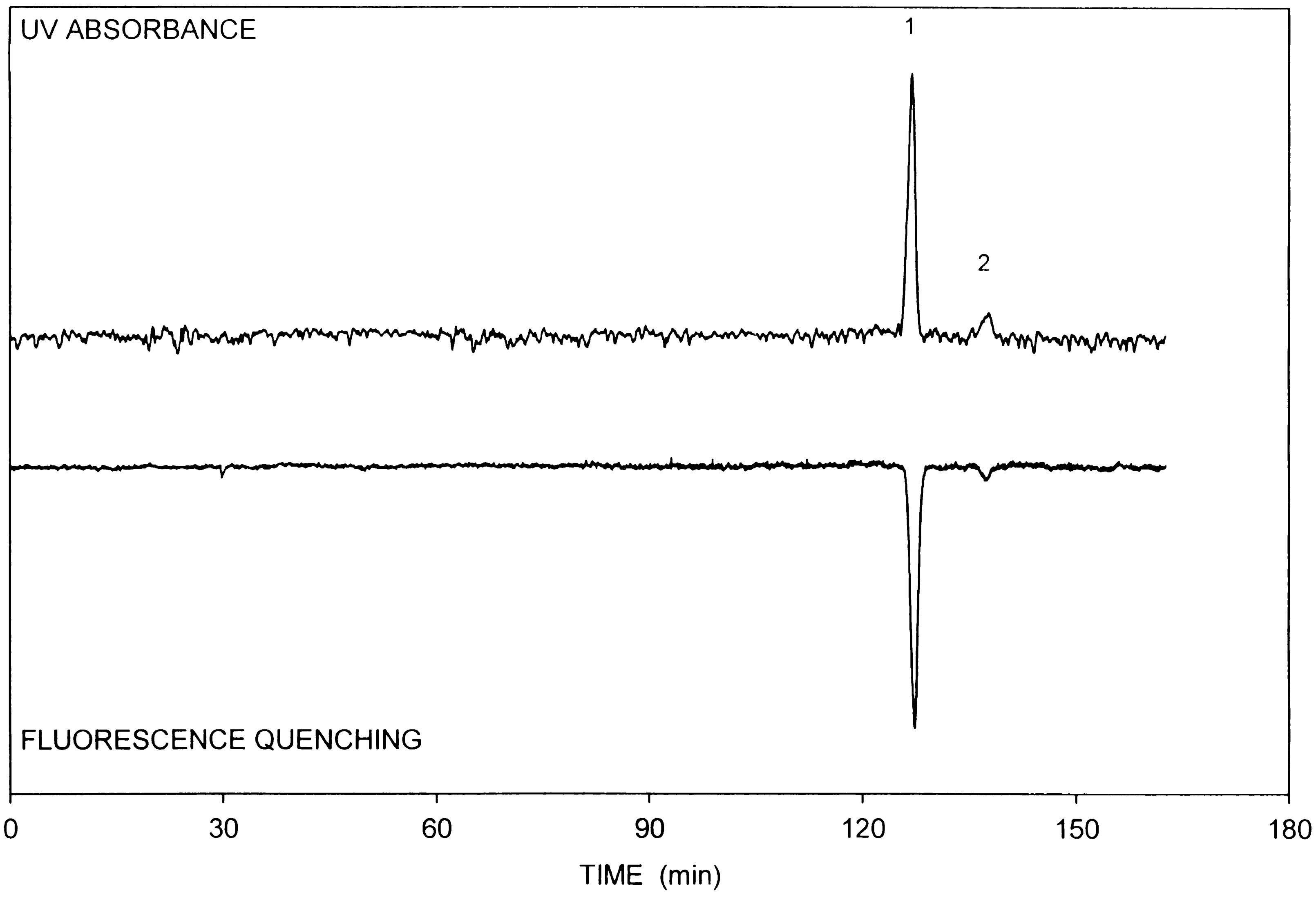

Figure 7-8: Analysis of an acetonitrile extract of C4(M112) explosive. Chromatographic conditions as given in Figure 7-7. Explosives: (1) RDX, (2) HMX.

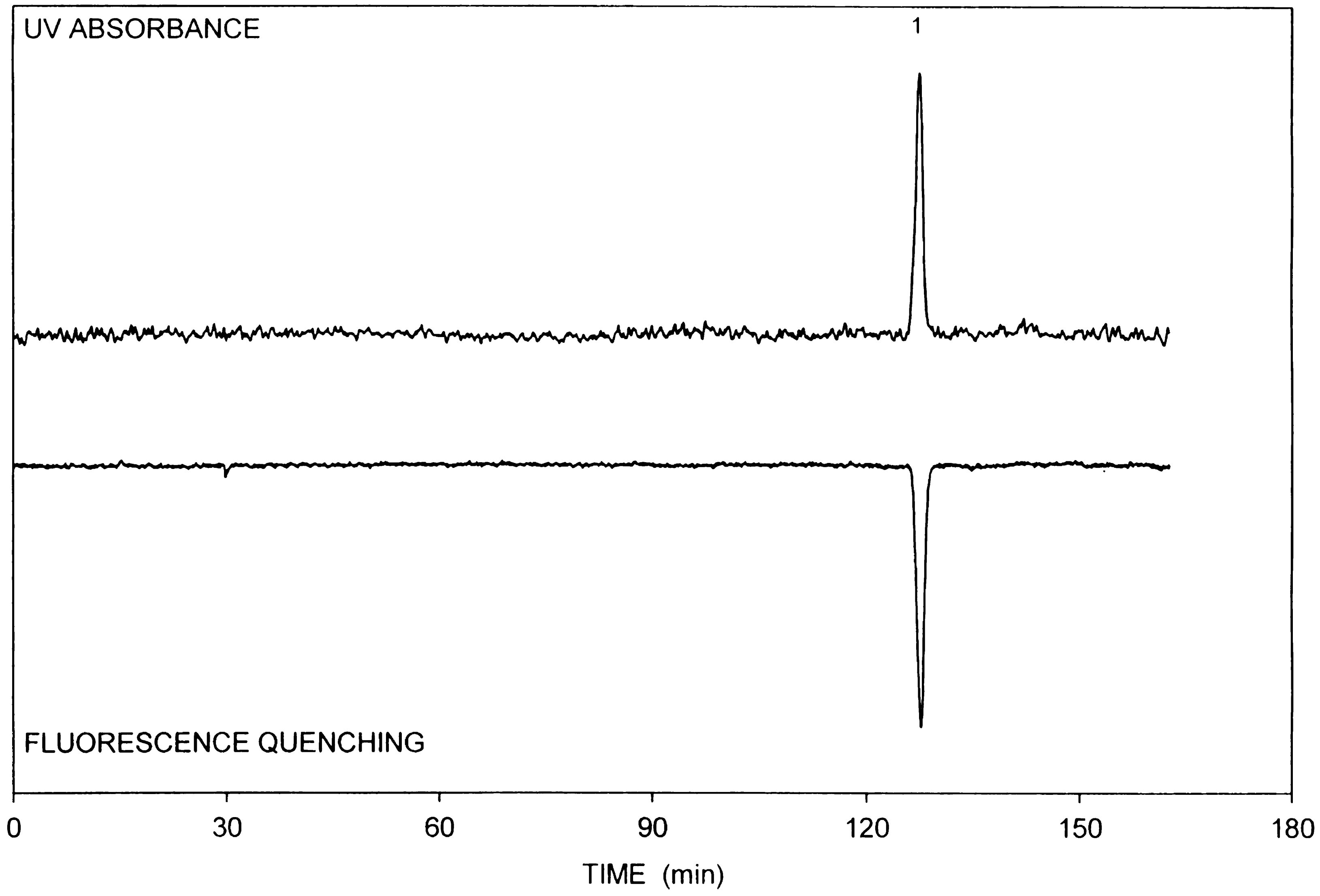

Figure 7-9: Analysis of an acetonitrile extract of Demex 100 explosive. Chromatographic conditions as given in Figure 7-7. Explosives: (1) RDX.

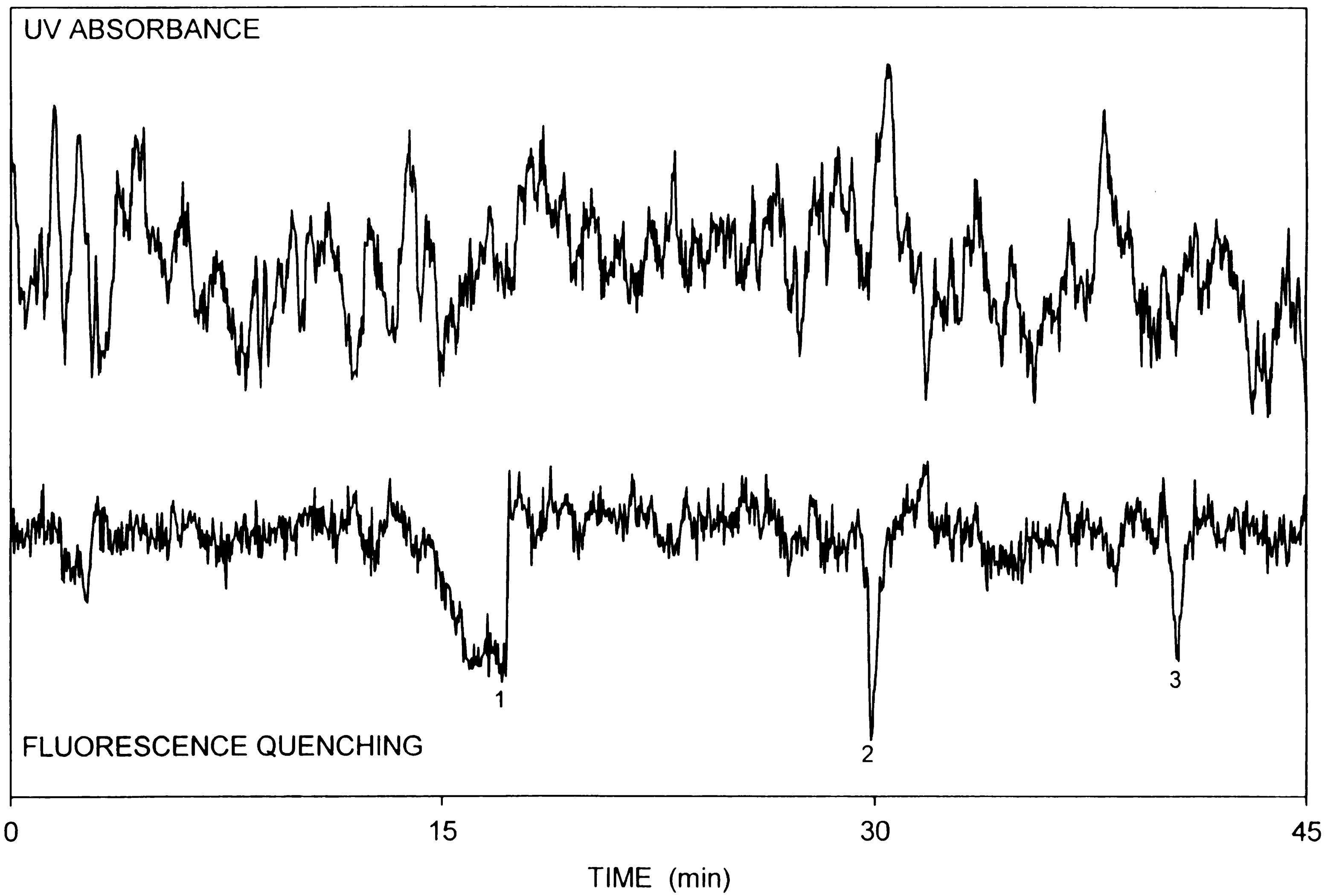

Figure 7-10: Analysis of an acetonitrile extract of Kinepak explosive. UV-visible absorbance detection at 220 nm, other chromatographic conditions as given in Figure 7-7. Explosives: (1) ammonium nitrate, (2) acetonitrile, (3) nitromethane.

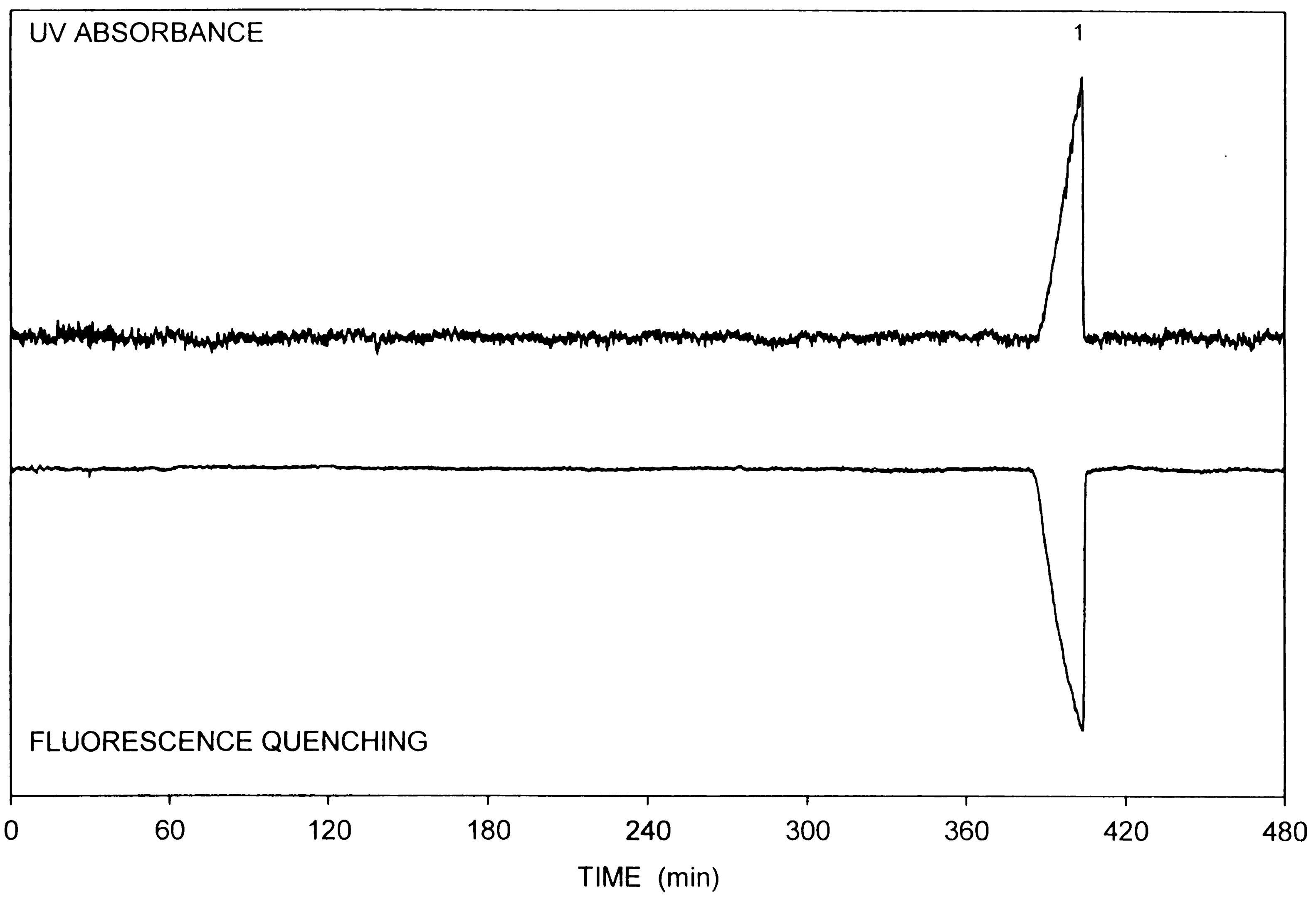

Figure 7-11: Analysis of an acetonitrile extract of commercial-grade TNT. Chromatographic conditions as given in Figure 7-7. Explosives: (1) 2,4,6-trinitrotoluene.

demonstrates greater sensitivity than UV-visible absorbance, but also the ability to detect both inorganic and organic materials.

The extract obtained from a commercial sample of TNT yields a single peak at a retention time appropriate for 2,4,6-trinitrotoluene (Figure 7-11). There is no evidence of either reductive or oxidative degradation products, which would be more common in an environmentally weathered sample. It is also noteworthy that the peak observed for TNT is highly asymmetric (fronting). One possible cause of this asymmetry is the presence of other TNT isomers that are not fully separated from the 2,4,6-TNT isomer. To examine this possibility, the sample was analyzed by ^{1}H NMR spectroscopy and confirmed to contain only the 2,4,6-TNT isomer. A second explanation is that a nonlinear isotherm may govern the interactions of 2,4,6-TNT with the stationary phase. Ideally, the concentration of solute in the stationary phase is linearly dependent on the concentration of solute in the mobile phase. However, when this is not the case, asymmetric peak shapes result. In particular, the fronting shape of 2,4,6-TNT implies that this solute has a greater tendency for self-association than for association with the octadecylsilica stationary phase. Therefore, as the concentration of the solute increases, there is an increased thermodynamic driving force for additional solute molecules to partition into the phase. This behavior is characteristic of a concave or Brunauer–Emmett–Teller (BET) Type III isotherm.[43-45] To examine this possibility, increasingly dilute samples were injected and the peak asymmetry was measured. On close inspection, even the most dilute explosive samples demonstrate a small persistent degree of

asymmetry for 2,4,6-TNT and the closely related explosive tetryl (see Figures 7-5 and 7-8). Both 2,4,6-TNT and tetryl have strong electron-withdrawing groups linked to an aromatic ring. The aromatic ring is highly electrophilic, whereas the nitro and nitramine groups are good electron donors. Therefore, it seems likely that these solutes would form stable charge-transfer complexes upon self-association. This suggests that a nonlinear isotherm is the most likely cause of the highly asymmetric peak shape for 2,4,6-TNT in Figure 7-11.

IV. Conclusions

Nitrated explosives are of intense interest to the environmental and forensic communities, but the methods of separation and detection for these compounds remain underdeveloped. Only after careful optimization of the mobile phase composition, temperature, and the application of a highly efficient capillary column were all 14 components of a standard mixture of explosives fully resolved in this study. This represents the first time liquid chromatography has successfully been used to separate this mixture, albeit at the cost of a lengthy analysis time.

A novel form of indirect detection based on fluorescence quenching was also evaluated. The ability of nitrated compounds to serve as efficient electron acceptors makes them powerful quenchers of fluorescence from PAHs such as pyrene. Stern–Volmer quenching constants follow systematic trends which increase with either the degree of nitration or the relative diffusion coefficient of the quencher. Furthermore, nitroaromatic quenchers displayed a unique wavelength dependence in their quenching constants as reflected in residual

structure after dividing unquenched and quenched emission spectra. This selective response appears to be based on interactions of the nitroaromatic quenchers with excited-state pyrene molecules, which stabilize the excited-state and shift the vibronic bands to slightly longer wavelengths. When adapted as an indirect detection method for liquid chromatography, fluorescence quenching has proven to be more sensitive than UV-visible absorbance for nitrated explosives. This is crucial as both environmental and forensic explosives samples often contain only trace amounts of the analytes of interest.

Finally, the ability of this methodology to analyze commercial explosives was demonstrated. Determining the composition of the samples allowed for the identification of the explosive as well as its potential origin in the case of RDX-based explosives. Furthermore, asymmetric peak shapes for the heavily nitrated aromatic species indicated a large driving force for their self-association.

V. References

---

1. R. Haas and G. Stork, *Fresenius Z. Anal. Chem.* **335**, 839 (1989).
2. R. Garg, D. Grasso, and G. Hoag, *Hazardous Waste and Hazardous Materials* **8**, 319 (1991).
3. W.J. Wuicik, W.L. Lowe, P.J. Marks, and W.E. Sisk, *Environmental Progress* **11**, 178 (1992).
4. T. Jenkins and M. Walsh, *Seminar on Technologies for Remediating Sites Contaminated with Explosives and Radioactive Wastes*, U.S. Environmental Protection Agency, Washington, DC (1993), Report No.: EPA/625/K-93/001.
5. A.B. Crockett, H.D. Craig, T.F. Jenkins, and W.E. Sisk, *Field Sampling and Selecting On-Site Analytical Methods for Explosives in Soil*, U.S. Environmental Protection Agency, Washington, DC (1996), Report No.: EPA/540/R-97/501.
6. [illegible] R. Midkiff, *Forensic Science Handbook*, R. Saferstein, Ed., [illegible]ents/Prentice Hall, Englewood Cliffs, pp. 222-226 (1982).

[illegible] Lyter, III, *J. Forensic Sci.* **28**, 446 (1982).

8. A.D. Beveridge, *Forensic Sci. Rev.* **4**, 17 (1992).
9. *Nitroaromatics and Nitramines by High Performance Liquid Chromatography (HPLC)*, U.S. Environmental Protection Agency, Washington, DC (1994), Report No.: SW-846 Update III, Method 8330.
10. C.A. Weisberg and M.L. Ellickson, *Am. Lab.* **30**, 32N (1998).
11. D.T. Burns and R.J. Lewis, *Anal. Chim. Acta* **307**, 89 (1995).
12. M.E. Walsh and T. Ranney, *J. Chromatogr. Sci.* **36**, 406 (1998).
13. K.G. Furton, J. Wang, Y.-L. Hsu, J. Walton, and J.R. Almirall, *J. Chromatogr. Sci.* **38**, 297 (2000).
14. P.H. Miyares, *Supercritical fluid chromatography for the analysis of nitroaromatics, nitramines and nitrate esters*, US Army Cold Regions Research and Engineering Laboratory, Hanover (1992), Report No.: 92-21.
15. J.E. Caton and W.H. Griest, *J. Liq. Chromatogr. Relat. Technol.* **19**, 661 (1996).
16. C.G. Bailey and C. Yan, *Anal. Chem.* **70**, 3275 (1998).
17. A. Hilmi and J.H.T. Luong, *Electrophoresis* **21**, 1395 (2000).
18. E. Mussenbrock and W. Kleiböhmer, *J. Microcol. Sep.* **7**, 107 (1995).
19. A. Hilmi, J.H.T. Luong, and A.-L. Nguyen, *Anal. Chem.* **71**, 873 (1999).
20. A. Hilmi, J.H.T. Luong, and A.-L. Nguyen, *J. Chromatogr. A* **844**, 97 (1999).
21. D.A. Cassada, S.J. Monson, D.D. Snow, and R.F. Spalding, *J. Chromatogr. A* **844**, 87 (1999).
22. S. Kennedy, B. Caddy, and J.M.F. Douse, *J. Chromatogr. A* **726**, 211 (1996).
23. G.R. Haugen, J.H. Richardson, J.E. Clarkson, and G.M. Hieftje, *Proceedings of the New Concepts Symposium and Workshop on Detection and Identification of Explosives*, U.S. Departments of Treasury, Energy, Justice, and Transportation, Reston, VA, pg. 249 (1978).
24. M.M. Ayad, *Z. Phys. Chem. (Munich)* **187**, 123 (1994).
25. Y. Rakicioglu, M.M. Young, and S.G. Schulman, *Anal. Chim. Acta* **359**, 269 (1998).
26. C.A. Heller, R.R. McBride, and M.A. Ronning, *Anal. Chem.* **49**, 2251 (1977).
27. H.H. Zeng, K.M. Wang, and R.Q. Yu, *Anal. Chim. Acta* **298**, 271 (1994).
28. K.J. Albert and D.R. Walt, *Anal. Chem.* **72**, 1947 (2000).
29. D. Rehm and A. Weller, *Israel J. Chem.* **8**, 259 (1970).
30. J.V. Goodpaster and V.L. McGuffin, *Appl. Spectrosc.* **53**, 1000 (1999).
31. L.R. Snyder and J.J. Kirkland, *Introduction to Modern Liquid Chromatography*, John Wiley and Sons, New York (1979).
32. R.J. Laub and J.H. Purnell, *J. Chromatogr.* **112**, 71 (1975).
33. R.J. Laub, *Physical Methods in Modern Chemical Analysis, Vol. 3.* T. Kuwana, Ed., Academic Press, New York, Chapter 5 (1983).
34. T.D. Schlabach and J.L. Excoffier, *J. Chromatogr.* **439**, 173 (1988).

35. P.J. Schoenmakers, H.A.H. Billiet, and L. de Galan, *Chromatographia* **15**, 205 (1982).
36. F.K. Ogasawara, Y. Wang, and V.L. McGuffin, *Appl. Spectrosc.* **49**, 1 (1995).
37. P. Suppan, *J. Chem. Soc., Faraday Trans. 1* **82**, 509 (1986).
38. J. Lakowicz, *Principles of Fluorescence Spectroscopy*, Plenum Press, New York (1983).
39. K. Kalyanasundaram and J.K. Thomas, *J. Am. Chem. Soc.* **99**, 2039 (1977).
40. W.E. Acree, Jr., S. Pandey, and S.A. Tucker, *Curr. Top. Solution Chem.* **2**, 1 (1997).
41. E.S. Yeung, *Acc. Chem. Res.* **22**, 125 (1989).
42. W.G. Palmer, M.J. Small, J.C. Dacre and J.C. Eaton, *Organic Energetic Compounds,* P.L. Marinkas, Ed., Nova Science Publishers, Commack, pg. 296 (1996).
43. S. Brunauer, P.H. Emmett, and E. Teller, *J. Am. Chem. Soc.* **60**, 309 (1938).
44. S. Brunauer, W.E. Demig, and E. Teller, *J. Am. Chem. Soc.* **62**, 1723 (1940).
45. L.R. Snyder, *Chromatography,* E. Heftmann, Ed., Van Nostrand Reinhold Company, New York, pg. 46 (1975).

CHAPTER 8

CONCLUSIONS AND FUTURE DIRECTIONS

While fluorescence quenching has long been a widely recognized phenomenon, the reliable application of selective fluorescence quenching to problems of analytical interest has been inhibited by a number of factors. These include poor understanding of the photophysical mechanism for selective quenching, laborious techniques for measuring the efficiency and selectivity of novel quenchers, a lack of quenchers that have been well-characterized, and few applications of selective quenching to the analysis of complex mixtures. This dissertation has attempted to address these deficiencies using a variety of theoretical and experimental techniques.

I. Ab Initio Calculations

Chapters 2 and 3 detail the use of ab initio quantum chemical calculations to investigate the mechanism by which alternant and nonalternant polycyclic aromatic hydrocarbons (PAHs) may be discriminated by selective quenching agents. In these calculations, ground- and excited-state properties were reliably predicted and agreed well with available experimental results. Importantly, systematic differences in the ground-state energy, excitation energy, electron distribution, and geometry of alternant and nonalternant PAHs were readily apparent. Studies of the interaction of pyrene and fluoranthene with nitromethane have shown that deactivation of the excited-state PAH can occur via direct energy transfer to the quencher or formation of a PAH–quencher ion

pair. However, symmetry selection rules dictate that formation of the ion pair is allowed, while direct energy transfer is forbidden. Furthermore, formation of an ion pair is energetically feasible only for pyrene, whereas this process is much less favorable for fluoranthene.

It is worthy to note that the calculations described here depict gas-phase interactions. Therefore, the prediction of solution-phase behavior is not reliable. This is reflected in part by the higher energy of the pyrene–nitromethane ion pair compared to its neutral excited-state complexes. As a result, there is a substantial energy deficit that must be overcome in order to form the ion-pair state. This deficit, calculated to be on the order of 0.7 – 0.8 eV, is substantially larger than the energy available to the PAH–quencher complexes under normal circumstances such as thermal motion (~200 cm^{-1} or ~0.025 eV) or excess electronic energy upon excitation (~0.4 eV for pyrene excited at 325 nm).

In response, the inclusion of a model for the solvation of the PAH–quencher complexes should lower the relative energy of the ion pair and enable more accurate predictions of solution-phase experimental data. Unfortunately, current computational models for solvation are incapable of accommodating excited-state molecules. Until that capability is realized, more approximate methods could be used. For example, the stabilization of a ground-state neutral complex, pyrene cation, and nitromethane anion by an appropriate solvation model could be calculated. The change in their calculated energy may provide a first approximation for the expected stabilization of an excited-state neutral complex and ion pair. However, this approach necessarily neglects the

non-trivial effect of solvation on the excitation energy of the complex as well as the energy of association between the neutral and ionic species.

Alternatively, the inclusion of additional solvent molecules surrounding the PAHs and PAH–quencher complexes in their ground and excited states may provide a more accurate simulation of a solution-phase environment. Specifically, a symmetric orientation of solvent molecules could form a crude solvent “cage” around the fluorophore and, in subsequent calculations, one solvent molecule could be replaced with a quencher of interest. While being computational intensive, this approach may be the best way to approach this problem at present.

Finally, there are some specific improvements to the computational methodologies that are likely to improve the accuracy of the ab initio results without causing an unacceptable increase in computational time. First, and as discussed in Chapter 2, the use of multireference configuration interaction techniques would correctly predict the order of the two lowest-lying singlet excited states of pyrene (and most likely benzo(*a*)pyrene). Second, charge-transfer appears to be the basis for the selective deactivation of alternant fluorophores such as pyrene. Therefore, inclusion of diffuse basis functions on the atoms of the fluorophore in addition to those of the quencher (as discussed in Chapter 3) would serve to more fully simulate these interactions.

II. Experimental Studies

Chapter 4 details the development and application of more rapid and accurate methods for the determination of Stern–Volmer constants. The system

as described demonstrated high sensitivity, achieved automated preparation and mixing of solutions by capillary flow injection methods, and was validated by comparison to traditional spectroscopic methods.

Continuing the development of reliable and rapid methods for evaluating the selectivity of novel quenchers will be crucial for future applications of this technique. In particular, further automation of the flow-injection apparatus described in Chapter 4 through inclusion of an auto-injector, computer-controlled gradient program, and fully integrated instrument control and data acquisition system would greatly aid this effort.

Chapter 5 examines a series of aliphatic amines as quenchers of alternant and nonalternant PAHs. It was found that these quenchers exhibit selectivity for nonalternant PAHs that tends to decrease with the electron-donating ability of the amine and with the number of amine groups. Among the quenchers studied, diisopropylamine was found to exhibit high efficiency and selectivity in acetonitrile, making it an attractive candidate for use in the analysis of complex mixtures of PAH isomers.

Of greatest interest for future developments in selective quenching is novel quenchers of not only alternant and nonalternant PAHs but other structurally similar compounds as well. For example, an initial study has indicated that triethylamine may selectively quench unsubstituted PAHs in the presence of PAHs with amino- functionalities (see Table 8-1). These data suggest that an even more powerful electron-donating amine such as triethylenediamine would be expected to efficiently quench unsubstituted PAHs

Table 8-1: Selective Quenching of PAHs and aza-PACs in the Presence of amino-PACs by Triethylamine

Fluorophore	**K_d (M^{-1})**
pyrene	45
1-aminopyrene	0.07
1-azapyrene	107
fluoranthene	179
3-aminofluoranthene	0.3
α^a	520

[a] Selectivity for PAHs and aza-PACs, defined as the average K_d for pyrene, 1-azapyrene, and fluoranthene divided by the average K_d for 10aminopyrene and 3-aminofluoranthene

(included alternant isomers) while amino-PAHs would be relatively unaffected.

Other potential schemes for discrimination of PAHs include the use of halogenated quenchers to selectively deactivate PAHs with either long fluorescence lifetimes or appropriate singlet-triplet energy levels. As noted in Chapter 5, nonalternant PAHs tend to have longer lifetimes in oxygenated solution than do their alternant isomers, so it may be possible to selectively promote phosphorescence among these compounds. The use of cyclodextrins to promote size selectivity is also possible. There is generally a fluorescence enhancement effect for a PAH located within the hydrophobic interior of a cyclodextrin, but covalently linking an efficient quencher to that region would enable the selective deactivation of PAHs above or below a particular ring number.

III. Analytical Applications

Chapter 7 describes the introduction of selective quenching agents into the column effluent after separation of complex mixtures of alternant and nonalternant PAHs. This method can provide class-selective profiles that characterize a sample and can simplify qualitative and quantitative analysis by reducing the number of interfering components. Discrimination of PAH isomers after separation could also be accomplished by immobilizing quenching substituents on a stationary phase and utilizing on-column fluorescence detection. If the collected emission was successfully spatially resolved, regions of the column with and without immobilized quenchers could be analyzed simultaneously. This would eliminate the need for mixing of quenching agents

with the mobile phase as well as multiple runs to acquire chromatograms with and without quencher present.

Chapter 8 describes the first time liquid chromatography has successfully been used to separate a standard mixture of nitrated explosives, albeit at the cost of a lengthy analysis time. The explosives were found to be powerful quenchers of fluorescence from PAHs such as pyrene. Furthermore, nitroaromatic quenchers displayed a selective response which appears to be based on their stabilization of the excited-state pyrene molecules. When adapted as an indirect detection method for liquid chromatography, fluorescence quenching has proven to be more sensitive than UV-visible absorbance.

The application of the selective interaction between pyrene and nitroaromatic quenchers shows great promise in the development of novel sensors. While many sensors have been based on the phenomenon of fluorescence quenching, they have generally suffered from a lack of selectivity and an inability to identify or classify unknown analytes. Sensors based on the quenching of pyrene immobilized on a polymer support, for example, would not only be sensitive but also be capable of discriminating nitroaromatic species from other explosives. The ability of such sensors to be portable is also an advantage to both forensic and environmental analysis, where on-site sampling can help guide criminal investigations and remediation efforts. Furthermore, as pyrene responds to many efficient quenchers, it could offer sensitivity to both organic and inorganic compounds that may be difficult to detect through other means. Hence, the analysis of low explosives such as black and smokeless powder, which contain high levels of inorganic nitrates, should also be feasible.

Finally, further improvements in the sensitivity and selectivity of indirect fluorescence quenching are also possible. This may be accomplished by lengthening the excited-state lifetime of the background fluorophore, either through removal of oxygen from the mobile phase and fluorophore solutions or through the use of phosphorescent compounds. As quenching constants are linearly dependent on fluorophore lifetime (see equation (1-1)), an increase in lifetime should result in a subsequent increase in the signal-to-noise ratio for the indirect fluorescence quenching method (see equation (7-5)). Lastly, if two spectrally-resolved fluorophores were used with differing electronic properties (i.e., pyrene and fluoranthene together with a CCD detector) the relative amount of quenching detected for each fluorophore would indicate the electron donating or withdrawing nature of the quencher.

APPENDICES

APPENDIX A

CALCULATED CARTESIAN COORDINATES (IN Å) FOR GROUND- AND EXCITED-STATE PAHs

Pyrene (S_0, ^1A_g)				Pyrene (S_1, $^1B_{2u}$)			
	x	y	z		x	y	z
C1	0.0000	2.4568	0.6697	C1	0.0000	2.4562	0.6816
C2	0.0000	1.2222	1.4227	C2	0.0000	1.2458	1.4245
C3	0.0000	0.0000	0.7163	C3	0.0000	0.0000	0.6887
C4	0.0000	0.0000	-0.7163	C4	0.0000	0.0000	-0.6887
C5	0.0000	1.2222	-1.4227	C5	0.0000	1.2458	-1.4245
C6	0.0000	2.4568	-0.6697	C6	0.0000	2.4562	-0.6816
C7	0.0000	-1.2222	1.4227	C7	0.0000	-1.2458	1.4245
C8	0.0000	-2.4568	0.6697	C8	0.0000	-2.4562	0.6816
C9	0.0000	-2.4568	-0.6697	C9	0.0000	-2.4562	-0.6816
C10	0.0000	-1.2222	-1.4227	C10	0.0000	-1.2458	-1.4245
C11	0.0000	1.2016	2.8139	C11	0.0000	1.2111	2.8218
C12	0.0000	0.0000	3.5007	C12	0.0000	0.0000	3.5140
C13	0.0000	-1.2016	2.8139	C13	0.0000	-1.2111	2.8218
C14	0.0000	1.2016	-2.8139	C14	0.0000	1.2111	-2.8218
C15	0.0000	0.0000	-3.5007	C15	0.0000	0.0000	-3.5140
C16	0.0000	-1.2016	-2.8139	C16	0.0000	-1.2111	-2.8218
H17	0.0000	3.3848	-1.2140	H17	0.0000	3.3892	-1.2170
H18	0.0000	3.3848	1.2140	H18	0.0000	3.3892	1.2170
H19	0.0000	2.1302	3.3573	H19	0.0000	2.1374	3.3682
H20	0.0000	0.0000	4.5760	H20	0.0000	0.0000	4.5882
H21	0.0000	-2.1302	3.3573	H21	0.0000	-2.1374	3.3682
H22	0.0000	-3.3848	1.2140	H22	0.0000	-3.3892	1.2170
H23	0.0000	-3.3848	-1.2140	H23	0.0000	-3.3892	-1.2170
H24	0.0000	-2.1302	-3.3573	H24	0.0000	-2.1374	-3.3682
H25	0.0000	0.0000	-4.5760	H25	0.0000	0.0000	-4.5882
H26	0.0000	2.1302	-3.3573	H26	0.0000	2.1374	-3.3682

Pyrene (S_2, $^1B_{1u}$)				Fluoranthene (S_0, $^1A_1$)			
	x	y	z		x	y	z
C1	0.0000	2.4391	0.6882	C1	0.0000	0.0000	-0.9055
C2	0.0000	1.2359	1.4207	C2	0.0000	0.0000	-2.2890
C3	0.0000	0.0000	0.7011	C3	0.0000	1.2775	-2.9162

C4	0.0000	0.0000	-0.7011	C4	0.0000	-1.2775	-2.9162
C5	0.0000	1.2359	-1.4207	C5	0.0000	1.1681	-0.1111
C6	0.0000	2.4391	-0.6882	C6	0.0000	-1.1681	-0.1111
C7	0.0000	-1.2359	1.4207	C7	0.0000	0.7054	1.2961
C8	0.0000	-2.4391	0.6882	C8	0.0000	-0.7054	1.2961
C9	0.0000	-2.4391	-0.6882	C9	0.0000	1.4030	2.4859
C10	0.0000	-1.2359	-1.4207	C10	0.0000	-1.4030	2.4859
C11	0.0000	1.2047	2.8394	C11	0.0000	0.6927	3.6821
C12	0.0000	0.0000	3.5223	C12	0.0000	-0.6927	3.6821
C13	0.0000	-1.2047	2.8394	C13	0.0000	2.3782	-0.7324
C14	0.0000	1.2047	-2.8394	C14	0.0000	-2.3782	-0.7324
C15	0.0000	0.0000	-3.5223	C15	0.0000	2.4121	-2.1563
C16	0.0000	-1.2047	-2.8394	C16	0.0000	-2.4121	-2.1563
H17	0.0000	3.3736	-1.2209	H17	0.0000	1.3494	-3.9898
H18	0.0000	3.3736	1.2209	H18	0.0000	-1.3494	-3.9898
H19	0.0000	2.1335	3.3814	H19	0.0000	2.4786	2.4965
H20	0.0000	0.0000	4.5974	H20	0.0000	-2.4786	2.4965
H21	0.0000	-2.1335	3.3814	H21	0.0000	1.2251	4.6164
H22	0.0000	-3.3736	1.2209	H22	0.0000	-1.2251	4.6164
H23	0.0000	-3.3736	-1.2209	H23	0.0000	3.3033	-0.1836
H24	0.0000	-2.1335	-3.3814	H24	0.0000	-3.3033	-0.1836
H25	0.0000	0.0000	-4.5974	H25	0.0000	3.3705	-2.6442
H26	0.0000	2.1335	-3.3814	H26	0.0000	-3.3705	-2.6442

Fluoranthene (S$_1$, ^{1}B$_2$)				Benzo(*a*)pyrene (S$_0$, ^{1}A')			
	x	y	z		x	y	z
C1	0.0000	0.0000	-0.8881	C1	0.0000	-0.6706	3.1380
C2	0.0000	0.0000	-2.2969	C2	0.0000	0.7268	2.7402
C3	0.0000	1.2734	-2.8984	C3	0.0000	1.0429	1.3578
C4	0.0000	-1.2734	-2.8984	C4	0.0000	1.7473	3.6692
C5	0.0000	1.1867	-0.0822	C5	0.0000	2.3896	0.9572
C6	0.0000	-1.1867	-0.0822	C6	0.0000	0.0000	0.3732
C7	0.0000	0.7365	1.2480	C7	0.0000	-0.7536	-1.9567
C8	0.0000	-0.7365	1.2480	C8	0.0000	-1.3681	0.8073
C9	0.0000	1.4304	2.4850	C9	0.0000	-2.3658	-0.1183
C10	0.0000	-1.4304	2.4850	C10	0.0000	-1.6491	2.2331
C11	0.0000	0.7207	3.6397	C11	0.0000	2.6802	-0.4451
C12	0.0000	-0.7207	3.6397	C12	0.0000	1.6972	-1.3628
C13	0.0000	2.4303	-0.7319	C13	0.0000	0.3094	-0.9869
C14	0.0000	-2.4303	-0.7319	C14	0.0000	3.0822	3.2641
C15	0.0000	2.4326	-2.1182	C15	0.0000	3.4006	1.9296
C16	0.0000	-2.4326	-2.1182	C16	0.0000	-2.0894	-1.5066

H17	0.0000	1.3586	-3.9702
H18	0.0000	-1.3586	-3.9702
H19	0.0000	2.5050	2.4991
H20	0.0000	-2.5050	2.4991
H21	0.0000	1.2312	4.5856
H22	0.0000	-1.2312	4.5856
H23	0.0000	3.3545	-0.1844
H24	0.0000	-3.3545	-0.1844
H25	0.0000	3.3802	-2.6282
H26	0.0000	-3.3802	-2.6282

Benzo(*a*)pyrene (S_1, $^1A'$)

	x	y	z
C1	0.0000	-0.7293	3.1284
C2	0.0000	0.6525	2.7705
C3	0.0000	0.9912	1.3748
C4	0.0000	1.6693	3.7228
C5	0.0000	2.3845	1.0032
C6	0.0000	0.0000	0.4018
C7	0.0000	-0.6878	-1.9803
C8	0.0000	-1.3842	0.7938
C9	0.0000	-2.3760	-0.1826
C10	0.0000	-1.6985	2.1829
C11	0.0000	2.6982	-0.3777
C12	0.0000	1.7264	-1.3335
C13	0.0000	0.3409	-1.0071
C14	0.0000	3.0128	3.3444
C15	0.0000	3.3624	2.0030
C16	0.0000	-2.0790	-1.5474
C17	0.0000	-3.1040	-2.5189
C18	0.0000	-2.8209	-3.8560
C19	0.0000	-1.4726	-4.2858
C20	0.0000	-0.4494	-3.3804
H21	0.0000	-2.7345	2.4728
H22	0.0000	-0.9913	4.1717
H23	0.0000	4.3998	1.7187
H24	0.0000	3.7325	-0.6731
H25	0.0000	2.0290	-2.3617
H26	0.0000	1.4094	4.7663
H27	0.0000	3.7789	4.0978
H28	0.0000	-3.4075	0.1234
H29	0.0000	0.5569	-3.7504

C17	0.0000	-3.1495	-2.4521
C18	0.0000	-2.8981	-3.7852
C19	0.0000	-1.5615	-4.2437
C20	0.0000	-0.5284	-3.3605
H21	0.0000	-2.6797	2.5409
H22	0.0000	-0.8969	4.1895
H23	0.0000	4.4300	1.6172
H24	0.0000	3.7096	-0.7574
H25	0.0000	1.9652	-2.4004
H26	0.0000	1.5083	4.7181
H27	0.0000	3.8625	4.0040
H28	0.0000	-3.3929	0.2030
H29	0.0000	0.4726	-3.7442
H30	0.0000	-4.1620	-2.0885
H31	0.0000	-3.7069	-4.4936
H32	0.0000	-1.3624	-5.3003

Benzo(*a*)pyrene (S_2, $^1A'$)

	x	y	z
C1	0.0000	-0.7157	3.1277
C2	0.0000	0.6472	2.7739
C3	0.0000	0.9983	1.3890
C4	0.0000	1.6824	3.7476
C5	0.0000	2.3762	1.0232
C6	0.0000	0.0000	0.3960
C7	0.0000	-0.7062	-2.0045
C8	0.0000	-1.3768	0.7895
C9	0.0000	-2.3683	-0.1993
C10	0.0000	-1.6938	2.1665
C11	0.0000	2.6927	-0.3624
C12	0.0000	1.7163	-1.3168
C13	0.0000	0.3465	-0.9877
C14	0.0000	2.9990	3.3729
C15	0.0000	3.3532	2.0178
C16	0.0000	-2.0702	-1.5724
C17	0.0000	-3.0960	-2.5399
C18	0.0000	-2.8090	-3.8877
C19	0.0000	-1.4852	-4.3071
C20	0.0000	-0.4546	-3.3708
H21	0.0000	-2.7291	2.4579
H22	0.0000	-0.9873	4.1684
H23	0.0000	4.3913	1.7365

H30	0.0000	-4.1261	-2.1829
H31	0.0000	-3.6144	-4.5805
H32	0.0000	-1.2515	-5.3378

Benzo(*b*)fluoranthene (S_0, $^{1}A'$)

	x	y	z
C1	0.0000	2.1789	-1.7643
C2	0.0000	0.8253	-1.3605
C3	0.0000	0.6038	0.0000
C4	0.0000	-0.3570	-2.2149
C5	0.0000	-0.6910	0.6144
C6	0.0000	1.6194	0.9686
C7	0.0000	-1.6323	-1.6073
C8	0.0000	2.9240	0.5576
C9	0.0000	3.1845	-0.8278
C10	0.0000	-0.4471	2.0729
C11	0.0000	0.9440	2.2866
C12	0.0000	-1.7827	-0.1658
C13	0.0000	-2.7777	-2.4254
C14	0.0000	-0.2826	-3.6187
C15	0.0000	1.4529	3.5701
C16	0.0000	-1.3191	3.1431
C17	0.0000	0.5694	4.6430
C18	0.0000	-0.8007	4.4324
C19	0.0000	-1.4130	-4.3918
C20	0.0000	-2.6769	-3.7896
H21	0.0000	4.2068	-1.1620
H22	0.0000	2.4423	-2.8054
H23	0.0000	3.7432	1.2544
H24	0.0000	-2.7791	0.2407
H25	0.0000	2.5142	3.7445
H26	0.0000	-2.3836	2.9890
H27	0.0000	-1.4689	5.2749
H28	0.0000	0.9531	5.6476
H29	0.0000	0.6780	-4.0986
H30	0.0000	-3.7470	-1.9584
H31	0.0000	-3.5632	-4.3981
H32	0.0000	-1.3296	-5.4638

H24	0.0000	3.7265	-0.6590
H25	0.0000	2.0192	-2.3455
H26	0.0000	1.4130	4.7889
H27	0.0000	3.7709	4.1213
H28	0.0000	-3.4006	0.1048
H29	0.0000	0.5539	-3.7360
H30	0.0000	-4.1190	-2.2071
H31	0.0000	-3.6065	-4.6087
H32	0.0000	-1.2477	-5.3555

Benzo(*b*)fluoranthene (S_1, $^{1}A'$)

	x	y	z
C1	0.0000	2.1009	-1.8106
C2	0.0000	0.7725	-1.3863
C3	0.0000	0.5872	0.0000
C4	0.0000	-0.4397	-2.1866
C5	0.0000	-0.6875	0.6510
C6	0.0000	1.6648	0.9575
C7	0.0000	-1.7075	-1.5322
C8	0.0000	2.9897	0.4742
C9	0.0000	3.1698	-0.8858
C10	0.0000	-0.3987	2.0365
C11	0.0000	1.0618	2.2182
C12	0.0000	-1.8344	-0.1221
C13	0.0000	-2.8756	-2.3495
C14	0.0000	-0.4020	-3.5978
C15	0.0000	1.6031	3.5321
C16	0.0000	-1.2353	3.1748
C17	0.0000	0.7592	4.5915
C18	0.0000	-0.6705	4.4107
C19	0.0000	-1.5400	-4.3475
C20	0.0000	-2.7983	-3.7049
H21	0.0000	4.1706	-1.2799
H22	0.0000	2.3433	-2.8564
H23	0.0000	3.8318	1.1415
H24	0.0000	-2.8148	0.3171
H25	0.0000	2.6683	3.6754
H26	0.0000	-2.3036	3.0596
H27	0.0000	-1.2944	5.2860
H28	0.0000	1.1481	5.5933
H29	0.0000	0.5501	-4.0959
H30	0.0000	-3.8355	-1.8636

H31	0.0000	-3.6975	-4.2954
H32	0.0000	-1.4841	-5.4209

APPENDIX B

CALCULATED INFRARED-ACTIVE VIBRATIONS FOR GROUND-STATE PAHs

Table B-1: Calculated Ground-State Infrared Frequencies for Pyrene

		Theory (HF/6-31G*)		Experiment (Gas Phase)[31,33]	
Symmetry	Assignment[31]	Frequency (cm^{-1})	I (relative)	Frequency (cm^{-1})	I (relative)
b_{3u}	-	95	0.003	95	-
b_{3u}	-	209	0.065	214	-
b_{2u}	-	340	0.010	350	-
b_{1u}		481	0.019		
b_{3u}		484	0.015		
b_{2u}		522	0.027		
b_{1u}		668	0.013		
b_{3u}	C–C bend	702	0.230	708	0.5
b_{3u}	C–H bend	753	0.098	740	0.2
b_{1u}		797	0.056		
b_{3u}	C–H bend	847	1.000	837	1.0
b_{2u}		913	0.002		
b_{1u}		972	0.011		
b_{3u}		984	0.023		
b_{2u}		1024	0.005		
b_{1u}	C–H bend	1070	0.026	1095	0.1
b_{2u}		1160	0.030		
b_{2u}	C–H bend	1179	0.055	1182	0.1
b_{1u}		1216	0.016		
b_{2u}		1225	0.022		
b_{1u}	C–C stretch	1420	0.101	1432	0.1
b_{2u}		1422	0.054		
b_{1u}		1427	0.008		
b_{2u}		1494	0.022		
b_{1u}	C–C stretch	1598	0.168	1596	0.1
b_{2u}		1615	0.028		
b_{1u}		2983	0.021		
b_{1u}		2986	0.001		

b_{2u}		2993	0.178		
b_{2u}		3005	0.705		
b_{1u}	C–H stretch	3010	0.728	3051	0.9

Table B-2: Calculated Ground-State Infrared Frequencies for Fluoranthene

		Theory (HF/6-31G*)		Experiment (Gas Phase)[31]	
Symmetry	Assignment[31]	Frequency (cm^{-1})	I (relative)	Frequency (cm^{-1})	I (relative)
b_1		101	0.021		
b_1		161	0.023		
b_2		198	0.001		
b_1		294	0.004		
a_1		338	0.002		
b_1		426	0.006		
b_1		451	0.000		
b_2		454	0.004		
a_1		468	0.013		
b_2		541	0.004		
a_1		541	0.031		
b_2		595	0.001		
b_1		612	0.125		
a_1		652	0.019		
b_2		740	0.025		
b_1	C–H bend	750	0.159	741	0.3
a_1		775	0.036		
b_1	C–H bend	777	1.000	773	1.0
b_1	C–H bend	824	0.344	825	0.1
a_1		862	0.006		
b_1		922	0.006		
b_2		946	0.006		
b_1		949	0.015		
b_2		956	0.002		
b_1		989	0.014		
a_1		995	0.027		
a_1		1008	0.020		
b_2		1053	0.005		
a_1		1068	0.009		
b_2		1090	0.065		
a_1		1100	0.011		
b_2		1127	0.029		
a_1		1157	0.014		
b_2		1168	0.012		
a_1		1205	0.002		

b_2		1208	0.005		
a_1		1263	0.005		
b_2		1272	0.010		
b_2		1324	0.001		
a_1		1339	0.010		
a_1		1371	0.213		
a_1		1406	0.080		
b_2	C–C stretch	1426	0.145	1426	0.2
a_1	C–C stretch	1447	0.571	1454	0.4
b_2		1461	0.040		
b_2		1480	0.062		
a_1		1580	0.001		
a_1		1607	0.000		
b_2		1615	0.009		
a_1	C–C stretch	1620	0.019	1609	0.1
b_2		1632	0.003		
b_2		2985	0.022		
b_2		2985	0.000		
a_1		2986	0.014		
a_1		2992	0.074		
b_2		2996	0.005		
a_1		2998	0.274		
b_2		3003	0.251		
b_2	C–H stretch	3009	0.688	3066	0.7
a_1		3010	0.367		
a_1		3014	0.316		

Table B-3: Calculated Ground State Infrared Frequencies for Benzo(*a*)pyrene

		Theory (HF/6-31G*)		Experiment (Gas Phase)[31]	
Symmetry	Assignment[31]	Frequency (cm^{-1})	I (relative)	Frequency (cm^{-1})	I (relative)
a"		57	0.004		
a"		82	0.000		
a"		148	0.009		
a"		179	0.001		
a'		204	0.010		
a"		208	0.068		
a"		276	0.000		
a"		294	0.000		
a'		319	0.001		
a'		366	0.002		
a"		381	0.001		
a'		439	0.009		

a"		453	0.034		
a'		462	0.006		
a'		495	0.049		
a"		495	0.004		
a'		504	0.013		
a"		511	0.005		
a"		532	0.050		
a'		544	0.008		
a"		549	0.001		
a'		588	0.012		
a'		615	0.066		
a"		661	0.001		
a'		675	0.029		
a"	C–C bend	679	0.149	687	0.3
a'	C–C bend	734	0.021	741	0.5
a"		740	0.010		
a"	C–H bend	752	0.534	757	1.0
a"		762	0.328		
a'		790	0.124		
a"		795	0.002		
a"		808	0.004		
a'		820	0.002		
a"	C–H bend	835	0.674	822	0.5
a"	C–H bend	855	0.100	847	0.3
a'		858	0.045		
a"	C–H bend	901	0.343	879	0.4
a"		913	0.094		
a'		936	0.006		
a"		963	0.021		
a"		977	0.010		
a'		983	0.028		
a"		985	0.009		
a"		994	0.002		
a'		994	0.006		
a"		996	0.002		
a'	C–C stretch	1040	0.004	1023	0.2
a'		1061	0.030		
a'	C–C stretch	1072	0.003	1079	0.1
a'		1104	0.004		
a'		1132	0.006		
a'		1139	0.006		
a'		1158	0.042		
a'		1177	0.005		
a'	C–C stretch	1182	0.020	1185	0.1

a'		1203	0.052		
a'		1214	0.017		
a'		1240	0.079		
a'	C–C stretch	1264	0.009	1263	0.1
a'		1286	0.011		
a'		1298	0.002		
a'		1319	0.000		
a'		1335	0.014		
a'		1388	0.089		
a'		1393	0.035		
a'		1415	0.011		
a'		1418	0.019		
a'		1436	0.008		
a'		1465	0.089		
a'		1491	0.023		
a'		1504	0.052		
a'		1574	0.065		
a'		1592	0.013		
a'		1605	0.069		
a'		1613	0.015		
a'		1631	0.094		
a'		1652	0.013		
a'		2984	0.002		
a'		2985	0.024		
a'		2987	0.004		
a'		2990	0.058		
a'		2991	0.014		
a'		2996	0.192		
a'		2997	0.337		
a'		3006	0.538		
a'	C–H stretch	3011	1.000	3056	0.9
a'		3012	0.180		
a'		3025	0.046		
a'		3049	0.358		

Table B-4: Calculated Ground-State Infrared Frequencies for Benzo(*b*)fluoranthene

		Theory (HF/6-31G*)		Experiment (Gas Phase)[31]	
Symmetry	Assignment[31]	Frequency (cm^{-1})	I (relative)	Frequency (cm^{-1})	I (relative)
a"		64	0.008		
a"		92	0.001		
a"		113	0.018		

a"		148	0.000		
a'		157	0.001		
a"		228	0.007		
a'		257	0.002		
a"		266	0.006		
a'		318	0.002		
a"		319	0.001		
a'		377	0.001		
a"		417	0.001		
a"		426	0.007		
a"		460	0.021		
a'		465	0.006		
a"		501	0.066		
a'		525	0.037		
a'		545	0.028		
a"		547	0.002		
a'		574	0.017		
a"		602	0.000		
a'		603	0.091		
a"		618	0.014		
a'		647	0.003		
a'		667	0.006		
a"		730	0.137		
a"	C–H bend	745	0.408	741	1.0
a"		751	0.263		
a'		762	0.019		
a"		764	0.003		
a"	C–H bend	775	1.000	774	0.4
a'		778	0.017		
a"		813	0.032		
a'		833	0.008		
a"		866	0.017		
a"		882	0.007		
a'		909	0.009		
a"	C–H bend	911	0.174	887	0.2
a"		915	0.019		
a"		950	0.014		
a"		962	0.029		
a'		971	0.025		
a"		979	0.015		
a"		990	0.000		
a'		990	0.041		
a"		995	0.000		
a'		1001	0.026		

a'		1023	0.002		
a'		1045	0.005		
a'		1072	0.035		
a'		1080	0.023		
a'		1089	0.007		
a'		1122	0.044		
a'		1129	0.029		
a'		1138	0.014		
a'		1163	0.010		
a'		1172	0.025		
a'		1202	0.025		
a'		1225	0.048		
a'		1235	0.025		
a'		1266	0.002		
a'		1272	0.058		
a'		1290	0.047		
a'		1316	0.157		
a'	C–C stretch	1346	0.041	1374	0.1
a'		1402	0.082		
a'		1430	0.306		
a'	C–C stretch	1442	0.108	1442	0.2
a'		1450	0.382		
a'		1457	0.050		
a'		1476	0.069		
a'	C–C stretch	1525	0.166	1524	0.1
a'		1581	0.006		
a'	C–C stretch	1598	0.099	1599	0.2
a'		1612	0.033		
a'		1615	0.020		
a'		1616	0.014		
a'		1646	0.009		
a'		2985	0.009		
a'		2986	0.009		
a'		2988	0.083		
a'		2992	0.019		
a'		2994	0.066		
a'		2996	0.205		
a'		3003	0.003		
a'	C–H stretch	3004	0.725	3071	0.6
a'		3010	0.078		
a'		3014	0.518		
a'		3016	0.430		
a'		3026	0.442		

MICHIGAN STATE UNIVERSITY LIBRARIES
3 1293 02125 9084